



Universiteit
Leiden
The Netherlands

Tales of Orion : the interplay of gas, dust, and stars in the interstellar medium

Ochsendorf, B.B.

Citation

Ochsendorf, B. B. (2015, September 1). *Tales of Orion : the interplay of gas, dust, and stars in the interstellar medium*. Retrieved from <https://hdl.handle.net/1887/34931>

Version: Not Applicable (or Unknown)

License: [Leiden University Non-exclusive license](#)

Downloaded from: <https://hdl.handle.net/1887/34931>

Note: To cite this publication please use the final published version (if applicable).

Cover Page



Universiteit Leiden



The handle <http://hdl.handle.net/1887/34931> holds various files of this Leiden University dissertation.

Author: Ochsendorf, Bram Benjamin

Title: Tales of Orion : the interplay of gas, dust, and stars in the interstellar medium

Issue Date: 2015-09-01

Tales of Orion

The interplay of gas, dust, and stars
in the interstellar medium

Cover design: Angelica Consejo. Background image credit front cover (adapted): Rogerio Bernal Andreo (Deep Sky Colors). Image credit back cover (adapted): J. Bally/D. Devine/B. Reipurth/NOAO/AURA/NSF.

Tales of Orion

The interplay of gas, dust, and stars
in the interstellar medium

Proefschrift

ter verkrijging van
de graad van Doctor aan de Universiteit Leiden,
op gezag van Rector Magnificus prof. mr. C. J. J. M. Stolker,
volgens besluit van het College voor Promoties
te verdedigen op dinsdag 1 september 2015
klokke 15:00 uur

door

Bram Benjamin Ochsendorf

geboren te Wijhe
in 1986

Promotiecommissie

Promotores: Prof. dr. A. G. G. M. Tielens
Prof. dr. L. Kaper (University of Amsterdam)

Overige leden: Prof. dr. J. Bally (University of Colorado at Boulder)
Prof. dr. B. T. Draine (Princeton University)
Prof. dr. M.-M. Mac Low (American Museum of Natural History)
Prof. dr. P. P. van der Werf
Prof. dr. H. J. A. Röttgering

Contents

1	Introduction	9
1.1	The interstellar medium	11
1.1.1	Infrared missions	12
1.1.2	Interstellar dust	14
1.2	The interplay of gas, dust, and stars	15
1.2.1	Formation and evolution of H II regions and wind-blown-bubbles	15
1.2.2	OB associations, supernovae, and superbubbles	19
1.2.3	Dust as a tracer and intermediary of radiative feedback	22
1.2.4	Summary: the energy balance of the ISM	24
1.3	Orion as a benchmark study	25
1.4	This thesis	27
2	Blowing in the wind: The dust wave around σ Ori AB	29
2.1	Introduction	30
2.2	Observations	31
2.3	Stellar properties and local physical conditions	32
2.3.1	Basic stellar properties and space velocities	32
2.3.2	Wind properties	34
2.3.3	Photo-evaporation flow	35
2.4	Bow waves and dust waves	36
2.4.1	Dust distribution	37
2.4.2	Dust mass	38
2.5	Physics of bow waves and dust waves	40
2.5.1	Dust component	40
2.5.2	Gas component	42
2.5.3	Modeling the interaction between the flow and σ Ori AB	42
2.6	Results	44
2.6.1	Coulomb interactions	46
2.6.2	Bow shock scenario	48
2.7	Discussion	50
2.7.1	Grain charge and Coulomb interaction	54
2.8	Conclusion	56
2.A	IR arcs around candidate weak-wind stars	57
3	A bimodal dust grain distribution in the IC 434 H II region	59
3.1	Introduction	60
3.2	Observations	61
3.3	The expanding H I shell surrounding Orion OB1b	61
3.3.1	The GS206-17+13 shell: mass and kinetic energy	61
3.3.2	Driving source of the GS206-17+13 shell	63
3.3.3	Space velocities of Orion OB1b and approach of σ Ori	64
3.4	Dust emission from the IC 434 region	65
3.4.1	Morphological structures	65
3.4.2	Spectral energy distributions	67

3.4.3	Are we tracing emission from the ionized gas?	67
3.5	The flow of dust into the IC 434 region	76
3.5.1	Modeling the flow of ionized gas	76
3.5.2	Flow parameters	78
3.5.3	The formation of dust waves	80
3.5.4	The equilibrium- and minimum radius of a dust wave	81
3.6	Modeling results	83
3.6.1	A bimodal dust distribution	83
3.7	Discussion	85
3.7.1	Derived dust properties	85
3.7.2	Limitations of the model	87
3.7.3	PAH emission from the ionized gas	88
3.8	Conclusions	89
4	Radiation-pressure-driven dust waves inside bursting interstellar bubbles	91
4.1	Introduction	92
4.2	Observations and method	93
4.2.1	Hydrodynamical simulations	93
4.3	Results	93
4.3.1	Hydrodynamical simulations of RCW 120	95
4.3.2	Model for dusty photo-evaporation flows	98
4.3.3	Location of dust waves and dust-gas coupling	100
4.4	Discussion and conclusion	103
5	Nested shells reveal the rejuvenation of the Orion-Eridanus superbubble	107
5.1	Introduction	108
5.2	Observations	108
5.3	Results	109
5.3.1	Dust in Barnard's Loop	109
5.3.2	Dust and gas in the Orion-Eridanus superbubble	112
5.3.3	Expanding shells within the Orion-Eridanus region	118
5.4	Discussion	123
5.4.1	An updated picture of the Orion-Eridanus superbubble	124
5.4.2	The nested shells and their relation to Orion OB1	131
5.4.3	Evolution of the Orion-Eridanus superbubble	132
5.4.4	Dust processing in superbubbles	140
5.5	Summary	141
6	Summary & outlook	143
	Bibliography	149
	Curriculum Vitae	159
	Publications	161
	Nederlandse Samenvatting	163
	Acknowledgements	167

1

Introduction

The constellation of Orion is one of the most discernable patterns in the northern hemisphere, and has acted as an important beacon for generations throughout history. Orion stands central in many mythological tales. One of my personal favorites describes the figure of Orion, the hunter, standing by the river Eridanus, hunting the celestial animals Taurus and Lepus together with his loyal companions, Canis Major and Canis Minor. In modern astronomy, the Orion region remains one of the best studied regions in the sky. The region is favorably placed offset from the Galactic plane, limiting the confusion with unrelated structures along the same line of sight. Furthermore, it harbors the nearest region of ongoing massive star formation, and because of its proximity, allows observations to resolve structures down to \sim AU scales only to unveil a brilliant amount of detail, while stellar parallaxes can be measured to provide clues to the space motion of its stars.

Figure 1.1 offers a multi-wavelength view of the entire Orion star forming region, tracing infrared emission from cosmic dust, while ionized gas is captured through narrow-band imaging at optical wavelengths. The image stretches over a magnificent extent of the sky and, moreover, demonstrates the advent of observational facilities that allow us to probe interstellar structures across the electromagnetic spectrum unseen to the human eye. The positions of the constellation's seven most recognizable stars are overplotted. By now, we know that Orion has given birth to some $\sim 10^4$ stars in the last 10 - 15 Myr, scattered in clusters and subgroups over the entire region, which in its entirety is known as the Orion OB association. The feedback from the most massive stars have left their mark on the surrounding interstellar material, creating a highly complex and chaotic environment. In this respect, figure 1.1 is striking, and captures the interaction of gas, dust, and stars on every observable scale, underlining the importance of gas- and dust dynamics in our quest to fully comprehend the physical processes that determine the formation and evolution of stars and their interaction with the interstellar medium (ISM).

In this thesis, I aim to obtain a better understanding of the interactions between gas, dust, and stars in the ISM, by using the Orion region as a benchmark model. The interplay between these constituents remains poorly understood, as results from ever better observational facilities continuously throw theorists back to the drawing board to revisit some of the most fundamental questions in ISM research. Yet, these observational opportunities offer the astronomical community with a new vantage point of the ISM that gives rise to so much new research fields. Still, to advance our understanding of the ISM of galaxies, in first principle, we need to acquire a deep understanding of the interplay between stars and their surroundings. How do massive stars and OB associations shape the neighboring ISM? How much energy is coupled to the ISM through their supernovae, stellar winds, and UV radiation, and how does this reflect on the phase structure of the ISM? How are molecular clouds formed and destroyed? How does stellar feedback regulate star formation efficiency? How are galactic outflows driven, and what is exactly the

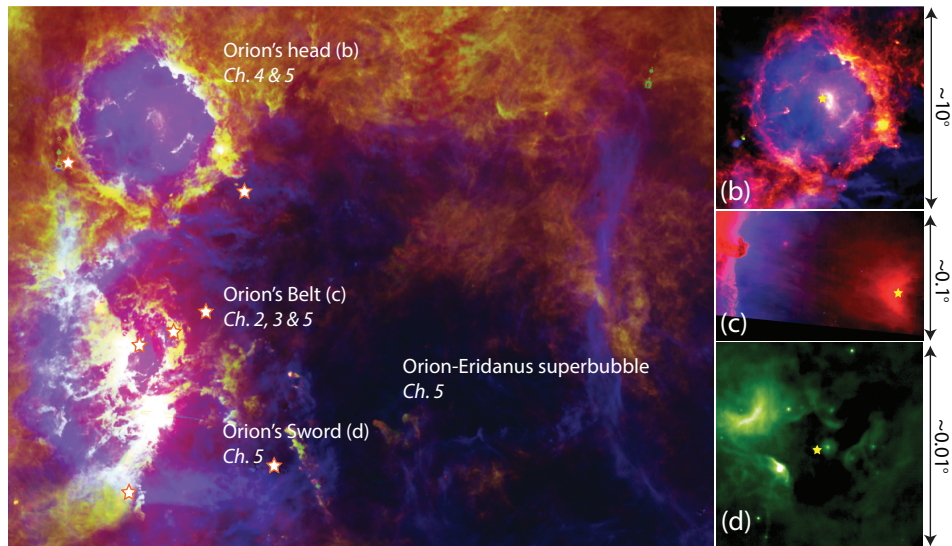


Figure 1.1: (a) Three-color image of part of the Orion-Eridanus region. $H\alpha$ (blue) reveals ionized gas, surrounded by a layer of carbonaceous molecules (polycyclic aromatic hydrocarbons) or stochastically-heated small dust grains, traced by the $12\ \mu\text{m}$ passband of the *Wide-field Infrared Explorer* (WISE; Sec. 1.1.1) shown in green. Red is 353 GHz emission detected by the *Planck* satellite, tracing columns of cold (20 K) dust. The polycyclic aromatic hydrocarbons/small grains trace the ultraviolet-illuminated edges of the clouds containing cold dust, resulting in that red and green blend to form yellow. The field of view stretches $\sim 28^\circ \times 38^\circ$ on the sky. Overplotted are the bright stars of the Orion constellation, and explicitly labelled are subregions within Orion that form the starting point and/or subject of research in the denoted chapters of this thesis. (b), (c) & (d): Infrared arc-like structures wrap around stars in Orion (yellow asterisks) on every observable scale. Figure (b) is a multi-degree view of the λ Ori region (Orion's head), figure (c) is an arcminute-scale picture of the σ Ori region in Orion's Belt (note the Horsehead Nebula on the left), while figure (d) is an arcsecond-scale zoom of the Trapezium region within Orion's sword. The arcs can be exploited to quantify the interaction between stars with their surroundings (Sec. 1.2.3) and exemplify the importance of dynamics within the interstellar medium.

role of the halo and the intergalactic medium (IGM) in the mass and energy budget of the ISM? In the following chapters of this thesis, I will attempt to tackle some of these questions by using novel and perhaps somewhat unconventional approaches, which are needed to evolve from equilibrium models to an ISM that is highly turbulent, filled with dynamical structures on all observable scales.

In the remainder of this introduction, some historical breakthroughs and recent development in ISM research will be highlighted. We will briefly touch upon how past infrared missions have been exploited to trace the structure and evolution of the ISM. Interstellar dust is a key player in this regard and stand central in this thesis work: we will discuss the (dis)advantages of dust as a tracer of, e.g., star formation, and the structure and physics of the ISM. Subsequently, the main dynamical effects of massive stars on the ISM will be reviewed. We will follow this somewhat chronologically, starting with the formation of H II regions and the main forces that drives the expansion of these ionized volumes, and

will discuss several mechanisms that may influence the evolution of H II regions. Photo-evaporation flows of ionized gas are important carriers of mechanical energy: we will briefly discuss flow structures and how they depend on the shape of ionization fronts. We will then move towards larger scales, and discuss the formation of superbubbles through the collective efforts of radiation, stellar winds, and supernovae of massive stars. We will devote a special subsection on dust and its importance to the radiative feedback of massive stars to their surroundings, which will constitute a major part of this thesis. We will then summarize and discuss how the different mechanisms contribute to the kinetic energy budget of the ISM, i.e., how does stellar feedback couple to the dust and gas, in what way this relates to the velocity and density structure of the ISM, and how this impacts the formation of subsequent generations of stars. Finally, we set out on a journey in the constellation of Orion, and discuss its importance and usage as a benchmark to ISM and star formation studies.

1.1 The interstellar medium

Our view of the Galactic system has undergone numerous paradigm-changing discoveries since the development of astronomical instrumentation flourished. The view that the cosmos consisted of more than just stars immersed in an empty void was kick-started with observations of the Orion Nebula by Fabri de Peiresc in 1610 (Dufay 1957), Huygens (1659), and Messier (1771), who included the Orion nebula in his catalogue of nebulae and star clusters as its forty-second entry ('M42'). Herschel (1789) described the bright patch located in the sword of Orion as "*an unformed fiery mist, the chaotic material of future suns*". It was soon accepted that many objects in the sky could be classified as 'nebulae', i.e., bright bodies that appeared unresolved to the telescopes at the time. Building upon the work of Herschel (1789), the first comprehensive catalogue of nebulae was compiled by Dreyer (1888) in the *New General Catalogue*, including all types of objects that are observed in deep space, such as planetary nebula, emission nebula, H II regions, and galaxies, which often showed a spiral structure and were therefore classified as 'spiral nebulae'. The Orion nebula is listed here as object NGC 1976. In 1904, Hartmann (1904) discovered that in the spectrum of δ Orionis, the calcium K line did not follow the periodic displacements of the photospheric lines caused by the orbital motion of the star. The narrow line profile seemed to be detached from the stellar photosphere and, therefore, Hartmann (1904) concluded that it must have originated from space located along the line of sight towards δ Orionis. Other stars revealed the same phenomenon and, in addition, more distance stars showed stronger absorption of the detached lines. Thus, gas (or matter in general) was shown to exist freely in space, filling the medium between the stars, much like a rarefied gas.

Early photographs of the Milky Way from 1869 onwards revealed dark, sharply defined spots of sky exhibiting a clear absence of stars. The existence of the black patches in the sky were already mentioned by Herschel (1785), which he described as 'Openings in the Heavens'. Barnard (1919) examined these apparent openings, but concluded that they must constitute clouds or structures of opaque material that stand out strong and black against the light of many unresolved stars behind them. Trumpler (1930) then showed through a study of open clusters in the Milky Way that their sizes and magnitudes could only be explained by a widespread absorption in space that was correlated with

distance, and produced the first reddening curves by measuring the color excess between ‘visual’ and ‘photographic’ magnitude. The wavelength dependence of the starlight extinction could only be explained by small, solid particles that absorb starlight on a spectral range much broader than the discrete, narrow bands from transitions of specific atoms or molecules. In the end, these results led to the belief that solid particles must reside in space alongside the gaseous material obvious from absorption spectra.

By now, we know that the space between stars is filled with a dilute mixture of atoms, molecules, and dust grains, which we call the interstellar medium (ISM). As quoted from D. Osterbrock (1984), “*The interstellar medium is anything not in stars*”. While this is true by definition, it disregards that the ISM and stars are intimately linked. Stellar feedback through ultraviolet (UV) radiation, winds, and supernova explosions dominate the energy input into the ISM and generate shockwaves that collect gas and dust in giant shells. Atomic and molecular clouds collapse and condense in these shells and, once they become gravitationally unstable, may form a new generation of stars of which the most massive constituents will, in their turn, end their lives as a supernova. After the lifetime of each stellar generation, the material of the ISM will become enriched with heavy materials created through nucleosynthesis.

The physics of the ISM is a crucial part in many areas of astronomy, such as the formation and evolution of stars and entire galaxies. It regulates molecule- and dust grain synthesis, which together constitute the very building blocks of planetesimals required to form planetary systems and, ultimately, life itself. The first global models of the ISM consisted of a two-phase medium (e.g., Field et al. 1969), in which a cold cloud phase and a warm intercloud phase could co-exist through thermal and pressure equilibrium set by the relevant heating and cooling processes. This was later extended to a three-phase model by implementing a third hot coronal phase created by shock waves from supernova explosions (McKee & Ostriker 1977). While these early models have had their success in explaining many of the basic principles of the ISM, neither picture has proven to be complete. Observations from, e.g., the *Spitzer Space Telescope* and the *Herschel Space observatory*, revealed that a significant fraction of the interstellar medium is dynamic, clumpy, and filamentary (Fig. 1.2), likely caused by an interplay between stellar feedback and the ISM. However, additional sources of pressure may contribute, such as magnetic fields, cosmic ray heating, and turbulent motions that stir the phases of the ISM in a non-linear fashion. Indeed, the existence of large volumes of gas at temperatures that are traditionally thought to be thermally unstable (Heiles 2001) prove that our knowledge of the ISM may be far from complete. Besides the phase structure of the ISM, the mysterious origin of the diffuse interstellar bands (Herbig 1995) and the 2175 Å extinction bump (Draine 1989) imply that we do not have a complete census of the constituents of the ISM. Nonetheless, tremendous progress is being made both observationally and computationally, with observational facilities pushing the boundaries of both sensitivity and spatial resolution, and computational facilities that are able to incorporate an ever increasing amount of ‘realism’ into simulations, such as fully self-consistent hydrodynamics including gas-phase transitions, chemical networks, dust physics, and star formation- and feedback.

1.1.1 Infrared missions

Infrared astronomy has classically been hampered by the fact that the Earth’s atmosphere is largely opaque in this wavelength region. While in the wavelength range 1 μm - 30 μm

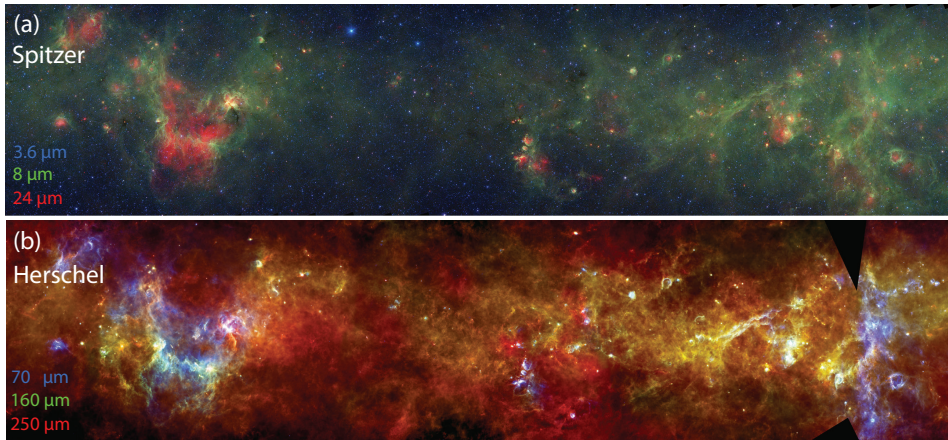


Figure 1.2: Panoramic view of the Galactic plane, stretching between $318 > l > 310$ degrees longitude that crosses the Circinus and Centaurus constellations. In visible light, this area of the Galactic plane is nearly featureless, obscured by dust that figures prominently in the infrared images from *Spitzer* (a) and *Herschel* (b). These observatories introduced a paradigm shift in our view of the interstellar medium, which appeared to be highly dynamic and turbulent. As this figure illustrates, dust is a unique tool to trace the structure of the ISM on all resolvable scales. Image credit *Spitzer*: NASA/JPL-Caltech/Univ. of Wisconsin. Image credit *Herschel*: ESA/PACS & SPIRE Consortium, Sergio Molinari, Hi-GAL Project.

several windows still exist where the atmosphere is (partly) transparent, for wavelengths between $30 \mu\text{m}$ and $400 \mu\text{m}$ the atmosphere is fully opaque. In order to allow infrared studies of astronomical objects in this wavelength range, one must get above as much of the Earth's atmosphere as possible. People thought of mountains, flying balloons, aircrafts, and even space. In this regard, infrared missions literally took off in the 1970's with the launch of the *Kuypers Airborne Observatory* (KAO; 1974), which was later followed-up by the first infrared space mission, the *Infrared Astronomical Satellite* (IRAS; 1983), marking the beginning of a golden era in infrared space observatories that included the *Infrared Space Observatory* (ISO; 1995), the *Spitzer Space Telescope* (2003), the *Herschel Space Observatory* (2009), *Planck* (2009), and the *Wide-field Infrared Survey Explorer* (2009). Finally, in 2010 the *Stratospheric Observatory for Infrared Astronomy* (SOFIA) aboard a heavily modified 747 airplane saw first light. Each of these missions had its own specific features and goals, pushing the boundaries of infrared astronomy in either spatial resolution, sensitivity, and/or sky coverage.

The contents of this thesis largely revolve around observations taken with most of the aforementioned infrared observational facilities. Here, we particularly mention the large-scale, high-resolution surveys of the Galactic plane, *Spitzer/GLIMPSE* (Fig. 1.2a; Benjamin et al. 2003), *Spitzer/MIPS-GAL* (Fig. 1.2a; Carey et al. 2009), and *Herschel/Hi-GAL* (Fig. 1.2b; Molinari et al. 2010). The *GLIMPSE* survey at $3.6 \mu\text{m}$ primarily traces the stellar content of the Galaxy, while at $8 \mu\text{m}$ Polycyclic Aromatic Hydrocarbons (PAHs) are probed that are located within photo-dissociation regions where UV photons penetrate, making the $8 \mu\text{m}$ band a robust tracer of PDRs and (massive) star formation activity. Heated by starlight, warm dust at $\sim 100 \text{K}$ emits within the $24 \mu\text{m}$ mid-IR

wavelength channel of the MIPS GAL survey. The Herschel/Hi-GAL survey extended the high-resolution coverage of the Galactic plane towards longer wavelengths, providing spatially resolved emission maps of the cold component (~ 20 K) of interstellar dust. Together, these missions reveal an incredible richness of detail in the intricate interactions between gas, dust, and stars that drives the evolution of the ISM (Fig. 1.2).

1.1.2 Interstellar dust

The infrared studies discussed in Sec.1.1.1 revealed that interstellar dust is a ubiquitous component of the cosmos that pervades the Milky Way (Fig. 1.2) and other galaxies. Dust acts as a blanket that extinguishes the light from background sources in a way that is directly related to the intrinsic properties of the grains. Dust is a minor ($\sim 1\%$ in mass of the ISM), yet crucial component of the ISM. It is the dominant source of opacity of the ISM at wavelengths above 912 \AA , and by this controls the appearance of galaxies at these wavelengths by absorbing visual and ultraviolet light, and re-emitting it in the infrared. Dust stands central within interstellar chemistry by providing a surface that acts as a catalyzer for reactions between species, by shielding molecular regions from dissociating stellar radiation fields, and by controlling gas phase densities through the accretion and release of gas species onto/from their mantles. Dust grains control the temperature of the ISM as they account for much of the enriched elements that provide cooling through gas emission lines, while the photo-electric effect is considered to be the most important heating mechanism of (neutral) interstellar gas. In short, dust can be used as a tracer of gas masses and star formation rates, while probing the structural, physical, and evolutionary conditions of the ISM.

The above emphasizes the key position that dust holds within the physical and chemical processes that govern the ISM of galaxies. However, many of these details on interstellar dust are based on empirical grounds, as the precise composition or physical properties of dust grains remain largely unknown. A coherent picture of dust composition and physical characteristics in the various phases of the ISM can only be accomplished by confronting theory and laboratory work with observations. In the last few decades, dust models of increasing sophistication have been constructed, often incorporating polycyclic aromatic hydrocarbons, graphite, and ‘astronomical silicates’. These models have proven to be able to model quite robustly the extinction, emission, polarization, and abundances of dust in the diffuse ISM at high Galactic latitudes (e.g., Li & Draine 2001; Draine & Li 2007; Compiègne et al. 2011). However, these models are now being challenged by present-day observations of increasing sensitivity and angular resolution from the different phases present in the ISM. One simplifying assumption often made is that dust grains are spherical, even though dust is expected to coagulate to large, fluffy aggregate structures in molecular clouds (Ossenkopf & Henning 1994; Ormel et al. 2009). It is unclear to what extent the grains retain this shape when exposed to the harsh conditions of the diffuse ISM, as the grains will be processed through UV radiation, shocks, and thermal sputtering with the gas (Tielens et al. 1994; Jones et al. 1996). Indeed, dust cycles from clouds to the diffuse phase of the ISM (Tielens 1998, 2013) and the evolution of its composition, geometry, and optical properties seem to evolve when moving from one phase to the other (Jones 2014).

1.2 The interplay of gas, dust, and stars

The Galactic ecosystem is in constant motion due to the interaction between the ISM and the stars that are immersed within it. Stars tend to form within groups or large clusters (Lada & Lada 2003), and albeit small in number compared to their lower-mass siblings, the most massive component of the stellar population dominates the thermal and velocity structure of the ISM through their intense radiation, powerful stellar winds, and devastating supernova explosions. The constant input of radiative and mechanical energy provides feedback mechanisms that results in an ISM that is, irrefutably, a sight to be seen (Fig. 1.2).

The high-angular resolution and high sensitivity of *Spitzer* revealed that the Galactic plane is dominated by structures or shells on all spatial scales that appear complete ('ring-like') or partially complete ('filamentary-like'). As practically none of these structures are associated with supernova remnants, they must be powered by stars with spectral type B9 or earlier in order to produce the radiation fields required to excite PAHs. Therefore, Churchwell et al. (2006) hypothesized that these rings and filaments represent the PDRs of dynamically formed H II regions from massive stars, and hypothesized that the rings were two-dimensional projections of spherical bubbles. Further investigation revealed that about 86% of the bubbles classified by Churchwell et al. (2006) and Churchwell et al. (2007) are associated with H II regions (Deharveng et al. 2010) and must be blown by stars of spectral type B2 or earlier. Invoking the help of the general public, some 6000 'bubbles' have now been identified (Simpson et al. 2012) that span a wide range of morphologies and sizes that relate to their stellar content, evolutionary state, and structure of the ISM in which they expand. These works, exploiting the sensitivity and resolution of *Spitzer*, clearly demonstrated the major impact of massive stars and their dominance over the global structure of the ISM. Yet, when the *Spitzer* image is compared with the *Herschel* image (Fig. 1.2), one can see that the PAHs merely trace the tip of the iceberg. The *Herschel* passbands, sensitive to dust at lower temperatures, reveal that the ISM is dynamical in regions that escaped the attention of *Spitzer*. The impact of massive stars reach far beyond the PDRs traced by the PAHs. Indeed, stellar feedback initiates shocks waves that plow through the ISM and collect mass in dense, neutral shells. Given the short lifetime of massive stars, Fig. 1.2 represents a snapshot in the evolution of our Galaxy, yet provides clues to its history that has seen numerous generations of stars, each of which must have left its imprint on the structure of the ISM seen to date.

1.2.1 Formation and evolution of H II regions and stellar wind-blown-bubbles

Massive stars generate an intense radiation field containing numerous photons with energies above 13.6 eV that are able to ionize hydrogen. Once a massive star is born, the initial evolutionary stage of the ionized volume (the H II region) occurs rapidly, as the ionization front (IF) rushes through the surrounding material until the Strömgren radius is reached (Strömgren 1939), where the total amount of recombinations equals the ionizing photon rate from the star. The photo-ionization suddenly heats the gas towards 10^4 K, and the overpressure of the photo-ionized gas with respect to the (neutral) ambient ISM will drive an expansion of the H II region. The interior density drops with time as the H II region ex-

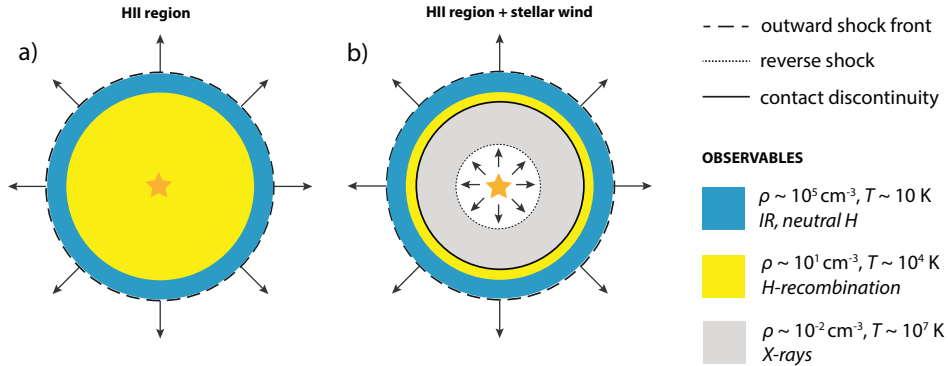


Figure 1.3: (a): The structure of an H II region driven by overpressure of ionized gas (Spitzer 1978). (b) Same as (a), but including the effect of a stellar wind (Weaver et al. 1977). The legend denotes media separated by different temperatures and densities (parameters corresponding to a ‘classical’ H II region, see text), including their observational tracers.

pands in size. For example, an ultra-compact H II region such as the G29.97-0.02 region (Wood & Churchwell 1989) contains a hydrogen number density of $\sim 10^4 \text{ cm}^{-3}$ inside a region of radius $\sim 0.05 \text{ pc}$. By the time the region has evolved to a classical H II region, such as the RCW120 region (Zavagno et al. 2007), the density has dropped to $\sim 10^1 - 10^2 \text{ cm}^{-3}$ within a radius of $\sim 10 \text{ pc}$. If the expansion of the H II region occurs supersonic with respect to the ambient material, a shockwave will run out from the IF on the neutral side that sweeps up the ISM and collapses into a dense ($\sim 10^5 \text{ cm}^{-3}$), cool ($\sim 10 \text{ K}$) shell, which dust component is detectable at IR wavelengths. This is the idealized view of the expansion of an H II region in a homogeneous medium (Fig. 1.3a; Spitzer 1978).

Besides the radiative feedback stemming from UV photons that ionize the surrounding gas, massive stars inject mechanical energy through powerful stellar winds that contain mass and momentum. The theory of stellar wind-blown-bubbles (WBB) stems from the seminal work of Castor et al. (1975) and Weaver et al. (1977). The stellar wind expands freely until it clashes with the surrounding medium when ram pressure equilibrium between both media is reached. From that moment on, one shock wave will move outwards, shocking and sweeping up the ambient ISM in a dense shell. This shell is ionized up to the point where ionizing photons are able to penetrate. At the same time, a reverse shock moves inwards, shocking the stellar wind and leaving behind a hot ($\sim 10^7 \text{ K}$), tenuous ($\sim 0.01 \text{ cm}^{-3}$) medium that should be detectable at X-ray wavelengths. Ultimately, part of the energy input of the stellar wind will do work on its surroundings (typically some 20%; van Buren 1986), setting the dense shocked ISM in motion to form an expanding shell, while the rest is stored as thermal energy of the hot gas. The pressure-driven expansion of an H II region, with and without the influence of a stellar wind, is depicted in Figure 1.3.

The cooling function (Dalgarno & McCray 1972) implies that radiative losses from the hot gas $\approx 10^6 \text{ K}$ within WBBs is small. However, heat conduction at the contact discontinuity (Fig. 1.3) between the hot gas of the bubble and that of the swept-up shell will thermally evaporate the dense shell and initiate a mass-flux into the bubble interior (Cowie & McKee 1977; Weaver et al. 1977), a process often referred to as *mass-loading*

(Hartquist et al. 1986). If radiative losses are ignored, the energy of the hot gas will remain the same, and an increase in mass will lower its temperature. Besides the evaporation of the bubble wall, dense (molecular) clouds that are overrun by the IF that end up being enclosed in the bubble will thermally evaporate and inject mass into the hot plasma (Arthur & Henney 1996; Everett & Churchwell 2010), further lowering the temperature compared to that from idealized models. At $T \lesssim 10^6$ K, radiative losses will become important and, at this point, energy will be lost from the system.

There are a number of ways that can dramatically affect the evolution of H II regions from that described above. First, given our current knowledge of the highly dynamic ISM, the idea of spherical bubbles expanding in an homogeneous medium is, in many cases, merely an oversimplification of reality. Inhomogeneities within the surrounding ISM will lead to asymmetries of the H II region as the expansion will accelerate to media of lower density. Second, the intrinsic motion of the ionizing source may lead to a cometary shape of the bubble in its direction of movement (Wood & Churchwell 1989). Third, magnetic fields might suppress the expansion rate perpendicular to the field lines (Krumholz et al. 2007). Fourth, dust mixed within H II regions will leave its footprint on the evolution of H II regions. On the one hand, dust will absorb ionizing photons that will shrink the H II region in size. On the other hand, radiation pressure on dust grains will add momentum to the surrounding gas so as to push on it, setting it in motion. Fifth, the clouds in which the bubbles are embedded are of finite size. In this respect, Israel (1978) noticed that a large number of H II regions were located near the edges of dense clouds and adopted the term ‘blister H II region’, given their suggestive appearance on the ‘skin’ of molecular clouds. Depending on the initial location of the formation of the H II region, the star with its bubble might break out of its natal envelope towards the so-called *blister* phase allowing the (hot) gas to leak from the bubble interior.

Ionization fronts and photo-evaporation flows of gas

A massive star will ionize its surroundings and will be encircled by an IF that separates the ionized volume from the neutral material. An IF is preceded by a shock front. The conditions of the gas at either side of this shock front are markedly different, and are connected through jump conditions (Spitzer 1978; Henney 2007). Let ρ , v , and P denote the density, velocity, and pressure of the gas, and indexes 0 and 1 refer to the pre- and post-shock gas. If one assumes mass and momentum conservation, and consider C_0 and C_1 as the isothermal sound speed at both sides of the shock front, it can be shown that only two types of shock fronts can exist (Shu 1992; Tielens 2005). The first type have velocities of $v > v_R \approx 2C_1$, and are called *R*-type (‘rarefied gas’) with $\rho_1 > \rho_0$. The second type is characterized by $v < v_D \approx C_0^2/2C_1$, and are called *D*-type (‘dense gas’) with $\rho_1 < \rho_0$. If the velocity of the shock exactly matches v_R or v_D , the shock front is called *R*-critical or *D*-critical, respectively. The velocity of the IF traveling behind the shock front will be determined by the ionizing photon flux and the density of the neutral (shocked) medium.

The subsequent movement of the gas away from the IF has previously been studied for a few prototypical cases. The recognition of blister H II regions (Sec. 1.2.1) initiated the study of the ionized gas in terms of a *champagne flow*, after the original model of Tenorio-Tagle (1979). In this scenario, the IF of an expanding H II region reaches the edge of the natal cloud and encounters the density discontinuity between the cloud and intercloud medium. A fast, isothermal shock will move into the intercloud medium, while

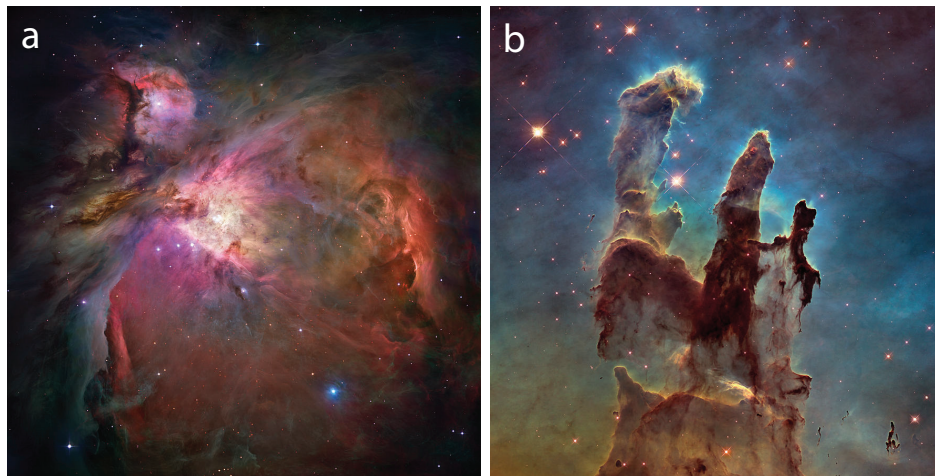


Figure 1.4: Examples of ionization fronts and ionized gas flows. **(a)** The Orion Nebula is a blister H II region that breaks out of the near-side of the Orion A Molecular cloud. The ionized gas streams away from the cloud surface (O’Dell 2001) and its structure can be viewed as the prototypical example of a *champagne flow* of ionized gas (Tenorio-Tagle 1979). Image credit: NASA, ESA, M. Robberto (STScI/ESA). **(b)** The ‘pillars of creation’ light up against the gaseous background of the Eagle Nebula (Hester et al. 1996). Here, the ionization front has wrapped around the condensations as dense knots of material withstanding photo-evaporation. The shape of the ionization front causes the emanating flow to differ from the champagne flow case, and is often referred to as a *globule flow* (Bertoldi 1989). Image credit: NASA, ESA, and the Hubble Heritage Team (STScI/AURA).

a rarefaction shockwave travels back through the H II region. Between the shock fronts, a champagne flow of ionized gas is set up. The pioneering studies from Tenorio-Tagle (1979) and Bedijn & Tenorio-Tagle (1981) considered a plane-parallel, non-steady case, where the gas density and velocity after break-out was described in analogy to the isothermal shock tube problem (Sod 1978), in which the ionized flow exhibits a linear velocity law and an exponential density gradient (See Fig. 1.5). Arguably, the most famous example of a champagne flow is the Orion Nebula (Sec. 1.3) bursting out of the near-side of the Orion molecular cloud (OMC): the extended blister geometry is easily detected in recombination lines, and the acceleration of the ionized gas away from the IF is traced by markers at different levels of ionization (O’Dell 2001). Another classical problem is the evaporation of dense knots or globules often observed within the (hot) ionized gas of star-forming regions (e.g., Koenig et al. 2008). Once a dense condensation is reached, the IF will slow down and wrap around the globule. In this case, the shape of the IF will become convex, and the ionized material expands and diverges as it accelerates away from the front. Early models of the globule flow problem were described in Dyson (1968) and Kahn (1969), and extended by Bertoldi (1989), in which the density of the ionized photo-evaporation flow increases sharply towards the IF, greatly exceeding that of the H II region as a whole, offering an explanation for the curved bright rims apparent as cometary globules (Koenig et al. 2008), and ‘elephant trunks’ (Hester et al. 1996) often observed within H II regions.

Henney et al. (2005) numerically investigated the evaporation of a cloud illuminated by a point source, and studied the structure of the ionized flow that evaporates from the cloud surface. The study unified the theories of champagne flows and globule flows in an elegant way. An IF that engulfs a flat, homogenous cloud illuminated by a point source will become concave, and the photo-evaporation flow emanating from this geometry will resemble a champagne flow structure, as the streamlines of the ionized gas do not diverge effectively (Henney et al. 2005). In practice, the ionized gas from a concave IF will accelerate more slowly compared to, e.g., the heavily divergent photo-evaporation flow from a convex-shaped globule (in analogy to Bertoldi 1989). We depict the dependence of the ionized flow structure on the shape of the IF in Fig. 1.5, assuming that the IFs are D-critical and, therefore, the gas leaves the IF at the sound speed of the ionized gas ($= C_{II}$). If we consider the gas to be isothermal, which is likely for the ionized gas as the heating is dominated by photo-ionization from the star, the gas accelerates away from the IF depending on the degree of divergence of the ionized flow. The acceleration will eventually decrease and the flow will reach a terminal velocity v_t , which occurs when the expansion and heating timescales of the gas become comparable and the isothermal approximation breaks down (Henney 2007). Thus, in short, the shape of the IF (convex, flat, or concave) and the incident ionizing photon flux (regulating the velocity of the IF into the cloud and the density of the ionized flow) uniquely determine the structure of the resulting photo-evaporation flow. In particular, the velocity v and density n regulate the structure of the flow as a function of distance x from the IF (Fig. 1.5), which we will refer to as the *flow parameters* of the ionized gas (Sec. 1.2.3).

Studying the structure of ionized gas flows is crucial to our understanding of the formation and evolution of H II regions. For example, the photo-evaporation of globules or the disruption of molecular clouds through champagne flows may contribute to the mass-loading of the hot interior of a stellar wind-blown-bubble or a superbubble (Sec. 1.2.2). Furthermore, the escape of material from the H II region interior will lead to depressurization, stalling the expansion of the volume, while the expelled gas will input kinetic energy and drive turbulent motions into the surrounding medium. Finally, photo-evaporation flows entrain dust particles, acting as a (significant) source of dust input into the bubble interior (Sec. 1.2.3).

1.2.2 OB associations, supernovae, and superbubbles

Early studies of space distributions of stars by Kapteyn (1914) and Pannekoek (1929) revealed that many stars appeared clustered on the sky. Today, it is known that massive stars tend to form in multiple systems or clusters (Zinnecker & Yorke 2007), bound together in large groups known as OB associations (e.g., de Zeeuw et al. 1999a). Studies of OB associations focus on characterizing the membership, structure, and kinematics of the stellar content of the association. The age distribution in many evolved OB associations imply that stars do not necessarily form coevally. For example, the Orion OB association (Orion OB1) reveals several subgroups that are distributed in a layered structure at different locations with respect to the Orion Molecular clouds (OMCs; Blaauw 1964; Brown et al. 1994). Star formation thus appears to have propagated through the molecular clouds episodically, where feedback from the older subgroups may have formed shock waves that compressed material from nearby regions, triggering the formation of a next generation

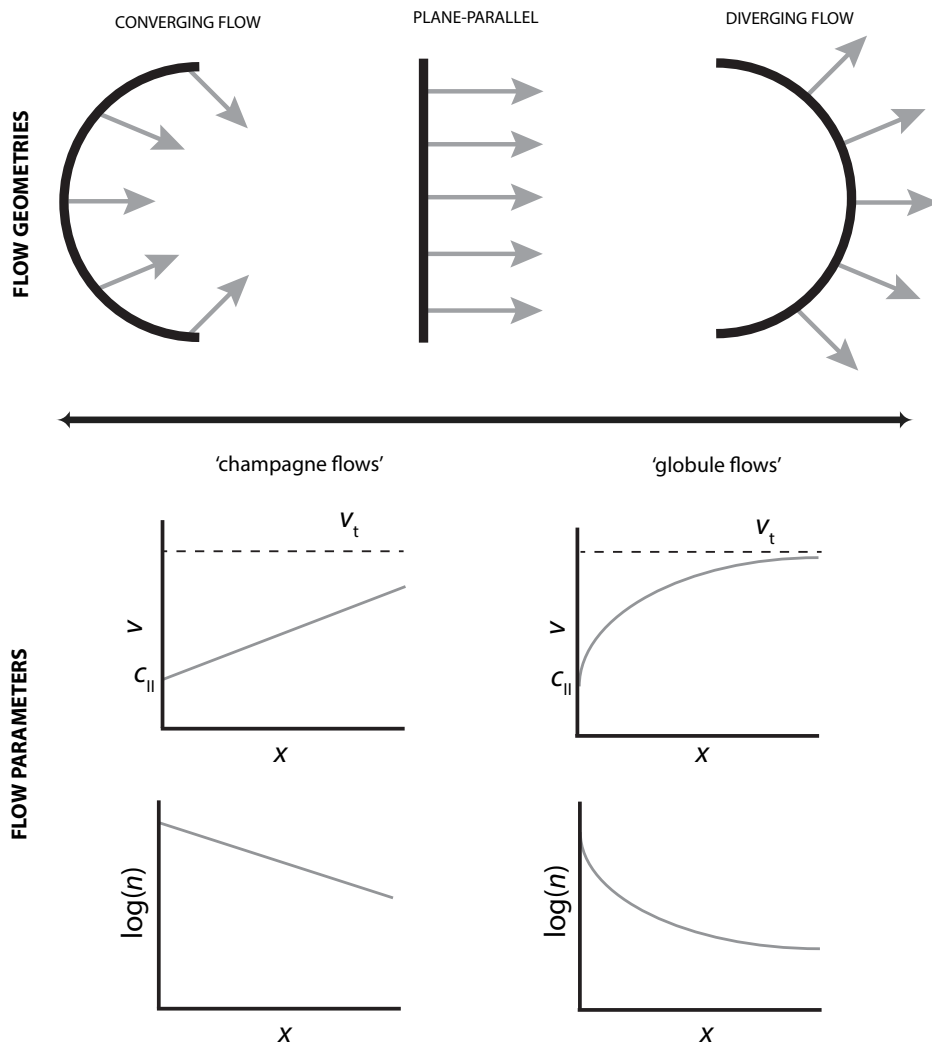


Figure 1.5: Photo-evaporation flows (grey arrows) from ionization fronts (black lines). The shape of the ionization front (concave, flat, convex) determines the structure of the photo-evaporation flow from the surface (Henney et al. 2005), in particular the *flow parameters* of the ionized gas. Concave ionization fronts lead to accelerating flows that resemble classical ‘champagne flows’, while convex ionization fronts will lead to ‘globule flows’.

of stars (Elmegreen & Lada 1977).

The tendency of massive stars to concentrate in OB associations has implications for the formation of H II regions and bubbles that surround the associations, and need to be contrasted with the theory of isolated bubbles around single stars described in Sec. 1.2.1. In an OB association, stars will form close to one another, such that their radiative and mechanical energy input will merge, and their combined efforts will lead to the formation

of large ($\sim 10^2$ pc), dynamic structures in the ISM that are often termed as superbubbles (e.g., McCray & Kafatos 1987).

Theoretically, the initial stage of the formation of a superbubble will be dominated by either the stellar winds or radiation pressure from the central OB association. At a certain time, the most massive component within the OB association will detonate as a SN within a pre-existing cavity. The SN ejecta will be launched at great velocity and introduce a large amount of mechanical energy into the surroundings. After a fast initial phase, where the SN ejecta expand freely until an amount of ISM material similar to its own mass is encountered, a reverse shock will heat the ejecta and its kinetic energy will be thermalized, from which point it will expand adiabatically because of the overpressure compared to the surrounding gas. When the temperature of the hot gas drops below $\sim 10^6$ K, radiative cooling will become important and the newly shocked material will cool and collapse into a thin shell to form a supernova remnant: a shell of compressed material will then move out from the OB association. Once the blast wave becomes subsonic, the energy of the remnant will thermalize and it will disperse its energy as a sound wave that pressurizes the interior medium of the superbubble. In case of repeated supernovae, interior blast waves can remain supersonic and reach the cooled outer shell of the superbubble, in which case the energy is radiated away, or the blast wave bounces and eventually thermalizes inside the interior (Mac Low & McCray 1988).

Observationally, the basic structure of superbubbles is expected to be similar to that created by the interaction of a stellar wind with the ISM: a dense, swept-up shell encapsulates a hot, tenuous interior. The dense supershells are easily discernible in maps of neutral (Heiles 1979) or ionized (Reynolds & Ogden 1979) hydrogen. The interiors of superbubbles can be traced in X-rays (Chu & Mac Low 1990a; Snowden et al. 1995), even though the measured X-ray luminosities do not always agree with the standard model (Weaver et al. 1977), a problem that is also encountered with observations of isolated bubbles (see Chu 2008, and references therein). Some superbubbles appear too bright at X-ray wavelengths, notably in the Large Magellanic Cloud (Chu & Mac Low 1990a). Several mechanisms have been proposed to explain the X-ray overluminosity, such as heating by shocks from off-center supernovae within the superbubble cavity (Chu & Mac Low 1990a) or enhanced metal abundances because of SN enrichment (Silich et al. 2001). Other superbubbles appear to be too dim in X-rays, possibly as a result of mass-loading (Sec. 1.2.1) that cools the interior of the superbubble, lowering the expected X-ray luminosity. Finally, X-ray emission has been observed beyond the outer dense shell of several superbubbles (Dunne et al. 2001), indicative of ‘blow outs’ of the superbubbles similar to the emergence of H II regions such as the blister H II region of the Orion Nebula, where ionized (Fig. 1.4) and hot gas (Güdel et al. 2008) are observed to leak out of the region.

Superbubbles expanding in the disk of a galaxy may eventually blow out of the plane when the size of the bubble reaches one or two gas layer scale heights of the neutral disk (Mac Low & McCray 1988). The opening angle of the blowout is inversely related to the Mach number of the shock at the blow-out region, forming either wide-angle jets or narrow chimneys that sets up an interaction between the disk and the extended halo (Norman & Ikeuchi 1989). The dense gas from the superbubble shell will be susceptible to Rayleigh-Taylor fragmentation instabilities, ultimately forming dense clumps that fall back to the disk (Mac Low et al. 1989). However, the hot gas will penetrate deep into the halo, where it settles on a much higher scale height (~ 1 kpc; Tielens 2005). Over-

all, the blow-out of superbubbles will initiate a large energy circulation that attributes to the metal enrichment of the halo or, in case the gas will be able to escape the potential well of the disk, the IGM. While only a small part of the mass of the superbubble is hurled into the halo, superbubble blowouts may still dominate the mass budget of the extended, low-density halo. Furthermore, the holes that are carved by the blowouts may offer channels through which radiation from the stars can ionize the halo and may even drive gas-dynamics (Silich & Tenorio-Tagle 2013) or momentum-driven galactic winds (Murray et al. 2005). In addition, the disk-halo connection will add to the mixing of (enriched) gas in the plane as matter rains back from the halo onto the galactic disk.

1.2.3 Dust as a tracer and intermediary of radiative feedback

While the ‘explosive’ feedback (Krumholz et al. 2014) from massive stars in the form of UV radiation (Dale et al. 2005; Walch et al. 2012), stellar winds (Toalá & Arthur 2011; Rogers & Pittard 2013), and from SN (Hill et al. 2012; Gatto et al. 2015) have traditionally gained much attention in explaining the origin of large expanding shells (Heiles 1984; Churchwell et al. 2006) and the evolution of the ISM into its filamentary, multi-scale appearance seen to date (Fig. 1.2), only recently the role of ‘momentum feedback’ has been assessed, in particular in the form of radiation pressure on dust (Krumholz & Matzner 2009; Draine 2011a; Silich & Tenorio-Tagle 2013). Radiation pressure provides yet another way of imparting kinetic energy to the gas and setting it in motion. As the radiative energy of a star over its lifetime ($\sim 10^{53}$ erg; Tielens 2005) greatly exceeds that of a stellar wind ($\epsilon E \sim 10^{49}$ erg; with ϵ the efficiency at which the mechanical luminosity of the star couples to the ISM as kinetic energy) or supernova ($\epsilon E \sim 10^{50} - 10^{51}$ erg; Veilleux et al. 2005), it constitutes a major potential source of energy. Most of the radiative energy of a star is used up to ionize and heat the gas and will be lost through radiative cooling. However, if only a small fraction of this energy couples as momentum to the gas through radiation pressure upon dust, this mechanism may play a crucial role in shaping the ISM around massive stars (Krumholz & Matzner 2009; Lopez et al. 2011) or launching galaxy-sized winds (Murray et al. 2005; Hopkins et al. 2011).

Because of its large cross-section compared to (ionized) gas, dust is the main absorber of radiation pressure. The change in momentum can indirectly be transferred to the gas through gas-grain collisions. It has been proposed that radiation pressure acting on dust produces density stratifications inside H II regions as the gas and grains move outwards coherently (Draine 2011a). Furthermore, radiation pressure may be the dominant source in driving the dynamics of giant H II regions (Krumholz & Matzner 2009) such as the 30 Doradus region (Lopez et al. 2011), but its importance relative to gas pressure becomes smaller when going to star clusters of lower ionizing luminosity, i.e., containing a single or a handful of OB stars, which is the typical cluster size in the near few kiloparsec of the solar neighborhood (Mathews 1969; Arthur et al. 2004). On the other hand, by including the central clusters mechanical luminosity and evolution of its radiative luminosity, Silich & Tenorio-Tagle (2013) showed that radiation pressure only dominates at the very early stages of H II region formation, irrespective of its mass and ionizing luminosity. The above described controversial results underline our poor understanding of the importance of radiation pressure as a mechanism of stellar feedback to the ISM. Moreover, theoretical work often relies on assumptions that simplify the analytical

or numerical analyses, but do not necessarily provide an accurate description of the exact radiative interaction of a massive star with its surroundings.

Much work on addressing radiation pressure feedback of massive stars has been performed theoretically (Yorke & Sonnhalter 2002; Krumholz & Matzner 2009; Hopkins et al. 2011). Observational work has been hampered by the fact that it is difficult to separate pressure contributions from the warm 10^4 K ($H\alpha$ emitting) gas, the hot 10^6 - 10^7 K (X-ray emitting gas), direct absorption of starlight, and dust-processed stellar radiation (re-emitted in the IR). Comparison of all these pressures has been limited to a few special cases, notably the 30 Doradus region in the Large Magellanic cloud, a study performed by Lopez et al. (2011) and Pellegrini et al. (2011). Still, these authors reach opposite conclusions regarding the importance of radiation pressure compared to the other forms of feedback, largely following from different assumptions that characterize the gas phases within the 30 Doradus region (for a review on the discrepancies, see Krumholz et al. 2014).

It seems advantageous to study the various forms of stellar feedback in regions well away from the complex geometries of star forming regions, or confusion caused by structures along the line-of-sight. While most massive stars are formed in OB star clusters, many are eventually ejected from their parent association: up to 25% of massive stars (Zinnecker & Yorke 2007) end up as OB-runaways with space velocities in excess of 30 km s^{-1} (Blaauw 1961). These stars can therefore travel notable distances away from their birth place. During their lifetime, massive stars in the field will interact with the ISM either through a stellar wind, or through radiation pressure. If a star moves supersonically with respect to its environment, a stellar wind will create a *bow shock* at the stand-off distance from the moving star, where the ram pressure and momentum flux of the stellar wind and the interstellar medium balance (van Buren & McCray 1988; Mac Low et al. 1991; Kaper et al. 1997). The swept-up material in the bow shock is heated by radiation of the OB star, making the dusty component of the shells visible in the infrared, while the gas component will be observable depending on the local density, the compression ratio of the pre- and post shock gas, and the contrast with the material of the ISM along the line of sight. Many of the arc-shaped infrared features surrounding OB stars detected by *IRAS* and, more recently, *WISE* have been associated with stellar-wind bow shocks, even though detection of their gaseous counterparts is limited to a few incidental cases. Using radio continuum data, Peri et al. (2015) found a total of 8 sources (out of 73 total) that - possibly - show gas emission coincident with the infrared arcs.

Radiation pressure from a moving OB star is expected to create a similar structure compared to the arc-shaped bow shocks. However, a fundamental difference between radiation pressure and a stellar wind is that the first predominantly acts upon the dust component of the ISM, and gas will follow this motion only if the coupling between both components is sufficient for the gas to be dynamically perturbed (see below), while the second acts on the gas component (pressure) of the ambient medium. Furthermore, in case of radiation pressure, the OB star does not need to move supersonically with respect to the ISM for the interstellar matter to be swept up in a shell. Thus, in principle, radiation-pressure-driven *bow waves* (van Buren & McCray 1988) may lead to IR arcs surrounding OB stars *without* any gaseous counterparts. However, no such structure has ever been detected in the ISM.

Forces governing dust dynamics

The movement of dust through the ISM is governed by a balance between the gravitation pull from massive bodies, radiation pressure from stars, and collisions or friction with gas particles. Gas drag either occurs through direct collisions, determined by the gas density and the grain geometrical cross-section, or through long-range Coulomb interactions. The theory is based on that developed by Chandrasekhar (1943) for dynamical friction within star clusters, but was reformulated for a test particle confined in a plasma by Spitzer (1962) and Draine & Salpeter (1979). The charge state of the grains is an important parameter in determining the magnitude of Coulomb coupling between gas and dust, and theories of spherical grains interacting with ions that exhibit a Maxwellian velocity distribution (Draine & Salpeter 1979; Tielens 2005) are often employed in the calculation of dust charge. Still, the derived charge states are heavily dependent on the assumed photo-ionization yields that remain poorly constrained by laboratory work (Willis et al. 1973; Abbas et al. 2006).

Ionization fronts offer a unique opportunity to study dust dynamics. The velocity and density jump across an IF, and the subsequent acceleration of the gas away from the front (Fig. 1.5) will lead to a significant change in momentum transfer between gas and dust. If the momentum transfer towards the grains is sufficient, dust will be *entrained* in the photo-evaporation flow and travel along with the gas. The entrainment process is dependent on several factors. On the one hand, it will depend on the *flow parameters* of the ionized gas (density and velocity of the ionized flow; Sec. 1.2.1). On the other hand, it will depend on the way the grains couple to the gas, a process that is intimately linked to dust grain characteristics such as mass, geometry, and charge state, all of which remain subject to debate (Sec. 1.1.2).

1.2.4 Summary: the energy balance of the ISM

From stars to the ISM: Over its lifetime, a massive stars radiates some 10^{53} erg that mainly serves to photo-ionize and heat surrounding gas and will eventually be radiated away. While the energy is not conserved, momentum can not be radiated away, and part of the radiative energy may couple to the ISM as kinetic energy, mainly through radiation pressure acting upon dust. The acquired momentum can then indirectly be transferred towards the gas through gas-grain collisions. The efficiency of this mechanism is dependent on various parameters and has never been tested observationally, such that its importance to the dynamics of the ISM remains unclear. Stellar winds shock heat gas, creating hot plasmas that expand and do work on their surroundings, delivering some $\sim 10^{49}$ erg (Tielens 2005) of kinetic energy, while the rest of the mechanical luminosity of the star will be stored as thermal energy of the hot gas. Similarly, the explosive power of SNe will transfer a fraction of its energy towards kinetic energy of the surrounding gas (10^{50} - 10^{51} erg; Veilleux et al. 2005).

The aforementioned feedback mechanisms of massive stars to the ISM manifests themselves as bubble HII regions (\sim few 10 pc), supernova remnants ($\sim 10^2$ pc), but as most of massive stars form in clusters, they tend to form superbubbles (\sim few 10^2 pc). Massive stars in the field may form stellar-wind-driven bow shocks or radiation-pressure-driven bow waves with radiation pressure, before ending their life as a SN.

From the ISM to stars: Massive stars will constantly stir the surrounding medium

and mainly push the gas and dust outwards from the location of star formation, limiting the gas supply and, ultimately, star formation efficiency. Thus, on the one hand, the energy input of massive stars tends to provide a negative feedback for continuing star formation, especially when considered that, in reality, all feedback mechanisms will act simultaneously. The shockwaves associated with the injected mechanical energy and the transfer of momentum will collect gas and dust in giant shells or filaments. Gas and dust interchange momentum and may move coherently when the coupling between both components is sufficient. On the other hand, compression of the interstellar material in the shells or filaments can lead to the condensation of atomic and molecular clouds that may form a new generation of stars.

1.3 Orion as a benchmark study

This introduction started off with a short description of the Orion region that immediately stressed its importance to studies of star formation and the ISM. While not specifically addressed in the contents of this thesis, it must be noted that studies of Orion has influenced many areas in astronomy. Multiple interstellar molecules have been discovered in Orion, such as CO (Wilson et al. 1970). The Hubble Space Telescope provided *direct* detection of dozens of evaporating protoplanetary disks ('proplyds'; O'Dell et al. 1993) surrounding young stellar objects that appear to be severely affected by the intense radiation field exerted by the main powerhouse of the Orion nebula, θ^1 Ori C, which provided insights and constraints on both star- and planet formation scenarios. Orion harbors such great detail that complete books have been written and filled on the characteristics of the region. Still, recent results indicate that some of the previous results regarding Orion need to be revised, while hidden treasures have yet to be uncovered. In the following paragraphs, we briefly discuss specific regions and characteristics of the Orion region that directly relate to the remaining content of this thesis.

The stars

In the past 15 Myr, the Orion region has given birth to $\sim 10^4$ stars across the mass spectrum (Bally 2008). The Orion OB association, Orion OB1, is divided in several subgroups and clusters that differ in age and location, partially being superimposed along the line of sight (Blaauw 1964; Brown et al. 1994). The stratification of the different subgroups and their relative position with respect to the OMCs indicate that star formation propagated through the pre-existing molecular clouds episodically, which connects well with the 'sequential star formation' scenario described by Elmegreen & Lada (1977). The members of the oldest subgroup, Orion OB1a ($\sim 8 - 12$ Myr; Bally 2008), may have triggered the formation of the Orion OB1b subgroup (3 - 6 Myr) towards the south in Orion's Belt, from which star formation seemed to have propagated further south in the Orion OB1c region (2 - 6 Myr), and perhaps the λ Ori region in the north (< 5 Myr). The youngest massive subgroup is the Orion OB1d subgroup (> 2 Myr), which includes the Orion Nebula cluster (ONC) located at the northern tip of the Orion Molecular A cloud. The ONC is the best studied star forming region in the sky. The most comprehensive studies have been performed by Hillenbrand (1997) and Megeath et al. (2012) that revealed thousands of (young) stellar objects, where the most massive stars are located in the cluster center.

Noteworthy here is the Trapezium system in the heart of the Orion Nebula (Fig. 1.1d), which appears to be a mass-segregated sub-cluster within the region. Smaller star forming clusters are spread in cores throughout the OMCs (Gibb 2008; Allen & Davis 2008). In addition, detections of numerous cometary clouds with heads pointing towards the Orion OB1 association are scattered throughout the Orion region and show signs of sequential star formation (e.g., Stanke et al. 2002; Lee et al. 2005; Bally et al. 2009).

Each ‘bursts’ of star formation has left its mark on the Orion region. The Orion OB1a group has injected energy and momentum and has, by now, completely emerged from the parent molecular cloud. The Orion OB1b group, some 50 pc to the east, still resides close to the molecular cloud and might have formed the protrusion out of OMC B apparent as the GS206+17-13 H I shell (Ehlerová & Palouš 2005). The supergiant status of the Belt stars indicate that a SN may already have gone off within this subgroup. The λ Ori group has formed the awe-inspiring, 10° sized spherical H II region (Reich 1978) encapsulated by a molecular ring or bubble (Maddalena & Morris 1987). The Orion OB1c and OB1d are still (partly) embedded (Hillenbrand 1997; Megeath et al. 2012). Despite their youth, they have already started to begin sculpting the OMCs and the ISM in their vicinity in the form of, e.g., the Orion nebula.

The sword

Already addressed in Sec. 1.2.1, the blister-like appearance of the Orion nebula is caused by a champagne flow of ionized gas streaming of the Orion Molecular Cloud (OMC) that is initiated by ionizing radiation of the main ionizing star, θ^1 Ori C. The large-scale gas flow contains only several solar masses of ionized gas, indicating that the champagne phase has only recently commenced, perhaps just some 1.5×10^4 yr ago (O’Dell et al. 2009). X-rays have been detected in the Extended Orion Nebula (Güdel et al. 2008) that reveals the leakage of the hot shocked wind gas from θ^1 Ori C into the surrounding medium.

The superbubble

Assuming a standard initial mass function, Bally (2008) inferred that about 30 - 100 stars more massive than $8 M_\odot$ have formed in Orion OB1, and argued that over the last 12 Myr, about 10 - 20 SNe have exploded in the region. The combined efforts of UV radiation, stellar winds, and SNe from Orion OB1 have continuously disrupted the star forming clouds and created a large X-ray emitting superbubble ($> 10^2$ pc) that spans over ~ 40 degrees or ~ 300 pc on the sky towards the Eridanus constellation (at a distance of 400 pc, here the assumed distance towards the Orion region; Menten et al. 2007), and may be evolving towards blowout of the Galactic plane (Mac Low & McCray 1988). Because of its proximity and evolutionary state, the Orion-Eridanus superbubble acts as a benchmark to the study of other superbubbles that lack the spatial information of the Orion region. The structure and evolution of the Orion-Eridanus superbubble will be thoroughly discussed in Chapter 5.

Stellar motions

The *Hipparcos* satellite has observed all nearby OB associations with the aim to obtain a

detailed knowledge of the stellar content and dynamics of nearby OB associations, which in its turn has allowed to address many fundamental questions on star formation, such as the dependence of star formation with respect to the location within giant molecular clouds, the conditions that set the initial mass function of stars, the importance of binaries and clusters, and the study of OB runaway stars (Brown et al. 1999). Indeed, some of the brightest stars of the Orion constellation (such as α Ori, β Ori, and κ Ori) may be OB runaways (Bally 2008). While *Hipparcos* proper motions provide clues to their past trajectories, the origin of these stars remain unclear. The interaction of α Ori with the surrounding medium becomes clear from the arc-shaped bow shock that envelops the star in its direction of movement (e.g., Decin et al. 2012), permitting to constrain mass-loss events from the central star and the characterization of the ambient ISM. Figure 1.1b, 1.1c, and 1.1d show similar arc structures on all observable scales that exemplify the interaction of the mechanical or radiative luminosity of the stars with the surrounding ISM.

1.4 This thesis

In this introductory chapter, I reviewed our current understanding of the interplay between stars and the ISM, and argued that Orion offers a unique opportunity to address many of the open questions presented in beginning of this chapter. Perhaps after this might one start to fully appreciate the significance of Fig. 1.1 and the level of detail that it harbors. In the next chapters of this thesis, some of the important and puzzling details that stand out in this picture will be addressed. For one, the ubiquity of mid-IR arcs that surround the main ionizing stars in Orion provide important clues to the dynamics of the ISM and the interaction between the stars with their surroundings, and the mediating role of dust therein. We will combine the dynamics of the gas, the dust, and the stars within Orion to quantify these interactions and to derive a novel method to study the properties and evolution of interstellar dust (Ch. 2 & 3), to explain the presence of dust in these harsh regions of space (Ch. 4), and to constrain the importance of dust as an intermediary of radiative feedback to the ISM (Ch. 4). The result have implications for many regions of massive star formation within our Galaxy and these will be discussed (Ch. 4). On larger scales, it is evident that the powerful processes accompanying (massive) star formation have turned the Orion region into its current complexity (Fig. 1.1). The image represents a snapshot in time, and the final chapter of this thesis will combine the previous derived knowledge on specific regions within Orion that forces us to revise our thinking on the history and evolution of the *entire* Orion-Eridanus region (Ch. 5). In detail, the next chapters will address the following:

Chapter 2 describes the interaction of radiation pressure of the σ Ori AB system with dust carried along by the IC 434 photo-evaporative flow of ionized gas from the dark cloud L1630/OMC B. We build a quantitative dynamical model for the radiative interaction of a dusty ionized flow with nearby (massive) stars, which is then employed to extract properties of the dust entrained within the ionized gas, such as the size distribution and charge state of the grains. We argue that this is the first example of a ‘dust wave’ created by radiation pressure of a massive star moving through the interstellar medium, discuss how our findings impact the importance of stellar winds, and reveal that dust waves should be common around stars showing the ‘weak wind phenomenon’.

Chapter 3 extends the results from chapter 2 by combining our dynamical model with numerical simulations of photo-evaporation flows, and the history and large-scale evolution of the Orion Belt region. We extend our analysis of the σ Ori dust wave over a much broader wavelength range, improve our dynamical model to constrain dust quantities such as geometry (porosity / fluffiness), as well as the efficiency of absorbing radiation pressure by the grains. We argue that the dust in the ionized gas of the IC 434 region cannot be explained by current dust models, as it is markedly different from that observed in the diffuse ISM, and place our findings in the context of recent studies on dust evolution.

Chapter 4 exploits Spitzer- and Herschel surveys of the Galactic plane to search for the signatures of dust waves, and reveals that dust waves are ubiquitous within the Galactic plane. We perform hydrodynamical simulations of expanding H II regions to investigate the conditions needed for the development of dust waves, and discuss that evolved H II regions are ideal candidates for observing dust waves and for studying the properties of dust in ionized regions of space. Dust waves within Galactic bubbles offer a solution regarding the presence and morphology of dust inside H II regions, and imply that winds are of limited importance in such systems, which may in its turn connect to observed weak-wind strengths and the difficulty in detecting diffuse X-rays around main-sequence stars. In addition, dust waves provide direct evidence that bubbles are relieving their pressure into the ISM through a champagne flow that inject turbulence into the ISM, while acting as a probe of the radiative interaction of a massive star with its surroundings.

Chapter 5 combines recent observational data with the results drawn from the previous chapters to arrive at new and more complete picture of the Orion-Eridanus superbubble. The superbubble is larger and more complex than previously thought, and displays an active interplay between star formation, stellar feedback, and ISM evolution. During the lifetime of the superbubble, H II region champagne flows and thermal evaporation of embedded clouds continuously mass-load the superbubble interior, while winds or supernovae from massive stars in Orion rejuvenate the superbubble by sweeping up the material from the interior cavities in an episodic fashion, possibly triggering the formation of new stars that form shells of their own. The cycle of mass-loading, interior cleansing, and star formation repeats until the molecular reservoir is depleted or the clouds have been disrupted, from which the superbubble will disappear and merge with the ISM.

2

Blowing in the wind: The dust wave around σ Ori AB

Observations obtained with the Spitzer Space Telescope and the WISE satellite have revealed a prominent arc-like structure at $50''$ (≈ 0.1 pc) from the O9.5V/B0.5V system σ Ori AB. We measure a total dust mass of $2.3 \pm 1.5 \times 10^{-5} M_{\odot}$. The derived dust-to-gas mass ratio is $\approx 0.29 \pm 0.20$.

We attribute this dust structure to the interaction of radiation pressure from the star with dust carried along by the IC 434 photo-evaporative flow of ionized gas from the dark cloud L1630. We have developed a quantitative model for the interaction of a dusty ionized flow with nearby (massive) stars where radiation pressure stalls dust, piling it up at an appreciable distance (> 0.1 pc), and force it to flow around the star. The model demonstrates that for the conditions in IC 434, the gas will decouple from the dust and will keep its original flow lines. Hence, we argue that this dust structure is the first example of a dust wave created by a massive star moving through the interstellar medium. Our model shows that for higher gas densities, coupling is more efficient and a bow wave will form, containing both dust and gas.

Our model describes the physics of dust waves and bow waves and quantitatively reproduces the optical depth profile at $70 \mu\text{m}$. Dust waves (and bow waves) stratify dust grains according to their radiation pressure opacity, which reflects the size distribution and composition of the grain material. It is found that in the particular case of σ Ori AB, dust is able to survive inside the ionized region. Comparison of our model results with observations implies that dust-gas coupling through Coulomb interaction is less important than previously thought, challenging our understanding of grain dynamics in hot, ionized regions of space.

We describe the difference between dust (and bow) waves and classical bow shocks created by the interaction of a stellar wind with the interstellar medium. The results show that for late O-type stars with weak stellar winds, the stand-off distance of the resulting bow shock is very close to the star, well within the location of the dust wave. In general, we conclude that dust waves and bow waves should be common around stars showing the weak-wind phenomenon, i.e., stars with $\log(L/L_{\odot}) < 5.2$, and that these structures are best observed at mid-IR to FIR wavelengths, depending on the stellar spectral type. In particular, dust waves and bow waves are most efficiently formed around weak-wind stars moving through a high density medium. Moreover, they provide a unique opportunity to study the direct interaction between a (massive) star and its immediate surroundings.

B. B. Ochsendorf, N. L. J. Cox, S. Krijt, F. Salgado,
O. Berné, J. P. Bernard, L. Kaper & A. G. G. M. Tielens
Astronomy & Astrophysics 563, A65 (2014)

2.1 Introduction

The initial expansion of H II regions is driven by rapid ionization around a young, massive star. Once the H II region is established, the overpressure of the ionized region will drive the expansion as the ionizing flux of the star dilutes with distance, sweeping up neutral gas in a shell. Dust inside the H II region will absorb ionizing flux and re-emit in the infrared (IR), stalling the expansion of the ionized material (Petrosian 1973; Draine 2011a). When the ionization front breaks out of the molecular cloud, a phase of rapid expansion of the ionized gas into the surrounding low density medium commences: the so-called champagne flow phase (Tenorio-Tagle 1979; Bedijn & Tenorio-Tagle 1981; Yorke 1986).

Massive stars have strong winds ($\dot{M} \sim 10^{-8} - 10^{-6} M_{\odot} \text{ yr}^{-1}$, $v_{\infty} \simeq 1000 - 2500 \text{ km s}^{-1}$; Kudritzki & Puls 2000). If these stars move supersonically with respect to their environment, a bow shock will be created at the stand-off distance from the moving star where the ram pressure and momentum flux of the wind and the interstellar medium balance (van Buren et al. 1990; Mac Low et al. 1991). The swept-up material in the bow shock is heated by the radiation of the OB star, making these structures visible in either shocked gas (Brown & Bomans 2005; Kaper et al. 1997) or warm dust radiating at infrared wavelengths (van Buren & McCray 1988). The Infrared Astronomical Satellite (IRAS; Neugebauer et al. 1984) all-sky survey detected many extended arc-like structures associated with OB-runaway stars, revealing that bow shocks are ubiquitous around stars with powerful stellar winds (van Buren et al. 1995; Peri et al. 2012). However, recent observations indicate that many late O-type dwarfs have mass-loss rates which are significantly lower than predicted by theory (Bouret et al. 2003; Martins et al. 2004), which raises questions whether the observed scale sizes of bow shocks around stars that display the weak-wind phenomenon can be accounted for by a wind-driven bow shock model. It has already been proposed by van Buren & McCray (1988) that radiation pressure driven bow waves are expected around stars with a low wind momentum flux. Until now, no such structure has been detected in the interstellar medium (ISM).

The IC 434 emission nebula is probably an evolved H II region, where the ionizing population of the large σ Orionis cluster has cleared away its immediate surroundings. Currently, the ionization front is eating its way into the L1630 molecular cloud and the ionized material is streaming into the H II region. The central component is a five-star system, found approximately one degree below Altinak, the easternmost star in Orion's Belt. This region also contains the characteristic Horsehead Nebula (Barnard 33), emerging as a dark nebula out of the large L1630 molecular cloud. Caballero (2008) has measured a distances of 334_{-22}^{+25} pc, although reported distances vary up to ~ 500 pc, as determined from colour-magnitude diagrams (Caballero et al. 2007). Previous studies have revealed a vast population of lower-mass stars and brown dwarfs belonging to the larger σ Ori open cluster (Béjar et al. 2011; Caballero 2007a). The dominant ionizing component of the system, σ Ori AB, is a 3 Myr old (Caballero 2008) close binary of spectral type O9.5V and B0.5V with a third massive companion (Simón-Díaz et al. 2011). The ionizing flux from the central stars illuminates IC 434 together with the mane of the Horsehead nebula. The presence of a $24 \mu\text{m}$ infrared arc-like structure near σ Ori has been noted previously by Caballero et al. (2008) (their Fig. 1, as well as Fig. 2 from Hernández et al. 2007), who designated the brightest knot as σ Ori IRS2. To the best of our knowledge, we present here the first detailed study of this unique and conspicuous infrared source.

We argue that the arc structure engulfing σ Ori AB presents the first detection of a *dust wave* in the ISM, where radiation pressure has stalled the dust which was carried along by a photo-evaporation flow of ionized gas. In Sec. 2.2, we present the observations and how we processed the data; Sec. 2.3 reviews the stellar properties and we derive local physical parameters; in Sec. 2.4 the observables and the global structure are presented; in Sec. 2.5 we propose the dust wave scenario to explain the observations; results are shown in Sec. 2.6 which we will discuss in Sec. 2.7. We conclude in Sec. 2.8.

2.2 Observations

IR photometry

Infrared (IR) photometry of the σ Ori cluster combines data from the *Wide-field Infrared Survey Explorer* (WISE; Wright et al. 2010), the Infrared Array Camera (IRAC; Fazio et al. 2004) and the Multiband Imaging Photometer (MIPS; Rieke et al. 2004) on board of the *Spitzer Space Telescope* and the Photodetector Array Camera and Spectrometer (PACS; Poglitsch et al. 2010) on the *Herschel Space Telescope*. The WISE atlas data were extracted from the All-Sky Data release and were mosaiced using Montage. IRAC data were observed in March 2004 as part of program ID 37 and were taken from the Spitzer Science Center archive as a post-Basic Calibrated Data (post-BCD) product. The post-BCD image with a $1^\circ \times 0.8^\circ$ field-of-view (FOV) combines BCD images of 30 seconds integration time each and was found to be of good quality. The MIPS $24 \mu\text{m}$ post-BCD data was also of sufficient quality and give a $0.75^\circ \times 1.5^\circ$ FOV in medium scan mapping mode with $160''$ steps. PACS $70 \mu\text{m}$ photometry was taken from the Herschel Science Archive (HSA) from the Gould Belt survey (André et al. 2010) with observation IDs 1342215984 and 1342215985. These PACS data were obtained in PACS/SPIRE parallel mode at high scanning speed ($60'' \text{ s}^{-1}$). The nominal full width at half maximum (FWHM) of the point spread function (PSF) for this type of observations is $5.9'' \times 12.2''$ for the blue ($70 \mu\text{m}$) channel. HIPE v.8 (Ott 2010) and Scanamorphos v.15 (Roussel 2012) were used to make maps of the IC 434 region after which the data was inter-calibrated with IRAS $70 \mu\text{m}$ data. Contamination by zodiacal light was subtracted using the SPOT background estimator, based on the COBE/DIRBE model (Kelsall et al. 1998).

H α imaging

H α narrow band data from the *Hubble Space Telescope* (HST), the Mosaic 1 wide field imager on Kitt Peak National Observatoy (KPNO) and the Southern H-Alpha Sky Survey Atlas (SHASSA) are used in this study. The HST image of the Horsehead was taken as part of the Hubble Heritage program (PI: K. Noll) and is used as a calibrator for the KPNO image. The calibrated KPNO image offers H α data at a high angular resolution ($0.26'' \text{ pix}^{-1}$), but does not extend towards σ Ori AB. Because of this, we complement our H α observations with data from the SHASSA mission. SHASSA provides a complete coverage of the northern hemisphere at a 0.8 arcminute resolution.

Spitzer/IRS spectral mapping

Spitzer/IRS (Houck et al. 2004) spectral maps from the Spitzer Science Center Archive

were obtained as part of the SPECH II program (PI: C. Joblin) in April 2008. Both Long-Low modules (LL) were used from the observations, which cover the 16-35 μm wavelength region at an angular resolution of $5''/\text{pixel}$. In addition, a dedicated offset position was taken at an IRAS dark position. Spectral cubes were built using CUBISM (Smith et al. 2007). CUBISM uses the 2D BCD data and allows for standard reduction operations such as sky subtraction and bad pixel clipping. In addition, slit and aperture loss correction functions appropriate for extended source calibration are applied and statistical errors originating from the IRS pipeline are propagated through CUBISM.

2.3 Stellar properties and local physical conditions

Figure 2.1 displays the mid-IR view of the IC 434 complex. Although diffuse structures are seen inside the H II region, the image shows a large cleared-out region with σ Ori AB slightly displaced from its center. The image shows that σ Ori AB is indeed the driving ionizing source of the region as numerous pillars of material, which are currently being photo-evaporated, are directed towards the star. The lower panels in Fig. 2.1 zooms into our region of interest: the σ Ori AB - L1630 region. Radiation from the star is ionizing the boundary of the molecular cloud, launching the material into the H II region. Extended emission at 24 μm and an arc structure, more pronounced at 12 μm , reveals the interaction of the ionized flow with either a stellar wind or radiation pressure emanating from σ Ori AB.

2.3.1 Basic stellar properties and space velocities

Table 2.1 lists basic stellar properties for σ Ori AB. We calculate the space velocity of σ Ori AB with respect to the Local Standard of Rest (LSR). Using these parameters, σ Ori AB has a space velocity of 15.1 km s^{-1} , with a position angle of 49.9° . For comparison, σ Ori D and σ Ori E have space velocities of 18.5 and 13.1 km s^{-1} , respectively.

The direction of the space velocity of σ Ori AB (see Sec. 2.3.1) suggests that it is moving towards the molecular cloud, increasing the relative velocity between the flow and the star. We note that it is possible that the observed space velocity of the σ Ori AB (as a member of the σ Ori cluster) represents the velocity of the entire region with respect to the Local Standard of Rest (LSR), which would imply that σ Ori AB is at rest with the L1630 molecular cloud. A comparison of radial velocities (with respect to the LSR) v_{LSR} of members of the σ Ori cluster (i.e., σ Ori AB, σ Ori D and σ Ori E) and the L1630 cloud reveal similar velocities: we calculate a mean v_{LSR} of 13 km s^{-1} for the σ Ori cluster members, whereas the L1630 cloud moves at a velocity of $v_{\text{LSR}} \sim 10 \text{ km s}^{-1}$ as seen through molecular observations (Maddalena et al. 1986; Gibb et al. 1995). Surely, a comparison of radial velocities alone will not resolve the question whether both structures are moving together or not, as these measurements only represent one component of the true space velocity. In this work, we will use the measured space velocity of σ Ori AB as the relative velocity between the cloud and the star, but we will address the implications on our conclusions if the two structures were at rest with one another.

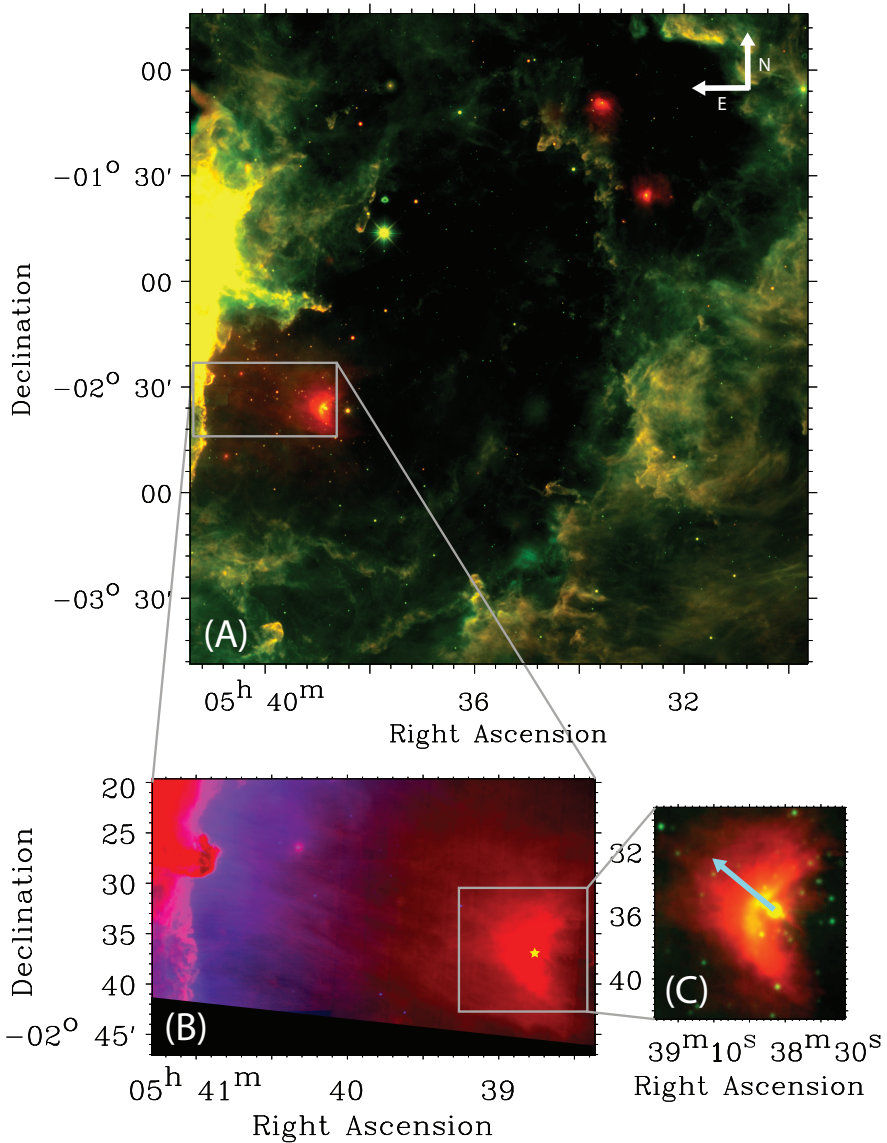


Figure 2.1: (a): Mid-IR view of the IC 434 region. The total field-of-view is $3.1^\circ \times 2.9^\circ$. Green is the WISE-3 $12 \mu\text{m}$ band; red is the WISE-4 $22 \mu\text{m}$ band. (b): Blown-up part of the upper image with different scaling to accentuate the extended emission around σ Ori AB. The Horsehead nebula is located at the top left. Here, blue represents $H\alpha$ taken with the KPNO 4m telescope, whereas red is MIPS $24 \mu\text{m}$ emission. The KPNO image does not extend over the entire field of view but cuts off $6'$ eastwards of σ Ori AB. (c): Close up of the environs of σ Ori AB. Green is WISE-3, while red is MIPS $24 \mu\text{m}$. Overplotted is the proper motion vector which displays the movement in the plane of the sky.

RA (J2000)	05:38:44.768	Caballero (2007a)
DEC (J2000)	-02:36:00.25	
Spectral type	O9.5V + B0.5 V	Hoffleit & Jaschek (1982)
L ($\log(L_\star/L_\odot)$)	4.78	Lee (1968)
$\log Q_0$ (s^{-1})	47.88	Martins et al. (2005a)
μ_α (mas yr^{-1})	4.61 ± 0.88	Perryman et al. (1997) [1]
μ_δ (mas yr^{-1})	-0.4 ± 0.53	Perryman et al. (1997)
μ_α (km s^{-1})	6.8	
μ_δ (km s^{-1})	5.7	
$v_{\text{rad}}(\text{LSR})$ (km s^{-1})	11.45	Caballero (2008)
d (pc)	334^{+25}_{-22}	Caballero (2008)
\dot{M} ($M_\odot \text{ yr}^{-1}$)	8.0×10^{-8}	Howarth & Prinja (1989)
	2.0×10^{-10}	Najarro et al. (2011)
v_∞ (km s^{-1})	1060	Howarth & Prinja (1989)
	1500	Najarro et al. (2011)
θ ($^\circ$)	49.9	This work
i ($^\circ$)	49.4	
v_\star (km s^{-1})	15.1	

Table 2.1: Stellar parameters for Sigma Ori AB (also known as 48 Ori, HD 37468, and HIP 26549) and calculated space velocity parameters. L is the luminosity of the star; Q_0 is the ionizing photon flux; v_{rad} is the radial velocity; μ_α and μ_δ are the proper motions in RA and DEC, respectively; d is the measured distance; \dot{M} is the mass-loss rate. The proper motion position angle θ is measured from north to east; i is the inclination angle with respect to the sky and v_\star is the total space velocity of σ Ori AB. [1] Values for proper motion published in van Leeuwen (2007) show a large discrepancy between different members σ Ori central cluster. Therefore, we adopt proper motion parameters from Perryman et al. (1997). In this case, proper motions between σ Ori AB are similar to the values for σ Ori D and σ Ori E listed in Caballero (2007a).

2.3.2 Wind properties

The winds from early O-type stars and early B-type supergiants are well described by the mass-loss recipe from Vink et al. (2000). However, the accuracy of this recipe has been questioned for stars with luminosity $\log(L/L_\odot) < 5.2$, in particular because of wind clumping and the weak-wind problem as described in Najarro et al. (2011) and Puls et al. (2008), but see Huenemoerder et al. (2012). This is because traditional mass-loss indicators (UV, H α) become insensitive at low mass-loss rates. Thus far, there are wind parameters for only a handful of late O-dwarf stars (Bouret et al. 2003; Martins et al. 2004; Najarro et al. 2011). Table 2.1 includes two different values for the mass-loss rate \dot{M} and the terminal wind velocity v_∞ of σ Ori AB. Earlier measurements by Howarth & Prinja (1989) were interpreted in terms of a much higher momentum flux. However, it is now well appreciated that the diagnostic use of UV wind lines is limited (Martins et al. 2005b; Puls et al. 2008). Najarro et al. (2011) categorized σ Ori AB as a weak-wind candidate after careful

modeling of spectral lines in the L-band. We believe that the latter value is closer to the true value given the extreme sensitivity of the Br α line flux for very low mass-loss rates (Auer & Mihalas 1969; Najarro et al. 1998; Lenorzer et al. 2004). The model presented in this work naturally follows from σ Ori AB being a weak-wind object; however, we will discuss the implications when one would use a higher momentum flux in Sec. 2.6.2 and in Appendix 2.A.

2.3.3 Photo-evaporation flow

The IC 434 H II region is a clear example of a flow of ionized gas, which is initiated when the ionization front breaks out of a dense confining molecular cloud environment into a surrounding tenuous medium. The density contrast will drive a strong isothermal shock into the low density region, while a rarefaction wave will plough into the ionized cloud gas. Material ionized at the edge of the molecular cloud is rapidly accelerated and driven into the low density region, starting the onset of a flow of ionized gas (a *champagne flow*; Tenorio-Tagle 1979; Tielens 2005). In the case of IC 434, it is the density contrast between the tenuous H II region and the high density L1630 cloud that has set up the flow of ionized gas towards σ Ori AB.

Figure 2.2 shows the root mean square (RMS) electron density derived from the observed H α emission measure (EM), assuming a path length of the emitting region along the line of sight. The EM is defined as $\int n_e^2 dl$, where n_e is the electron density and l the path length of the emitting region. We consider the H II region to be fully ionized, i.e., $n_e = n_H$, with n_H the hydrogen density.

We estimate the electron density in two independent ways. First, Compiègne et al. (2007) used the S[III] 19 and 33 μm fine-structure lines to determine the electron density just ahead of the Horsehead (within ~ 0.02 pc from the ionization front) to be $n_e \approx 100 - 350 \text{ cm}^{-3}$. Second, the local density at the ionization front is estimated by calculating the amount of ionizing photons J which land on the surface of the L1630 molecular cloud. Assuming a dust attenuation of $e^{-\tau} = 0.5$, Abergel et al. (2003) approximated this at $J = 0.8 \times 10^8 \text{ cm}^{-2} \text{ s}^{-1}$. Dividing this by the isothermal sound speed $c_s = (kT/\mu m_H)^{1/2} = 10 \text{ km s}^{-1}$ at $T_e = 7500 \text{ K}$ (Ferland 2003), we calculate a density of $n_H = n_e = J/c_s = 80 \text{ cm}^{-3}$, in close agreement with the value derived by Compiègne et al. (2007).

The EM of the flow is derived using the calibrated KPNO H α intensity together with standard conversion factors taken from Osterbrock & Ferland (2006). We measure EM = $1.8 \times 10^4 \text{ cm}^{-6} \text{ pc}$ at the ionization front. We can then pin down the path length l of the L1630 molecular cloud at the cloud surface using the derived density n_H . In this way, L1630 needs to extend 1 pc along the line of sight in order to reproduce the derived density.

We are particularly interested in the gas density further downstream, where the ionized flow interacts with σ Ori AB (see Fig. 2.1). For this, we need to adopt a density law between the star and the molecular cloud. As discussed in Sec. 2.1 and above, the density contrast between the tenuous H II region and the dense molecular cloud L1630 sets up a champagne flow streaming into the H II region (Tenorio-Tagle 1979). Strictly speaking, on a large scale the surface of the L1630 cloud will be convex, which will lead to a photo-evaporation flow following the nomenclature described in Henney et al. (2005). However, as the radius of curvature of the ionization front is much larger than the distance to the

ionizing source and as we are focussing on the material passing close to the star (which will originate from a small part of L1630), the analysis of Henney et al. (2005) suggest that we can approximate the structure of the flow as a champagne flow in a plane-parallel geometry. For this we will adopt the results for an isothermal shock tube as described in Bedijn & Tenorio-Tagle (1981) and Tielens (2005).

The initial velocity of the gas leaving the cloud surface is assumed to be comparable to the sound speed (i.e., a D-critical ionization front). The rarefaction wave moving into the ionized cloud gas sets up an exponential density gradient along which the gas is accelerated into the H II region. The continuity and momentum equations can then be used to show that the gas follows a linear velocity law defined as

$$dv_g = c_s \frac{d\rho_g}{\rho_g}. \quad (2.1)$$

Here, v_g and ρ_g are the velocity and density of the flow. Rewriting this in terms of the number density n , Eq. 2.1 integrates to (Bedijn & Tenorio-Tagle 1981)

$$n(r) = \frac{J}{c_s} \exp\left(\frac{r - R_s}{c_s t}\right), \quad (2.2)$$

where r is the distance from the star ($r \leq R_s$); R_s is the Strömngren radius (Strömngren 1939) (in our case: the distance between σ Ori and the molecular cloud), and t is the time which has passed since the material at the head of the flow had been ionized and started to move into IC 434.

We adopt an expansion law to describe the evolution of the path length l with distance from the molecular cloud. While the flow expands into the H II region, we increase the path length linearly. When the flow has reached σ Ori AB, we assume that the scale size of the emitting gas along the line of sight is equal to the traversed distance, i.e., the projected distance between L1630 and σ Ori AB of $d = 3.2$ pc at a distance of 334 pc. The ionized flow then shows a smooth drop in hydrogen density, ranging from $n_H = 100$ cm^{-3} at the cloud surface to $n_H = 10$ cm^{-3} near σ Ori AB. The result is shown in Fig. 2.2. We find that, due to the pressure gradient, the gas near σ Ori AB is accelerated to 35 km s^{-1} which is 3.5 times the local sound speed c_s . The timescale for the ionized gas to reach the star is then roughly 1.5×10^5 yr. Taking into account the space velocity of σ Ori AB, we calculate a maximum relative velocity between the star and the ionized flow of 50 km s^{-1} . In summary, Fig. 2.2 demonstrates that the density law is well described by an exponential density law with a scale height of 1 pc at the cloud surface. As the density at the ionization front is well determined from the intensity ratio of the S[III] fine structure lines, the only assumption that enters into this comparison is the linear expansion of the flow along the line of sight from 1 pc at the ionization front to ~ 3 pc at σ Ori.

2.4 Bow waves and dust waves

Figure 2.1 reveals an increase in emission at mid-IR wavelengths near σ Ori AB, peaking at a distance of $d = 0.1$ pc ahead of the star. Given that σ Ori AB is classified as a weak-wind candidate, we propose that the extended emission surrounding σ Ori AB represents the first detection of a radiation-pressure driven structure around a massive star moving

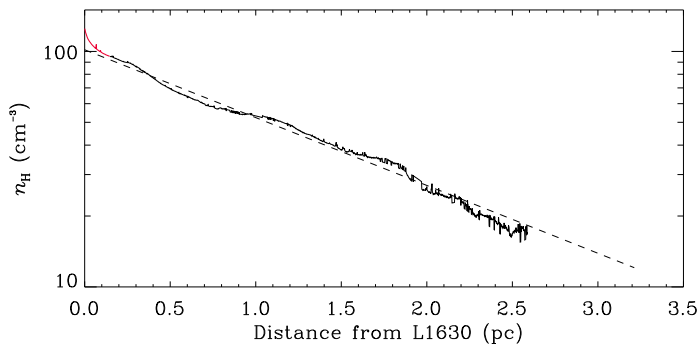


Figure 2.2: Density profile of the ionized photo-evaporation flow inside IC 434. The contribution of the Horsehead is plotted in red, which is only a small disturbance at the start of the flow. Small artifacts in the observed density profile persist after subtraction of background/foreground stellar features not associated with the flow. The observed profile reveals an exponential density gradient and is fitted using an appropriate density law (dashed line; see text). σ Ori AB is located at a distance of 3.2 pc.

through the ISM (van Buren & McCray 1988). The radiation pressure of σ Ori AB acts on the dust, stalling it at a distance ahead of the star where the ram pressure of the ISM material is balanced. We adjust the nomenclature as described by van Buren & McCray (1988) and distinguish between a *dust wave*, where dust is stopped and decouples from the gas, and a *bow wave*, where dust is stopped and gas stays coupled. This section will elaborate on information extracted from the IR observations, while Sec. 2.5 will deal with the physics of bow waves and dust waves.

2.4.1 Dust distribution

The dust color temperature is derived from the $24 \mu\text{m}$ and $70 \mu\text{m}$ intensities after convolving the PACS $70 \mu\text{m}$ image to the MIPS $24 \mu\text{m}$ beam using the convolution kernels described in Aniano et al. (2011). According to the Herschel PACS Instrument Calibration Centre (ICC), photometric measurements between PACS and MIPS are consistent within 17%¹. The dependence of dust emissivity on wavelength, β , is of little importance in our study as we are extrapolating towards long wavelengths where the intensity is low. In this work, we fix the emissivity at $\beta = 1.8$. Following Hildebrand (1983), the dust optical depth is estimated by

$$\tau_\nu = \frac{I_\nu}{B_{\nu, T_d}}, \quad (2.3)$$

where I_ν is the surface brightness and B_ν is the Planck function for dust temperature T_d . We evaluate Eq. 2.3 at $70 \mu\text{m}$. The dust color temperature map and the optical depth map at $70 \mu\text{m}$ are plotted in Fig. 2.3. Dust temperatures range from 50 ± 10 K to 75 ± 14 K near σ Ori AB while the optical depth τ_{70} ahead of the star increases by a factor of 2-3 compared to the region behind σ Ori AB.

¹PICC-NHSC-TN-029: <https://nhscdmz2.ipac.caltech.edu/pacs/docs/Photometer/PICC-NHSC-TN-029.pdf>

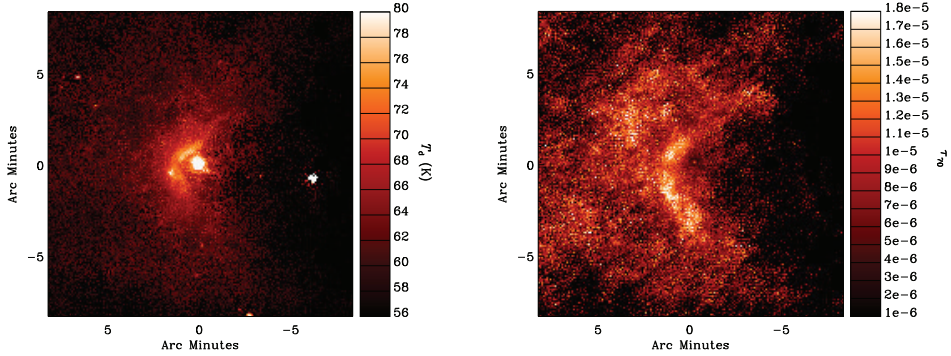


Figure 2.3: *Left:* MIPS $24\ \mu\text{m}$ versus $70\ \mu\text{m}$ PACS dust color temperature map. The scale size is $16.5' \times 16.5'$. Only pixels with values $> 3\sigma$ in the PACS $70\ \mu\text{m}$ image are plotted. North is up, east is to the left. *Right:* $70\ \mu\text{m}$ optical depth map.

2.4.2 Dust mass

The spectral energy distribution (SED) of the emission is extracted using an aperture which encapsulated the IR emission while minimizing stellar contamination by σ Ori AB. This allows us to study the average dust properties within the aperture. Subsequently, an average of several background positions absent of obvious emission is subtracted. A two-component modified blackbody function is then fitted to the IRAC $8.0\ \mu\text{m}$, WISE $12\ \mu\text{m}$, MIPS $24\ \mu\text{m}$ and PACS $70\ \mu\text{m}$ integrated intensities. We minimize the temperature variation across the aperture by focussing on the bright emission only. The IRAC 3.4 , 4.6 and $5.8\ \mu\text{m}$ images are heavily affected by diffraction patterns from σ Ori AB and could therefore not be used to extract reliable flux values. The two components are believed to represent different dust populations. The emission component peaking near $45\ \mu\text{m}$, radiating at a temperature $T = 68\ \text{K}$, is thought to originate from large dust grains or Big Grains (BGs), which are in thermal equilibrium with the radiation field. The other component emitting at shorter wavelengths, radiating at $T = 197\ \text{K}$, probably originates from Very Small Grains (VSGs). In typical ISM conditions, the VSGs are stochastically heated. Here, it is safe to assume that the intensity of the radiation field is high enough for the VSGs to be in thermal equilibrium and can therefore be fitted by a modified blackbody function.

UV derived mass

The total surface brightness I_{tot} is found by integrating the SED over frequency, yielding $I_{\text{tot}} = 7.6 \times 10^{-3}\ \text{erg s}^{-1}\ \text{cm}^{-2}\ \text{sr}^{-1}$. The total luminosity L_{IR} is then $L_{\text{IR}} = 4\pi I_{\text{tot}} S$, where S is the emitting surface area of the IR structure. With $d = 334_{-22}^{+25}\ \text{pc}$ and an aperture which subtends 1.3×10^4 square arcseconds on the sky, we have $S = 3.4 \pm 0.5 \times 10^{35}\ \text{cm}^2$ and thus $L_{\text{IR}} = 8.3 \pm 1.6\ L_{\odot}$. The stellar luminosity is taken from Lee (1968) and equals $L_{*} = 0.6 \times 10^5\ L_{\odot}$. The energy absorbed by the dust grains through UV photons is subsequently re-emitted in the IR. Therefore, a good estimate for the optical depth at UV wavelengths is given by the ratio $L_{\text{IR}}/L_{*} = \tau_{\text{UV}} = 1.4 \pm 0.3 \times 10^{-4}$. From the optical

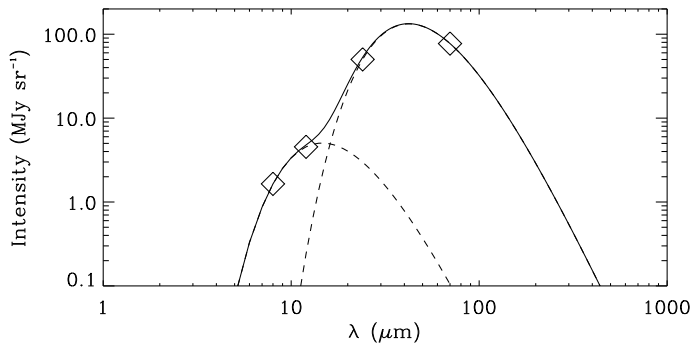


Figure 2.4: A two-component modified black body is fitted to SED of the extended IR emission around σ Ori AB.

depth at UV wavelengths, we can estimate the total dust mass $M_{\text{d,UV}}$ by assuming a grain opacity at UV wavelengths κ_{UV} and by multiplying with the surface area of a shell located at $r = 0.1$ pc:

$$M_{\text{d,UV}} = 4\pi r^2 \frac{\tau_{\text{UV}}}{\kappa_{\text{UV}}}. \quad (2.4)$$

We take $\kappa_{\text{UV}} = 1 \times 10^4 \text{ cm}^2 \text{ g}^{-1}$ (Weingartner & Draine 2001). In this way, we calculate a total dust mass of $M_{\text{d,UV}} = 8.4 \pm 1.6 \times 10^{-6} M_{\odot}$.

IR derived mass

It is possible to obtain an estimate of the total dust mass through the IR observations. $M_{\text{d,IR}}$ is directly proportional to the detected far-IR emission:

$$M_{\text{d,IR}} = \frac{\tau_{\nu}}{\kappa_{\nu}} S. \quad (2.5)$$

Here, $\kappa_{\nu} = 60 \text{ cm}^2 \text{ g}^{-1}$ at $70 \mu\text{m}$ (Weingartner & Draine 2001) and the average dust optical depth within the aperture is $\tau_{70} = 1.3 \pm 0.2 \times 10^{-5}$. We derive a total dust mass $M_{\text{d,IR}} = 3.7 \pm 0.7 \times 10^{-5} M_{\odot}$.

Summary on the observations

The total dust mass is approximated both through energy absorbed in the UV ($M_{\text{d,UV}}$) or directly through the IR $70 \mu\text{m}$ emission ($M_{\text{d,IR}}$). Our calculations show a discrepancy between both derived dust masses, i.e., $M_{\text{d,IR}}/M_{\text{d,UV}} = 4 \pm 0.8$. This discrepancy may simply reflect that the dust opacities at UV and far-IR wavelengths for dust in H II regions is very different from that calculated for (average) interstellar dust. In particular, Weingartner & Draine (2001) use a standard Mathis-Rumpl-Nordsieck (MRN) size distribution (Mathis et al. 1977), although the size distribution can be heavily affected during coagulation in the molecular cloud. A size distribution with relatively more large dust grains would reduce the opacity at UV wavelengths. A discrepancy between far-IR and UV derived dust

abundances has been noted by Salgado et al. (2012) for dust in H II regions. Considering the discrepancy between values derived in both methods, we adopt a total dust mass of $M_d = 2.3 \pm 1.5 \times 10^{-5} M_\odot$, which is the mean value of both earlier derived values (with the 1σ uncertainty). The total dust-to-gas mass fraction can then be approximated by comparing M_d with the amount of gas M_g contained in the same volume. We adopt a geometry of a spherical shell with thickness $dr \approx 25'' = 1.3 \times 10^{17}$ cm. The S[III] spectra show that there is no clear detection of an enhanced density structure in the gas coinciding with the observed dust arc (although high-resolution imaging is needed to conclude on the (non-)existence of a gaseous structure around σ Ori AB; see the discussion in Sec. 2.6.2). Here, we opted to extrapolate the large scale density distribution measured from the KPNO H α data. The gas density at the location of the dust arc is then about 10 cm^{-3} (Sec. 2.3.3). With $n_H = 10 \text{ cm}^{-3}$, we calculate a total gas mass of $M_g = 6.9 \pm 1.3 \times 10^{-5} M_\odot$. The total dust-to-gas mass ratio is then $M_d/M_g = 0.29 \pm 0.20$, significantly higher than the standard ratio in the ISM (~ 0.01). The derived dust-to-gas ratio implies that the dust number density has increased; we attribute this to radiation pressure acting on the dust grains, creating a *dust wave* ahead of σ Ori AB.

2.5 Physics of bow waves and dust waves

The dust wave around σ Ori AB is continuously fed by the photo-evaporation flow emanating from the L1630 molecular cloud. This flow is considered to be a two-component fluid of dust and gas particles, each of the components containing its own density, temperature and velocity structure. We follow the flow from L1630 to σ Ori AB. As the gas is being accelerated and approaches the star, it will drag along the dust grains through collisions. Inside the flow, dust grains will absorb photon energy and photon momentum from the ionizing star: while the energy is radiated away, the absorbed momentum causes the dust to be decelerated. We do not consider interaction with the stellar wind; it is assumed that the momentum flux of the wind is negligible compared to the radiation pressure. The ionized gas component of the flow has a negligible cross section for photon absorption, but exchanges momentum with the dust through drag. Through collisions of gas atoms with a dust grain, a significant amount of momentum from the dust can be transferred to the gas. This momentum is then distributed over all gas particles by internal collisions. Depending on the magnitude and efficiency of the momentum transfer, the gas and the dust component can stay coupled in the flow. The dust wave around σ Ori AB is caused by a balance between radiation pressure and the drag force. Below, we present a quantitative model describing the physics of this interaction.

2.5.1 Dust component

We write the equation of motion for dust as (Tielens 1983)

$$m_d \frac{dv_d}{dt} = -\frac{\sigma_d \bar{Q}_{rp} L_\star}{4\pi c r^2} + F_{\text{drag}} + F_{\text{Lorentz}}, \quad (2.6)$$

where m_d is the mass of the dust grain; r is the distance from the star; L_\star and c are the luminosity of the star and the speed of light; and σ_d and \bar{Q}_{rp} are the geometrical cross

section and the flux weighted mean radiation pressure efficiency of the grains. The first term on the right hand side of Eq. 2.6 describes the radiation pressure force F_{rad} . The term F_{Lorentz} is the Lorentz force and is described below. F_{drag} is the drag force due to interactions of the dust with atomic or ionic species i and equals (Draine & Salpeter 1979):

$$F_{\text{drag}} = 2\pi a^2 kT n_i \left(G_1(s_i) + z_i^2 \phi^2 \ln(\Lambda/z_i) G_2(s_i) \right). \quad (2.7)$$

Here, $s_i = \sqrt{m_i v_{\text{drift}}^2 / 2kT}$, m_i and z_i are the mass and charge of the interacting atoms or ions; a is the grain radius and v_{drift} is the relative velocity between the gas and the dust called the drift velocity. The drag force includes both the direct drag through collisions and the plasma drag through long range Coulomb interactions with ionic species and electrons. The electrostatic grain potential is defined by $\phi = Z_d e^2 / kT$, where Z_d is the grain charge and e is the elementary charge. Λ represents the Coulomb factor (Spitzer 1978):

$$\Lambda = \frac{3}{2ae|\phi|} \left(\frac{kT}{\pi n_e} \right). \quad (2.8)$$

The functions G_1 and G_2 are approximated by (Baines et al. 1965; Draine & Salpeter 1979)

$$G_1(s) \approx \frac{8s}{3\sqrt{\pi}} \left(1 + \frac{9\pi}{64} s^2 \right)^{1/2} \quad (2.9)$$

and

$$G_2(s) \approx s \left(\frac{3}{4}\pi^{1/2} + s^3 \right)^{-1}. \quad (2.10)$$

Grains with a velocity component perpendicular to the local magnetic field \mathbf{B} will gyrate around the field lines due to the Lorentz force F_{Lorentz} :

$$F_{\text{Lorentz}} = m_d \mathbf{v} \times \boldsymbol{\omega}_B. \quad (2.11)$$

The angular velocity $\boldsymbol{\omega}_B$ is given by

$$\boldsymbol{\omega}_B = \frac{z_d e}{m_d c} \mathbf{B}. \quad (2.12)$$

The drift velocity between the gas and the dust component can lead to the ejection of atoms from the surface of the dust into the gas phase. Grain-grain collisions will be negligible in the flow due to the low number density of grains compared to the gas. At low energies and for light projectiles, sputtering is caused by the reflection of an ion in a deeper layer of the grain. After the ion gets reflected, it knocks a surface atom into the gas phase. The rate of decrease in grain size is given by (Tielens et al. 1994)

$$\frac{da}{dt} = \frac{m_{\text{sp}}}{2\rho_s} v_{\text{drift}} n_i Y_i, \quad (2.13)$$

where m_{sp} and ρ_s are the mass of the sputtered atoms and the specific density of the grain material; and n_i and Y_i are the number density of the gas particles and the sputtering yield.

2.5.2 Gas component

The gas momentum equation does not contain the radiative deceleration term as the ionized hydrogen has a negligible cross section for photon absorption. We neglect gravitational attraction and therefore the equation of motion of gas consists of a balance between the pressure factor (Eq. 2.1) and the momentum transfer through interactions with dust grains:

$$\frac{dv_g}{dt} = v_g \frac{c_s}{\rho_g} \frac{d\rho}{dr} + \frac{n_d}{\rho_g} F_{\text{drag}}. \quad (2.14)$$

The term on the right hand side represents the amount of momentum transferred per second to a unit mass of gas. The dust number density n_d is taken from the MRN size distribution and the gas density ρ_g is adopted from Eq. 2.2. The ratio n_d/ρ_g is not constant, but will depend on the relative velocity of the gas and dust through the continuity equation.

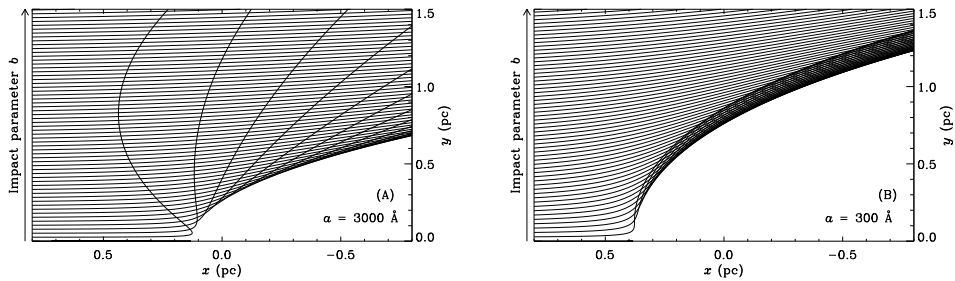
2.5.3 Modeling the interaction between the flow and σ Ori AB

To determine the velocity structure of the photo-evaporation flow, we integrate the coupled differential equations 2.6, 2.13 and 2.14 simultaneously using a fourth-order Runge-Kutta method in three dimensions. As we neglect grain-grain collisions, we could replace Eq. 2.6 with a set of equations for each grain size. The drag force in Eq. 2.14 should then be rewritten to account for the size distribution. For simplicity, we assume a single dust size distribution, but we will investigate the influence of grain size by solving the equations for several values of a . First, we consider a flow without grain charge and show that this reproduces the observations. Afterwards, we will discuss the inclusion of the Coulomb drag term described in Eq. 2.7 and the Lorentz force.

In our model, the x -axis is directed along the flow, which represents the projected distance from L1630 to σ Ori AB. The star is placed at the origin. The y -axis and z -axis represent the directions perpendicular to the flow, i.e., the direction in the plane of sky and the direction along the line of sight, respectively. The flow starts at the molecular cloud, positioned at $x = 3.2$ pc. We define the impact parameter b as the distance along the y -axis (see Fig. 2.5) at the start of the flow. A dust grain which approaches the star head-on ($b = 0$) will lose momentum by absorbing photons and be stopped at the point where the drag force F_{drag} balances the radiation pressure force F_{rad} . More specifically, an incoming dust grain will tend to overshoot its stopping distance, reaching a minimum distance to the star r_{min} depending on its momentum. Subsequently, it is pushed back by the radiation pressure force until an equilibrium radius r_{eq} is reached where $|F_{\text{rad}}/F_{\text{drag}}|$ equals unity. This results in a damped oscillation around r_{eq} . Particles with $b > 0$ will have similar trajectories, but will gain momentum in the y direction and therefore be pushed past the star in a shell-like structure. We define the radiation pressure opacity κ_{rp} , which determines the exact trajectory of a particle

$$\kappa_{\text{rp}} = \sigma_d \bar{Q}_{\text{rp}} / m_d. \quad (2.15)$$

We evaluate the model for two different values of κ_{rp} . For small grains, κ_{rp} is higher because the ratio of surface area over volume increases with smaller a . We have chosen



(a) Dust trajectories for a 3000 Å silicate grain trajectories for different values of impact parameter b .

(b) Same, but for a different value of κ_{rp} , which represents a 300 Å silicate grain.

Figure 2.5: Two dimensional plots of dust grain streamlines, evaluated for different grain sizes a . The x-axis represents the projected distance from L1630 to σ Ori, while the y-axis is the direction perpendicular to the line connecting L1630 and σ Ori AB, in the plane of the sky.

	Model A	Model B	Units
κ_{rp}	7×10^3	7×10^4	$\text{cm}^2 \text{g}^{-1}$
a	3000	300	Å
$n_{\text{d}}/n_{\text{g}}$	1.8×10^{-13}	1.7×10^{-11}	

Table 2.2: Parameters used in calculating the two different models shown in Fig. 2.5. a is the radius of the grain and ρ_{s} is the specific density of the grain material. These combinations of parameters represent a fiducial grain and do not necessarily represent grains taken from existing dust models.

the values of κ_{rp} in a way to clearly demonstrate the influence of grain size. The momentum of the incoming particle is determined by the grain size and the specific density ρ_{s} . In both models we choose $\rho_{\text{s}} = 3.5 \text{ g cm}^{-3}$, intermediate between the specific density of crystalline forsterite (3.21 g cm^{-3}) and fayalite (4.39 g cm^{-3}). For comparison, ideal graphite has a specific density of 2.24 g cm^{-3} . We set $\bar{Q}_{\text{rp}} = 1$ throughout the flow in both models. In reality, \bar{Q}_{rp} is dependent on r because it is averaged over the photon spectrum. This spectrum is altered due to attenuation of dust inside the H II region. The total dust optical depth is estimated at $e^{-\tau} = 0.5$ (Abergel et al. 2003) and the effect of the dust wave on the UV radiation field is negligible (see Sec. 2.4). The radiation pressure becomes important close to the star where the dust attenuation is low, which makes \bar{Q}_{rp} independent of r plausible. The initial dust number densities per H atom ($n_{\text{d}}/n_{\text{H}}$) are estimated using the MRN size distribution (Mathis et al. 1977) where we consider both the contribution of graphite and silicate grains. In this way, small grains have an abundance of $5.7 \times 10^{-11} \text{ H-atom}^{-1}$ for a bin size ranging from 100 Å to 500 Å. For the big grains, we use a bin size ranging from 1000 Å to 5000 Å. These grains have an abundance of $1.8 \times 10^{-13} \text{ H-atom}^{-1}$. The gas component follows the same density and velocity law as derived in Sec. 2.3.3. We calculate *a posteriori* the amount of momentum which the gas has acquired through collisions with the dust.

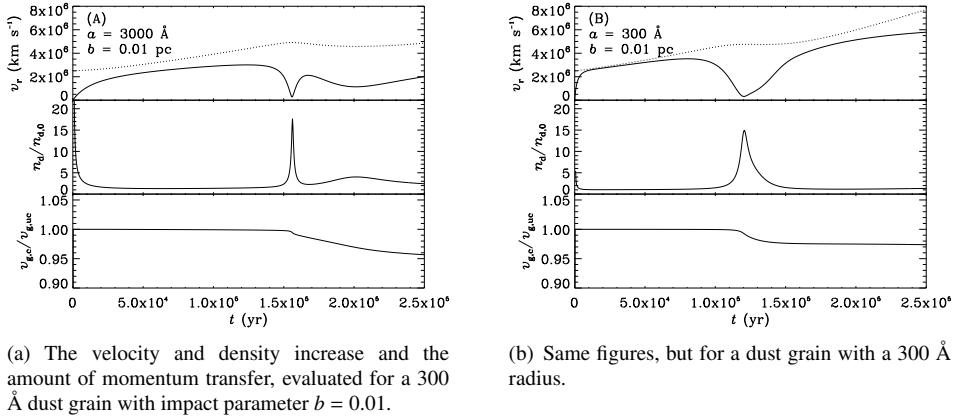


Figure 2.6: *Upper panels:* The radial velocity v_r of a dust grain (solid) and a gas particle (dotted, evaluated at the position of the dust grain in the frame of the star) as a function of time. At time $t = 0$, the gas is ionized and enters the H II region. *Middle panels:* The relative density increase in dust along the trajectory. This value approaches unity when the gas and dust are coupled. *Lower panels:* The velocity ratio of a gas particle $v_{g,c}$, after momentum transfer with the dust, to an uncoupled gas particle $v_{g,uc}$, which reflects the amount of momentum transferred from the dust to the gas.

2.6 Results

In Fig. 2.5 we plot trajectories along which a specific dust grain will travel. Model A represents a 3000 Å grain ($\kappa_{rp} = 7 \times 10^3 \text{ cm}^2 \text{ g}^{-1}$), while model B represents a 300 Å grain ($\kappa_{rp} = 7 \times 10^4 \text{ cm}^2 \text{ g}^{-1}$) with identical values for ρ_s ($= 3.5 \text{ g cm}^{-3}$) and \bar{Q}_{rp} ($= 1$). The effect of dust particle size is clearly seen. For larger values of κ_{rp} , radiation pressure is able to alter the direction of the grain further away from the star, even for trajectories with small initial b . While the distance which the particle overshoots is far less compared to model A, the stopping distance of the grain increases with high κ_{rp} . We calculate that a dust grain with $\kappa_{rp} = 6.7 \times 10^3 \text{ cm}^2 \text{ g}^{-1}$ (3300 Å) will be stopped at $d = 0.1 \text{ pc}$, which coincides with the peak emission of the dust wave at $24 \mu\text{m}$.

Figure 2.6 shows results for one specific trajectory with initial impact parameter $b = 0.01 \text{ pc}$. Our calculations show that a 300 Å grain will be accelerated on a short timescale, reaching the velocity of the gas at $t = 2.5 \times 10^3 \text{ yr}$. Momentum is lost gradually and r_{\min} is reached after $1.5 \times 10^5 \text{ yr}$, where the relative increase in number density peaks at 17 times the initial number density ($n_{d,0}$). Figure 2.6 also shows the ratio between the velocity of the gas with ($v_{g,c}$) and without ($v_{g,uc}$) momentum transfer with the dust. The gas will flow at a velocity of $0.97v_{g,uc}$ past the star and will therefore lose 3% of its initial momentum. Fig. 2.6 shows that the large grains (3000 Å) will be decelerated by the radiation pressure force before reaching the gas velocity. Even though the 3000 Å grains have lower velocities relative to the star compared to 300 Å grains, they have significantly more momentum and will therefore approach the star more closely. The time spent at r_{\min} is smaller because the radiation pressure force is far greater close to the star. However, we calculate that the total momentum transferred to the gas is small: gas flows at $0.96v_{g,uc}$ past the star.

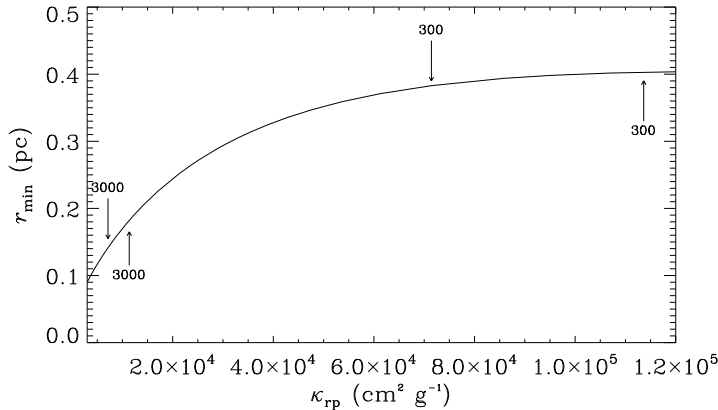


Figure 2.7: The point of closest approach to the star r_{\min} versus radiation pressure opacity κ_{rp} for trajectories with $b = 0$, assuming $\bar{Q}_{\text{rp}} = 1$ independent of grain size a . Labeled above the curve are typical grain sizes in angstroms for silicates. Below the curve are the corresponding grain size but for graphite grains.

The momentum of a grain depends on its size and composition, which will ultimately determine the trajectory of the particle. Larger grains will tend to move closer to the star compared to smaller grains. Consequently, dust will be stratified according to their size and specific properties. Figure 2.7 plots the minimum radius r_{\min} versus the radiation pressure opacity κ_{rp} . When comparing silicate and graphite grains of similar sizes, graphite particles are stopped further out from the star because of their low specific density.

The threshold energy for sputtering of hydrogen atoms from an amorphous carbon and silicate surface is $E = 0.5m_i v_{\text{drift}}^2 \sim 22$ eV (Tielens 2005). This energy is not reached in the flow, even at the stagnation point where the drift velocity is maximal. Indeed, the impact energy E should exceed the threshold energy with a factor of three to get effective sputtering of the grains. Therefore, we conclude that thermal sputtering of dust grains in the ionized flow is negligible.

We calculate the velocity of the dust and gas at each xyz point in space. We consider the problem to be axisymmetric along the y and z axes. Subsequently, we collapse the three-dimensional data cube along the line of sight and estimate the density increase using continuity: $\rho_d v_d = C$, where C is a constant. The result for grains with $\kappa_{\text{rp}} = 6.7 \times 10^3$ $\text{cm}^2 \text{g}^{-1}$ is then compared against the observations in Fig. 2.8. We scale the model to the observed value of τ_{70} at $x = 0.8$ pc. In this way, the model gives an absolute increase in density along the line of sight. In Fig. 2.8 we also show the solution of the model without radiation pressure. In this case, the dust will be accelerated as it is dragged by the gas and will follow the gas velocity law given by Eq. 2.1. When the radiation pressure force is included (i.e., Eq. 2.6), the dust will pile up in front of the star, resulting in a peak optical depth at $x = 0.1$ pc. The observed optical depth at $0.5 > x > 0.1$ pc is significantly above the model value, which we attribute to the presence of a population of smaller grains which are deflected at larger radii. At $x < 0$ pc, the optical depth is lower compared to the model without radiation pressure force. This cavity can not be explained by mere acceleration of dust past the star (see Fig. 2.6). The decrement in optical depth is only

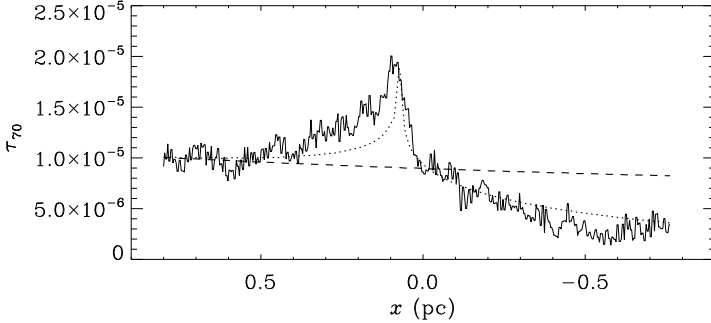


Figure 2.8: A cross cut of the optical depth map in Fig. 2.3 taken horizontally through the stagnation point of the dust wave (solid). Overplotted is a model without radiation pressure force (dashed) and a model with radiation pressure force (dotted).

reproduced by the model if we take trajectories with $|z| < 0.5$ pc into account. In other words, the observed optical depth at $70 \mu\text{m}$ (Fig. 2.3) only traces dust at a distance of $r < 0.5$ pc from σ Ori AB. This is because the $24 \mu\text{m}$ and $70 \mu\text{m}$ emission traces dust grains at a temperature of $\sim 30 - 100$ K.

In summary, we attribute the main peak in the optical depth map to large grains with $\kappa_{\text{TP}} > 1 \times 10^4 \text{ cm}^2 \text{ g}^{-1}$ ($a > 1500 \text{ \AA}$ for silicates). The enhanced optical depth in front of the main dust wave is then a result of grains with $\kappa_{\text{TP}} < 1 \times 10^4 \text{ cm}^2 \text{ g}^{-1}$ and is tracing smaller dust grains or different grain composition (graphite versus silicate). Therefore, dust waves (as well as bow waves) are natural grain sorters separating dust grains according to their radiation pressure opacities.

2.6.1 Coulomb interactions

Thus far we have neglected grain charging of the dust grains. The charge of an interstellar grain is determined by photo-ionization and positive ion recombination balanced with negative electron recombination. Under typical ISM conditions, this results in a positive grain charge due to the harsh conditions of the interstellar radiation field combined with low electron densities. In an H II region like IC 434, the electron density far exceeds that of the diffuse ISM. A good insight in the local physical parameters is needed in order to constrain the nature and magnitude of the grain charge.

The photo-ejection rate J_{pe} is dependent on the incident radiation field and the photo-ionization yield Y_{ion} ,

$$J_{\text{pe}} = \sigma_{\text{d}} \int_{\nu_{\text{Zd}}}^{\nu_{\text{max}}} \frac{J(\nu)}{h\nu} Q_{\text{abs}} Y_{\text{ion}}(Z_{\text{d}}, \nu) d\nu, \quad (2.16)$$

where J represents the mean radiation intensity calculated using a O9.5V Kurucz model atmosphere (Kurucz 1993) and Q_{abs} is the absorption efficiency of the grain material. We take Q_{abs} for silicates from Laor & Draine (1993). The photo-ionization yield Y_{ion} has been measured in laboratory experiments for energies up to 20 eV (Abbas et al. 2006), but experiments with higher energy photons are lacking and are very uncertain. Weingartner et al. (2006) investigated the role of extreme ultraviolet radiation and X-rays and

concluded that higher energy photons do not contribute significantly to the charge state of dust grains in H II regions ionized by OB stars. We follow Weingartner & Draine (2001) and take the ionization yield Y_{ion} as has been described there.

The photo-ejection rate is balanced by the electron recombination rate. Assuming a Maxwellian velocity distribution of the gas, the collisional rate J_e between electrons and a grain of positive charge Z_d is estimated with (Tielens 2005)

$$J_e(Z_d) = n_e s_e \left(\frac{8kT}{\pi m_i} \right)^{1/2} \pi a^2 \left(1 + \frac{|\nu|}{\epsilon} \right) \left[1 + \left(\frac{2}{\epsilon + 2|\nu|} \right)^{1/2} \right]. \quad (2.17)$$

Here we define the reduced temperature, $\epsilon = akT/q_e^2$ (with q_e being the charge of the electron), and the charge ratio between the dust and an electron, $\nu = Z_d/q_e$. If $\nu < 0$, the collisional rate increases because of electrostatic focussing. The charge distribution function is then calculated with Eq. 2.16 and 2.17,

$$\frac{f(Z_d + 1)}{f(Z_d)} = \frac{J_{pe}(Z_d)}{J_e(Z_d + 1)}, \quad (2.18)$$

where f is the fractional abundance of a dust grain with charge Z_d . The maximum charge of a dust grain is calculated at a distance $d = 0.1$ pc from the star. At these conditions, the peak of the charge distribution function lies at $Z_d = 195$ for a 300 \AA grain, whereas for a 3000 \AA grain this is $Z_d = 1809$.

A charged grain will not only have direct collisions with the gas (direct drag), but will also have long range Coulomb encounters with both electrons and ions (Coulomb drag). In addition, a grain will gyrate around the local magnetic field through the Lorentz force if it has a velocity component perpendicular to the field lines. The magnitude of both the Coulomb and the direct drag force is highly dependent on v_{drift} . At subsonic speeds, both direct and Coulomb drag forces are proportional to v_{drift} . In the supersonic regime, the direct drag force increases with v_{drift}^2 , while the Coulomb drag is proportional to v_{drift}^{-2} . Figure 2.9 relates the drag forces for a charged particle at 0.1 pc as a function of the Mach number $\mathcal{M} = v_{\text{drift}}/c_s$. In Sec. 2.3, we have shown that the maximum drift speed in the flow is $\mathcal{M} \sim 5$. As a result, it seems not justified to neglect the Coulomb drag force as it should dominate the total drag force throughout the entire flow.

Figure 2.9 also shows the radiation pressure force at 0.1 pc. Particles with $0.1\mathcal{M} < v_{\text{drift}} < 5\mathcal{M}$ will still be coupled to the gas at this distance. Figure 2.9(b) shows trajectories of a dust grain with $\kappa_{\text{rp}} = 6.7 \times 10^3$. Only at $d < 2.5 \times 10^{-2}$ pc, does the radiation pressure force become larger than the drag force and the dust will decouple from the gas. In contrast, particles with $b > 2.5 \times 10^{-2}$ pc stay coupled to the gas and will flow past σ Ori AB without being deflected since the radiation pressure is not able to overcome the Coulomb drag force at these distances.

The observed shape of the dust wave in Fig. 2.5 can only be reproduced if v_d at the wave front parallel and perpendicular to the flow are of same order. With the inclusion of the Coulomb drag force, decoupling occurs at $d = 2.5 \times 10^{-2}$ pc for large grains which does not agree with the observations (decoupling at $d = 0.1$ pc). In contrast, we have seen that by considering direct collisions only the observations are well reproduced. A further discussion on the exclusion of the Coulomb drag force is given in section 2.7.

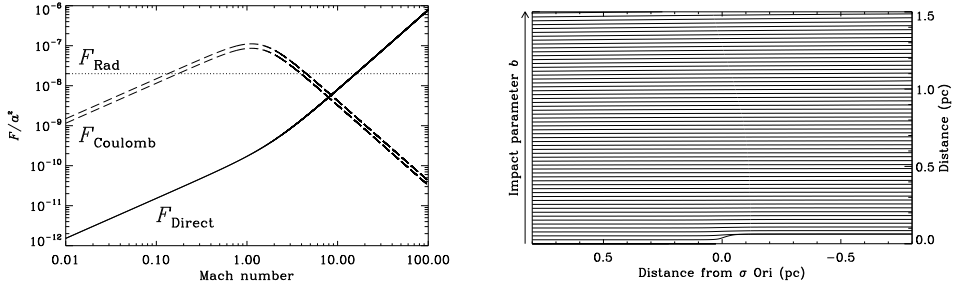


Figure 2.9: The dependence of the direct drag force and Coulomb drag force on drift velocity and the structure of the photo-evaporation flow with the inclusion of Coulomb drag. *Left:* Direct drag (solid line) and the Coulomb drag on a 300 Å dust grain with charge $Z_d = 195$ (upper dashed line) and a 3000 Å dust grain with charge $Z_d = 1809$ (lower dashed line). Plotted is the dependence of the drag forces on the relative velocity between the gas and the dust, expressed in the Mach number $M = v_{\text{drift}}/c_s$. The dotted horizontal line represents the radiation pressure force at $r = 0.1$ pc. *Right:* Calculated trajectories of a dust grain with $\kappa_{\text{TP}} = 6.7 \times 10^3$ including the Coulomb drag force. The grains only decouple from the gas very close to the star (i.e., $d < 0.025$ pc).

2.6.2 Bow shock scenario

One may question in what way the dust wave surrounding σ Ori AB differs from a bow shock (e.g., van Buren et al. 1990; Kaper et al. 1997). According to our definition stated in Sec. 2.4, a dust wave increases the number density of dust and will therefore solely emit at IR wavelengths with respect to the background emission, whereas a bow shock will shock both gas and dust and it is therefore possible to detect a bow shock in gas emission lines as well as IR wavelengths. This section elaborates on the gas emission expected from the structure if we were to treat it as a bow shock.

Equating the momentum flux of the stellar wind with the ram pressure of the star moving through the ISM, the stand-off distance r_s of a bow shock is given by (van Buren & McCray 1988)

$$r_s = 1.78 \times 10^3 \sqrt{\frac{\dot{M} v_\infty}{\mu_H n_H v_{\star\text{-ISM}}^2}} \text{ pc}, \quad (2.19)$$

where \dot{M} and v_∞ are the mass-loss from the star in $M_\odot \text{ yr}^{-1}$ and the terminal velocity of the stellar wind in km s^{-1} ; μ_H and n_H are the mean mass per hydrogen nucleus ($= 0.61$ for a fully ionized medium) and the hydrogen gas density in cm^{-3} ; and $v_{\star\text{-ISM}}$ is the relative velocity of the star with respect to the ISM in km s^{-1} . Plugging in numbers for σ Ori AB (Najarro et al. 2011) gives $r_s = 8 \times 10^{-3}$ pc (using $v_{\star\text{-ISM}} = 50 \text{ km s}^{-1}$, $\mu_H = 0.61$, $\dot{M} = 2.0 \times 10^{-10} M_\odot \text{ yr}^{-1}$ and the density profile for n_H derived in Sec. 2.3.3). This radius does not coincide with the observed peak emission at 0.1 pc.

Within the bow shock scenario, the gas emission should coincide with the peak of the IR dust emission if we assume the grains to be coupled to the gas. We note that large grains could potentially cross the shocked ambient gas, traversing into the shocked wind region due to their high momentum (Cox et al. 2013, in preparation). This would displace the peak IR emission from the peak gas emission if these grains dominate the

size distribution. Here, we assume efficient gas-dust coupling in the shocked region. The observed stand-off distance is only reproduced by increasing the wind momentum flux $\dot{M}v_\infty$ by a significant amount (a factor of ~ 300). For now, we adopt the wind parameters from Howarth & Prinja (1989) in order to estimate the gas density and hence the expected emission measure (EM) coming from a bow shock.

The temperature increase in a fully ionized medium is given by (Tielens 2005)

$$T_1 = 1.4 \times 10^1 \left(\frac{v_{\star\text{-ISM}}}{\text{km s}^{-1}} \right)^2 \text{ K}, \quad (2.20)$$

where T_1 represents the postshock temperature. At $T_1 \simeq 10^4$ K, the gas is cooled by permitted and (semi-)forbidden transitions, while collisional de-excitation is unimportant. In these circumstances, the post shock column density has to exceed the cooling-column density N_{cool} for a radiative shock to develop:

$$N_{\text{cool}} \simeq 8.2 \times 10^8 \left(\frac{v_{\star\text{-ISM}}}{\text{km s}^{-1}} \right)^{4.2} \text{ cm}^{-2}. \quad (2.21)$$

Given the expected relative velocity $v_{\star\text{-ISM}} = 50 \text{ km s}^{-1}$ and $T_1 = 3.5 \times 10^4$ K, $N_{\text{cool}} = 1.1 \times 10^{16} \text{ cm}^{-2}$. The shape of a bow shock near the stagnation point can be approximated by $x = y^2/3l$ (van Buren et al. 1990), where x and y are the coordinates parallel and perpendicular to the direction of motion. The column density of the swept-up material at the stand-off position can then be estimated using

$$N_{\text{H}} = 6.18 \times 10^{21} \sqrt{\frac{\dot{M}n_{\text{H}}v_\infty}{\mu_{\text{H}}n_{\text{H}}v_\star^2}} \text{ cm}^{-2}. \quad (2.22)$$

Here, the same units are used as in Eq. 2.19. Using the wind parameters of Howarth & Prinja (1989), the post-shock column density is estimated to be $4.6 \times 10^{18} \text{ cm}^{-2}$ and therefore we consider the shock to be radiative. A simple analytic expression for the thickness δ in pc of a radiative shock at the stagnation point is given through mass and momentum conservation (van Buren et al. 1990),

$$\delta = 16.6 \cdot \gamma_1 T_1 \sqrt{\frac{\dot{M}v_\infty}{\mu_{\text{H}}^3 n_{\text{H}} v_\star^6}} \text{ pc}, \quad (2.23)$$

where γ_1 is the ratio of specific heats in the preshock gas ($= 5/3$) and T_1 its temperature ($= 7500$ K). We calculate a thickness $\delta = 0.01$ pc; this corresponds to an angular size of $6''$ at a distance of 334 pc and a scale size along the line of sight of 0.1 pc, which indicates that the shock is resolved at the resolution of the KPNO $\text{H}\alpha$ image ($0.26''$). The shape and emission of a bow shock can be estimated as described in Wilkin (1996) assuming that the post-shock cooling is efficient (thin-limit approximation). The result is plotted in Fig. 2.10, where we have calculated the EM at the resolution of the KPNO $\text{H}\alpha$ image. We can predict the increase in emission measure seen at the wavelength of $\text{H}\alpha$ by convolving the computed profile with a Gaussian kernel of $1''$ in width (a typical value for astronomical seeing in the optical). At these conditions, we expect an increase of nearly 300% at the stagnation point with respect to the background emission measure of the entire photo-

evaporating flow at optical wavelengths.

The Spitzer/IRS spectra provides insight into the gas structure of the potential shock. Prominent lines in the 15-35 μm wavelength range are the S[III] 33.4 μm and S[III] 18.7 μm infrared fine-structure lines. Given the high critical densities and low excitation energy (compared to the electron temperature) of these lines, IR fine structure lines are good tracers of density variations in the emitting gas. Here, we have elected to use the 18.7 μm line because of its higher critical density ($1.2 \times 10^4 \text{ cm}^{-3}$) compared to the 33.4 μm line to exclude collisional de-excitation. As the gas density in the IC 434 photo-evaporative flow is well below the critical density, we expect a similar increase in the S[III] emission measure as plotted in Fig. 2.10, albeit somewhat lower due to the lower resolution of the IRS spectrograph compared to the resolution used in computing the profile in Fig. 2.10 ($1''$). At 19 μm , the FWHM of the PSF of the IRS is $\sim 5''$ (from the IRS instrument handbook 5.0); this would shift the peak value of the expected emission measure down to 230% the background value. However, in reality bow shocks are not so thin (e.g., Comeron & Kaper 1998), therefore the increase in emission measure may not be as pronounced as depicted in Fig. 2.10, which should be treated as a limiting case.

The covered regions of the IRS observations are overplotted in Fig. 2.11. In the lower panel of Fig. 2.11, the intensity of the S[III] 19 μm line is plotted as a function of distance from σ Ori AB. We only detect gas emission close to σ Ori AB, possibly originating from the immediate surroundings of the system. We do not detect a significant increase (i.e., $> 3\sigma$) in line emission at the position of the dust structure as is seen in the IR images (0.1 - 0.4 pc, or 50 - 200 $''$). However, the IRS observations are noisy; high resolution imaging of the σ Ori AB region is needed to conclude on the (non)-existence of a gaseous structure surrounding σ Ori AB. We emphasize that the weak stellar wind as derived by Najarro et al. (2011) is not able to create a bow shock with an associated IR arc at the observed scale size. σ Ori AB needs to have a powerful stellar wind such as measured by Howarth & Prinja (1989) to create an arc structure at the observed distance. This in turn should give strong increase in H α emission measure (or another gas tracer) which is yet to be observed. Here, we conclude that, inside the weak-wind scenario, the formation of a dust wave provides a very plausible alternative to the previously invoked bow shock designation.

2.7 Discussion

Within the dust wave scenario, the dust grain motions are affected by radiation pressure and drag force through interaction with gas particles. Our results indicate that the momentum transfer between the gas and dust is efficient at the start of the photo-evaporation flow. Small grains ($a < 1000 \text{ \AA}$) will initially be coupled to the gas, whereas larger grains ($a > 1000 \text{ \AA}$) will not be accelerated to the gas velocity. As the combined dust-gas flow travels into the H II region, the gas density decreases while the radiation pressure increases, which ultimately leads to a decoupling of gas and dust. The point of decoupling depends on the gas density and the dust grain properties, in particular the radiation pressure cross section per unit mass, κ_{rp} . Close to σ Ori AB, the number density of the dust particles have dropped to a level such that the total momentum transferred back to the gas is negligible. Therefore, the gas flows through the dust wave unhindered. Dust waves and bow waves can be distinguished by calculating if the dust is able to stop the gas along with it.

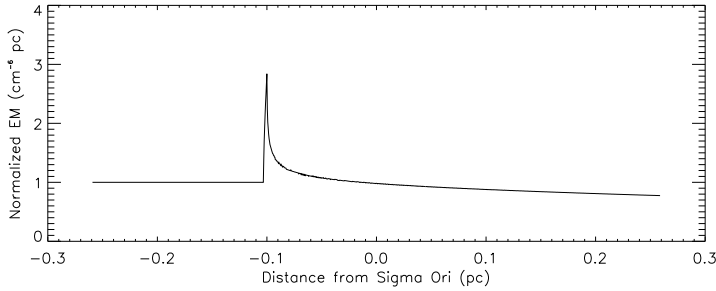


Figure 2.10: The emission measure from the gas expected from a bow shock as described in Wilkin (1996), normalized to the expected background emission measure of the entire flow. The computed emission profile at resolution $0.26''$ (the resolution of the KPNO $H\alpha$ image) has been convolved with a Gaussian of width $1''$ to account for (typical) astronomical seeing at the wavelength of $H\alpha$. A cut through the stagnation point and the star is shown, adopting wind parameters from Howarth & Prinja (1989) and ISM parameters calculated in section 2.5.

This enters in our theory through Eq. 2.14, where in the case of a dust wave the velocity of the gas (v_g) is equal to the relative velocity between star and ISM ($v_{\star-ISM}$).

In our analysis, we have implicitly assumed that the space velocity of σ Ori AB (15 km s^{-1}) represents the velocity between the L1630 molecular cloud and σ Ori AB (i.e., the cloud is static with respect to the ISM). It is uncertain whether this is true: the Galactic rotation model used to calculate space velocities is an estimate and large discrepancies can occur. The other extreme (i.e., the cloud is static with respect to σ Ori AB) will lower the velocity of the flow by a fixed offset of 15 km s^{-1} . This effect will only qualitatively influence our results in the form of a different size distribution of dust, as larger grains are needed to reach the projected distance of the dust wave ($0.1 > d > 0.4 \text{ pc}$). Similarly, as we have noted in Sec. 2.1, the distance towards σ Ori AB is uncertain. This would only change the projected distance between the star and cloud and not affect our main conclusions.

One may question the uniqueness of the dust wave around σ Ori AB. In order to create a dust wave (or a bow wave), the point where dust grains are stopped due to radiation pressure should exceed the stand-off distance of a bow shock, i.e., $r_{\min} > r_s$. In this way, radiation pressure will act on the dust instead of being shocked by the stellar wind. It is therefore critical to have a good understanding of the mechanism driving stellar winds in order to constrain wind parameters from host stars.

We evaluate the situation where a star is moving through the Warm Neutral Medium (WNM; $n_H \approx 0.5 \text{ cm}^{-3}$) with a speed of 10 km s^{-1} and compare numbers for r_{\min} and r_s . Figure 2.12 shows the relation r_{\min} versus luminosity L . Overplotted are predictions for the stand-off distance r_s using observed wind parameters (Eq. 2.19). Galactic O-stars with spectral type earlier than O6 and early type B-supergiants show $r_{\min} < r_s$. In general, these stars have a too powerful wind to create a dust wave. In contrast, the weak winds observed for dwarf stars with spectral type later than \sim O6-O7 are able to create a dust wave ($r_{\min} > r_s$).

We can generalize these conclusions by investigating the relation of r_{\min} and r_s with ISM number density (n_{ISM}) and stellar velocity (v_{\star}). At low densities, the drag force F_d

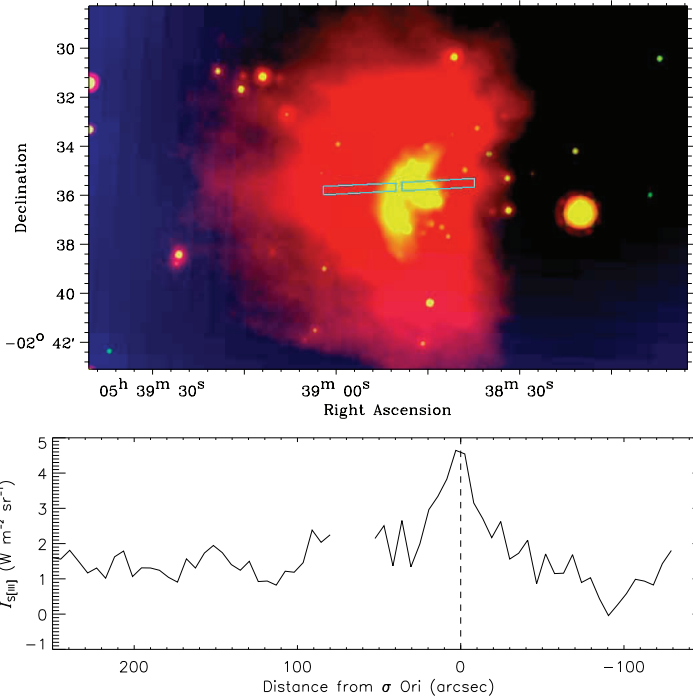


Figure 2.11: *Upper:* $0.45^\circ \times 0.2^\circ$ three color image of the IR emission around σ Ori AB. Red is WISE-4 $24 \mu\text{m}$, green is WISE-3 $12 \mu\text{m}$ and blue is $H\alpha$ from the SHASSA mission, smoothed over 5 pixels in order to remove star residuals. Overplotted are the Spitzer/IRS LL2 regions. *Lower:* Continuum subtracted and integrated intensity of the S[III] $18.7 \mu\text{m}$ line inside the IRS regions as a function of distance towards σ Ori AB (a positive distance corresponds to the region in front of the star). The dashed line marks the position of σ Ori AB. The IR arc is located at $\sim 0.1 - 0.4$ pc (the peak IR value being at ~ 0.1 pc), corresponding to 50 - 200 arcseconds in front of σ Ori AB.

in Eq. 2.6 becomes negligible and r_{\min} will be insensitive to a further decrease in density of the ambient medium. This is reflected in Fig. 2.13 at the point where the curve for r_{\min} turns over. At high densities, the dependency between r_{\min} and n_{ISM} is not straightforward and we opted to solve this numerically. The curves for r_{\min} and r_s run parallel at high densities ($r_{\min} \propto r_s \propto n_{\text{ISM}}^{-0.5}$). The same relation between r_{\min} and n_{ISM} is seen at different stellar velocities but for a subtle difference: at low v_\star , the point where the curve for r_{\min} turns over will shift to lower densities as the drag force can not be neglected at small velocities. The inverse holds for high v_\star . The stand-off distance r_s is plotted in Fig. 2.13 using wind parameters from Najarro et al. (2011) (weak-wind scenario) and Vink et al. (2000), respectively. It is clear that it is difficult to observe a dust wave around a star with a powerful wind described by Vink et al. (2000). This is not the case for weak-wind stars. In particular, Fig. 2.13 reveals that creating a dust wave is most efficient around relatively slow moving stars where the drag between gas and dust in the ISM is still important. For a typical stellar velocity of $v_\star = 10 \text{ km s}^{-1}$ this criterium holds for $n_{\text{ISM}} > 10 \text{ cm}^{-3}$. For a slowly moving star ($v_\star = 1 \text{ km s}^{-1}$) this drops to $n_{\text{ISM}} > 0.1 \text{ cm}^{-3}$. In summary, it is

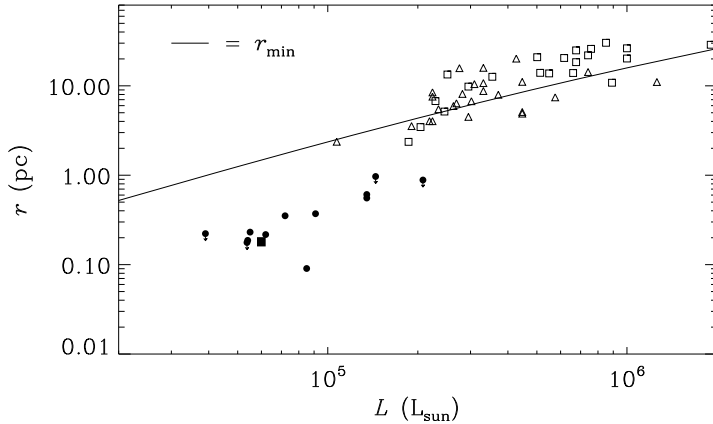


Figure 2.12: The solid curve shows r_{\min} for dust grains with $\kappa_{\text{tp}} = 6.7 \times 10^3 \text{ cm}^2 \text{ g}^{-1}$ plotted as a function of luminosity L , assuming typical parameters for the stellar velocity ($= 10 \text{ km s}^{-1}$) and an ISM density similar to the WNM ($= 0.5 \text{ cm}^{-3}$). Overplotted are Galactic O-stars (open squares) and B-supergiants (open triangles) where wind parameters are taken from Puls et al. (1996) and Crowther et al. (2006). The filled circles are weak-wind objects from Bouret et al. (2003), Martins et al. (2004) and Najarro et al. (2011). σ Ori AB is marked as the filled square symbol.

possible to create a dust wave around virtually all weak-wind stars. Only high-velocity runaway stars moving through low density ISM regions will more likely create a bow shock rather than a dust wave.

The Galactic sample of weak-wind candidates contains 22 sources, from which 5 have detected arc structures around them best observed at mid-IR wavelengths ($\sim 20 \mu\text{m}$) (Gvaramadze et al. 2012a): HD34078, HD48099, HD48279, HD149757 and HD216898. These structures are traditionally explained as bow shocks (Gvaramadze et al. 2012a; Peri et al. 2012). We have investigated if these structures could be explained as a dust wave. In Appendix 2.A, we compare the observed stand-off distance for these structures with (1) the expected stand-off distance within the bow shock scenario (both weak-wind and normal-wind) and (2) the location of a dust wave within the dust wave/bow wave scenario, as presented in this work. We conclude that the observed arc structures can only be explained by bow shocks if the stars have strong winds, close to the value predicted by the Vink et al. (2000) mass loss recipe (HD149757 may be an exception to this rule; see Gvaramadze et al. 2012a). Unfortunately, the mass loss rate of late type O-dwarf stars is still being debated, and until now no observations exist that could distinguish the above mentioned structures as stellar wind driven or radiation pressure driven; high-resolution imaging of gas tracers might help to resolve this issue. Here we emphasize that, within the weak-wind scenario, these arc structures are well described by a dust wave.

Each of the first four previously named weak-wind candidates with IR arcs are runaway-OB stars, however with moderate proper motions ($25\text{-}40 \text{ km s}^{-1}$) except for HD34078 (150 km s^{-1}). Nevertheless, this seems to contradict the above discussion where we concluded that dust waves and bow waves are created most efficiently around slowly moving stars. This is obviously an observational bias: runaways provide a unique possibility to study massive stars individually, as they moved away from their often obscured formation

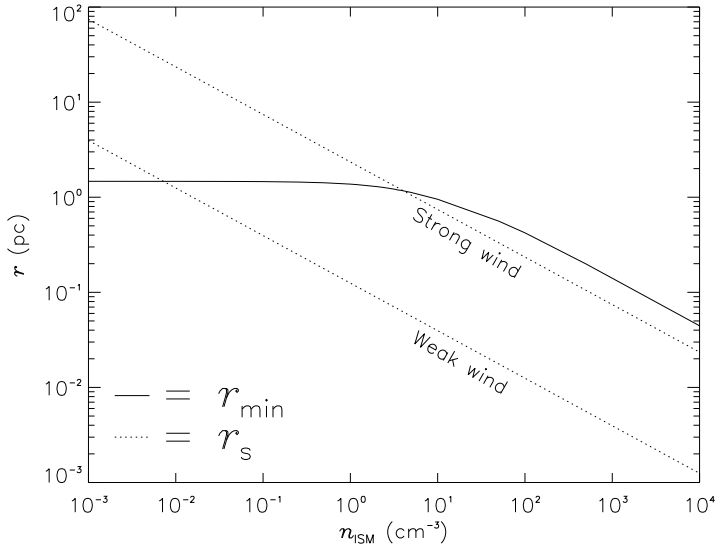


Figure 2.13: r_{\min} and r_s as a function of ISM number density n_{ISM} . The stand-off distance r_s is plotted using wind parameters from Najarro et al. (2011) (lower dotted line) and Vink et al. (2000) (upper dotted line). r_{\min} reaches a maximum at $n_{\text{ISM}} < 10 \text{ cm}^{-3}$ where the drag force F_d becomes negligible. r_s and r_{\min} show the same dependency on ISM density for $n_{\text{ISM}} > 10 \text{ cm}^{-3}$.

sites. The lifetime of massive stars is in general too short to create a dust wave around stars with low space velocity. In contrast, lower mass stars intrinsically have a lower space velocity, a longer lifetime and can be studied individually. These stars would therefore be ideal candidates to observe a dust wave, but a detection will be hampered by limiting spatial resolution with current IR instrumentation.

One of the key parameters to be able to detect a dust wave is the dust temperature. The temperature of silicates depends on the incident radiation field: $T_d \propto (L/r_{\min}^2)^{1/6}$. Figure 2.12 shows that r_{\min} is roughly proportional to L , which leads to $T_d \propto (1/L)^{1/6}$. Figure 2.14 shows T_d as a function of L . In the WNM, dust waves around massive O-stars should be observed at FIR wavelengths, whereas dust waves around B-stars are best observed at mid-IR wavelengths. Clearly, these estimates depend on the choice of local physical parameters. The dust wave around σ Ori AB is a striking example: due to the high density and the high relative velocity caused by the ionized flow, r_{\min} decreases as compared to a similar structure in the WNM. Therefore, T_d rises to 70 K and the dust wave lights up at wavelengths detectable to WISE and Spitzer.

2.7.1 Grain charge and Coulomb interaction

The Coulomb interaction potential is originally derived by Chandrasekhar (1943) for dynamical friction in a cluster of stars but redefined for a test particle confined in a plasma by Spitzer (1962) and Draine & Salpeter (1979). This theory treats each dust particle as being independent of one another, which is justified when the Debye screening length $\lambda_D = (kT/4\pi n_e)^{1/2}$ is smaller than the average intergrain distance $n_d^{-1/3}$. The grains inside the H II region are expected to contain high positive charges. We have argued that the

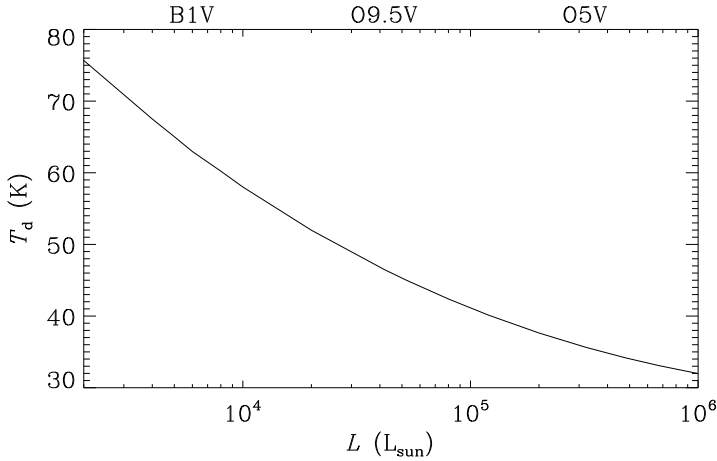


Figure 2.14: Dust temperature T_d for silicate grains ($\kappa_{\text{rp}} = 6.7 \times 10^3 \text{ cm}^2 \text{ g}^{-1}$), located at r_{min} , plotted as a function of luminosity L . For comparison, several spectral types for main sequence stars are plotted on the top axis.

expected charge leads to a large coupling between the gas and dust through Coulomb interactions, which can not be reproduced with our model when compared with observations. Therefore, we have concluded that the Coulomb drag force in the photo-evaporation flow approaching σ Ori AB can not be as efficient as is described in theory. We note that ionization yields for interstellar grains could be lower than expected. In Sec. 2.6.1, we already discussed the uncertainty of photo-electric yields for higher energies, but even for lower energies, these yields remain uncertain. This can partly be attributed to the fact that these measurements have been made on flat surfaces of bulk material of astrophysical composition. Bulk yields can differ significantly from yields of individual dust grains (Draine 1978). For example, yield curves for carbon and silicate as measured by Willis et al. (1973) and Abbas et al. (2006) differ by an order of magnitude. In addition, recent laboratory studies have revealed that high electric fields can spontaneously occur in solid films around cosmic dust analogs (Plekan et al. 2011). This is due to dipole alignment in the solid films and can create electrical fields of up to $10^{10} \text{ V cm}^{-1}$. This can have a significant impact on the grain charge, depending on the orientation of the electrical field.

It is also possible that we have underestimated the relative velocity between the star and material in the flow. A larger velocity would cause the dust to approach the star more closely and the Coulomb drag force will decrease by an order of magnitude. Specifically, if we increase the flow velocity by a factor 2 (i.e., $v_g = 100 \text{ km s}^{-1}$), we need to increase the radiation pressure efficiency by a factor of 2, i.e., $\bar{Q}_{\text{rp}} = 2$, which is still comparable with the value from Laor & Draine (1993).

Aspects of grain charge have never been studied directly in the ISM and theory relies on idealized models. Laboratory studies show that there are still key uncertainties in both photo-electric yields of cosmic dust analogs as well as on electric fields of solid films. Furthermore, dust properties in H II regions could be different from those in the diffuse ISM (Salgado et al. 2012). Dust waves will provide a unique environment to study the interaction of dust in an ionized environment.

2.8 Conclusion

In this paper we have argued that the arc-shaped emission surrounding σ Ori AB is a dust wave. Radiation pressure has created a structure ahead of the star where dust is being piled up, sorting the dust grains according to their radiation pressure opacities. A dust wave discriminates itself from a bow wave through the decoupling of the gas. We emphasize that to form the dust wave around σ Ori AB, Coulomb interactions have to be unimportant to reach sufficient decoupling between dust and gas. This suggests that we may not fully understand the processes controlling dust charging in hot, ionized regions in space such as H II regions.

We have shown that a dust wave, where radiation pressure acts on the surrounding medium, differs fundamentally from a classical bow shock, where the ram pressure of the star and ISM balance. It has already been proposed by van Buren & McCray (1988) that radiation-pressure-driven structures should exist around stars where the expected momentum flux from the stellar wind is low. No shock heating of gas is needed in the dust wave scenario, which explains the absence of gas emission lines in observations of bow shocks, in our case the S[III] observations. We note that observing bow shocks in the mid-IR is in general more efficient than in the optical. For example, typical conditions for a bow shock created by a massive runaway star moving through the ISM ($v_{\star} = 50$ km/s, $n_{\text{H}} = 1$ cm $^{-3}$) give $EM \sim 25$ cm $^{-6}$ pc (van Buren 1993), which is hardly detectable in present low-resolution all sky optical surveys. On the other hand, even though the dust optical depth is small, the high luminosity of the star ($> 10^5 L_{\odot}$) results in a significant surface brightness of the dust at mid-IR wavelengths (~ 10 MJy/sr) which is easily detectable with IR instrumentation such as IRAS, Spitzer and more recently, WISE.

σ Ori AB is a suitable candidate to observe a dust wave. First, the ionized flow from the L1630 molecular cloud creates a smooth homogeneous background without interfering factors which are often seen in regions where radiation pressure is important. For example, mass-loss variability in AGB stars or more complex geometries of compact H II regions will confuse a dust wave or bow wave with its surroundings. In the special case of σ Ori AB, these disturbing factors are minimal and the dust wave can be seen in great contrast against the underlying flow. Second, σ Ori AB has been classified as a weak-wind candidate (Najarro et al. 2011). According to this scenario, the bow shock stand-off distance should lie at $r_s = 8 \times 10^{-3}$ pc ($\sim 4''$) (see Sec. 2.6.2). If σ Ori AB would have a powerful stellar wind according to wind parameters derived by Howarth & Prinja (1989), the bow shock stand-off distance would lie at a greater distance from the star ($r_s = 0.13$ pc). In this case, incoming dust from the flow might be shocked by the stellar wind before it would reach the dust wave zone.

We argue that dust waves and bow waves should be common around stars with weak winds. Accurate wind parameters are still scarce for low mass loss rates, but it has become clear that stars with $\log(L/L_{\odot}) < 5.2$ show the weak-wind phenomenon. Although dust waves and bow waves are more likely to be formed around lower mass stars moving slowly through the ISM, only the most massive stars will create a structure which has a large enough separation from the star to resolve at IR wavelengths. Valuable information on dust properties can be probed by studying the size and geometry of a dust waves and bow waves. This could give a handle in studying the properties of dust inside different phases of the ISM and H II regions, which remain until now poorly understood.

Acknowledgements

Studies of interstellar dust and chemistry at Leiden Observatory are supported through advanced ERC grant 246976 from the European Research Council, through a grant by the Dutch Science Agency, NWO, as part of the Dutch Astrochemistry Network, and through the Spinoza premie from the Dutch Science Agency, NWO. NLJC acknowledges support from the Belgian Federal Science Policy Office via the PRODEX Programme of ESA.

2.A IR arcs around candidate weak-wind stars

In Tab. 2.3, we list parameters necessary for the calculation of the location of a bow shock (r_s) or dust wave/bow wave (r_{\min}) for the weak-wind candidates around which an IR-arc is observed. We calculate the stand-off distance both for the weak-wind scenario ($r_{s,\text{weak}}$) and the normal wind scenario ($r_{s,\text{Vink}}$). In most cases, the local ISM density is taken from references in the literature. However, for HD48279 and HD216898 these values are not directly measured. For these sources we used the average density along the line of sight, which may not be representative for the local density. r_{\min} is calculated with the model presented in this paper for a streamline with impact parameter $b = 0$. The grains approach the star with velocity v_* from infinity (i.e., a large radius compared to the distance travelled during the lifetime of the star) and are stopped in front of the star at r_{\min} . The listed r_{\min} contains two different values, where the lower value corresponds to 3000 Å silicate grains and the higher value to 300 Å silicate grains. Grains with sizes between these values are stratified in a region bounded by the listed values.

Using weak wind parameters, the calculated stand-off distance $r_{s,\text{weak}}$ is well below r_{obs} . The other goes for the stand-off distance $r_{s,\text{Vink}}$ using the theoretical recipe from Vink et al. (2000): except for σ Ori AB, $r_{s,\text{Vink}}$ exceeds r_{obs} . We conclude that in order to reproduce the IR arcs at r_{obs} , the stars need to have stellar winds close to the normal wind scenario. In the dust wave scenario, the region bounded by the 3000 Å and 300 Å grains encapsulates the observed peak distance of the arc structure r_{obs} , and can explain the IR structures at the observed locations. HD34078 is most likely a special case; neither a stellar wind nor radiation pressure can explain the observed location of the peak IR emission, due to the extreme high velocity of the star and the high density of the molecular cloud or core which it recently encountered. More observations are required to further constrain the relevant physical parameters of this system.

Star	Sp. T	d (kpc)	N_{H} (cm^{-2})	n_{H} (cm^{-3})	n (cm^{-3})	u^* (km s^{-1})	u_{∞} (km s^{-1})	M^{weak} ($M_{\odot} \text{yr}^{-1}$)	M^{Vink} ($M_{\odot} \text{yr}^{-1}$)	r_{obs} (pc)	$r_{\text{s,weak}}$ (pc)	$r_{\text{s,Vink}}$ (pc)	r_{min} (pc)
HD34078	O9.5V ⁽¹⁾	0.4	1.8e21	1.4	2e3 ^{(3)*}	150 ⁽⁵⁾	800 ⁽¹⁾	3.2e-10 ⁽¹⁾	4.2e-8 ⁽¹⁾	0.06	1.7e-4	1.9e-3	5e-3-8e-3
HD48099	O5.5 ⁽²⁾	1.5	1.4e21	0.35	1 ⁽⁴⁾	39 ⁽⁵⁾	2800 ⁽²⁾	2.5e-8 ⁽²⁾	2.1e-6 ⁽²⁾	1.85	0.48	4.49	0.52-2.73
HD48279	O8.5V ⁽²⁾	1.5	2.0e21	0.45	...	30 ⁽⁶⁾	1700 ⁽²⁾	1.6e-9 ⁽²⁾	1.6e-7 ⁽²⁾	0.43	0.19	1.73	0.22-1.73
HD149757	O9.5V	0.1	5.0e20	1.15	4 ⁽⁷⁾	26.5	1500	1.6e-9 ⁽⁷⁾	1.3e-7 ⁽⁷⁾	0.16	0.07	0.60	0.17-0.80
HD216898	O9V ⁽⁸⁾	0.6	1.1e21**	0.60**	...	24.8	1700 ⁽⁸⁾	4.5e-10 ⁽⁸⁾	6.0e-8 ⁽⁸⁾	0.56	0.10	1.98	...
σ Ori AB	O9.5V	0.3	10	50	1500	2.0e-10 ⁽⁹⁾	8.0e-8***	0.1	6e-3	0.13	0.10-0.40

Table 2.3: IR arcs around candidate weak-wind stars. Column definitions: d is the distance; N_{H} and n_{H} are the total column density and average number density of atomic hydrogen along of sight; n is a directly measured local ISM number density (see below); M^{weak} and M^{Vink} are the weak-wind values as given in the corresponding references and the mass-loss as predicted by the theoretical recipe described in Vink et al. (2000); r_{obs} is the observed projected distance where the emission peaks in the WISE 22 μm images (assuming the listed d); $r_{\text{s,weak}}$, $r_{\text{s,Vink}}$ are the calculated through spectral type, density, velocity, and u_{∞} ; r_{min} is the predicted location of the dust wave in the model described in this work. r_{min} calculated through spectral type, density, velocity, and listed for 3000 Å and 300 Å grains, respectively. References: (1) Martins et al. (2005a); (2) Martins et al. (2012); (3) Boissé et al. (2009); (4) Brown & Bomans (2005); (5) Perri et al. (2012); (6) Gvaramadze et al. (2012b); (7) Gvaramadze et al. (2012a); (8) Marcolino et al. (2009); (9) Najarro et al. (2011). Distances and (average) column densities from Gudennavar et al. (2012) (for HD216898 d was not listed and is calculated through the measured *Hipparcos* parallax from van Leeuwen 2007). *: HD34078 is a fast runaway star which has recently encountered a molecular cloud or core not along the line of sight, therefore the average density along the line of sight is not representable in calculating the stand-off distance. **: There is no column density of atomic hydrogen measured for HD216898; the listed column density (and the derived average density) is for molecular hydrogen. ***: For consistency, we list M from Howarth & Prinja (1989), value used throughout this work. This value is consistent with the Vink et al. (2000) prediction, seen by comparison with the other O9.5V stars HD34078 and HD149757.

3

A bimodal dust grain distribution in the IC 434 H II region

Studies of dust evolution and processing in different phases of the interstellar medium is key to understanding the lifecycle of dust in space. Recent results have challenged the capabilities and validity of current dust models, indicating that the properties of interstellar dust evolve as it transits between different phases of the interstellar medium.

In this work, we characterize the dust content from the IC 434 H II region, and present a scenario that results in the large-scale structure of the region seen to date. We conduct a multi-wavelength study of the dust emission from the ionized gas, and combine this with modeling, from large scales that provide insight into the history of the IC 434/L1630 region, to small scales that allow us to infer quantitative properties of the dust content inside the H II region.

The dust enters the H II region through momentum transfer with a champagne flow of ionized gas, set up by a chance encounter between the L1630 molecular cloud and the star cluster of σ Ori. We observe two clearly separated dust populations inside the ionized gas, that show different observational properties, as well as contrasting optical properties. Population A is colder (~ 25 K) than predicted by widely-used dust models, its temperature is insensitive to an increase of the impinging radiation field, is momentum-coupled to the gas, and efficiently absorbs radiation pressure to form a dust wave at 1.0 pc ahead of σ Ori AB. Population B is characterized by a constant [20/30] flux ratio throughout the H II region, heats up to ~ 75 K close to the star, and is less efficient in absorbing radiation pressure, forming a dust wave at 0.1 pc from the star.

Our conclusion is that the dust inside IC 434 is bimodal. The characteristics of population A are remarkable and can not be explained by current dust models. We argue that large porous grains or fluffy aggregates are potential candidates to explain much of the observational characteristics. Population B are grains that match the classical description of spherical, compact dust. The inferred optical properties are consistent with either very small grains, or large grains in thermal equilibrium with the radiation field. Our results confirm recent work that stress the importance of variations in the dust properties between different regions of the ISM.

3.1 Introduction

The advent of high-resolution infrared (IR) imaging during the last decade has provided indisputable evidence that dust resides within the ionized gas of H II regions, rather than being associated with photo-dissociation regions along the line of sight (e.g., Povich et al. 2007; Paladini et al. 2012). More than often, the discussion in literature is focussed on the question of what kind of dust population is able to survive inside an H II region, as the physical conditions in these regions predict that dust will be removed and/or destroyed in the ionized gas, either through radiation pressure, a stellar wind, dust sublimation, or dust sputtering (Inoue 2002; Everett & Churchwell 2010; Draine 2011a).

The work of Chini et al. (1986) triggered the thought of a separate dust component inside H II regions, which was supported by the model presented in Everett & Churchwell (2010), who discussed the possibility of evaporating cloudlets overrun by the ionization front (IF), resupplying the ionized gas with a new generation of dust. Paladini et al. (2012) showed that the IR emission from evolved H II regions is typically stratified as follows: polycyclic aromatic hydrocarbons (PAHs; Tielens 2008) and cold dust (~ 20 K) trace the PDR and a dense shell of the H II region, respectively, while $24 \mu\text{m}$ emission peaks inside the ionized gas, close to the central source. Ochsendorf et al. (2014b) proposed a new scenario to simultaneously explain the presence and morphologies of the mid-IR emission inside H II regions. Whereas several authors attribute the $24 \mu\text{m}$ emission inside ionized regions to the increase of VSGs compared with BGs (Flagey et al. 2011; Paradis et al. 2011), the analysis of the IR arc in IC 434 (Ochsendorf et al. 2014a) (from now: Paper 1) revealed that the increased heating by stellar photons from the nearby star can explain the mid-IR emission.

Besides the intrinsic nature of the dust inside H II regions, recent studies (Salgado et al. (2012), Paper 1) have indicated that dust properties inside H II regions may differ from that used in widely-used dust models of the diffuse interstellar medium (ISM) (Li & Draine 2001; Compiègne et al. 2011). In addition, results from the *Planck* mission indicate that dust properties evolve when transiting from one region of the ISM to another (e.g., Planck Collaboration et al. 2014a). Here, we focus on dust grains entrained within photo-evaporation flows, and follow the evolution as they transit from the molecular cloud phase to ionized regions of space.

We examine the dust content and processes governing the properties of the dust inside H II regions, using the IC 434 region as a benchmark model. The multitude of observations available for the region, its large angular extent, and its profitable location well outside the Galactic plane, makes IC 434 a suitable candidate to pursue this question. We extend the work and analysis described in Paper 1 to the far-IR. The new observations allow us to probe the dust content of the IC 434 region on a wide range of wavelengths which reveals a new dust population in the H II region. When combined with the theoretical model described in Paper 1, the analysis provides a means to constrain the properties of the dust entrained in the ionized gas flow of the IC 434 region. In particular, we will argue that the dust content in IC 434 is best explained through a bimodal distribution, which differs significantly from that seen in the diffuse ISM. We discuss our findings in the light of dust evolution inside the molecular cloud from which the dust is evaporated, such as the formation of aggregates through coagulation, and through recent findings of dust evolution as constrained by, e.g., the *Planck* mission.

In Sec. 3.3, we set the stage by digging into the history of the large-scale structure of the IC 434/Orion B molecular cloud region, that provides us with an updated and improved model for the ionized gas flow in IC 434 (as compared to Paper 1), necessary to derive the properties of the dust introduced into the H II region. In Sec. 3.4, we present the observations. After characterizing the global properties of the dust, we combine the observations with detailed modeling in Sec. 3.5, to derive properties of the emitting grains coming from the ionized gas. The results of the modeling are described in Sec. 3.6. We discuss our findings in Sec.3.7, and conclude in Sec. 3.8.

3.2 Observations

The observations used in this work are in part described in Paper 1, but are extended with *Herschel* observations at $\lambda > 70 \mu\text{m}$, *Planck* observations (Planck Collaboration et al. 2014c), and the *Planck* dust model R1.20 (Planck Collaboration et al. 2014a). PACS 160 μm and SPIRE 250 μm , 350 μm and 500 μm photometry were taken from the *Herschel* Science Archive (HSA) from the Gould Belt survey (André et al. 2010) with observation IDs 1342215984 and 1342215985. *Herschel* data was inter-calibrated with IRAS 70 μm (PACS 70 μm), *Planck* 857 GHz (PACS 160 μm , SPIRE 250 μm and 350 μm), and *Planck* 545 GHz (SPIRE 500 μm) through the method described in Bernard et al. (2010). The *Herschel* resolutions are 8.4'' (70 μm), 13.5'' (160 μm), 18.2'' (250 μm), 24.9'' (350 μm), and 36.3'' (500 μm), respectively, for parallel mode observations at ($60'' \text{ s}^{-1}$) scan rates.

The reduction of Spitzer/IRS observations is described in Paper 1, but is extended here with the Short-Low (SL) modules, covering the 5 - 15 μm region. The IRS SL detector suffered from a background level, causing apparent gradients throughout the modules and mismatches between the SL1 and SL2 spectra. This background level persisted after background subtraction of the BCD images and affected the reduced spectra. Following Sandstrom et al. (2012), we opted to correct the BCD images with the use of the inter-order regions that resulted in a significant improvement of the quality of the spectra.

3.3 The expanding H I shell surrounding Orion OB1b

In this section, we connect the IC 434 H II region with the large-scale structure of the Orion Belt region. We will argue that the large IR bubble, approximately centered on the open cluster of σ Ori, is blown by the Belt star ϵ Ori, and that σ Ori has crossed the distance from the Orion OB1c region, currently approaching the L1630 molecular cloud. Besides that the analysis provides a new insight into the history and evolution of the Belt region, the argumentation ultimately leads to the development of the flow model described in Sec. 3.5 and, subsequently, the derivation of grain properties that are entrained within the ionized gas.

3.3.1 The GS206-17+13 shell: mass and kinetic energy

The HI shell GS206-17+13 (Ehlerová & Palouš 2005), centered at $(l,b) = (206.1,-17.5)$, has a central radial velocity of $v_{\text{LSR}} = 12.8 \text{ km s}^{-1}$ and an expansion velocity of roughly $v_{\text{exp}} = 8 \text{ km s}^{-1}$. It extends $\sim 2^\circ \times 4^\circ$ ($13 \times 26 \text{ pc}$ at 385 pc; see below) in HI, and is

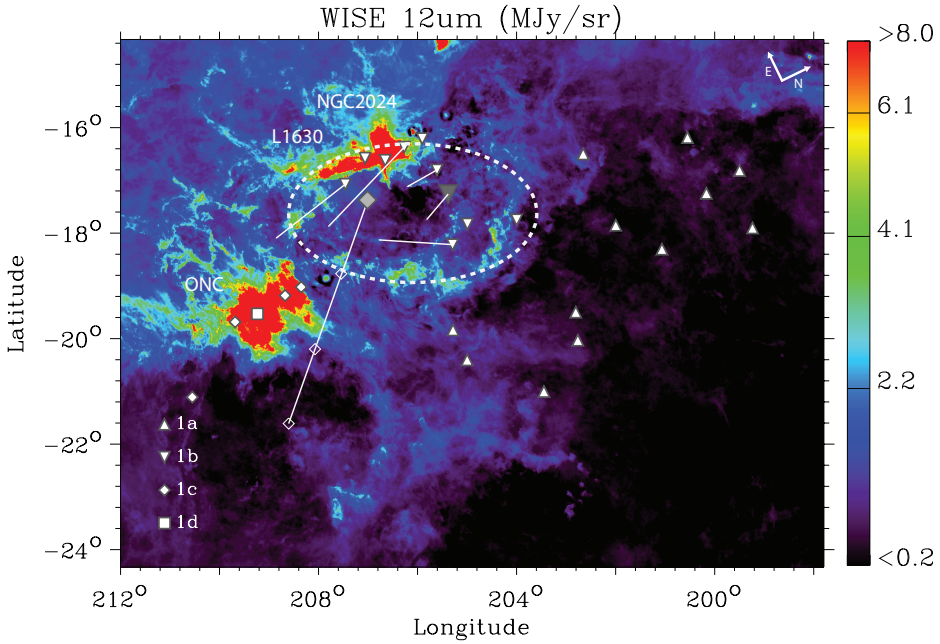


Figure 3.1: The WISE mid-IR view of the region surrounding the Orion OB association at $12\ \mu\text{m}$. The different sub-groups of the Orion OB association are overplotted for stars of spectral type B2 and earlier (Brown et al. 1994), where the oversized symbols represent σ Ori (diamond) and ϵ Ori (inverted triangle), respectively. The $12\ \mu\text{m}$ emission reveal the edges of the Orion molecular clouds as they are being illuminated by the ionizing flux of members of the Orion OB association. Also shown are several prominent structures in the image: the L1630 molecular cloud, the emission nebula NGC2024, and the Orion Nebular cloud (ONC). Of particular interest here is the bubble centered at $(l, b) = (206.1, -17.5)$, which is the IR counterpart of the GS206-17+13 HI shell (Ehlerová & Palouš 2005) and encircles the members of Orion OB1b (dashed outline). Overplotted in solid lines are the space motions of the stars, tracing *back* the motion of the stars in the plane of the sky during 1 Myr. For σ Ori, this trajectory has been extended to 3 Myr, where the open diamond symbols mark 1 Myr, 2 Myr, and 3 Myr.

also seen at mid- to far-IR wavelengths (Fig. 3.1). Apparently, it is centered on the Orion OB1b association and σ Ori. The total mass in the shell is estimated by adopting a dust emissivity per unit mass of gas, κ_ν , which is often modeled as a power law in the form of $\kappa_\nu = (10)\nu^\beta$, with the frequency ν in THz (Beckwith et al. 1990) and β the spectral index of the dust opacity. It should be noted that this relation could be more complex, depending on the exact grain properties (e.g., Planck Collaboration et al. (2014a), and references therein). We use the τ_{353} (optical depth at 353 GHz) and the β maps from the Planck dust model R1.20 (Planck Collaboration et al. 2014a), and define an aperture that encloses the bubble shell seen in WISE and Planck images. We estimate the contribution of Galactic emission along the line-of-sight unrelated with the bubble shell by determining the value of τ_{353} in a region close by at the same Galactic latitude ($\sim 23\%$ of the total emission), and subtract this from the optical depth measured within the aperture. With $\kappa_\nu = 2.1\ \text{cm}^{-2}$

g^{-1} at 353 GHz, and $\beta = 1.5$ as constrained by the Planck model, we calculate the total dust mass of the shell $M_d = (\tau_{353}/\kappa_v)S$, with S the physical size of the emitting region. We find a total dust mass of $M_d = 34 M_\odot$ or, equivalently, a gas mass of $M_g = 3400 M_\odot$ (using a gas-to-dust ratio $R = 100$). By distributing the mass back into a homogeneous sphere with radius 20 pc (the average radius of the HI shell), we find an average density of $n_{\text{local}} = 4.1 \text{ cm}^{-3}$, i.e., the original density in which the bubble expanded. Then, the total kinetic energy of the shell can be estimated with the expansion model described in Chevalier (1974):

$$\frac{E_{\text{tot}}}{\text{erg}} = 5.3 \times 10^{43} \left(\frac{n_{\text{local}}}{\text{cm}^{-3}} \right)^{1.12} \left(\frac{r_{\text{sh}}}{\text{pc}} \right)^{3.12} \left(\frac{v_{\text{exp}}}{\text{km s}^{-1}} \right)^{1.4} \quad (3.1)$$

Here, r_{sh} is the observed radius of the shell. Using $n_{\text{local}} = 4.1 \text{ cm}^{-3}$, $r_{\text{sh}} = 20 \text{ pc}$ and $v_{\text{exp}} = 8.0 \text{ km s}^{-1}$, we find $E_{\text{tot}} = 5 \times 10^{49} \text{ erg}$, which is only a factor of few lower than the typical kinetic energy injected by a SN ($\sim 10^{50} \text{ erg}$; Veilleux et al. 2005).

3.3.2 Driving source of the GS206-17+13 shell

The GS206-17+13 shell is filled with ionized gas that is known as the IC 434 emission nebula. The bright gas emission results from the ionizing flux of the central massive component of the σ Ori cluster, the triple-star-system σ Ori AB at $d = 385 \text{ pc}$ (Simón-Díaz et al. 2011; Caballero 2008) that is part of a quintuple system (van Loon & Oliveira 2003; Caballero et al. 2007), evaporating the L1630 cloud and launches a champagne flow into the expanding bubble. In this respect, it is tempting to attribute the expanding shell to the continuous input of the stellar wind of σ Ori AB to its surroundings. However, σ Ori is a young system ($t_{\text{age}} = 2\text{-}3 \text{ Myr}$; Caballero 2008) which exhibits a weak-wind ($\log(\dot{M}) = -9.7 M_\odot \text{ yr}^{-1}$, $v_\infty = 1500 \text{ km s}^{-1}$; Najarro et al. 2011). This amounts to an integrated mechanical luminosity of $L_{\text{mech}} = 1/2 \dot{M} v_\infty^2 t_{\text{age}} = 1.3 \times 10^{46} \text{ erg}$, of which only $\sim 10\%$ will couple as kinetic energy to the ISM (van Buren et al. 1990; Veilleux et al. 2005). This excludes σ Ori as the driving source of the expanding GS206-17+13 shell.

The Orion OB1b sub-association is centered on Orion's belt and has age estimates ranging from 1.7 Myr (Brown et al. 1994) to 8 Myr (Blaauw 1964). However, as noted by Bally (2008), the supergiant status of the Orion Belt stars (ζ Ori, ϵ Ori, and δ Ori) imply an age of the 1b association of at least 5 Myr. We find 11 stars of spectral type B2 or earlier within the Orion OB1b association (Brown et al. 1994). Remarkably, the massive members of the Orion OB1b association are positioned along the GS206-17+13 shell (Fig. 3.1), which provide clues to their origin.

The GS206-17+13 HI shell is located at $v_{\text{LSR}} = 12.8 \pm 7.8 \text{ km s}^{-1}$; Ehlerová & Palouš (2005). The most massive star in this v_{LSR} range is the B0I supergiant ϵ Ori at $d = 606_{-130}^{+227} \text{ pc}$ (van Leeuwen 2007), with wind parameters $\log(\dot{M}) = -5.73 M_\odot \text{ yr}^{-1}$ (Blomme et al. 2002) and $v_\infty = 1600 \text{ km s}^{-1}$ (Kudritzki et al. 1999). A simple calculation shows that ϵ Ori can provide the kinetic energy of the GS206-17+13 shell within $\sim 11 \text{ Myr}$ (assuming a constant wind strength and 10% kinetic efficiency), which is a reasonable timescale compared to the estimated age of the Orion OB1b association. Surely, the supergiant stars ζ Ori and δ Ori could have been part of the formation of the GS206-17+13 shell. However, the *Hipparcos* distances towards ζ Ori and δ Ori, $d = 225_{-28}^{+39} \text{ pc}$ and $d = 212_{-23}^{+30} \text{ pc}$ (van Leeuwen 2007), respectively, compared to the average distance of the stars located within

the velocity extent of the expanding HI shell ($v_{\text{LSR}} = 12.8 \pm 7.8 \text{ km s}^{-1}$), $d = 440 \text{ pc}$, renders this scenario implausible. This difference in distance is reflected in the low radial velocity $v_{\text{LSR}} = 1 \text{ km s}^{-1}$ for both $\zeta \text{ Ori}$ and $\delta \text{ Ori}$, compared to the velocity extend of the HI shell, which places the stars outside of the bubble. Perhaps, the stars have been thrown out of the cluster through dynamical interaction in the young OB1b cluster. Reynolds & Ogden (1979) already noted that $\delta \text{ Ori}$ does not have a clear H II region surrounding it, implying that the ionizing radiation can escape freely into the Orion-Eridanus superbubble cavity (Brown et al. 1995) instead of illuminating the surroundings of the star, i.e., the GS206-17+13 shell. We conclude that the stars at $d = 440 \text{ pc}$ are the best candidates for driving the expansion of the GS206-17+13 shell, with $\epsilon \text{ Ori}$ as the main contributor.

3.3.3 Space velocities of Orion OB1b and approach of $\sigma \text{ Ori}$

We calculate LSR space velocities of the stars belonging to the Orion 1b association following the method described in Cox et al. (2012), using proper motions and radial velocities, and correcting for the solar motion (Coşkunoğlu et al. 2011). Proper motions are taken from van Leeuwen (2007), except for the case of $\sigma \text{ Ori}$, where due to the complex nature of the system the new reduction of the *Hipparcos* catalogue did not produce an acceptable solution ($\mu_{\alpha} \cos \delta = 22.63 \pm 10.83 \text{ mas}$ and $\mu_{\delta} = 13.45 \pm 5.09 \text{ mas}$, van Leeuwen 2007, versus $\mu_{\alpha} \cos \delta = 4.61 \pm 0.88 \text{ mas}$ and $\mu_{\delta} = -0.40 \pm 0.53 \text{ mas}$, Perryman et al. 1997). The new reduction is also inconsistent with proper motion measurements from other members of the central quintuple system of $\sigma \text{ Ori}$, $\sigma \text{ Ori D}$ ($\mu_{\alpha} \cos \delta = 0.79 \pm 0.92 \text{ mas}$ and $\mu_{\delta} = -0.90 \pm 0.47 \text{ mas}$, van Leeuwen 2007) and $\sigma \text{ Ori E}$ ($\mu_{\alpha} \cos \delta = 2.2 \pm 0.92 \text{ mas}$ and $\mu_{\delta} = -1.4 \pm 0.47 \text{ mas}$, Caballero 2007b). Hence, for $\sigma \text{ Ori}$ the proper motion values of Perryman et al. (1997) are used. Figure 3.1 overplots the resulting space velocities for stars with v_{LSR} within the velocity extent of the expanding GS206-17+13 HI shell. The plotted trajectories can be traced *back* in time, and show that it is possible that the stars have dispersed to their current location projected along the bubble shell. In particular, the stars at the northern side of the GS206-17+13 shell at longitude $l > 206^\circ$ seem to be moving out of the bubble, influencing the morphology of the shell traced at $12 \mu\text{m}$ in the direction of movement. This asymmetry is also seen as an elongation of the HI shell in Galactic longitude (Ehlerová & Palouš 2005), and indicates that the Orion OB1b stars indeed have a relative velocity with respect to the Orion B molecular cloud and the GS206-17+13 shell. We add here as a caveat that due to the the location of Orion in the anti-direction of the Galactic center, the motion of the OB association is mostly directed radially away from the Sun (Brown et al. 1994; de Zeeuw et al. 1999a), which complicates precise measurement of proper motions. In addition, the distance towards some of the more distant stars in Orion OB1b gives rise to *Hipparcos* parallax errors of 40 - 50%. In this respect, the Gaia mission (de Bruijne 2012; Perryman et al. 2001) is expected to improve proper motion measurements and distance determinations towards the members of Orion OB1.

Based on its spatial proximity, $\sigma \text{ Ori}$ has often been classified as being part of the Orion OB1b association. Bally (2008) already noted that the age of the system ($\sim 2\text{-}3 \text{ Myr}$; Caballero 2008) is incompatible with the age of the Orion OB1b association ($> 5 \text{ Myr}$, Sec. 3.3.2). Therefore, Bally (2008) tentatively classified the $\sigma \text{ Ori}$ cluster as being part of the Orion OB1c association. Following Paper 1, the radial velocity v_{LSR} of $\sigma \text{ Ori}$

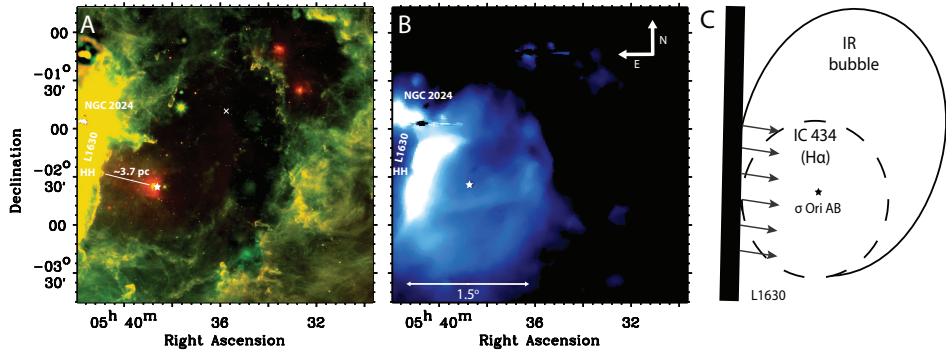


Figure 3.2: (A) Two color composite in the mid-IR of the region around σ Ori AB (white asterisk). Green is WISE 12 μm , whereas red is WISE 22 μm . The large IR counterpart of the GS206-17+13 HI shell surrounds σ Ori AB. The east-side of the bubble is marked by the large molecular cloud L1630, which includes the Horsehead Nebula (HH). The projected distance between the Horsehead and σ Ori, as shown by the white line along which the Spitzer/IRS observations are positioned (Fig. 3.4), is about 0.5 degrees or 3.7 pc (at 385 pc; Caballero 2008). The white cross reveals the offset position used for the Spitzer/IRS background subtraction. (B) Smoothed $H\alpha$ image from SHASSA (4' resolution). The gas emission around σ Ori AB (IC 434) originates from a photo-evaporation flow of the L1630 molecular cloud. The bright part appears roughly circular with a radius $\sim 0.75^\circ$. (C) Schematic view of the same region, showing the IR bubble (solid outline) and the $H\alpha$ emission (dashed circle), created by the photo-evaporation flow (arrows) of the L1630 molecular cloud (filled black rectangle).

and the L1630 cloud are similar ($\sim 10 \text{ km s}^{-1}$; Maddalena et al. 1986; Gibb et al. 1995). The proper motion of σ Ori translates to a velocity of 10 km s^{-1} ; we will use this value as the relative velocity, v_{rel} , between the cloud and σ Ori AB in Sec. 3.6. Then, the trajectory of space motion at 1 Myr, 2 Myr, and 3 Myr shows that σ Ori AB can cross the distance from the Orion OB1c region to its current location. Indeed, the sub-association Orion OB1c has an estimated age of 2 Myr to 6 Myr (Blaauw 1964; Warren & Hesser 1978; Bally 2008), which would solve the age discrepancy as described above. However, this assumes that the observed space velocity represents the relative velocity between cloud and star, but the actual traversed distance could be smaller if the bulk motion of the Orion region is co-moving with the stars (i.e., $v_{\text{rel}} < 10 \text{ km s}^{-1}$). In any case, as the σ Ori cluster approaches the L1630 cloud, the ionizing flux reaching the cloud surface increases, resulting in the bright photo-evaporation flow seen to date (Sec. 3.5.2), known as the IC 434 emission nebula.

3.4 Dust emission from the IC 434 region

3.4.1 Morphological structures

Figure 3.2a shows the mid-IR view of the region surrounding IC 434. The WISE 12 μm is dominated by PAH emission tracing the PDR surfaces directly adjacent to the IF. However, the gas content in the same region shows a different morphology (Fig. 3.2b):

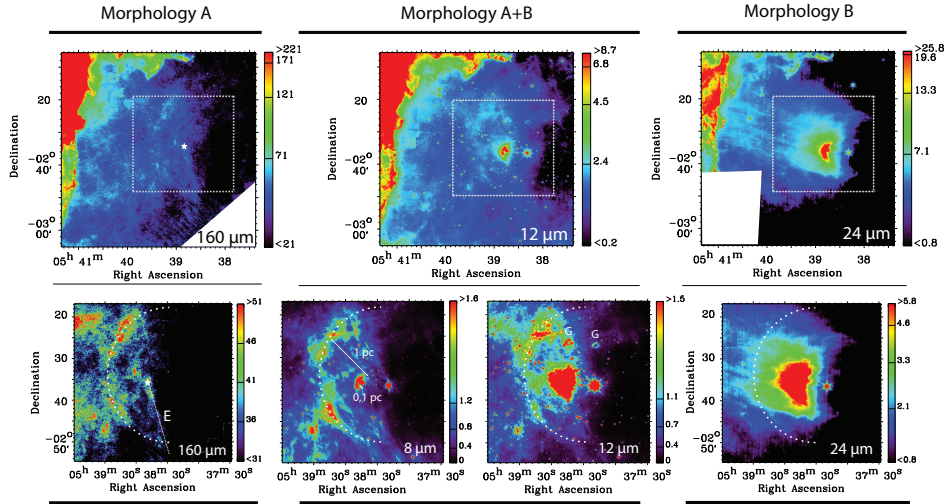


Figure 3.3: Two different infrared morphologies within IC 434. In all panels: north is up, east is to the left. Morphology A is evident at every wavelength except for $24\ \mu\text{m}$, and shows a diffuse structure emanating from the entire L1630 molecular cloud. Morphology B is a relative narrow structure, ranging from the L1630 molecular cloud towards σ Ori AB (white asterisk in the $160\ \mu\text{m}$ images), where it interacts with radiation pressure from the star at projected distance $0.1 < d \leq 0.4\ \text{pc}$ (Paper 1), forming the inner dust wave that is visible at wavelengths $\lambda < 24\ \mu\text{m}$. The $8\ \mu\text{m}$ and $12\ \mu\text{m}$ images show a combination of both morphologies (A+B). The lower panels zoom into the direct surroundings of σ Ori AB and cover the region in the dotted white box seen in the upper panels. The $8\ \mu\text{m}$, $12\ \mu\text{m}$ and $160\ \mu\text{m}$ images show another arc-like structure at a distance of $\sim 1\ \text{pc}$ away from the star (dashed line), forming the outer dust wave. The $12\ \mu\text{m}$ suffer from several ghost features ('G'). The $160\ \mu\text{m}$ image reveals an extended collimated flow (dotted line) away from the σ Ori AB, not seen at $8\ \mu\text{m}$ and $12\ \mu\text{m}$, which is possibly an evaporating member ('E') of the large σ Ori cluster. The color bars show the brightness scale in units of MJy/sr.

the bulk of the $\text{H}\alpha$ emission concentrates within a smaller region with radius $\sim 0.75^\circ$ ($\sim 5\ \text{pc}$ at a distance of $385\ \text{pc}$) inside the mid-IR bubble (Fig. 3.2c). The ionized gas originates from the evaporation of the L1630 molecular cloud by the ionizing flux of σ Ori AB. This gas flow effectively introduces dust into the ionized gas through momentum transfer.

Figure 3.3 shows the distribution of dust inside the IC 434 region at wavelengths $8\ \mu\text{m} \geq \lambda \geq 160\ \mu\text{m}$. The $24\ \mu\text{m}$ dust emission surrounding σ Ori AB has earlier been attributed to a *dust wave* (Paper 1). Here, we report the detection of emission from the ionized gas (Sec. 3.4.3) at $8\ \mu\text{m}$, $12\ \mu\text{m}$, and at *Herschel* wavelengths longwards of $160\ \mu\text{m}$. The $12\ \mu\text{m}$ WISE filter is broad (ranging from $7\ \mu\text{m} - 17\ \mu\text{m}$), and in principle is sensitive to both warm dust radiating at $100\ \text{K} - 200\ \text{K}$ and transiently heated particles, such as Very Small Grains (VSGs) and IR fluorescence from PAHs. While PAHs mainly show up in broad emission features at $5\ \mu\text{m} - 18\ \mu\text{m}$, VSGs typically reveal a continuum from $\lambda > 13\ \mu\text{m}$, which could be a real continuum or a superposition of multiple blended spectral features (Cesarsky et al. 2000; Abergel et al. 2002).

After inspection of the images at different wavelengths, one can distinguish two separate morphological IR emission structures inside the H α emitting volume (Fig. 3.3). On the one hand, there is a component seen at all wavelengths but for 24 μm (morphology 'A'). This component is characterized through its large diffuse scale and clearly associated with the full extent of the L1630 cloud. The morphology is spread throughout the entire IC 434 nebula, ultimately culminating in an arc-shaped increase in emission to the east of σ Ori AB at a projected distance of $d \sim 1$ pc (best observed at 8 μm), together with a clear drop-off in emission to the west of the star. For the remainder of this work, we will refer to this arc-like structure at $d = 1$ pc as the outer dust wave (ODW), due to the striking resemblance of the structure with the dust wave observed at 0.1 pc (see below). On the other hand, there is the emission detected with WISE and Spitzer at 22 μm and 24 μm which is clearly distinct from morphology A, peaking at $d \sim 0.1$ pc and revealing a relative narrow flow (morphology 'B'). This flow seems to be connected to a bright part of the L1630 cloud which is almost symmetrically positioned around the Horsehead Nebula, again forming an arc-like structure that peaks in intensity at $d \sim 0.1$ pc. We will refer to this structure as the inner dust wave (IDW). Close to the star, the IDW lights up at 12 μm and 8 μm due to heating of the grains and an increased dust-to-gas ratio (Paper 1).

3.4.2 Spectral energy distributions

To get insight in the properties of the emitting dust in the H II region, we constructed SEDs from the WISE, MIPS, PACS and SPIRE photometric points. All images were convolved to the point spread function of the SPIRE 500 μm band using the kernels described in Aniano et al. (2011). Subsequently, a common 'dark' spot in the maps was chosen for background subtraction (centered at $05^h37^m00^s -01^d52^m29^s$). The absolute uncertainties on the photometry are estimated at 10% for the WISE and Spitzer images, while we use uncertainties of 20% for PACS and 15% for SPIRE, respectively (Bernard et al. 2010). We extract SEDs corresponding to the regions covered by IRS (regions 1-7; Fig. 3.4) and complement these with two regions at both dust arcs, located at 1 pc (ODW) and 0.1 pc (IDW), respectively. The results are shown in Fig. 3.4.

3.4.3 Are we tracing emission from the ionized gas?

The analysis of the remainder of this paper assumes that the diffuse dust emission from morphology A and B (Sec. 3.4.1) originates from within the ionized gas of the IC 434 emission nebula. For morphology B, this is obvious from the bright interaction zone close to σ Ori AB (Paper 1). Below, we will argue that the same is true for morphology A.

Both for the continuum and the spectroscopic observations, we have subtracted a background value to exclude dust associated with the GS206-17+13 shell and contamination along the line-of-sight (Fig. 3.2). This method may leave some residual structure if the bubble shell is not homogeneous. However, H₂ emission at 9.7 μm , 12.3 μm , and 17.0 μm immediately disappear (Fig. 3.4b&c) when moving from region 1 (dominated by the Horsehead PDR) towards region 2 - 7, indicating a transition from the shielded PDR to the atomic/ionized gas, attesting to the success of the correction for the background emission from any surrounding neutral material. Moreover, morphology A is clearly separated from the L1630 molecular cloud, filling the H α emitting region (Fig. 3.4) with diffuse

emission, ranging from the L1630 molecular cloud to σ Ori. Furthermore, morphology A contains a limb-brightened arc at a projected distance of 1 pc east of the star (more pronounced in associated $8\ \mu\text{m}$ emission; see below), upstream in the flow of ionized gas, and it abruptly terminates when moving towards the west-side of the star, both indicative of an interaction with σ Ori AB, and arguing against a connection to background material. Indeed, in the photo-evaporation flow, most of the material is expected to be located near the symmetry axis connecting the star and the cloud (Sec. 3.5.2). Within this framework, the total diffuse dust emission located between the star and the cloud represents a dust reservoir that has evaporated of the L1630 molecular cloud, and is moving along with the ionized gas, some of which has not yet reached the interaction zone ahead of σ Ori AB.

Emission observed in the WISE $12\ \mu\text{m}$ band and IRAC $8\ \mu\text{m}$ closely follow the spatial morphology of the cold dust of Morphology A. As can be seen from the Spitzer/IRS spectra shown in Fig. 3.4b&c, the WISE $12\ \mu\text{m}$ is picking up PAH emission from the $7.7\ \mu\text{m}$ and $11.3\ \mu\text{m}$ band. The dust continuum from VSGs inside the H II region (region 2 - 6) only rises at $\lambda > 20\ \mu\text{m}$ (see Sec. 3.4.3), well outside the WISE filter edge ($\sim 17\ \mu\text{m}$). We note that emission from [NeII], arising from the IC 434 emission nebula, potentially contaminates the detection in the broad WISE filter. However, if the [NeII] emission were to dominate the observed flux in the WISE band, this would follow the smooth, exponential appearance from the H α emission measure (Fig. 3.2b), which is not seen in the observations. We conclude that WISE traces PAH emission. The IRAC $8\ \mu\text{m}$ band also traces PAH emission. By realizing that the cold dust observed by *Herschel*, and the PAH emission as seen by *WISE* and *Spitzer* are spatially related (Fig. 3.4), we can use the evolution of the mid-IR PAH spectrum to answer the question if morphology A traces a dust component that is located *inside* the ionized gas (Fig. 3.5). In this respect, we note that Compiègne et al. (2007) already showed that the PAH emission originates from within the ionized gas through correlation with ionized gas tracers.

The intensity ratio of the $7.7\ \mu\text{m}$ to $11.3\ \mu\text{m}$ PAH features is a well-known indicator of the charge state of PAHs (e.g., Szczepanski & Vala 1993; Bauschlicher 2002), as neutral species emit significantly less in the $6 - 9\ \mu\text{m}$ region compared to charged species (Allamandola et al. 1999). Figure 3.5 plots the $7.7/11.3\ \mu\text{m}$ intensity ratio, which initially decreases from region 1 to 2: Compiègne et al. (2007) argue that, initially, the PAHs become more neutral due to the increase of free electrons across the IF. Subsequently, from region 2 to region 6 the $7.7/11.3\ \mu\text{m}$ ratio shows a steady increase inside the H II region, indicating an overall increase of the (cationic) charge state of the PAHs. Thus, the PAHs are located inside the ionized gas: we are probing emission from regions that are located increasingly closer to the star. The combination of a decrease of electrons available downstream in the ionized flow with a gain of stellar photons increases the ionization parameter γ (Tielens 2005), defined as $G_0 T^{1/2}/n_e$. Here, G_0 is the hardness of the radiation field in units of the Habing field (Habing 1968), T is the temperature of the (ionized) gas, and n_e is the electron number density. A 'typical-sized' interstellar PAH with 50 carbon atoms will become more positively charged as γ increases, and the cationic state will dominate at $\gamma \gtrsim 10^4$ (Tielens 2005). In region 7, we are tracing a region PAH-free cavity around the star and we cannot trace the charge ratio reliably anymore (see Sec. 3.7.3). The observed relation of the $7.7/11.3\ \mu\text{m}$ ratio with γ (Fig. 3.5) is in reasonable agreement with observations of the Orion Bar and NGC 2023 (Galliano et al. 2008).

Another proxy for the charge state of PAHs is the $11.0\ \mu\text{m}$ feature due to C-H out of

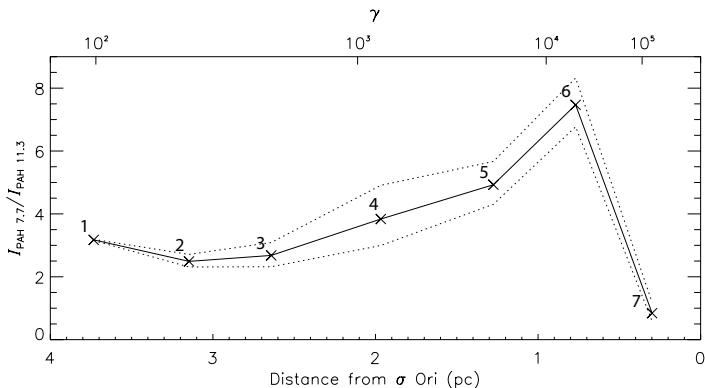


Figure 3.5: The evolution of the PAH 7.7 μm over 11.3 μm intensity ratio as a function of distance into the H II region, tracing the ionization state of the PAH molecules (e.g. Bauschlicher 2002; Szczepanski & Vala 1993). The intensities of the bands are measured with PAHFIT (Smith et al. 2007). The ratio shows a systematic rise with distance into the H II region, indicating that the molecules reside within the ionized gas, and a dramatic drop in the region closest to the ionizing star. The numbers correspond to the regions drawn in Fig. 3.4; the dotted lines show the 1σ uncertainty constrained by the quality of the spectra. The upper axis plots the ionization parameter γ (Tielens 2005).

plane bending modes of cationic PAHs (e.g., Hony et al. 2001; Rosenberg et al. 2011). Indeed, we find a hint of the 11.0 μm feature in regions 5 - 6 close to the star, but the quality of the IRS spectrum prevents us from making a conclusive statement on a detection of the 11.0 μm satellite feature.

In summary, we argue that morphology A represents a dust population entrained within ionized gas of the IC 434 emission nebula because of the following:

- (1) We subtracted the background to exclude dust associated with the GS206-17+13 shell: analysis of the Spitzer/IRS spectrum reveals the absence of the H_2 feature immediately after leaving the Horsehead PDR: there is no neutral region associated with the spectra of regions 2 - 7 (Fig. 3.4).
- (2) PAH emission shows a tight correlation with the long wavelength dust emission associated with morphology A (Fig. 3.3).
- (3) PAHs are increasingly charged when moving to regions projected closer towards the σ Ori AB. Thus, the PAHs are located *inside* the ionized gas. This conclusion was also reached by Compiègne et al. (2007), based upon observations of the Horsehead nebula. Consequently, the same holds for the cold dust emission from morphology A that is seen co-spatial with the PAH emission.
- (4) The diffuse emission from morphology A culminates in an arc-shaped emission around σ Ori AB, accompanied by a clear-drop in emission and a cavity behind the star, both indicating an interaction of the dust with σ Ori AB close to the symmetry axis connecting the star and cloud (Sec. 3.5).

Region	1	2	3	4	5	6	7
Location	PDR	H II	DW				
$\log(G_0)$	2.0	2.2	2.3	2.5	2.9	3.3	4.2
[20/30]	0.28	0.20	0.21	0.19	0.22	0.21	0.33

Table 3.1: The strength of the radiation field G_0 (Habing 1968), and the [20/30] continuum flux ratio for the regions in Fig. 3.4. Region 1 is located partly inside the Horsehead photo-dissociation region (PDR), whereas regions 2-7 are located inside the H II region. Region 7 is projected on top of the dust wave surrounding σ Ori AB. The [20/30] ratio is insensitive to the increase of G_0 inside the H II region, except in region 7, where the dust reaches thermal equilibrium (see text).

VSGs: 15 μm - 35 μm mid-infrared spectra

The IRS observations were designed to follow the evolution of the mid-IR spectrum in an increasing radiation field. The 15 μm - 35 μm spectra (Fig. 3.4c) show gas emission lines from [S III] and [Si II], typical for an ionized nebula. In addition, as region 1 is (partly) located inside the Horsehead PDR, molecular H_2 emission is seen along with the PAH emission plateau, ranging from 16 μm - 19 μm . A steep continuum at $\lambda > 15 \mu\text{m}$ reveals the presence of VSGs, as the intensity of the radiation field, $\log(G_0) = 2.0$, is too low for classical grains, or Big Grains (BGs), to produce continuum emission in the mid-IR. This continuum decreases between region 1 and region 2, but persists throughout the H II region and shows a remarkable constant spectral slope (see Tab. 3.1) as revealed by the flux continuum ratio at 20 μm and 30 μm , [20/30]. The carbonaceous nature of the carriers of the mid-IR continuum emission (often assumed for the VSGs in dust models) is confirmed through the absence of the silicate emission feature at 20 μm (e.g., van Boekel et al. 2003), but for an opposing view see Li & Draine (2002).

The constant slope strongly implies the presence of stochastically-heated VSGs that survive throughout the H II region, as a constant flux ratio does not reflect a dust population in TE inside an increasing radiation field. The decrease in observed flux between the PDR (region 1) and the H II region (region 2 - 7) likely comprises a sub-population of VSGs that do not survive the transition from the PDR into the H II region. We have labelled the responsible carriers in Fig. 3.4b: note that in region 7, where $\log(G_0) = 4.0$, both VSGs and BGs are expected to be in TE and can both be responsible for the increase of the ratio [20/30] in region 7. In this respect, the observed dust temperature of this component at the IDW (73-82 K), and the reduced UV-to-IR opacity (Sec. 3.4.3) argue in favor of BGs, consistent with the findings in Paper 1. Note that these BGs can both be of carbonaceous or silicate nature; the peak temperature is too low for the 10 μm and 20 μm silicate features to be in emission.

Cold dust: far-infrared spectral energy distribution

It is common to model the observed dust SED with a single modified blackbody (MBB) function. However, due to the presence of VSGs in the H II region, which contribute to the emission observed at $\lambda \leq 70 \mu\text{m}$, this is not a straightforward task (Anderson et al. 2012). As the SED clearly reveals the presence of a warm dust component (Fig. 3.4), we exclude the 24 μm and 70 μm data for all regions, except for region 7 and the IDW. Here,

we assume that the dust component emitting at $24 \mu\text{m}$ and $70 \mu\text{m}$ has reached TE with the radiation field, and perform a two-component blackbody fit to the SED.

The cold component reveals a striking constant appearance throughout the H II region, characterized by temperatures of $T_{d,C} \sim 23 \text{ K} - 26 \text{ K}$, and low spectral emissivity, $\beta \sim 0.7 - 1.0$. Still, these values of β are within what is expected for the derived dust temperatures (Veneziani et al. 2010; Planck Collaboration et al. 2011). Note however, that the parameters T_d and β seem degenerate, and derived values are sensitive to systematic effects induced from photometric calibration uncertainties to different grain temperatures superpositioned along the line-of-sight (see Juvela & Ysard 2012), and dust optical properties (Jones 2014). Nevertheless, the constant appearance of the SED is curious, considering that the impinging radiation field varies significantly (Tab. 3.1). For the warm component, we fix $\beta = 1$ due to the lack of data points with respect to free parameters, a value appropriate for the spectral index in the (mid-)IR (Mennella et al. 1995). Then, the warm component reaches a maximum temperature of $T_{d,H} = 82 \text{ K}$ at the position of the IDW ($d = 0.1 \text{ pc}$).

As the cold dust does not contribute much at $70 \mu\text{m}$ at the location of the IDW ($< 10\%$), the addition of the extra component at long wavelengths does not change the results obtained in Paper 1. However, the peak dust temperature of the hot dust depends on the choice of β : for a value of $\beta = 1.8$ for the hot component (as was used in Paper 1), the peak temperature decreases to $T_{d,H} = 73 \text{ K}$. The addition of the hot component does affect the fit in region 7 by increasing β and lowering $T_{d,C}$, because here the hot component contributes significantly at $70 \mu\text{m}$. This implies that the single-component fits in region 1 - 6 overestimate $T_{d,C}$ slightly. Indeed, by fixing the spectral emissivity at $\beta = 1.5$ (as measured by *Planck* for IC 434; Planck Collaboration et al. 2014a), yield $T_{d,C} = 19 \text{ K} - 20 \text{ K}$ for region 1 - 6. The larger value of β as measured by *Planck* is most likely caused by different dust populations and mixing of temperatures, as the Planck model samples the spectral emissivity at a $30'$ resolution, and does not correct for contamination along the line-of-sight. The high angular resolution of *Herschel*, and our careful background subtraction isolates the emission from the ionized gas. Still, to determine the actual temperature and spectral emissivity of dust in the H II region with a single MBB fit is not straightforward, due to the presence of multiple dust components *inside* the ionized gas, as reflected by the SEDs.

In Sec. 3.4.1, we showed that the far-IR emission in IC 434 is dominated by morphology A, which fills the H II region and forms the ODW at $d = 1 \text{ pc}$ to the east of the star. The dust population accountable for morphology A is distributed *inside* the H II region, ranging from region 1 ($d = 3.7 \text{ pc}$) to the ODW ($d = 1 \text{ pc}$) (Sec. 3.4.3), close to the symmetry axis (Sec. 3.5). Radiation pressure from the star prohibits the dust from drawing closer (Sec. 3.5.3). In a first attempt to constrain the properties of the grains responsible for morphology A, we use DUSTEM (Compiègne et al. 2011) to predict the shape of the dust FIR SED by using a radiation field evaluated at the projected distance to $\sigma \text{ Ori AB}$. Compared to the single-temperature MBB fit, DUSTEM allows for a range of equilibrium temperatures, a natural consequence of the size distribution and composition of interstellar dust.

Figure 3.6 shows the predicted SED by DUSTEM for both region 1 and the ODW. The result are shown for two scenarios. First, we use grain species (both amorphous carbon and silicates) and size distributions that successfully reproduce the extinction and

		Reg. 1	ODW	IDW
	d (pc)	3.7	1	0.1
	$\log(G_0)$	2.0	3.0	5.1
MBB	$T_{d,C}$ (K)	23 (19)	27 (20)	82 (74)
DUSTEM	$T_{eq,S}$ (K) 0.1 μm	31	47	100
	$T_{eq,S}$ (K) 1.0 μm	20	31	65
	$T_{eq,C}$ (K) 0.1 μm	34	55	130
	$T_{eq,C}$ (K) 1.0 μm	21	33	74

Table 3.2: Dust temperatures T_d for grains at the location of region 1, the outer dust wave (ODW), and the inner dust wave (IDW), derived through 1) a modified-blackbody-fit (MBB) and 2) DUSTEM modeling of the equilibrium temperature for a 0.1 μm silicate grain and 1.0 μm silicate grain ($T_{eq,S}$) and amorphous carbon grain ($T_{eq,C}$). Also listed are the projected distance d , and the hardness of the radiation field, G_0 (Habing 1968). The observed cold component $T_{d,C}$ is calculated with β as a free parameter (see Fig. 3.4), and by choosing $\beta = 1.5$ as given by the Planck dust model (Planck Collaboration et al. 2014a), denoted between brackets.

emission properties of a selected region of the diffuse ISM at high Galactic latitude (the DHGL model; Compiègne et al. 2011). In this case, the small end of the size distribution dominates in surface area, which causes the predicted dust emission to peak at short wavelengths, causing DUSTEM to be unable to reproduce the observed SED. Second, by *only* including very large silicate grains in the size distribution a reasonable fit can be obtained, as explained below. Table 3.2 compares $T_{d,C}$ from the modified-blackbody fit, at the location of region 1 and the ODW, with equilibrium dust temperatures of graphite and silicate grains calculated with DUSTEM. The results for the IDW region are also listed. While DUSTEM predicts that the grains are significantly heated, resulting in a total temperature increase of $\sim 50\%$ between region 1 and the ODW (because of the increase of stellar flux as they approach the star), the modified black body fits reveal that the cold dust component only increases $\sim 15\%$ in temperature. This result highlights the main puzzle presented by the FIR SEDs of the H II region: a cold dust population, whose temperature is rather insensitive to an increase in radiation field. Below, we will outline two scenarios that might explain the remarkable properties of the grains responsible for Morphology A.

A reasonable fit for region 1 can be obtained by *only* including silicate grains larger than 1 micron to the fit. Silicates have lower equilibrium temperatures compared to amorphous carbon, and the size distribution composed of very large grains pushes the peak of the predicted dust emission to longer wavelengths. Still, this grain population is not able to fit the observed SED at the ODW region, as the predicted dust emission peaks blueward of the observed SED. This can perhaps be solved if the grains deviate from the classical spherical description. For example, the equilibrium temperature T_{eq} of fluffy aggregates is thought to be lower, compared to their compact counterparts (typically about 10% - 20%; Fogel & Leung 1998). This is because UV, visible and near-IR absorptivity remain similar as fluffiness is increased, whereas the sub-mm emissivity increases significantly (Bazell & Dwek 1990). An intuitive explanation for the presence of large aggregates inside the H II region arises when realizing that the grains are 'freshly' evaporated from the molecular cloud (Sec. 3.5) in which the grain are thought to coagulate to large, fluffy aggregate structures (Ossenkopf & Henning 1994; Ormel et al. 2009). This argumentation

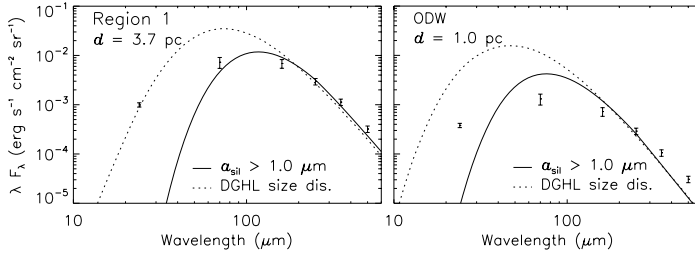


Figure 3.6: Modeling of the far-infrared spectral energy distribution using DUSTEM (Compiègne et al. 2011). Two panels are shown, corresponding to two different regions (Fig. 3.4). The left panel shows region 1 ($d = 3.7$ pc); the right panel displays the outer dust wave region (ODW; $d = 1$ pc). Overplotted is the predicted dust emission for two different composition and size distribution of grains (see text).

connects well with the work of Martin et al. (2012), that used BLAST and IRAS images of selected regions in Vela of moderate column density to show considerable variations in, e.g., the submillimeter opacity (as compared to the diffuse ISM). The authors argued that the inferred grain properties may reflect past histories in the evolution of the grains, such as coagulation in dense regions.

Besides a rather rigorous change in the size distribution and invoking fluffiness or porosity, another explanation for the observed low dust temperatures for Morphology A (as compared to predictions made by DUSTEM) can be linked to recent results from, e.g., the *Planck* mission. Planck Collaboration et al. (2014a) argue that T_{obs} is not a simple tracer of the radiation field, but rather probes variations in dust properties (grain structure, material change, and size distributions). Similar results are reported in Planck Collaboration et al. (2014b): through comparison with the Draine & Li (2007) physical model, the authors show that the location of the peak wavelength of the dust SED does not only trace the intensity of the radiation field (like DUSTEM), but also intrinsic variations of dust properties. Other results from the *Planck* mission (Planck Collaboration et al. 2014a) include that dust in specific region of the ISM is more emissive than those used in dust models from Li & Draine (2001) and Compiègne et al. (2007), which would lower the equilibrium temperature with respect to that computed using these grain models. In conclusion and as pointed out by Jones (2014), dust models that do not allow for the evolution of grain properties as they transit between different regions of the ISM, will be challenged in the light of new observational evidence obtained by *Planck* and *Herschel*.

Dust- and gas mass inside IC 434

The total dust mass in IC 434 is determined by deriving the average τ_{353} from the Planck model R1.20 (Planck Collaboration et al. 2014a) inside an aperture that encloses the bright H α emission from the emission nebula. We find $\tau_{353} = 1.5 \times 10^{-5}$. The total dust mass can then be estimated directly through $M_{\text{d,IR}} = \frac{\tau_{\lambda}}{\kappa_{\lambda}} S$ (Hildebrand 1983), where S is the size of the aperture and κ_{λ} is the grain opacity at wavelength λ . If $\kappa_{353} = 1.9 \text{ cm}^2 \text{ g}^{-1}$ (Weingartner & Draine 2001), then the total dust mass in IC 434 equals $M_{\text{d,IR}} = 2.3 M_{\odot}$.

The total gas mass inside IC 434 can be estimated by integrating the gas density

profile, given by the $H\alpha$ observations (Sec 3.5.2), out to a distance of 9 pc (the apparent extent of the bright $H\alpha$ emission). This yields a total hydrogen column of $N_H = 1.6 \times 10^{20} \text{ cm}^{-2}$. We assume that the gas evaporates of a $9 \text{ pc} \times 9 \text{ pc}$ surface from the L1630 molecular cloud (Sec. 3.5.2). Then, the total gas mass in the IC 434 emission nebula is $M_g \approx 100 M_\odot$. The total dust-to-gas ratio in the IC 434 region is therefore ~ 0.02 , similar to that seen in the diffuse ISM (~ 0.01). A thorough study of gas-to-dust ratios in large-scale photo-evaporation flows could reveal if dust entrainment significantly enriches the ISM with grain materials.

Dust opacities of the ODW in the UV and IR

Following the method and using parameters described in Paper 1 for the IDW, we estimate the optical depth of the ODW at UV wavelengths through aperture photometry at $\tau_{\text{UV}} = 1.2 \times 10^{-3}$, with a corresponding dust mass of $M_{\text{d,UV}} = 7.4 \times 10^{-3} M_\odot$. In contrast, following the same method for $M_{\text{d,IR}}$ as described in Sec. 3.4.3 and by using $\kappa_{160} = 10 \text{ cm}^2 \text{ g}^{-1}$ (Weingartner & Draine 2001), then the total mass in the ODW from the IR observations at $160 \mu\text{m}$ is $M_{\text{d,IR}} = 0.16 M_\odot$. Thus, we find for the dust content in the ODW, $M_{\text{d,IR}}/M_{\text{d,UV}} = 22$. This effect was already noted for the warm component in Paper 1 and in the W3 region (Salgado et al. 2012), and implies that the dust opacities at UV and IR wavelengths for the cold dust component are also very different from that seen for the diffuse ISM: this may well be a general characteristic for dust inside H II regions. Similar results are observed in (molecular) clouds where the dust opacity is altered, reflected in a flattening of the dust extinction curve towards UV wavelengths (Cardelli et al. 1989). Often, this is attributed to dust coagulation or a dearth of small particles in the dust size distribution.

Summary on the observations

The total dust-to-gas ratio inside IC 434 is ~ 0.02 . The ODW contains 5 - 10% of the total dust content ($2.3 M_\odot$) inside IC 434. The dust content inside the ionized gas can be divided in two different populations, following two separate morphologies (Fig. 3.4).

Morphology B (Fig. 3.2) shows the signatures of carbonaceous VSGs in regions 1 - 6, responsible for the constant [20/30] flux inside the H II region. The emission from this component is most pronounced at $24 \mu\text{m}$. The reduced UV-to-NIR opacity, and the inferred peak dust temperature (73 K - 82 K) at $d = 0.1 \text{ pc}$ indicate that large grains also populate morphology B and perhaps dominate the emission from the IDW (results from Paper 1). These BGs are only visible close to the star as the grains heats up.

Morphology A (Fig. 3.2) is a combination of cold dust at $\lambda \geq 160 \mu\text{m}$, and mid-IR emission from PAHs at $8 \mu\text{m}$ and $12 \mu\text{m}$ emission that is tightly correlated with the cold dust throughout the H II region. The PAHs show an increasing level of charge state in regions at smaller projected distances from the ionizing star, providing convincing evidence that the PAHs are located inside the ionized gas and therefore, the grains from morphology A are located in the H II region as well.

Dust temperatures of morphology A are between $23 \text{ K} < T_{\text{d,C}} < 26 \text{ K}$ (depending on the exact value of β); this is colder than expected for a typical size distribution of dust in the diffuse ISM, as predicted by DUSTEM. We have pointed out that the cold temperature can be explained by (porous/fluffy) micron-sized grains. This is consistent with the reduced UV-to-IR opacity compared to that observed for dust in the diffuse ISM, and we

have connected these observations to the molecular cloud phase from which the grain are evaporated. However, even these large grains cannot explain the temperature dependence that seem insensitive to an increase in intensity of the radiation field. This might confirm recent results, indicating that the peak wavelength of the SED is not determined by the intensity of the radiation field alone (Planck Collaboration et al. 2014a,b), but also traces changes in grain properties (e.g., Jones 2014).

3.5 The flow of dust into the IC 434 region

As has been discussed in Sec. 3.3.3, σ Ori approaches the L1630 molecular cloud to create a champagne flow that enters into the expanding bubble, blown by the Orion OB1b association (Fig. 3.1). The increase in the ionizing flux impinging the L1630 molecular cloud with time will strengthen the champagne flow. Note that this scenario differs from Paper 1, that considered a stationary champagne flow. The ionized gas accelerates into the H II region and, subsequently, drags the dust along with it. The work in Paper 1 describes the theoretical framework to derive the properties of the dust grains introduced into the H II region and provides an analysis of the IDW surrounding σ Ori AB. In this section, we extend this work by considering the emission from morphology A as well (observed at $8 \mu\text{m}$, $12 \mu\text{m}$, and longwards of $160 \mu\text{m}$). Furthermore, we present how one can use dust waves to constrain geometry (porosity/fluffiness) and the radiation pressure efficiency of the grains.

3.5.1 Modeling the flow of ionized gas

Henney et al. (2005) investigated the evaporation of a cloud illuminated by a point source, and the structure of the ionized flow emanating of the cloud surface. In their hydrodynamical models, the photo-evaporation flows are found to be steady during a large part of their evolution, in which the flow properties change only on timescales much longer than the dynamic time for flow away from the IF. In the steady phase, the flow resembles a 'champagne flow' (Tenorio-Tagle 1979) or a 'globule flow' (Bertoldi 1989), depending on the curvature of the IF.

An IF that engulfs a flat, homogenous cloud illuminated by a point source will become concave, and the photo-evaporation flow emanating from this geometry will resemble a champagne flow structure, as the streamlines do not diverge effectively (Henney et al. 2005). In practice, the ionized gas from a concave IF will accelerate more slowly compared to, e.g., the photo-evaporation flow from a convex-shaped globule (Bertoldi 1989). The relative slow acceleration of the gas will increase the effective flow thickness, h_{eff} , defined as $n_0^2 h_{\text{eff}} = \int n^2 dr$, where n_0 is the ionized gas density and r is the distance from the star to the IF. Thus, the shape of the IF (convex, flat, or concave) and the incident ionizing flux *uniquely* determine the structure of the resulting photo-evaporation flow.

We envision the approach of σ Ori to the L1630 molecular cloud as follows. We consider the L1630 molecular cloud as a flat IF, ionized by an (approaching) point source. By combining the density prescription that reproduces the observed emission from the IC 434 region (Eq. 3.2) with the results of the numerical models of Henney et al. (2005), we developed a flow model that improves the model described in Paper 1 substantially. We restrict the modeling of the flow to the symmetry axis connecting the star and the

cloud, because the flow properties are dominated by the immediate surroundings of the symmetry axis (Henney et al. 2005), as will be addressed in Sec. 3.5.2. Moreover, the photo-evaporation models from Henney et al. (2005) show that in the case of a flat IF illuminated by a single point source, the streamlines do not diverge at the distance between star and cloud, so we can consider the gas flow to be moving one-dimensionally (i.e., orthogonal to the surface of the molecular cloud) constant along the line-of-sight. Thus, the symmetry axis provides a decent approximation for the (two-dimensional) structure of the flow between the cloud and the star. In short, the analysis results in an increased line-of-sight extent of the cloud compared to Paper 1, but is consistent with the numerical models of Henney et al. (2005) and comparable to the size of the L1630 molecular cloud.

The photo-evaporation flow from the L1630 molecular cloud resembles a champagne flow following the prescription of Tenorio-Tagle (1979). In this scenario, the density contrast between a cloud and the inter cloud medium drives a shock into the inter cloud medium, while a rarefaction wave travels back into the cloud, setting up a champagne flow that accelerates the gas to supersonic velocities as the gas moves away from the IF. The density distribution of the champagne flow can be described by an exponential density gradient (Bedijn & Tenorio-Tagle 1981; Tielens 2005):

$$n(r) = n_0 \exp\left[\frac{r - R_s}{R_0}\right]. \quad (3.2)$$

Here, n_0 is evaluated at the IF and equals J/c_s , where J is the ionizing flux reaching the cloud and c_s is the isothermal sound speed in the ionized gas. The value R_s is the distance between the cloud and the star, and $R_0 = c_s t$ is the scale length of the flow, where t is the time since the ionized gas started to stream into the H II region. We follow the conclusions of Henney et al. (2005) by adopting a constant flow thickness as the star approaches the cloud, i.e., the scale height of the flow, R_0 (see Eq. 3.2), will adjust itself to the distance between the IF and the star, R_s . In particular, the effective flow thickness for a flat IF is $h_{\text{eff}} \approx 0.35R_s$ (Henney et al. 2005, Fig. 7).

Thus, assuming that the density gradient can be described by Eq. 3.2 (Paper 1) and an effective flow thickness of $h_{\text{eff}} = 0.35R_s$, one can solve for the scale height R_0 of the exponential flow by writing $n_0^2 h_{\text{eff}} = \int_0^{R_s} (n(r))^2 dr$. To determine the complete structure of the flow as the ionizing star draws closer, we now only have to solve for the ionizing flux, J , reaching the cloud surface at any given time. The ionizing flux will increase as the star advances towards the cloud and will accelerate the IF, increasing the ionized gas density streaming into the H II region. Consequently, the number of recombinations between the star and the cloud will increase and, in its turn, lower the amount of photons reaching the cloud surface. The actual amount of photons reaching the cloud is determined by integrating the number of recombinations in a column r extending from the star ($r = 0$) to the IF ($r = R_s$):

$$J = J_0 - \int_0^{R_s} \beta_B (n(r))^2 dr = \frac{\beta_B J^2 R_0}{2c_s^2} (1 - \exp[-2R_s/R_0]), \quad (3.3)$$

where $J_0 = Q_0/4\pi r^2$ is the ionizing flux from the star, in the case that none of the photons are absorbed within the H II region. Equation 3.3 yields the solution:

$$\frac{2J_0}{J} = 1 + \sqrt{1 + \frac{Q_0 \beta_B R_0}{4\pi r^2 2c_s^2} (1 - \exp[-2R_s/R_0])}. \quad (3.4)$$

This result is similar to the one reported in Bedijn & Tenorio-Tagle (1981), except their solution is written in terms of number density; we opted to follow the method from Spitzer (1978) and provide the solution in term of stellar fluxes. With the density prescription, we can solve for the scale height R_0 of the flow using the previous mentioned relationship, $n_0^2 h_{\text{eff}} = \int_0^{R_s} (n(r))^2 dr$. With $n_0 = J/c_s$, and $h_{\text{eff}} = 0.35R_s$, it is easily shown that $R_0 = 0.46R_s$.

3.5.2 Flow parameters

Consider the L1630 molecular cloud as a uniformly distributed, extended cloud. We take for the ionizing flux of σ Ori AB $\log(Q_0) = 47.56$ photons s^{-1} , appropriate for an O9.5V star (Martins et al. 2005a). We let the star approach the cloud at a velocity of 10 km s^{-1} (Sec. 3.3.3), which after 3 Myr (the adopted age of σ Ori; Caballero 2008) results in the configuration seen to date: a projected distance of 3.7 pc between the L1630 cloud and σ Ori AB. At $t = 0$, we assume that a steady photo-evaporation flow already fills the medium between the star and cloud (see Fig. 3.3).

Figure 3.7 reveals the evolution of the flow parameters, v_f and n_H , as σ Ori travels towards the cloud at a velocity of $v_\star = 10 \text{ km s}^{-1}$ (Sec. 3.3.3). The velocity of the flow, v_f , is obtained after integration of Eq. 3.2, resulting in a linear velocity law. The initial velocity of the gas is $v_f = 10 \text{ km s}^{-1}$ (a D-critical front; Spitzer 1978) and, because of the constant scale height R_0 (Henney et al. 2005), reaches the same maximum velocity of $v_f = 32 \text{ km s}^{-1}$ at all times when the gas reaches the location of the star. Taking into account the relative velocity between star and cloud, this amounts to a maximum relative velocity of 42 km s^{-1} .

The density structure of the flow at $t = 3 \text{ Myr}$ reaches $n_H = 35 \text{ cm}^{-3}$ at the cloud surface. This density is offset by a factor of ~ 3 with the earlier derivation described in Paper 1. This difference follows from the choice of Q_0 : in Paper 1, the O9.5V model atmosphere of Schaerer & de Koter (1997), with an ionizing luminosity of $\log(Q_0) = 48.25$ photons s^{-1} , was taken to calculate the incident flux on the L1630 cloud. Here, we use instead the updated model atmospheres from Martins et al. (2005a) and take $\log(Q_0) = 47.56$ photons s^{-1} . The decrease of ionizing photons effectively lowers n_H . In addition, we calculate the balance between recombinations and photo-ionization appropriate for a champagne flow structure with Eq. 3.4, whereas in Paper 1 we had followed the work from Abergel et al. (2002) and Spitzer (1978) that calculate J_0 in a spherical geometry. While a spherical, globule-like geometry is appropriate for the small evaporation zone for the Horsehead considered in Abergel et al. (2002), it clearly is not applicable to the entire champagne-flow from the L1630 molecular cloud (e.g., Fig. 3.7). The S[III] lines that were used in Compiègne et al. (2007) (and that we had adopted in Paper 1) are close to or below the critical density, and its usage to derive reliable densities is questionable. Therefore, lacking other reliable density tracers that can pin down the initial density at the IF, calculating the amount of photons that reach the molecular cloud in time, using the appropriate density laws from Eqs. 3.3 and 3.4, is the most reliable way in constraining the flow parameters in the IC 434 nebula. In addition, we compare with numerical models

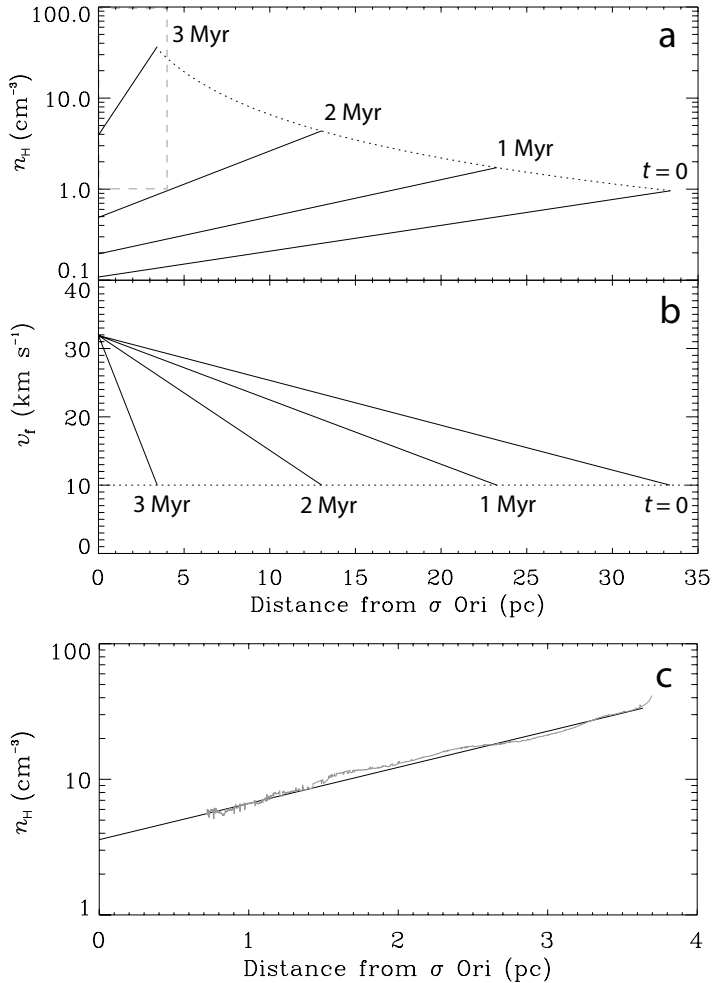


Figure 3.7: (a) Density structure n of the champagne flow as σ Ori moves toward the cloud (Sec. 3.3.3). The different curves represent the density structure after time t : 0 Myr, 1 Myr, 2 Myr, and 3 Myr. The dotted line shows the evolution of the density at the IF, n_0 . The grey dashed box shows the outline of the region of the flow. To transform this to the frame between star and cloud, one has to add the relative velocity between the star and cloud, $v_{\star} = 10$ km s⁻¹. (b) Velocity structure of the flow. (c) The density profile at $t = 3$ Myr, overplotted with the observed density profile from the H α emission measure, assuming a constant scale size of the emitting gas along the line of sight of $l = 9$ pc (see text).

from Henney et al. (2005) to obtain a better description of the ionized flow of the L1630 molecular cloud.

The lower density n_{H} remains compatible with the observed H α emission measure from the IC 434 region, as the electron density depends on the scale size of the emitting gas through $n_{\text{e}} = \sqrt{EM/l}$. Here, EM and l are the emission measure and the scale size

along the line-of-sight of the emitting volume, and $n_e (= n_H)$ is the electron density of the (fully) ionized gas. Thus, by lowering n_e by a factor of 3, l has to increase factor of 3^2 along the line-of-sight to reproduce the EM of the ionized flow, which amounts to $l = 9$ pc at the L1630 molecular cloud, similar to the angular extent of the IC 434 region (Fig. 3.2).

While strictly speaking, Eqs. 3.3 and 3.4 hold for the symmetry axis only (extending from the star to the cloud radially), the bulk of the emission measure originates from the region within one unit distance R_s from the symmetry axis (Henney et al. 2005, Fig. 5a) and, therefore, the dust emission from the H II region will largely be located within this region. In the case of IC 434, this amounts to an emitting area of ~ 7.5 pc centered on the symmetry axis, consistent with our adopted line-of-sight extent of the L1630 molecular cloud. Even though our adopted geometry and flow structure is consistent with numerical results from Henney et al. (2005) and the size of the L1630 cloud on the sky, we note that the observed EM can be used with *any* l to match an exponential density gradient inside the H II region, depending on the choice of R_0 . We look into this dependency by investigating our results after varying the scale height R_0 in Sec. 3.7.

In summary, we have updated the photo-evaporation model compared to the one described in Paper 1 by using (1) a more recent model atmosphere, (2) a better prescription of calculating the 'insulating' layer of recombining material streaming of the molecular cloud (Eqs. 3.3 & 3.4), (3) a comparison with numerical results for photo-evaporation flows from Henney et al. (2005), and (4) and allowed for the time evolution of the flow as σ Ori approaches the cloud. The exponential density gradient (Fig. 3.7a) and the adopted scale height (Sec. 3.5.1) reproduces the observed H α emission measure well if the IC 434 region measures 9 pc along the line of sight, in agreement with the photo-evaporation models of Henney et al. (2005). Note, that while the updated flow structure does affect some of the results derived in Paper 1, the main conclusions do not change and the derived grain properties are only affected marginally, as we will discuss in Sec. 3.6.

3.5.3 The formation of dust waves

In this section, we briefly review the dust wave phenomenon. Following Paper 1, the equation of motion for dust is written as:

$$m_d v_d \frac{dv_d}{dr} = -\frac{\sigma_d \bar{Q}_{rp} L_\star}{4\pi cr^2} + 2\sigma_d kT n_i \frac{8s}{3\sqrt{\pi}} \left(1 + \frac{9\pi}{64} s_i^2\right)^{1/2}. \quad (3.5)$$

The first term on the right hand side is the radiation pressure force, F_{rad} , and contains: the geometrical cross-section of the grain, σ_d ; the radiation pressure efficiency (averaged over the incident radiation field), \bar{Q}_{rp} ; and the speed of light, c . The second term is the collisional drag force (Draine & Salpeter 1979), F_{drag} , and contains: the Boltzmann constant, k ; the temperature and number density of the gas (of species i), T and n_i ; and $s_i = (m_i v_{\text{drift}}^2 / 2kT)^{1/2}$, with v_{drift} the drift velocity of the dust through the gas. Furthermore, m_d is the dust mass and v_d is the dust velocity.

As the grains flow along with the gas into the H II region through the drag force, F_{drag} , the radiation pressure of the star, F_{rad} , will act on a dust grain contained within the flow and will cause it to lose momentum. As the dust is slowed down, it will be pushed through the gas with drift velocity v_{drift} , transferring momentum towards the gas. We

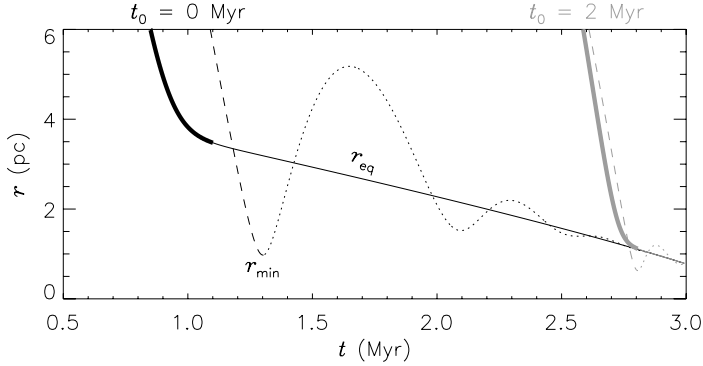


Figure 3.8: The trajectories of two grains with different value of geometrical cross-section over dust mass (see text), ξ , exemplifying the difference between the equilibrium radius, r_{eq} (solid line; high ξ), and the minimum radius, r_{min} (dashed/dotted line; low ξ) versus time t for dust approaching the star radially. Both curves assume $\bar{Q}_{\text{rp}} = 2$. Black curves represent dust entering the H II region at $t_0 = 0$ Myr, while grey curves correspond to the same situation at $t_0 = 2$ Myr.

consider collisional drag only, as Coulomb interactions do not seem to dominate the drag term for dust-gas momentum transfer inside IC 434 (Paper 1). Eventually, for a dust grain approaching the star radially (i.e., zero impact parameter), the dust will be stopped at the equilibrium radius, r_{eq} , upstream with respect to the star, where $|F_{\text{rad}}/F_{\text{drag}}|$ equals unity. If at this point the amount of momentum transfer between gas and dust is insufficient for the gas to be dynamically perturbed, gas and dust will decouple significantly, resulting in an increase of dust upstream relative to the star as the gas flows along unhindered: the formation of a *dust wave*. Dust grains approaching the star with a non-zero impact parameter will be pushed around the star, resulting in an arc-shaped structure. For a detailed description of the physics of a dusty photo-evaporation flow we refer to (Paper 1).

3.5.4 The equilibrium- and minimum radius of a dust wave

The radiation pressure opacity, κ_{rp} , determines the trajectory of a dust grain as it moves toward and passes the star :

$$\kappa_{\text{rp}} = \bar{Q}_{\text{rp}}\sigma_{\text{d}}/m_{\text{d}} \equiv \bar{Q}_{\text{rp}}\xi. \quad (3.6)$$

In Paper 1, it was shown that the radiation pressure force of σ Ori AB stratifies grains ahead of the star in a *bounded* region at $0.1 \text{ pc} < d < 0.4 \text{ pc}$ for a given range of κ_{rp} . The analysis was limited to grains with $\bar{Q}_{\text{rp}} = 1$, from which a size distribution of the grains contained in the dust wave was inferred assuming compact particles, i.e., $m_{\text{d}} = 4/3\pi a^3 \rho_{\text{s}}$, with m_{d} dust mass, a the grain radius and ρ_{s} the specific density. However, given Eq. 3.6, we can obtain the same values of κ_{rp} by allowing for variation of \bar{Q}_{rp} , and a corresponding change in ξ . For example, a grain with $\bar{Q}_{\text{rp}} = 1$ and a compact geometry will have exactly the same value of κ_{rp} as a grain with $\bar{Q}_{\text{rp}} = 0.1$ and ξ increased by a factor of 10 (a fluffy/porous geometry). We attempt to break this degeneracy by comparing our

modeling results with observations (Sec. 3.6).

The inner boundary of a dust wave is determined by grains that have a low ratio of ξ . Considering grains at same m_d , smaller values of ξ correspond to more compact grains. Due to inertia, these grains will slowly accelerate and, moreover, tend to overshoot r_{eq} due to their large intrinsic momentum, reaching the minimum radius r_{min} constrained by ξ (Fig. 3.8).

For sufficient high ξ , the grains will be *momentum coupled* with the gas of the flow. In this case, a negligible amount of momentum is used to accelerate the grains, from which follows $F_{\text{rad}} = F_{\text{drag}}$ (Eq. 3.5). Then, all momentum absorbed by the grains will be passed to the gas, and the grains will have a steady drift velocity through the gas *independent* of grain size (Kwok 1975; Tielens 1983). The equilibrium radius, r_{eq} , is populated by grains that are momentum coupled, whose exact value will only depend on the flow parameters, v_f and n , and the value of the radiation pressure opacity \bar{Q}_{rp} . High values of ξ either corresponds to very small dust grains (e.g., VSGs), or large grains with a low specific density, such as porous grains or fluffy aggregates. It is good to note here that porosity and fluffiness are not directly related. Whereas the porosity is a measure of the volume filling factor of a grain (e.g., Bazell & Dwek 1990) and contains no information on its morphological structure, a fluffy or filamentary grain is often described by a fractal dimension (e.g., Fogel & Leung 1998). Grains with the same porosity can have very different fractal dimension. However in this work, only ξ enters Eq. 3.5, and we can not distinguish between porosity and fluffiness.

Figure 3.8 depicts the difference between r_{min} and r_{eq} ($\bar{Q}_{\text{rp}} = 2$). The curve for r_{min} is calculated for a 1000 Å compact silicate grain ($\log(\xi) = 4.03$). In contrast, the curve for r_{eq} is calculated for a grain of similar mass, but with a geometrical cross-section σ_d increased by a factor of 100 ($\log(\xi) = 6.03$), to mimic a highly porous or fluffy grain that is momentum-coupled with the gas. The equilibrium radius r_{eq} shrinks with t , because the density and velocity of the ionized gas increases, pushing the dust towards the star as F_{drag} rises. We plot trajectories for dust emanating from the L1630 molecular cloud at $t_0 = 0$ Myr, at which point F_{drag} is still relatively small (Fig. 3.7): the compact grains overshoot significantly, and the difference $r_{\text{eq}} - r_{\text{min}}$ is high. The effect of inertia is also seen in the difference in time t at which the grains reach r_{eq} and r_{min} : the compact grains are accelerated more slowly, thus reaching r_{min} at a later stage compared to the grains that are coupled to the gas and reach r_{eq} . However, the importance of the inertia of the grains will decrease with t as σ Ori approaches the cloud and the ionized gas flow develops in strength, exemplified by the curves for dust launched at $t_0 = 2$ Myr. Note that the damped oscillation of r_{min} around r_{eq} is a peculiarity of the streamline approaching the star radially. In reality, dust along this streamline will flow around the star when the dust has reached r_{min} (Ochsendorf et al. 2014b) and, therefore, only the dashed part of r_{min} is physically relevant. The same applies to momentum coupled grains: after the grains reach r_{eq} , they will be pushed past the star. The thin part of the solid line reveals r_{eq} for all momentum-coupled grains that arrive at r_{eq} between $1.1 \text{ Myr} \leq t \leq 2.8 \text{ Myr}$.

In summary, for given flow parameters and adopting a dust size distribution, dust grains will be stratified in a region ahead of the star, stretching from r_{eq} (small or porous grains) towards r_{min} (compact, large grains), depending on ξ . These radii mark the location where the dust reaches minimal velocities with respect to the star, resulting in high dust densities: a dust wave. The radiation pressure efficiency, \bar{Q}_{rp} , effectively offsets r_{eq}

and r_{\min} with respect to the star, as \bar{Q}_{rp} only enters F_{rad} in Eq. 3.5. Values for \bar{Q}_{rp} depend on grain properties and the incident radiation field (Li & Draine 2001; Draine 2011a). For a radiation field typical of that of an O9.5V star, compact, spherical grains of size ~ 1000 Å can have an efficiency factor as high as $\bar{Q}_{\text{rp}} \approx 2$. In contrast, small grains of 10 Å have $\bar{Q}_{\text{rp}} \approx 0.1$, while for the largest grain sizes with $2\pi a \gg \lambda$, \bar{Q}_{rp} approaches unity.

3.6 Modeling results

For the flow parameters estimated in Sec. 3.5.2, and $\bar{Q}_{\text{rp}} = 1.5$, which is a reasonable estimate for classical silicate and graphite grains larger than ~ 0.01 μm (see Draine 2011a, Fig. 7), at $t = 3$ Myr (the present situation) the equilibrium radius equals $r_{\text{eq}} = 0.7$ pc. At the same time, $r_{\min} = 0.3$ pc for 0.25 μm grains, typically the largest grains available in the size distribution of the diffuse interstellar medium (Mathis et al. 1977; Weingartner & Draine 2001). Thus, for $\bar{Q}_{\text{rp}} = 1.5$ and assuming an ISM size distribution, dust will be stratified between 0.3 pc $< r < 0.7$ pc ahead of the star, which is to be compared to the observed projected distances of the dust waves. Surely, the actual difference between σ Ori and the dust waves could be larger than the projected distance due to an inclination of the system. However, this effect should be small, as observations indicate that σ Ori AB and the Horsehead (and, therefore, the L1630 molecular cloud associated with the Horsehead) lie approximately at the same distance (Habart et al. 2005).

In contrast to the region bounded by r_{\min} and r_{eq} as described above, the IR emission from the IC 434 region (Fig. 3.3) revealed two clearly separated morphologies with corresponding dust arcs at a projected distance of $d = 1$ pc (the ODW; morphology A) and $d = 0.1$ pc (the IDW; morphology B). While in our model, r_{\min} can be lowered by introducing large grains ($a > 0.25$ μm) into the size distribution (these have lower r_{\min} due to their large momentum), r_{eq} determines the outer region of the dust wave, which can only be increased to match the observed value (1 pc) by allowing for a larger value of \bar{Q}_{rp} (Eq. 3.6). However by increasing \bar{Q}_{rp} , consequently, r_{\min} will rise and divert from 0.1 pc. Therefore, a continuous interstellar size distribution will not reproduce the two-folded nature of morphology A versus morphology B, as described in Sec. 3.4, and the segregation of the dust can only be reproduced by invoking a bimodal dust distribution, separating the dust into their current morphologies and observational characteristics.

3.6.1 A bimodal dust distribution

Section 3.5.4 discussed that momentum-coupled grains reach r_{eq} , the outer radius of a dust wave, and that \bar{Q}_{rp} effectively offsets the interaction region between r_{eq} and r_{\min} from the star (Eq. 3.6). In Fig 3.9, we visualize this, and plot r_{eq} at $t = 3$ Myr for a grid of \bar{Q}_{rp} and ξ . This diagram reveals the necessary grain properties to place momentum-coupled grains at the observed positions of the ODW and the IDW, respectively. Above a certain value of ξ , the grains will obtain sufficient inertia such that they are no longer momentum-coupled. The division between both regimes shifts to large values of ξ , as \bar{Q}_{rp} increases. This is because radiation pressure becomes more efficient, prohibiting the grains from overshooting r_{eq} .

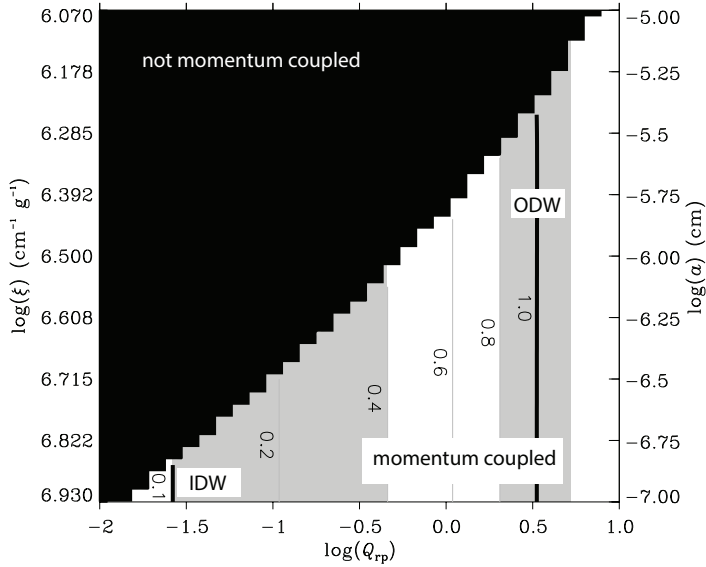


Figure 3.9: Location of the equilibrium radius r_{eq} in pc (contours) of momentum coupled grains at $t = 3$ Myr (present situation), evaluated for a grid of radiation pressure efficiencies \bar{Q}_{tp} and ratios of geometrical cross-section to the mass of the grain, ξ . The thick black contours represent $r_{\text{eq}} = 0.1$ and $r_{\text{eq}} = 1.0$, respectively, corresponding to the peak intensities of the inner dust wave (IDW) and outer dust wave (ODW). The light-shaded areas mark the boundaries in projected distance at which the dust waves are observed Fig. (3.3). The black area represent grains that overshoot r_{eq} to reach r_{min} , and are thus not momentum coupled. The vertical axis on the right denotes the grain radius if the grain mass is distributed in a compact geometry.

Dust population A

The ODW at $d = 1$ pc places a tight constraint on the nature of grains responsible for morphology A. We have demonstrated that for the flow parameters in IC 434 (Sec. 3.5.2) and $\bar{Q}_{\text{tp}} = 1.5$, $r_{\text{eq}} = 0.7$ pc. Therefore, we conclude that in order to place dust at the ODW, the grains have to be momentum coupled, for these grains account for the outer regions of the dust wave measured from the star. Subsequently, we can search for the value \bar{Q}_{tp} that places r_{eq} at $d = 1$ pc in Fig. 3.9: momentum coupled grains with radiation pressure efficiency $2 \leq \bar{Q}_{\text{tp}} \leq 5$ could reproduce the ODW around 1 pc.

The required \bar{Q}_{tp} is larger than commonly accepted (Li & Draine 2001). Indeed, the above described constraints (momentum-coupled, high \bar{Q}_{tp}), combined with the results from Sec. 3.4.3 (low T , insensitive to G_0), seem to be incompatible with any grain material used in the dust models of, e.g., Draine & Li (2007); Compiègne et al. (2011). Here, we note that the grains need to be large to account for the cold temperatures (Sec. 3.4.3), yet in order to assure momentum coupling with the gas, $\log(\xi) \gtrsim 6.3$ (Fig. 3.9). This implies that a large silicate grain with a mass equal to a compact grain with $a = 1 \mu\text{m}$ and $\rho_s = 3.5 \text{ g cm}^{-3}$ will need an increase of geometrical cross-section by a factor of ~ 50 to assure momentum-coupling with the gas. At $a = 0.1 \mu\text{m}$, this factor decreases to 17. We defer a further discussion on the remarkable properties of morphology A to Sec. 3.7.

Dust population B

The presence of the IDW at $0.1 < d < 0.4$ pc, exhibiting the observational characteristics described in Sec. 3.4.2, indicates the presence of dust grains different in nature compared to morphology A. Here, there are two scenarios to consider.

First, the Spitzer/IRS LL spectra, shown in Fig. 3.4, revealed that the $24 \mu\text{m}$ emission from the H II region outside of the IDW is dominated by carbonaceous VSGs (Sec. 3.4.3). Within this framework, the IDW can be formed by these small, compact grains, that are easily momentum-coupled to the gas, yet are less efficient in absorbing the radiation pressure from the star. Figure 3.9 shows that momentum-coupled grains with radiation pressure efficiency $0.03 \leq \bar{Q}_{\text{rp}} \leq 0.50$ could reproduce the IDW at $0.1 < d < 0.4$ pc. These values for \bar{Q}_{rp} are consistent with values obtained for classical compact grains of size $a < 0.01 \mu\text{m}$ (Li & Draine 2001; Draine 2011a).

Second, large, compact BGs that overshoot r_{eq} due to inertia can explain the presence of the IDW (this scenario was already described in Paper 1). For large, compact grains, \bar{Q}_{rp} approaches unity (Draine & Li 2007; Draine 2011a). Then, for the flow parameters adopted, grains of size $a = 0.5 \mu\text{m}$ reach the inner parts of the dust wave at $d \sim 0.1$ pc (in Paper 1, we derived $a = 0.33 \mu\text{m}$ due to the different flow parameters; Sec. 3.5.2). This is a very large size above the typical cut-off for grains in the ISM ($a \approx 0.25 \mu\text{m}$; Weingartner & Draine 2001). The exact dust grain size to reach the inner part of the wave depends on the adopted flow parameters, as well as the momentum of the grain.

The grains that populate the IDW can therefore be explained by either VSGs with low \bar{Q}_{rp} that have reached r_{eq} , or large, compact BGs for which \bar{Q}_{rp} reaches unity. The reduced UV-to-NIR opacity (Sec. 3.4.3) and the observed dust color temperature of the IDW at 0.1 pc (73 K - 82 K, Sec. 3.4.2) hints towards large grains (Tab. 3.2), consistent with the conclusion from Paper 1: a carbonaceous VSG of size $1 \times 10^{-3} \mu\text{m}$ will reach $T_{\text{eq}} = 170$ K at a projected distance of 0.1 pc towards the star, while a large grain of $0.5 \mu\text{m}$ reaches a temperature $T_{\text{eq}} = 75$ K.

3.7 Discussion

The simultaneous presence of two clearly separated dust morphologies inside IC 434, with separate dust waves at projected distance of 0.1 pc and 1.0 pc, can not be explained with a continuous size distribution like that observed for selected regions of the diffuse interstellar medium. Combining modeling (Sec. 3.6) with the constrains derived through observations (Sec. 3.4.2), we have argued that the dust in IC 434 is bimodal in nature.

3.7.1 Derived dust properties

Population A is characterized observationally by a cold temperature (20 K - 26 K; depending on the spectral emissivity β) that is below the equilibrium temperature of classical dust grains predicted by DUSTEM (Compiègne et al. 2011). Moreover, the temperature of this population as derived from a MBB fit to the SED only increases by $\sim 15\%$ (Sec. 3.4.3), while the incident stellar flux increases by an order of magnitude: DUSTEM predicts a temperature increase of 50% for typical ISM grains (Sec. 3.4.2). We find a discrepancy between UV and IR inferred mass of dust contained in the ODW (Sec. 3.4). Modeling of

the photo-evaporation flow reveals that the corresponding dust wave at 1.0 pc can only be reproduced if the grains are momentum-coupled with the gas, which can be obtained by increasing the geometrical cross-section of the grains by factors of 17 and 50 for grains with a mass equivalent to a compact (silicate) grain of $0.1 \mu\text{m}$ and $1.0 \mu\text{m}$, respectively. Furthermore, they need to be highly effective in absorbing radiation pressure ($\bar{Q}_{\text{rp}} \geq 2$; Sec. 3.6.1). In contrast, population B is characterized observationally by mid-IR at ~ 24 emission throughout the H II region, complemented with the IDW that peaks in intensity at 0.1 pc. The emission in the H II region outside of the IDW is caused by VSGs out-of-equilibrium with the radiation field, supported by the IRS spectra. However, the dust wave at 0.1 pc can be explained both by VSGs, but also by BGs that are invisible throughout the H II region and only start to emit at mid-IR wavelengths close to the star as the grains heat up (consistent with the IRS spectrum of region 7). The modeling in Sec. 3.6.1 reveals that either momentum-coupled grains with $\bar{Q}_{\text{rp}} < 1$, or very large compact grains with $\bar{Q}_{\text{rp}} = 1$ can cause the dust wave at 0.1 pc. The color temperature of 73 K - 82 K, and the reduced UV-to-NIR opacity argue for the latter scenario (consistent with Paper 1).

Population B is consistent with grain properties used in current dust models (e.g., Li & Draine 2001; Compiègne et al. 2011), and we connect this population to the warm dust observed in many H II regions (Chini et al. 1986; Paladini et al. 2012; Ochsendorf et al. 2014b). However, we note that Paper 1 argued that the charging of these grains deviate significantly from that predicted by theory (e.g., Draine & Salpeter 1979), consistent with the dust waves in the RCW 120 and RCW 82 H II regions (Ochsendorf et al. 2014b). However, the characteristics of population A are perhaps even more remarkable, and a critical review seems appropriate to place our findings in context with recent developments in our understanding of dust modeling and evolution.

The cold temperature of morphology A (Sec. 3.4.3) and the reduced UV-to-NIR opacity (Sec. 3.4.3) argue for large grains, and the requirement for momentum-coupling with the gas indicates a fluffy or porous structure (Sec. 3.6.1). Indeed, detailed modeling (Ossenkopf & Henning 1994; Ormel et al. 2009) and observational evidence (Steinacker et al. 2010) indicate that grains reach large sizes inside dense cores ($< 1 \mu\text{m}$), from which the presence of large aggregates seems intuitive. The observations may reflect their past evolution in the cloud as the grains are evaporated into the H II region (see for a similar conclusion Martin et al. 2012). However, the constant temperature of population A in a varying radiation field, derived from the MBB fits, will pose a problem to every available dust model. A possible explanation is that the size distribution is heavily affected inside the H II region through processing by the intense radiation field of σ Ori AB. In this scenario, the radiation field destroys the smallest grains, which suppresses the small end of the size distribution. This effect was already seen in Sec. 3.4.2, where a population of VSGs did not seem to survive the transition from the well-shielded PDR of the Horsehead nebula into the H II region. An alternative explanation stems from the results from Planck Collaboration et al. (2014a) and Planck Collaboration et al. (2014b), who show that the peak wavelength of the SED does not trace the intensity of the radiation field only (Sec. 3.4.3): the authors argue that this may be a signature of grain properties that are evolving as the grains transit from one region to another. This argumentation could in principle be applied to the transition of the dust in IC 434 between the dense molecular cloud phase to the H II region. Still, the derived (high) \bar{Q}_{rp} for this population remains unexplained:

it is questionable if dust aggregates are indeed efficient radiation absorbers. For example, Bazell & Dwek (1990) conclude that the optical properties of fractal grains do not change significantly compared to their compact counterparts, which would imply $\bar{Q}_{\text{TP}} \leq 2$ (Li & Draine 2001; Draine 2011a). The detailed optical properties of grains containing chemical inhomogeneities and differing fractal dimensions remain poorly understood; in this respect, more theoretical research that constrain the optical properties of dust aggregates is necessary.

In conclusion, while the analysis of the dust budget in the IC 434 region provides insight into the properties of the grains residing in the ionized gas, some of the results are incompatible with current modeling and should be subject to further questioning. Indeed, evidence is accumulating that the 'standard model' of interstellar dust is incapable to explain the variations of grain properties when moving from one region of the ISM to another (for a recent review, see Jones 2014). The findings of this work support this view, and indicates that our knowledge of dust may be far from complete. Perhaps, we are tracing unknown grain materials. Further laboratory experiments on cosmic dust analogues and theoretical calculations on the optical properties of large aggregates must be used in designing the next generations of dust models, which should also incorporate the evolution of grain materials and properties during the lifecycle of the grains in the ISM.

3.7.2 Limitations of the model

The derived dust parameters depend on the adopted stellar parameters, as well as the model of the approach of σ Ori towards the L1630 molecular cloud. Luckily, the density structure of the flow is well constrained by observations and reveals an exponential dependency with distance from the cloud. However, our choice for the ionizing flux of σ Ori AB, $\log(Q_0) = 47.56$ photons s^{-1} (Martins et al. 2005a), is low compared to values predicted by other model atmospheres. For example, the model atmosphere from Schaerer & de Koter (1997) has $\log(Q_0) = 48.25$ photons s^{-1} for a O9.5V spectral type star. Because we consider a constant effective flow thickness (Henney et al. 2005), a higher value of Q_0 would only increase the density of the ionized gas, thereby increasing F_{drag} . An increase of ionizing flux would therefore lead to an increase of our derived values for \bar{Q}_{TP} , and vice versa.

The dependency on the flow scale height R_0 is less straightforward, and we opted to solve this numerically. As discussed in Sec. 3.5.2, the adopted value of R_0 ($= 0.46R_s$) is appropriate for a photo-evaporation flow emanating from a flat IF (Henney et al. 2005). This choice of R_0 reproduces the $H\alpha$ emission measure with constant scale size l . In Fig 3.10, we vary R_0 and plot the dependency on our results for \bar{Q}_{TP} . Only when R_0 is smaller than $0.46R_s$, corresponding to a diverging flow, are our results for \bar{Q}_{TP} significantly affected. This is because in this case, the gas reaches higher velocities, yet has a lower density. The *total* amount of momentum transfer between the dust and gas in time decreases, lowering F_{drag} and, therefore, lowering \bar{Q}_{TP} to place r_{eq} at the required distances. This result was already observed in Ochsendorf et al. (2014b): momentum transfer between gas and dust is most efficient in slow-moving, high-density photo-evaporation flows. In this respect, at high R_0 , the flow parameters do not change significantly and barely affects \bar{Q}_{TP} anymore.

To conclude, the observed $H\alpha$ emission measure is well described by an exponential

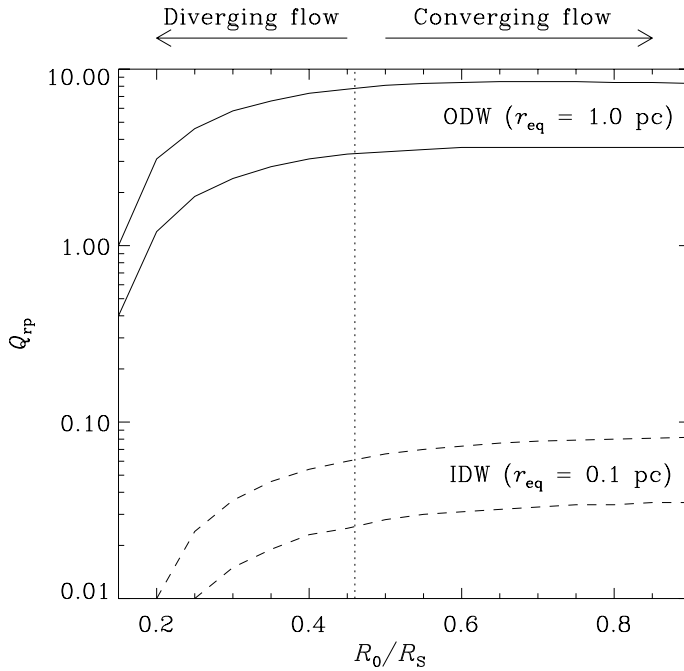


Figure 3.10: The influence of the adopted structure for the champagne flow on the derived values of the radiation pressure efficiency, \bar{Q}_{rp} . Plotted is \bar{Q}_{rp} versus the scale height of the flow, R_0 , normalized to the distance star - cloud, R_s . The dashed line marks the scale height, corresponding to a flat ionization front, and is the one assumed in our calculations. Smaller values of R_0 correspond to increasingly diverging flows, characterized by a fast acceleration of the gas. Larger values of R_0 correspond to thick flows that accelerate more slowly. Plotted is \bar{Q}_{rp} such that the equilibrium radius equals $r_{eq} = 1.0$ (solid lines) and $r_{eq} = 0.1$ (dashed lines). The upper curves correspond to an ionizing flux of $\log(Q_0) = 48.25$ photons s^{-1} (Schaerer & de Koter 1997), the lower curves correspond to an ionizing flux of $\log(Q_0) = 47.56$ photons s^{-1} (Martins et al. 2005a).

power law, $n \propto \exp[-r/R_0]$, which implies that that the gas does not accelerate efficiently like that in a globule flow, where $n \propto r^{-2}$ (Bertoldi 1989). Therefore, low values for R_0 ($< 0.46R_s$) are unlikely for the photo-evaporation flow in IC 434, while our results for \bar{Q}_{rp} will not be significantly altered for $R_0 > 0.46R_s$.

3.7.3 PAH emission from the ionized gas

In Sec. 3.4.1, we have shown that morphology A is both traced by thermal emission of large dust grains at $\lambda \geq 160 \mu\text{m}$, and by IR fluorescence of PAHs, emitting at $8 \mu\text{m} - 12 \mu\text{m}$. In the framework of dusty photo-evaporation flows, it seems peculiar that PAHs and large dust grains are spatially correlated. PAHs are easily dragged along by a flow of ionized gas, whereas large grains will lag behind due to inertia. We propose that PAH molecules are formed *inside* the H II region through shattering upon grain-grain collisions between the separate grain populations in the flow, that couple different to the gas and move at

non-identical velocities. Sputtering is not efficient for the physical conditions inside the IC 434 region (Paper 1). Once being formed, the PAHs are destroyed quickly through photo-dissociation after UV photon absorption, expected at the intensity of the radiation field (Tielens 2005). This could explain why PAHs and large grains are seen co-spatial, and results in the absence of PAHs within ~ 1 pc from the star. This cavity is likely seen in the evolution of the PAH spectrum (Fig. 3.5), where a discontinuity is observed in the $7.7 \mu\text{m}$ over $11.3 \mu\text{m}$ intensity ratio between region 6 and region 7. A detailed model describing the collision- and fragmentation process, and the evolution of the PAH emission spectrum inside the H II region is beyond the scope of this paper, and will be presented in a forthcoming work (Ochsendorf et al., in prep.).

3.8 Conclusions

We have carried out a combined observational- and modeling study of the IC 434 region and the GS206-17+13 shell that surrounds it. We characterized the dust emission from the H II region (Secs. 3.4 & 3.6), with the use of an updated flow model (Sec. 3.5) that resulted from an analysis of the large-scale structure of the Belt region seen to date (Sec. 3.3). The important findings are listed below:

1. The GS206-17+13 shell is driven by the Orion OB1b association, rather than the σ Ori cluster, derived through a study of space motions, and by comparing the kinetic energy of the expanding shell to the mechanical output of the Orion OB1b members and the weak-wind system of σ Ori AB (Sec. 3.3). The space motion of σ Ori AB is directed toward the L1630 molecular cloud, and can be traced back to the Orion OB1c association, in line with the suggestion of Bally (2008) that assigned the σ Ori cluster to the younger Orion OB1c association. This would solve the apparent mismatch between the age of σ Ori (~ 3 Myr; Caballero 2008) to the Orion OB1b association (> 5 Myr; Bally 2008). Besides that the aforementioned analysis of the Belt region results in a flow model necessary to derive the grain properties in the H II region, it provides new insight in the history of the Belt region that will be of great interest for research on the Orion OB association and stellar feedback in OB associations. The Orion region is far from fully understood, and with the upcoming results from the Gaia mission, its study provides a benchmark case that has implications for the evolution of OB associations in general.
3. The global structure of the IR emission revealed two separate morphologies (morphology A & B) associated with a dust wave at 1.0 pc and 0.1 pc, respectively. We have attributed this segregation to a bimodal dust distribution (population A & B), and have characterized both populations through their observational properties and through modeling of the grain trajectories.
4. A dust wave stratifies dust grains in a region stretching from r_{eq} (momentum-coupled grains) towards r_{min} (non-momentum-coupled grains), depending on the geometrical cross-section over dust mass, ξ . The radiation pressure efficiency, \bar{Q}_{rp} , effectively offsets r_{eq} and r_{min} from the star.

5. Population A has a cold dust temperature (20 K - 27 K; depending on the spectral emissivity) derived from MBB fits, below the equilibrium temperature of 'classical' grains at the incident radiation field (20 K - 55 K for grains $0.1 \mu\text{m} - 1.0 \mu\text{m}$) predicted by DUSTEM. PAH emission is seen co-spatial with population A, and the increasing charge state of the molecules reveal that both the PAHs and population A reside within the ionized gas. The dust wave at 1 pc, associated with population A, can only be reproduced if the grains are momentum-coupled with the gas ($\log(\xi) > 6.25$), for which the grain need to have a significant increased geometrical cross section compared to compact grains. We have argued that the porous or fluffy aggregates that are formed inside the L1630 molecular cloud are good candidates to explain the above described characteristics of population A. However, the high radiation pressure efficiency ($\bar{Q}_{\text{rp}} \geq 2$), and the evolution of the temperature that does not seem to trace an increase of radiation field only, can not be explained by current dust models, but confirms recent results by, e.g., *Planck* (Planck Collaboration et al. 2014a,b), indicating that our understanding of interstellar dust may be limited (Jones 2014).
6. Population B is reminiscent of warm dust, often observed towards the centers of H II regions (Chini et al. 1986; Paladini et al. 2012; Ochsendorf et al. 2014b). Here, we reveal that it is characterized by mid-IR emission around $24 \mu\text{m}$ from VSGs throughout the H II region (region 1 - 6), and a dust wave at 0.1 pc from the star where the dust reaches TE with $T_{\text{d}} \sim 73 \text{ K} - 82 \text{ K}$. The dust wave at 0.1 pc can be reproduced if the grains are either momentum-coupled small grains ($\log(\xi) > 6.9$, $\bar{Q}_{\text{rp}} < 1$), or large, compact grains ($a \approx 0.5 \mu\text{m}$, $\bar{Q}_{\text{rp}} = 1$) that approach the star closely due to inertia. These values for \bar{Q}_{rp} are consistent with prediction from theory. The reduced UV-to-NIR opacity, and the observed dust color temperature of the IDW are consistent with the BG scenario, confirming the results from Paper 1.
7. The presence of PAH emission inside the H II region is linked to shattering of grain material upon grain-grain collisions.

Acknowledgements

Studies of interstellar dust and chemistry at Leiden Observatory are supported through advanced ERC grant 246976 from the European Research Council, through a grant by the Dutch Science Agency, NWO, as part of the Dutch Astrochemistry Network, and through the Spinoza premie from the Dutch Science Agency, NWO.

4

Radiation-pressure-driven dust waves inside bursting interstellar bubbles

Massive stars drive the evolution of the interstellar medium through their radiative and mechanical energy input. After their birth, they form ‘bubbles’ of hot gas surrounded by a dense shell. Traditionally, the formation of bubbles is explained through the input of a powerful stellar wind, even though direct evidence supporting this scenario is lacking. Here we explore the possibility that interstellar bubbles seen by the *Spitzer*- and *Herschel* space telescopes, blown by stars with $\log(L/L_{\odot}) \lesssim 5.2$, form and expand because of the thermal pressure which accompanies the ionization of the surrounding gas. We show that density gradients in the natal cloud or a puncture in the swept-up shell lead to an ionized gas flow through the bubble into the general interstellar medium, which is traced by a *dust wave* near the star, which demonstrates the importance of radiation pressure during this phase. Dust waves provide a natural explanation for the presence of dust inside H II bubbles, offer a novel method to study dust in H II regions and provide direct evidence that bubbles are relieving their pressure into the interstellar medium through a champagne flow, acting as a probe of the radiative interaction of a massive star with its surroundings. We explore a parameter space connecting the ambient density, the ionizing source luminosity, and the position of the dust wave, while using the well-studied H II bubbles RCW 120 and RCW 82 as benchmarks of our model. Finally, we briefly examine the implications of our study for the environments of super star clusters formed in ultraluminous infrared galaxies, merging galaxies, and the early Universe, which occur in very luminous and dense environments and where radiation pressure is expected to dominate the dynamical evolution.

B. B. Ochsendorf, S. Verdolini, N. L. J. Cox,
O. Berné, L. Kaper & A. G. G. M. Tielens
Astronomy & Astrophysics 566, A75 (2014)

4.1 Introduction

The morphological appearance of mid-infrared (MIR) bubbles in the disk of the Galaxy is traditionally explained by the interaction of a stellar wind with the surrounding gas (Weaver et al. 1977). In this scenario, stellar winds from massive stars drive shock waves in their surroundings, which sweep up the ambient gas and produce a cavity filled with hot ($T \sim 10^7$ K), tenuous ($n_{\text{H}} \sim 0.01 \text{ cm}^{-3}$), collisionally ionized gas surrounded by a dense ($n_{\text{H}} \sim 10^5 \text{ cm}^{-3}$) shell. Assisted by volunteers from the general public, some 5000 bubbles have now been identified in the Galactic plane (Churchwell et al. 2006; Simpson et al. 2012).

The evolution of expanding H II regions has been addressed numerically in several recent papers, investigating the influence of the initial cloud structure on bubble expansion (i.e., Walch et al. 2013) and the effect of stellar winds (Dale et al. 2013). In addition, a theoretical study including stellar winds is described in Raga et al. (2012). Still, observations challenge our understanding on wind-blown bubbles (WBB). First, detection of the hot gas through X-ray emission has proven to be elusive for bubbles powered by a handful of OB stars. Diffuse X-ray emission has only been detected towards sources with extreme mass-loss (Wolf-Rayet bubbles; Toalá et al. 2012; Toalá & Guerrero 2013), extreme ionizing power (M17 and the Rosette nebula; Townsley et al. 2003), and superbubbles created by interior supernova remnants (Chu & Mac Low 1990b). Explanations for the lack of X-ray detections inside the vast majority of the bubbles include mass loading, thermal conduction, and leakage of the hot gas from the bubble (Harper-Clark & Murray 2009; Arthur 2012). Second, recent observations show that winds from O stars with $\log(L/L_{\odot}) \lesssim 5.2$ (Martins et al. 2005b; Marcolino et al. 2009) may be less powerful than thought (the weak-wind problem; Puls et al. 2008; Najarro et al. 2011), which in its turn is challenged by recent X-ray observations of a stellar wind described in Huenemörder et al. (2012). Third, dust grains are expected to evacuate the interiors of WBBs on short timescales ($\sim 10^5$ yr) by either acceleration or sputtering due to friction with high-velocity gas ($\sim 2000 \text{ km s}^{-1}$) from the stellar wind (Everett & Churchwell 2010). Yet, high-resolution infrared observations show that H II bubbles include a significant amount of dust in their interiors (Deharveng et al. 2010; Martins et al. 2010; Anderson et al. 2012). The evaporation of small, dense cloudlets could resupply the hot gas with a new generation of dust grains (Everett & Churchwell 2010). While this mechanism can explain the presence of dust inside H II bubbles, it does not produce in a natural way the morphology of the (mid-)IR radiation: arc-shaped and peaking close to the ionizing source.

Driven by the difficulties in connection with the model of WBBs outlined above, we have explored the possibilities of H II bubble formation by thermal pressure (Spitzer 1978) instead of a stellar wind. We present the observations and the methods in Sec. 4.2. In Sec. 4.3, we show that the morphological appearance of dust inside H II bubbles, blown by stars with $\log(L/L_{\odot}) \lesssim 5.2$, is often characterized by an arc-like structure emitting in the infrared (IR), and propose that these arcs are dust waves (Ochsendorf et al. 2014a), where radiation pressure has stalled the dust carried along by a photo-evaporation flow of ionized gas. We test our hypothesis by performing hydrodynamical simulations of the well-known H II bubble RCW 120 and present a model for studying the coupling between gas and dust, and for predicting the location of a dust wave. We discuss our findings and summarize our conclusions in Sec. 4.4.

Survey	Passband	Reference
SuperCOSMOS	0.656 μm	Parker & Phillipps (1998)
Spitzer/GLIMPSE	8 μm	Benjamin et al. (2003)
Spitzer/MIPSGAL	24 μm	Carey et al. (2009)
Herschel/Hi-Gal	250 μm	Molinari et al. (2010)
NVSS	1.4 GHz	Condon et al. (1998)
SUMSS	843 MHz	Bock et al. (1999)

Table 4.1: Surveys used in this study.

4.2 Observations and method

The Galactic plane has been observed at a wide range of wavelengths, allowing for a multi-wavelength study of the H II bubbles seen in the GLIMPSE survey (Churchwell et al. 2006). We explored several large-scale surveys that are publicly available online. We summarize these surveys in Tab. 4.1.

4.2.1 Hydrodynamical simulations

Hydrodynamical simulations were produced with FLASH HC (hybrid characteristics), a modified version of FLASH (Fryxell et al. 2000) that includes radiative transfer (Rijkhorst et al. 2006). FLASH is a publicly available, modular, parallel, adaptive-mesh-refinement hydrodynamical code. The transfer of ionizing radiation is carried out by the method of hybrid characteristics, which efficiently traces rays across the block-structured adaptive-mesh-refinement grid and computes the intensity of radiation at every computational cell. We adopted the on-the-spot approximation, that is, all the ionizing photons produced by recombinations to the ground state were assumed to be absorbed locally, making the radiation transfer equation more simple to solve. Since its first description by Rijkhorst et al. (2006), the HC scheme has been improved, as described in Raicevic (2010) and Verdolini (2014). The updated version of the scheme was employed in the radiative-transfer-code comparison project by Iliev et al. (2009), and tested further for high-density medium in Verdolini (2014).

For the simulations presented in this work, we allowed the grid to refine and de-refine according to the second-order density derivative. This choice has the effect of increasing the resolution elements where the density changes on a small spatial scale. Along the edges of the H II region the resolution increases up to the maximum permitted, which allowed us to properly follow the evolution of the region without an excessive use of computational power.

4.3 Results

Figure 4.1 presents RCW 120 and RCW 82, which are two well-isolated bubbles, allowing for a detailed study of their morphology and characteristics (Zavagno et al. 2007; Pomarès et al. 2009). The two bubbles are powered by stars below the so-called weak-wind limit (i.e. $\log(L/L_{\odot}) \lesssim 5.2$): the ionizing source of RCW 120 is a star of spectral type O6V -

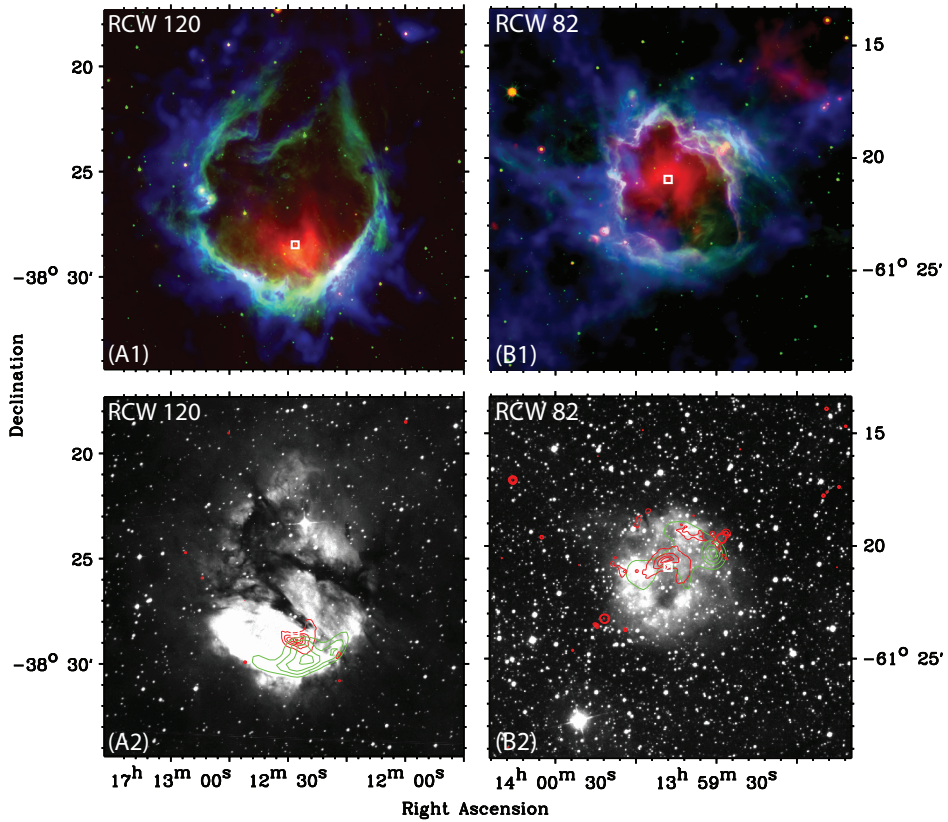


Figure 4.1: (A1) H II bubble RCW 120 is ionized by a central source (white square) of spectral type O6V - O8V (Zavagno et al. 2007; Martins et al. 2010). Spitzer/IRAC observations at $8\ \mu\text{m}$ (green) trace PAH emission from the inner edge of the bubble, while arc-shaped $24\ \mu\text{m}$ emission from large $\sim 100\ \text{K}$ dust grains, as seen by Spitzer/MIPS, peaks close to the central star (red). The Herschel/SPIRE $250\ \mu\text{m}$ observations are plotted in blue, revealing high column densities of cold ($\sim 15\text{-}30\ \text{K}$) dust surrounding the bubble. Sequential star formation can occur in the swept-up material because the shells are prone to gravitational instabilities (Zavagno et al. 2007; Pomarès et al. 2009; Martins et al. 2010). The shell appears to be broken towards the top side. (A2) $\text{H}\alpha$ SuperCOSMOS image, overlaid with contours of Spitzer/MIPS $24\ \mu\text{m}$ (red) and NVSS radio continuum emission at $1.4\ \text{GHz}$ (green), revealing the distribution of gas and dust inside the bubble. Contour levels are max - 80% - 60% - 40%. (B1 & B2) RCW 82 is ionized by two stars of spectral type O7V - B2V (Pomarès et al. 2009). Images B1 and B2 use the same color scheme as A1 and A2, respectively. The radio continuum data for RCW82 are taken from SUMSS at $843\ \text{MHz}$ with contour levels max - 80% - 60% - 40%. In this case, the bubble appears to be broken towards the bottom.

O8V (Zavagno et al. 2007; Martins et al. 2010), while RCW 82 is ionized by two stars of spectral type O7V - B2V (Pomarès et al. 2009). The dust properties of both regions have been discussed in Anderson et al. (2012); their analysis, however, focused on the cold component ($10\text{-}35\ \text{K}$) seen at long wavelengths ($> 70\ \mu\text{m}$), which predominantly traces large columns of material of the dense shell. In this work, we focus on the warm

dust component, seen at $24\ \mu\text{m}$, inside the ionized region of H II bubbles (see also Watson et al. 2008; Deharveng et al. 2010).

The warm dust component at $24\ \mu\text{m}$ is characterized by arc-shaped emission that peaks close to the ionizing source and reveals that dust resides well within the borders of the swept-up shell, which is traced by $8\ \mu\text{m}$ emission and appears to be broken or punctured. To study the spatial distribution of gas and compare it with dust, we used high-resolution H α emission data and complemented this with (low-resolution) radio continuum data not affected by extinction in the line of sight. These properties - an arc-shaped structure at $24\ \mu\text{m}$ and an incomplete shell traced at $8\ \mu\text{m}$ - are common properties of H II bubbles (Watson et al. 2008; Deharveng et al. 2010), see also Verdolini et al., in prep. We note that ionized gas traces the emission along the line of sight, whereas $24\ \mu\text{m}$ emission predominantly arises from dust heated to temperatures of $\sim 100\ \text{K}$ near the star. This emission could either originate from small stochastically heated particles, often referred to as very small grains (VSGs), or big grains (BGs) in thermal equilibrium with the radiation field (e.g., Paladini et al. 2012). Whereas several authors attribute the $24\ \mu\text{m}$ emission inside ionized regions to the increase of VSGs compared with BGs (Paradis et al. 2011; Flagey et al. 2011), the analysis of the IR arc in IC 434 revealed that the increased heating by stellar photons from the nearby stars, $\sigma\ \text{Ori AB}$, can explain the MIR emission (Ochsendorf et al. 2014a). Here, we sidestep this problem and note that the emission from $24\ \mu\text{m}$ and H α /radio throughout the bubble interiors shown in Fig. 4.1 are not spatially correlated: dust emission peaks close to the ionizing source, while the ionized gas does not follow this trend. This implies that gas and dust are (partially; see Sec. 4.4) decoupled inside RCW 120 and RCW 82.

We propose that H II bubbles, blown by stars with $\log(L/L_\odot) \lesssim 5.2$, are formed by thermal pressure of the gas that accompanies ionization and not by a stellar wind. The proposed scenario is depicted in Fig. 4.2. Using the well-studied bubble RCW 120 as reference, we performed hydrodynamical simulations to test our hypothesis.

4.3.1 Hydrodynamical simulations of RCW 120

Stars capable of creating large bubbles are thought to form inside infrared dark clouds (IRDCs), which have typical sizes of 1-3 pc, densities of $\sim 10^4\ \text{cm}^{-3}$, masses of $\sim 10^4\ M_\odot$ (Rathborne et al. 2006) and are contained in a larger scale molecular cloud. We attempted to model the conditions inside an IRDC by constructing a computational domain containing a Bonnor-Ebert (BE) sphere of mass $\sim 7 \times 10^5\ M_\odot$ and radius $\sim 9\ \text{pc}$. The observed density profiles of cloud cores are close to those seen in the BE model (Ballesteros-Paredes et al. 2003; Pirogov 2009) and, therefore, are often used in cloud-core simulations (e.g. Girichidis et al. 2011).

A BE sphere is an isothermal gas sphere in hydrostatic equilibrium in a pressurized medium. As initial condition, we set a density profile that follows the BE sphere solution, and did not include unnecessary calculations due to the presence of gravity. We omitted the force of gravity in our simulations because we are only interested in the interaction of the ionizing photons of the star with the surroundings, not in the formation of the star itself. We generated an initial equilibrium solution without gravity by fixing a constant pressure in the computational box and by changing the temperature accordingly. We placed the star $\sim 3\ \text{pc}$ *offset* from the center of the sphere. Dust is not included in our

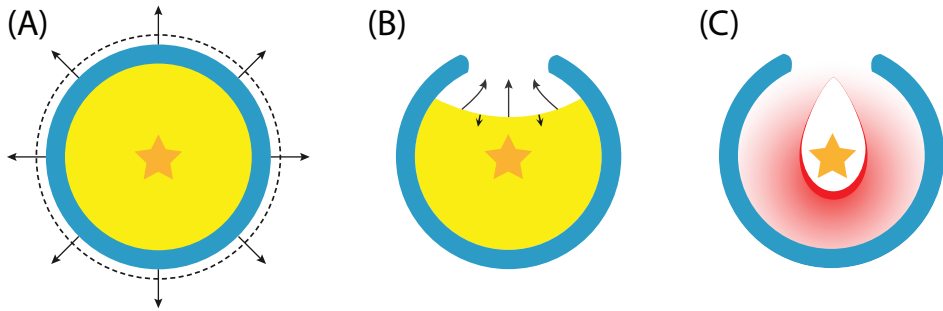


Figure 4.2: (A) Overpressure of the hot, ionized interior (yellow) will cause the bubble to expand inside the natal cloud, sweeping up neutral gas in a dense shell (blue) (Spitzer 1978). If the expansion is supersonic, a shock front forms on the neutral side of the shell (dashed line). (B) If the ionized gas contains a density gradient and/or the bubble is punctured, a flow of ionized gas will stream towards lower density and ultimately into the surrounding ISM, relieving the bubble from its pressure (Tenorio-Tagle 1979). (C) Dust is dragged along in an ionized flow, where ‘upstream’ dust approaching the ionizing source will be heated and halted by radiation pressure, resulting in a *dust wave* or *bow wave* (Ochsendorf et al. 2014a) (see Sec. 4.3.2 and 4.4), which can be traced at mid-infrared wavelengths (red).

simulations; however, dust and gas are poorly coupled in evolved H II regions (see Sec. 4.4). Dust competes for ionizing photons and will shrink the H II region in size, which is captured in the uncertainty of ionizing power of the central source and will not affect our conclusions. The number of ionizing photons Q_0 is set to 3.8×10^{48} photons s^{-1} (Zavagno et al. 2007). We followed the evolution of the H II bubble during the first few Myr of expansion.

Fig. 4.3 shows the results of a two-dimensional simulation with a maximum refinement level equal to 6. Initially, the star creates an expanding sphere of ionized gas, surrounded by a thick shell of neutral swept-up material (Spitzer 1978). However, the density gradient of the BE sphere causes the expansion to accelerate towards low density immediately after ionization ($t < 1$ Myr), initiating a photo-evaporation flow inside the ionized gas. Eventually ($1 < t < 2$ Myr), the swept-up shell reaches the edge of the sphere; gas inside the bubble is accelerated to $15\text{--}20$ km s^{-1} . After $t > 3$ Myr, the shell breaks open towards the low-density region, while the ionized gas inside the H II region reaches velocities of about 40 km s^{-1} . As the so-called champagne flow phase develops (Tenorio-Tagle 1979), the relative velocity between the ionized gas in the flow and the star increases (Fig. 4.4), creating the conditions required for the development of a dust wave (see Sec. 4.3.2 and 4.3.3). We note that the velocity of the flow, v_f , depends on the starting conditions of the simulations; in particular, the offset of the star from the cloud center and the steepness of the density gradient in the parental cloud, where higher velocities are obtained within a lower density or a steeper gradient. This will be thoroughly addressed in a forthcoming paper (Verdolini et al., in prep).

Fig. 4.4 shows the velocity of the ionized gas and the amount of kinetic energy (E_k) transferred to the surrounding ISM, calculated through a three-dimensional simulation with a maximum refinement level equal to 5. We saved computing power by running

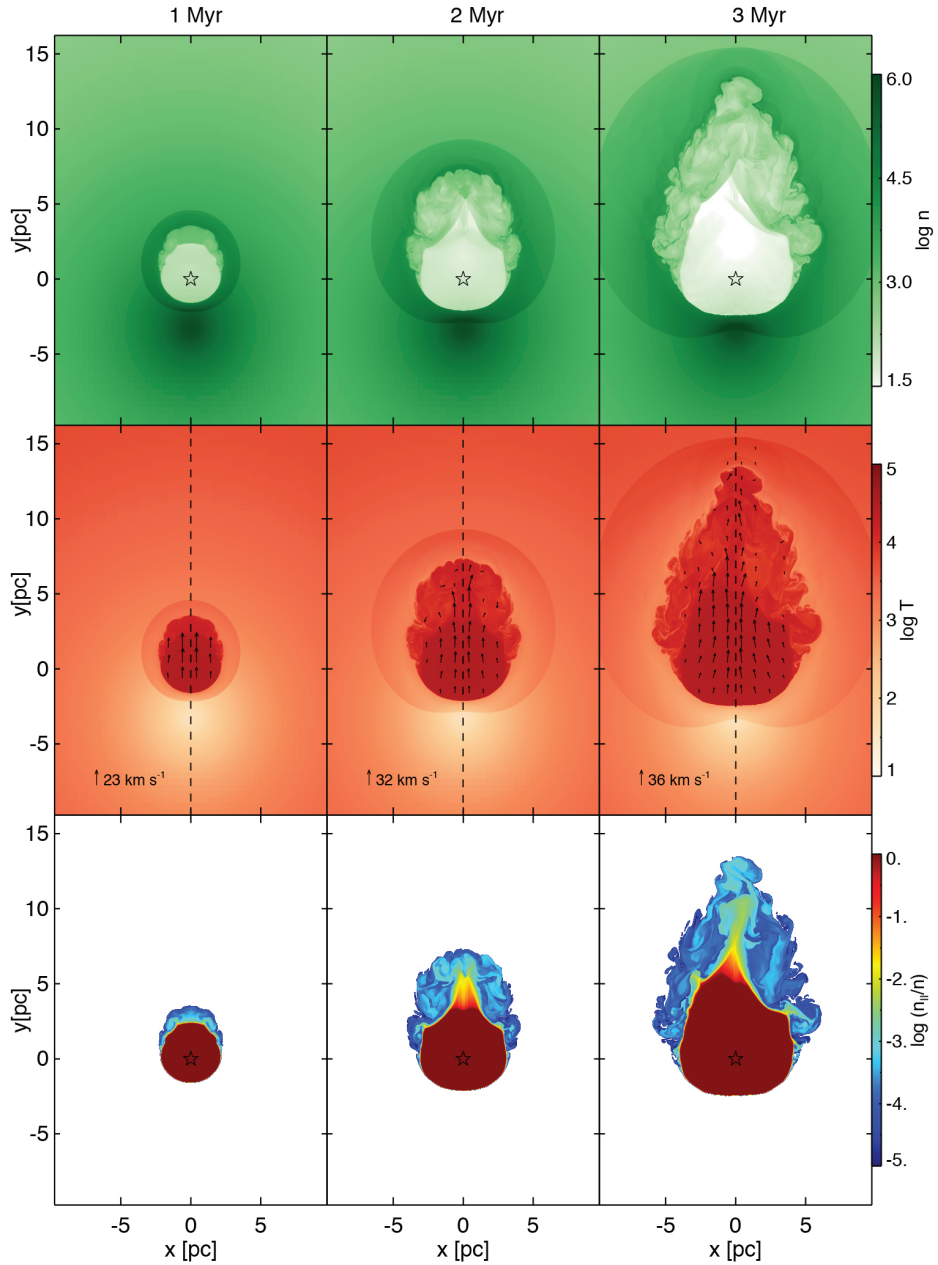


Figure 4.3: Two-dimensional hydrodynamical simulation of an expanding H II region offset from the center of a Bonnor-Ebert sphere. From top to bottom row, the logarithm of number density n , temperature T , and ionization fraction n_{II}/n of a slice through the yz -plane at the location of the star are shown. We trace the velocity of the gas in the three-dimensional simulation along the dashed line (see Fig. 4.4A). Each column corresponds to a snapshot of the simulation at 1, 2, and 3 Myr. The vectors represent the velocity field in the middle row; the legend indicates the maximum velocity.

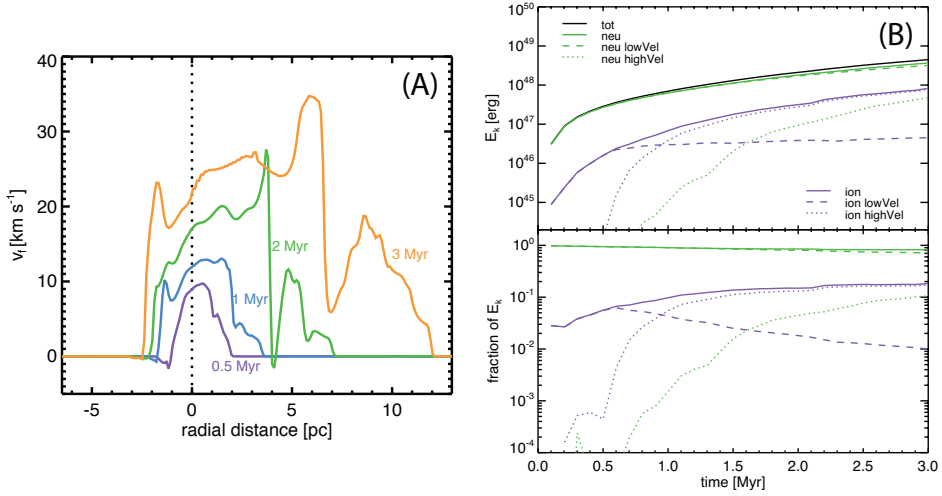


Figure 4.4: (A) Gas velocity along a line in the three-dimensional simulation, which runs from the star through the opening of the bubble (as exemplified in Fig. 4.3). Plotted are the velocity profiles at different times t . The star is located at the dotted line. The sharp increase of the velocity close to the ionization front at $t = 1$ Myr and $t = 3$ Myr are turbulent motions induced by the finite grid of the simulation. Velocities of the gas with respect to the star range from $v_f = 5$ to $v_f = 20$ km s^{-1} . (B) Kinetic energy E_k contained in the three-dimensional simulation (top panel) and fractional distribution of E_k (bottom panel). We separate E_k located into the neutral gas (green), the ionized gas (purple) and their total (black line), which are further divided into the subsonic (dashed) and the supersonic (dotted) part of each component.

the simulation at a lower refinement level than in the two-dimensional case shown in Fig 4.3. This change in resolution does not affect the result of the run, because the energy budget of the simulation does not depend on the refinement level (Verdolini 2014; Freyer et al. 2003). We traced the amount of energy in sub- (<10 km s^{-1}) and supersonic (>10 km s^{-1}) components of the ionized and neutral gas, respectively. Our calculations show that initially, most of the energy is in the neutral shell of swept-up gas. As the neutral shell is accelerated, E_k is transferred into the neutral gas moving supersonically. The total energy deposited rises steadily as the expanding shell sweeps up ambient material, reaching $\sim 10^{50}$ erg over the lifetime of the star (~ 10 Myr).

4.3.2 Model for dusty photo-evaporation flows

The density gradient inside the bubble shown in Fig. 4.3 leads to a flow of ionized gas towards lower density. The hydrodynamical simulation did not contain dust; however, in reality, dust will be contained inside the flow and be coupled to the gas through gas-grain interactions. The motion of a dust grain contained in a photo-evaporation flow can be calculated by solving a set of coupled differential equations, including the equation of motion, which balances the radiation pressure force from the star with the drag force through collisions with the gas. Here, we write the relevant equations used in this work, but for a detailed description of the physics of a dusty photo-evaporation flow we refer to

Ochsendorf et al. (2014a).

The equation of motion for dust is written as:

$$m_d v_d \frac{dv_d}{dr} = -\frac{\sigma_d \bar{Q}_{\text{rp}} L_{\star}}{4\pi c r^2} + F_{\text{drag}}, \quad (4.1)$$

where v_d is the velocity of the dust, and the first term on the right-hand side represents the radiation pressure F_{rad} ; m_d is the grain mass; r is the distance to the star; L_{\star} and c are the luminosity and the speed of light; σ_d and \bar{Q}_{rp} are the geometrical cross-section and the flux-weighted mean radiation pressure efficiency of the grain. The collisional drag force F_{drag} is estimated through (Draine & Salpeter 1979)

$$F_{\text{drag}} = 2\sigma_d k T n_i \frac{8s}{3\sqrt{\pi}} \left(1 + \frac{9\pi}{64} s_i^2\right)^{1/2}, \quad (4.2)$$

where k is the Boltzmann constant, T and n_i are the temperature and number density of the gas (of species i) and $s_i = (m_i v_{\text{drift}}^2 / 2kT)^{1/2}$, with v_{drift} the drift velocity, which is the relative velocity of the grains with respect to the gas. The equation of motion of gas consists of a balance between momentum gained (or lost) through a pressure gradient and the momentum transfer through interactions with dust grains,

$$v_g \frac{dv_g}{dr} = v_g \frac{c_s}{\rho_g} \frac{d\rho_g}{dr} + \frac{n_d}{\rho_g} F_{\text{drag}}, \quad (4.3)$$

where v_g and ρ_g are the velocity and density of the gas, respectively, and c_s is the local sound speed. The dust number density n_d is calculated from the MRN size distribution. The ratio n_d/ρ_g is not constant, but will depend on v_{drift} and follows from the equations of continuity.

Consider a dusty photo-evaporation flow, with initial velocity v_f , approaching a star radially. The radiation pressure of the star F_{rad} will act on a dust grain contained within the flow, which in this particular case will cause it to lose momentum (i.e., lower v_f). As the dust is slowed down, it will be pushed through the gas with drift velocity v_{drift} , transferring momentum towards the gas through the drag force F_{drag} . Eventually, the dust will be stopped at a point r_{min} ahead of the star, where the radiation pressure F_{rad} balances the drag force F_{drag} . If at this point the amount of momentum transfer between gas and dust is insufficient for the gas to be dynamically perturbed, the two components will decouple, resulting in an increase of dust upstream relative to the star as the gas flows along unhindered. Dust grains approaching the star with a non-zero impact parameter will be pushed around the star, resulting in an arc-shaped structure (Ochsendorf et al. 2014a). The slow-down of the dust will increase the dust number density through continuity, resulting in a pile-up of dust ahead of the star. This structure has been dubbed a *dust wave*, the appearance of which will resemble the situation depicted in Fig. 4.2C. Dust waves allow us to test the properties of dust in H II regions: for example, the study of the dust wave in IC 434 implied that dust and gas in IC 434 are not coupled through Coulomb interactions, which is the reason why the plasma drag and Lorentz force are omitted in Eq. 4.2 (Ochsendorf et al. 2014a). This unexpected result challenges our understanding of the physics of dust in H II regions, as the grains are expected to be highly charged and to be tightly coupled to the gas through Coulomb focusing.

We explored the effects of different relevant astronomical environments on the momentum transfer between gas and dust, which determines whether gas and dust will decouple to form a dust wave, or remain coupled to form a bow wave, where gas and dust flow around the star together (Ochsendorf et al. 2014a). To do so, we solved the situation sketched above, where a photo-evaporation flow approaches a star radially from the edge of the H II region, for a range of ionizing luminosities Q_0 and densities n_H .

- The ionizing luminosity Q_0 determines the size of the H II region (Tielens 2005, p. 243); the Strömgren radius of the H II region is used as the starting point of the flow. Furthermore, Q_0 sets the magnitude of the radiation pressure force F_{rad} through extrapolation of O-star parameters listed in Martins et al. (2005a).
- The density n_H regulates the collisional drag force, F_{drag} , as is shown in Eq. 4.2 (we consider collisions with hydrogen only). A higher density leads to more collisions and, consequently, a higher momentum transfer between both components.

We evaluated our model for densities in the range $10 < n_H < 10^7 \text{ cm}^{-3}$ and for ionizing luminosities in the range $47 < \log(Q_0) < 54 \text{ photons s}^{-1}$. Through our choice of n_H and Q_0 , we set up a parameter space that covers a wide variety of astronomical environments, depicted in Fig. 4.5. Furthermore, we calculated the solutions of our model grid assuming several constant flow velocities v_f of 5, 10, and 20 km s^{-1} , which represent typical velocities of ionized gas at the location of the star (Fig. 4.4A). Note that in reality, gas will accelerate into the H II region along a pressure gradient (represented by the first term on the right-hand side of Eq. 4.3, and seen in Fig. 4.4 through increase of v_f). Much of this acceleration will, however, occur close to the ionization front; adopting a constant velocity is a good first approximation. Our aim is to identify the physical parameters that dominate the momentum transfer between gas and dust, the bulk of which happens close to the star, where F_{rad} increases and stops the dust, and we fully expect that the initial acceleration is largely irrelevant for this discussion.

4.3.3 Location of dust waves and dust-gas coupling inside a photo-evaporation flow

Figure 4.6A plots the location of the dust wave r_{min} for 3000 Å silicate grains of specific density $\rho_s = 3.5 \text{ g cm}^{-3}$, which is contained in a one-dimensional flow approaching the illuminating star radially from the edge of the H II region. The size and specific density of the grains set the inertia of the incoming grains with respect to the star and enters Eq. 4.1 through $m_d = \frac{4}{3}\pi a^3 \rho_s$, where a is the radius of the grain. We take $\bar{Q}_{\text{rp}} = 1$ and $n_d/n_H = 1.8 \times 10^{-13}$ (which is the integrated number density of carbonaceous and silicate dust grains for a bin size of the MRN distribution ranging from 1000 Å to 5000 Å Tielens 2005, p.157). The results in Fig. 4.6A are shown for several constant flow velocities v_f .

The dust waves in RCW 120 and RCW 82 are *observed* at 0.23 and 0.41 pc (Zavagno et al. 2007; Pomarès et al. 2009), and are well reproduced with a flow speed of $v_f \sim 10\text{-}20 \text{ km s}^{-1}$, which is reached in our hydrodynamical simulation after $t > 1 \text{ Myr}$ (Sec. 4.3.1). For comparison, RCW 120 is thought to be $\sim 2.5 \text{ Myr}$ old (Martins et al. 2010). The exact position of r_{min} will depend on the radiation pressure on the one hand and the flow parameters (i.e., the velocity v_f and density n_H of the flow) on the other hand. Fig. 4.6A

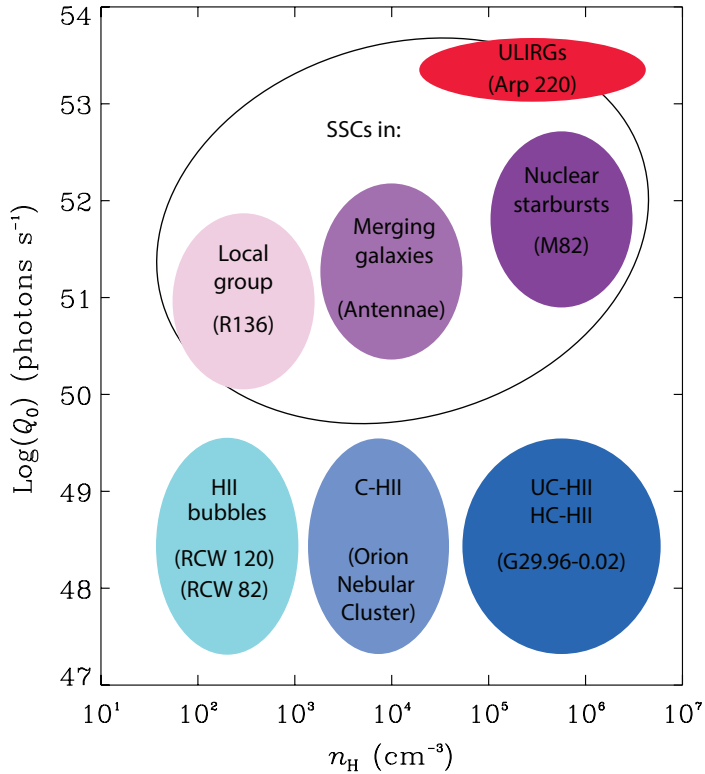


Figure 4.5: Astronomical environments covered by the parameter space through our choice of the ionizing luminosity Q_0 and density n_{H} . Among the environments shown are ultra-compact and hyper-compact H II regions (UC- H II/HC- H II), compact H II regions (C- H II), and evolved H II bubbles, as discussed in this work. We also show super star clusters (SSCs) in the Local Group, merging galaxies, starburst galaxies, and ultra luminous infrared galaxies (ULIRGs). Prototypical candidates of each class are denoted between brackets (for references, see Fig. 4.6).

shows that the dependence of r_{min} on v_{f} is weak. In contrast, v_{f} has a strong effect on the momentum transfer from the dust to the gas, as described below.

The amount of momentum transferred from the dust to the gas depends on the gas density n_{H} and on the flow velocity v_{f} . The ambient number density n_{H} sets the number of collisions between gas and dust. At high n_{H} , the collisions between gas and dust increase in frequency and the amount of momentum transfer to the gas is larger. The velocity of the flow v_{f} sets the time t that it takes for the flow to travel the distance from the edge of the Strömngren sphere towards the central source. Furthermore, t determines how much momentum can be transferred to the gas over time. Our calculations show that even though fast evaporation flows eventually lead to a higher drift velocity of the grains v_{drift} through the gas (i.e., a higher F_{drag}) and therefore more momentum transfer between the grains to the gas per unit time, the short timescale for a fast photo-evaporation flow to reach r_{min} causes the *total* momentum transferred to decrease compared with a slow-moving flow of similar density n_{H} . To summarize, momentum transfer between gas and

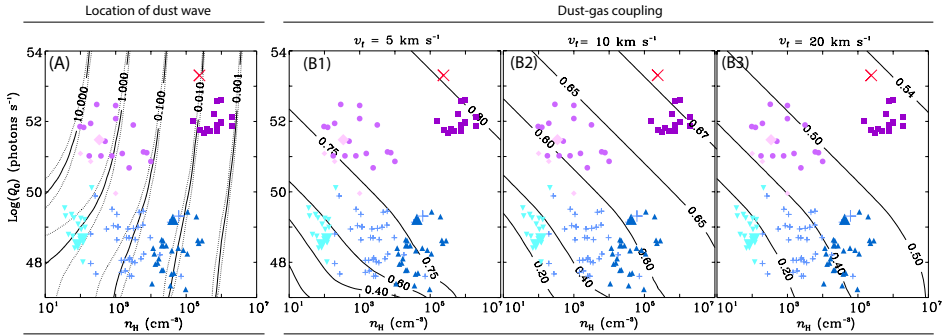


Figure 4.6: (A) Location of a dust wave r_{\min} (black contours) in pc evaluated for a grid of ionizing source luminosities Q_0 and ambient densities n_H for $v_f = 10 \text{ km s}^{-1}$. The dotted contours represent r_{\min} calculated with $v_f = 5 \text{ km s}^{-1}$ and 20 km s^{-1} (a lower flow velocity will move the contours to the *right* in this figure). Overplotted are different astronomical objects, located in regimes drawn in Fig. 4.5: UC-H II /HC-H II; \blacktriangle (Wood & Churchwell 1989), C-H II; $+$ (Garay et al. 1993) and evolved H II bubbles; \blacktriangledown (Paladini et al. 2012). We also show SSCs in the Local Group; \blacklozenge (compiled from Turner 2009), merging galaxies; \bullet (Gilbert & Graham 2007), starburst galaxies; \blacksquare (McCraday & Graham 2007), and ULIRGs; \times (Anantharamaiah et al. 2000). Larger symbols correspond to prototypical candidates of a class denoted between brackets Fig. 4.5. (B1), (B2), and (B3) Coupling strength C (black contours), evaluated for a flow velocity $v_f = 5 \text{ km s}^{-1}$, 10 km s^{-1} , and 20 km s^{-1} .

dust is most efficient in a slow-moving, high-density photo-evaporation flow.

We have expressed the amount of momentum transfer through the coupling strength parameter C , which is a measure of the efficiency of momentum transfer between gas and dust and defined as $C = 1 - p_1/p_0$, where p_0 and p_1 are the initial momentum of the gas (set by v_f) and the momentum of the gas at the position where dust reaches r_{\min} , respectively. Note that in our model, the dust number density per unit mass of gas ($=n_d/\rho_g$) is determined through the relative velocity of the gas and dust through the continuity equation and, as such, is not defined at r_{\min} where the dust velocity v_d reaches zero. This is a peculiarity of the streamline approaching the star radially: in reality, dust along this streamline will acquire momentum in a random direction because of Brownian motion and flow past the star before the dust is stopped completely. Therefore, we opted to evaluate the momentum transfer up to the point where the dust reaches a velocity to the expected Brownian motion velocity $v_B = \sqrt{8kT/\pi m_d} = 2.6 \times 10^{-4} \text{ km s}^{-1}$.

If $C = 1$, dust and gas remain perfectly coupled inside a photo-evaporation flow, and gas will be stopped along with dust. Observationally, a high value of C will express itself in a low contrast between gas and dust and both components would appear to be spatially correlated (a bow wave), similar to the appearance of a stellar-wind bow shock (van Buren et al. 1990; Kaper et al. 1997). When $C < 1$, dust and gas decouple and a higher contrast between dust and gas distribution will be seen in sources with decreasing C (a dust wave). In panels B1, B2, and B3 of Fig. 4.6, we plot C at different flow velocities v_f . In all cases, C is lowest in evolved bubble H II regions, which is the main reason that a high contrast between the distribution of gas and dust can be seen inside these sources. However, v_f has a significant impact on the magnitude of momentum transfer: for example, at $v_f = 5 \text{ km s}^{-1}$, $C \sim 0.5$ for RCW 120 and RCW 82. In contrast, at $v_f = 20 \text{ km s}^{-1}$, $C < 0.2$. Again,

gas and dust couple relatively well in slower photo-evaporating flows, which could lead to the appearance of a bow wave (Ochsendorf et al. 2014a), where dust and gas move around the star together.

4.4 Discussion and conclusion

The IR emission inside H II bubbles is often characterized by arc-structures, as exemplified in RCW 120 and RCW 82. We have argued that these structures can be explained as dust waves induced by photo-evaporating flows inside H II bubbles, which are initiated either by a density gradient inside the bubble or an opening in the bubble shell. The escaping gas will eventually be replaced by a flow of ionized gas evaporating from the inner wall of the swept-up shell. This mechanism provides a natural explanation for the presence and morphology of dust emission seen in the interior of H II bubbles (Deharveng et al. 2010; Martins et al. 2010). Our simulations confirm that an O8 V star can form a bubble of several pc across in typical IRDC conditions without a stellar wind. The bubble is inflated by overpressure of the ionized gas and reveals a similar structure as in RCW 120 and RCW 82, where an ionized gas volume surrounded by a dense shell opens up to one side in order to create a fast champagne flow.

In this work, we investigated bubble H II formation in the absence of a stellar wind. As outlined in Sec. 4.1, recent observations have challenged the WBB model (Weaver et al. 1977), given the weak-wind strengths measured for stars with $\log(L/L_{\odot}) \lesssim 5.2$, the difficulty in detecting diffuse X-rays around main-sequence stars, and the presence and morphology of dust inside H II bubbles. We do not imply that stellar winds are intrinsically absent in these bubbles; the scenario presented here offers an alternative scenario for the formation and evolution of H II bubbles seen by Spitzer and Herschel because it circumvents the previously mentioned problems. The bubble sample of Beaumont & Williams (2010) indicates that the majority of H II bubbles are indeed blown by stars below the weak-wind limit (i.e. $\log(L/L_{\odot}) \lesssim 5.2$), even after correcting the distance toward the bubbles, which were shown by Anderson & Bania (2009) to be systematically higher than the values reported by Beaumont & Williams (2010). However, sources approaching luminosities of $\log(L/L_{\odot}) \sim 5.2$ may have a stellar wind contributing to the morphology of gas and dust (see Draine 2011a). Moreover, several large bubbles powered by a cluster of stars, with luminosities near to or possibly exceeding the weak-wind limit, also exhibit IR arcs in their interior, for instance, the W5 region (Koenig et al. 2008). In this case, dust and gas seem to follow a similar morphology inside the bubble (Deharveng et al. 2012), which either is the signature of a bow wave or the effect of a stellar wind, as it is unlikely that both the dust and gas will penetrate in the inner region of a WBB dominated by the free-flowing wind (Weaver et al. 1977), and will flow around this region together. More simulations to study gaseous flows inside WBBs will help in understanding the evolution and morphology of bubbles around sources that approach or exceed the weak-wind limit. Nevertheless, dust waves provide direct evidence for the importance of bubble champagne flows, irrespective of the dominant source of expansion (i.e. thermal pressure or stellar winds).

Dust waves require an appreciable flow speed ($v_f > 10 \text{ km s}^{-1}$) of the gas near the star for the dust to significantly decouple from the gas. This is reproduced in our models by placing the star offset from the center of a Bonnor-Ebert sphere, whose density gradient

leads to a significant acceleration of the gas after ionization of the cloud material. In addition to the acceleration that is needed to segregate the gas and dust to create a dust wave, the density gradient in the cloud also leads to (narrow) openings through which the gas is vented into the ISM, which is characteristic for many bubbles such as RCW 120 and RCW 82 (Zavagno et al. 2007; Pomarès et al. 2009; Deharveng et al. 2010).

We note that the evolution of interstellar bubbles can be affected by several other mechanisms, such as the motion of the ionizing source, which leads to a cometary shape of the bubble in the direction of movement (Wood & Churchwell 1989), and an external magnetic field, which adds anisotropic pressure to the bubble (Bisnovatyi-Kogan & Silich 1995), possibly leading to elongated shapes aligned along the Galactic field lines (Pavel & Clemens 2012). This does not seem to apply for RCW 120 and RCW 82, given the near-spherical appearance of the two regions. In addition, we note that grain charging inside H II regions is not fully understood, and motions of dust grains in IC 434 does not seem to be influenced by Coulomb interaction with the plasma (Ochsendorf et al. 2014a). For IC 434, the morphological appearance of the photo-evaporation flow indicates a free flow of the gas and a magnetic field, if present, would then most likely be oriented perpendicular to the cloud surface. Again, it is unclear whether a similar explanation applies to the bubbles studied in this paper.

Large turbulent instabilities arise once the ionized flow inside the bubble clashes with the dense shell; the signatures of Kelvin-Helmholtz and Rayleigh-Taylor instabilities are clearly seen in Fig. 4.3. However, this does not affect the formation of the dust wave contained *within* the ionized part of the bubble, because the flow energy of the ionized gas is much higher than the turbulence energy, resulting in a smooth, laminar flow of ionized gas in the interior of the bubble as exemplified in Fig. 4.3. Moreover, gas and dust are only weakly coupled inside evolved H II regions (see Fig. 4.6), which minimizes the influence of turbulence on the motion of dust inside a photo-evaporation flow.

Our models predict that the flow becomes highly supersonic across the bubble, channeling its contents into the surrounding ISM. For the most common type II supernova progenitor (late O/early B-stars with a main-sequence lifetime of ~ 10 Myr), some 10^{50} erg of kinetic energy can be deposited into the ISM. This is similar to the typical supernova energy ($\sim 10^{51}$ erg, of which $\sim 10\%$ is transferred to kinetic energy of the interstellar gas; Veilleux et al. 2005). Moreover, while on a large scale the structure of the ISM is dominated by the walls and chimneys associated with superbubbles created by supernovae breaking into the Galactic halo, Spitzer- and Herschel surveys demonstrate that on smaller scales the structure of the ISM is controlled by the H II bubbles and photo-evaporation flows discussed here.

The momentum transfer between dust and gas in evolved H II bubbles such as RCW 120 and RCW 82 is insufficient for the gas to be dynamically perturbed. This makes these objects ideal candidates for observing dust waves and for studying the properties of dust in H II regions and their dynamical interaction with stellar radiation and gas. However, the velocity of the flow is an important factor: at low velocities, gas remains coupled more efficiently and can form a bow wave. This situation will resemble a stellar wind bow-shock configuration (van Buren et al. 1990; Kaper et al. 1997), where gas and dust peak at a position upstream and produce a drop in emission measure downstream with respect to the star. In regions of high density such as the (ultra)-compact H II regions, the collision rate between dust and gas increases and the coupling between the two compo-

nents tightens. Dust and gas also couple well in SSC environments such as R136 in the 30 Dor region and the nuclear starburst in M82. In particular in the latter, dust and gas show similar morphologies near the SSCs that are launching a galactic wind (Gandhi et al. 2011). Radiation pressure is expected to play a key role in the gas and dust dynamics in ULIRGs such as Arp 220. These immense star-forming galaxies will be most efficient in driving gas dynamics through coupling with dust, thereby limiting the efficiency of star formation (Andrews & Thompson 2011).

Recent studies (Krumholz & Matzner 2009; Draine 2011a; Silich & Tenorio-Tagle 2013) have explored the importance of radiation pressure for the dynamics of gas around young star clusters. This mechanism is poorly understood, mainly because of our limited understanding of the interplay between radiation pressure, dust, and gas. The study of photo-evaporation flows and dust waves provides us with a unique laboratory to directly study the momentum coupling of stellar radiation and the surrounding medium, which largely proceeds through the dust and is crucial for the implementation in current state-of-the-art models on star and galaxy formation and evolution throughout the history of the Universe.

Acknowledgements

Studies of interstellar dust and chemistry at Leiden Observatory are supported through advanced ERC grant 246976 from the European Research Council, through a grant by the Dutch Science Agency, NWO, as part of the Dutch Astrochemistry Network, and through the Spinoza premie from NWO. NLJC acknowledges support from the Belgian Federal Science Policy Office via the PRODEX Programme of ESA. The software used in this work was in part developed by the DOE NNSA-ASC OASCR Flash Center at the University of Chicago.

5

Nested shells reveal the rejuvenation of the Orion-Eridanus superbubble

The Orion-Eridanus superbubble is the prototypical superbubble due to its proximity and evolutionary state. Here, we provide a synthesis of recent observational data from *WISE* and *Planck* with archival data, allowing to draw a new and more complete picture on the history and evolution of the Orion-Eridanus region. We discuss the general morphological structures and observational characteristics of the superbubble, and derive quantitative properties of the gas- and dust inside Barnard's Loop. We reveal that Barnard's Loop is a complete bubble structure which, together with the λ Ori region and other smaller-scale bubbles, expands within the Orion-Eridanus superbubble. We argue that the Orion-Eridanus superbubble is larger and more complex than previously thought, and that it can be viewed as a series of nested shells, superimposed along the line of sight. During the lifetime of the superbubble, H II region champagne flows and thermal evaporation of embedded clouds continuously mass-load the superbubble interior, while winds or supernovae from the Orion OB association rejuvenate the superbubble by sweeping up the material from the interior cavities in an episodic fashion, possibly triggering the formation of new stars that form shells of their own. The steady supply of material into the superbubble cavity implies that dust processing from interior supernova remnants is more efficient than previously thought. The cycle of mass-loading, interior cleansing, and star formation repeats until the molecular reservoir is depleted or the clouds have been disrupted. While the nested shells come and go, the superbubble remains for tens of millions of years.

5.1 Introduction

The Orion-Eridanus superbubble is a nearby (~ 400 pc) expanding structure that is thought to span $20^\circ \times 45^\circ$ on the sky (Reynolds & Ogden 1979; Bally 2008; Pon et al. 2014a). Because of its proximity and evolutionary stage, it is traced at a multitude of wavelengths (Heiles et al. 1999), serving as a benchmark to the study of superbubbles. The expansion of the bubble is most likely connected to the combined effects of ionizing UV radiation, stellar winds, and a sequence of supernova explosions from the Orion OB association, Orion OB1 (Blaauw 1964; Brown et al. 1994).

The line of sight expansion of the Orion-Eridanus superbubble is previously estimated at $\sim 15 \text{ km s}^{-1}$ through line-splitting of $H\alpha$, which also revealed a total ionized gas mass of $8 \times 10^4 M_\odot$ and a kinetic energy of $E_{\text{kin}} > 1.9 \times 10^{50}$ erg (Reynolds & Ogden 1979). Large-scale spectroscopic mapping of the entire Orion-Eridanus region in HI reported a larger expansion velocity of the superbubble of $\sim 40 \text{ km s}^{-1}$ with a mass of $2.5 \times 10^5 M_\odot$, containing a kinetic energy of 3.7×10^{51} erg (Brown et al. 1995), which is shown to be consistent with the integrated mechanical luminosity exerted by Orion OB1 ($\sim 10^{52}$ erg; Brown et al. 1995). The expansion of the superbubble is also traced through high-velocity (HV) and intermediate-velocity (IV) gas in several lines of sight toward Orion (Cowie et al. 1979; Welty et al. 2002). Soft X-rays emanate from the million-degree plasma in the interior of the superbubble (Burrows et al. 1993; Snowden et al. 1995).

Here, we present observations of recent all-sky surveys with *WISE* and *Planck*, and combine them with existing sky surveys to provide a new and more complete insight in the history and evolution of the Orion-Eridanus region. In particular, we will reveal that Barnard's Loop is part of a complete bubble structure, separate from the Orion-Eridanus superbubble, that sweeps up the mass-loaded interior of the pre-existing superbubble. It is argued that the Orion-Eridanus superbubble is larger and more complex than previously thought, and that the entire morphological appearance of the superbubble can be viewed as a series of nested shells, superimposed along the line of sight. The shells originate from explosive feedback from Orion OB1 that accelerates, sweeps up, and compresses the superbubble interior plasmas in an episodic fashion to form nested shells within the Orion-Eridanus superbubble. We explore the origin of the shells, their relation with the subgroups of Orion OB1, and their impact on the molecular clouds and star formation efficiency within Orion. We discuss our findings in terms of the long-term evolution of the superbubble. We present the observations in Sec. 5.2 and our results in Sec. 5.3. We discuss our findings in Sec. 5.4 and summarize in Sec. 5.5.

5.2 Observations

We made use of the all-sky surveys from *Planck* (Planck Collaboration et al. 2014c), the *Wide-field Infrared Explorer* (WISE; Wright et al. 2010), the Leiden/Argentina/Bonn survey of Galactic HI (LAB; Kalberla et al. 2005), the *ROSAT* soft X-ray background (ROSAT SXR; Snowden et al. 1997), and an all-sky $H\alpha$ map that combines several large-scale surveys (Finkbeiner 2003), including the Southern H-alpha Sky Survey Atlas (SHASSA; Gaustad et al. 2001), the Virginia-Tech Spectral-line Survey (VTSS; Dennison et al. 1998), and the Wisconsin $H\alpha$ Mapper (WHAM; Haffner et al. 2003).

5.3 Results

Figure 5.1 reveals the large-scale structure of the Orion-Eridanus superbubble. In $H\alpha$, the region exhibits various filamentary structures, including Barnard’s Loop (Barnard 1894) and the Eridanus filaments (e.g., Pon et al. 2014b). Projected on top of Barnard’s Loop are the Orion A and Orion B molecular clouds (OMC A and OMC B), the Orion Nebula cluster (ONC) associated with the Orion Nebula, and the IC 434 emission nebula that is characterized by a champagne flow of ionized gas (Tenorio-Tagle 1979; Sec. 5.3.3). Another prominent feature is the λ Orionis bubble, a 10° circular H II region, encapsulated by a swept-up shell of gas and dust. Below we refer to different parts of the superbubble in R.A./decl. space (see the orientation in Fig. 5.1).

Figure 5.2 shows cross-cuts through the Orion-Eridanus superbubble, revealing the gas- and dust structures of the superbubble and its interior components. Note that Barnard’s Loop peaks dramatically in the ionized gas, while in the dust and neutral hydrogen it is only seen as a modest increase in the *Planck*, *WISE*, and LAB channels (Fig. 5.2(a)-(c)). At this point, we find no evidence that a dense shell encapsulates the ionized portion of Barnard’s Loop, whose presence was predicted by Cowie et al. (1979) (Sec. 5.4). In contrast, the cross-cut shown in Fig. 5.2d that traces the western bubble shell at high latitudes reveals a stratified structure, where a dust/H I shell is clearly observed to encapsulate the Eridanus C filament. The absence of an H I shell associated with Barnard’s Loop is surprising and encouraged us to investigate the gas- and dust content of Barnard’s Loop and the Orion-Eridanus superbubble in more detail; our findings are presented in the next sections.

5.3.1 Dust in Barnard’s Loop

Optical depth

Heiles et al. (2000) defined two small regions of Barnard’s Loop that are clear of any dense molecular clouds along the line of sight; we use the same apertures in the following analysis (‘BL_{top}’ and ‘BL_{bot}’; Fig. 5.1) to characterize the dust contained in Barnard’s Loop. The distance toward Barnard’s Loop is uncertain; here, we will assume that Barnard’s Loop lies at the distance of the Orion Nebula (400 pc; Menten et al. 2007; Sandstrom et al. 2007). Electron densities inside Barnard’s Loop are estimated at $n_e = 2.0 \text{ cm}^{-3}$ (Heiles et al. 2000), and at $n_e = 3.2 \text{ cm}^{-3}$ from the surface brightness of the $H\beta$ line (O’Dell et al. 2011). A similar analysis of the $H\alpha$ surface brightness here leads to $n_e = 3.4 \text{ cm}^{-3}$, after correcting for limb brightening (a factor 7; O’Dell et al. 2011) of a constant density shell with an apparent radial thickness of 1° , which amounts to 7 pc at the distance of 400 pc.

Using $n_e = 3.4 \text{ cm}^{-3}$ and a radial thickness of 7 pc, adopting a normal gas-to-dust ratio of $N_H/A_V = 1.9 \times 10^{21} \text{ cm}^{-2} \text{ magnitude}^{-1}$ (Bohlin et al. 1978), where N_H is the column density of hydrogen and A_V the visual extinction, and a UV-to-visual dust absorption ratio of 1.8 (Tielens & Hollenbach 1985), the radial dust optical depth for UV photons with energies between 6 and 13.6 eV is $\tau_{UV} = 0.07$.

Through a modified-blackbody fit to the *Planck* data, the *Planck* R1.20 dust model provides all-sky maps of dust optical depth (at 353 GHz), temperature, spectral index, and the total dust emission integrated over frequency. We obtain an observed optical depth of Barnard’s Loop at 353 GHz, $\tau_{353,\text{obs}}$, by correcting the value of the optical depth

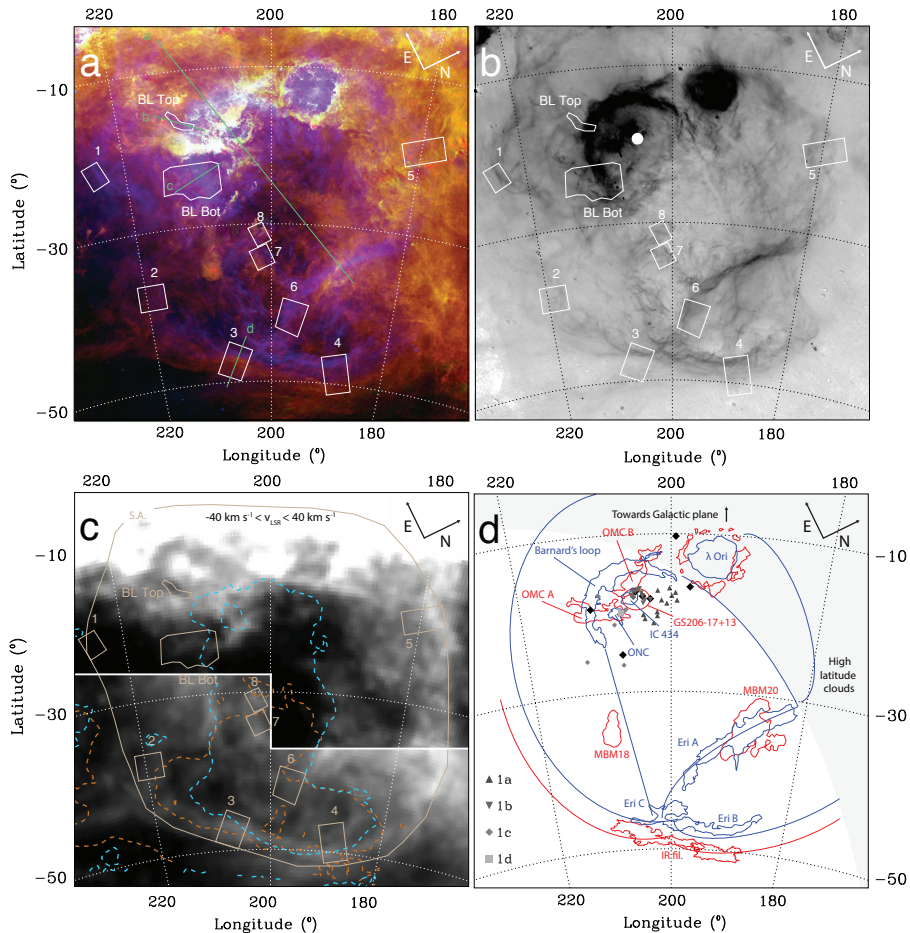


Figure 5.1: (a) Three-color image of the Orion-Eridanus superbubble. H α (blue) reveals ionized gas, surrounded by a layer of PAHs or stochastically heated small grains, traced by the WISE 12 μ m band (green). Red is *Planck* 353 GHz that probes cold (20 K) dust. The PAHs/small grains trace the UV-illuminated edges of clouds of cold dust so that red and green blend to form yellow. To the northeast lies the Galactic plane, while to the northwest lie high-latitude clouds (e.g., Schlafly et al. 2014). The numbered boxes define the apertures discussed in Sec. 5.3.2; the light-green solid lines are cross-cuts used in Fig. 5.2. (b) Same as panel (a), but only showing H α emission. The white dot marks the flux-weighted center of the H α bubble (Reynolds & Ogden 1979). (c) LAB -40 km s $^{-1}$ $< v_{\text{LSR}} < 40$ km s $^{-1}$ HI emission (Brown et al. 1995). Overlaid are contours of *ROSAT* 0.25 keV (orange dashed) and *ROSAT* 0.75 keV diffuse X-rays (light blue dashed). The 0.75 keV emission projected in Barnard's Loop originates from the ONC and IC 434 regions, but is blended with diffuse emission from the superbubble. The white solid line marks a different scaling to accentuate the faint HI filament intersecting apertures 2-4. Also plotted is the shape of the superbubble aperture (S.A.; see text) (d) Schematic representation of the region. H α gas structures are shown in blue lines/contours; dust structures are plotted in red. The solid lines trace faint filaments of the region to guide the eye in panels (a) & (b). Black diamonds are the stars that form the constellation of Orion. Members of Orion OB1 (Blaauw 1964; Brown et al. 1994) with spectral type B2 or earlier are shown in different grey symbols shown by the legend. See text for the different abbreviations.

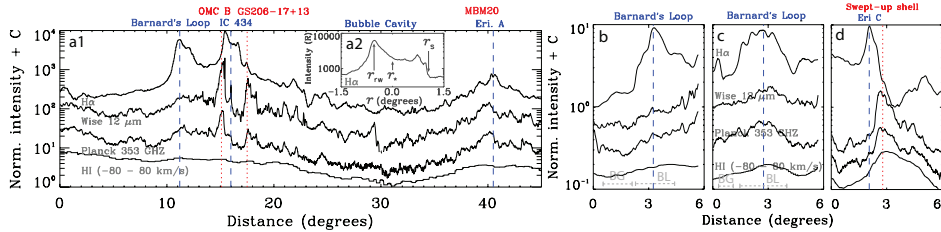


Figure 5.2: Profiles of cross-cuts defined in Fig 5.1a. Cuts start at the labelled side in Fig. 5.1a. **(a1)** Along the cut from left to right: Barnard’s loop; the Orion B molecular cloud (OMC B) and the IC 434 emission nebula, the GS206-17+13 shell; the excavated bubble interior; and the MBM 20 high-latitude cloud, overlapping the Eri A $H\alpha$ filament. The dashed vertical lines highlight several prominent features seen in the gas (blue) and in dust (red). **(a2)** Inset of the IC 434 emission nebula $H\alpha$ profile, plotted as intensity (in units of Rayleigh) as a function of distance from the ionizing star r (in degrees). The emission profile exhibits the structure of a champagne flow of ionized gas (Tenorio-Tagle 1979). We have marked the location of the ionizing star, σ Ori (r_*), the shock front (r_s), and the rarefaction wave (r_{rw}). See Sec. 5.3.3 for a full description of the champagne flow structure. **(b & c)** Cuts through Barnard’s loop (BL_{top} and BL_{bot}; Heiles et al. 2000), revealing a single peak most prominently seen in $H\alpha$. The dashed lines on the bottom define the bins where the mean optical depth at 353 GHz, $\tau_{353,obs}$, from the *Planck* dust model R1.20 (Planck Collaboration et al. 2014a) is measured (see text): ‘BL’ is the bin for Barnard’s Loop, ‘BG’ is the bin for the background determination. **(d)** Cut through the western edge of the superbubble, coincident with the Eri C filament. Here, the gas and dust reveal a stratified structure, where the ionized gas peaks inside the dust shell.

from the Planck model at the location of Barnard’s Loop for a background value. For this method we use the bins defined in Figs. 5.2b&c: as Barnard’s Loop is not encapsulated by a dense shell (Fig. 5.2 and Sec. 5.3.2), we determine the background in a region just outside of the ionized portion of Barnard’s Loop (which is significant: $\sim 60\%$ of the total value for both regions). In this way, we isolate the dust grains contained within the ionized part of Barnard’s Loop. Then, the *observed* optical depths are $\tau_{353,obs} = 9.0 \times 10^{-6}$ (for BL_{top}) and $\tau_{353,obs} = 5.1 \times 10^{-6}$ (BL_{bot}). We can compare this to the *expected* optical depth, $\tau_{353,cal}$, from the density (3.4 cm^{-3}), estimated line-of-sight depth (45 pc for a 1° thickness) and the opacity at 353 GHz ($\sigma_\nu = 7.9 \times 10^{-27} \text{ cm}^2 \text{ H}^{-1}$) appropriate for the diffuse ISM (Planck Collaboration et al. 2014a). We calculate $\tau_{353,cal} = 4.0 \times 10^{-6}$, in close agreement with $\tau_{353,obs}$, which implies that dust mixed with the ionized shell of Barnard’s Loop is alike to dust seen in the diffuse ISM.

Temperature

Heiles et al. (2000) concluded that grain temperatures in Barnard’s Loop are higher than in HI regions, and proposed that $Ly\alpha$ photons might contribute to the heating of the dust. However, direct heating from the radiation field of Orion OB1 was not considered in their study. We derive an intensity of $G_0 = 14$ reaching Barnard’s Loop in units of the Habing field (Habing 1968), taking into account the radiation from the 7 most massive stars in Orion OB (θ Ori C, δ Ori, ι Ori, θ Ori A, σ Ori, ϵ Ori, ζ Ori), using stellar parameters from Martins et al. (2005a). However, O’Dell (2001) shows that radiation from the Orion

Nebula (θ Ori C and θ Ori A) might not reach Barnard’s Loop, as the nebula is optically thick to ionizing radiation in all directions, except possibly to the southwest. This would decrease G_0 to 11.

The observed dust temperatures from the *Planck* model in BL_{top} and BL_{bot} are $T_d = 18.7$ K and $T_d = 20.5$ K. These values are consistent with temperatures found by Heiles et al. (2000), $T_d = 19.6$ K and $T_d = 20.3$ K for BL_{top} and BL_{bot}, respectively, and the mean value $T_d = 19.7$ K for the entire sky (Planck Collaboration et al. 2014a), even though G_0 in BL is significantly raised above the average interstellar radiation field of the solar neighborhood (= 1.7 Habing field; Tielens 2005). For comparison, at $G_0 = 14$ a ‘typical’ $0.1 \mu\text{m}$ silicate (graphite) grain would be heated toward $T_d = 19.2$ (22.5) K (Tielens 2005). At $G_0 = 11$, this would be $T_d = 18.6$ (21.8) K. In this respect, Planck Collaboration et al. (2014a) and Planck Collaboration et al. (2014b) argue that observed dust temperatures do not simply trace the intensity of the radiation field, but in addition reflects changes in grain properties, such as the size distribution, grain structure, and material changes. In any case, for both BL_{top} and BL_{bot}, we do not see the necessity of an extra heating source to account for the observed grain temperatures, such as Ly α heating (Heiles et al. 2000).

5.3.2 Dust and gas in the Orion-Eridanus superbubble

Global observational characteristics

The all-sky surveys listed in Sec. 5.2 allow us to determine the global observational characteristics of the Orion-Eridanus superbubble, which is of potential use to the study of more distant superbubbles that lack the spatial information of the Orion-Eridanus region. We use apertures that encompass the entire superbubble, the OMCs, and Barnard’s Loop, respectively. For the OMCs and Barnard’s Loop, these apertures coincide with the outlines depicted in Fig. 5.1d. While the full extent of the Orion-Eridanus superbubble will be thoroughly discussed in the remainder of this paper, here we already choose the ‘entire superbubble aperture’ to encompass the majority of the H α emission observed in Fig. 5.1b, while tracing the outside of HI filaments seen at $-40 \text{ km s}^{-1} > v_{\text{LSR}} > 40 \text{ km s}^{-1}$ (Fig. 5.1c), corresponding to the velocity extent in which the Orion-Eridanus superbubble has previously been identified (Brown et al. 1995). We measure the H α luminosity and total far-IR to submillimeter luminosity contained within the apertures, which are compared with stellar parameters of Orion OB1.

For the entire superbubble, we proceed as follows. The north and east sides of the superbubble aperture extend close to the Galactic plane and high-latitude clouds. The encompassed IR emission will therefore be contaminated by emission along the line of sight not related to the superbubble. While disentangling the separate contributions to the IR is not straightforward, we attempt to isolate the emission from our region of interest by measuring the average far-IR integrated intensity, $I_{\text{IR,fil}}$, within the aperture labeled as ‘IR fil.’ (Fig. 5.1d), i.e., the dusty shell that encapsulates the limb-brightened Eridanus B and C filaments known to be associated with the superbubble. The intensities are taken from the *Planck* R1.20 dust model (Planck Collaboration et al. 2014a) that uses *IRAS* $100 \mu\text{m}$ and *Planck* 857, 545, and 353 GHz data to determine the total integrated far-IR intensity. Subsequently, we define emission from regions that are much brighter than observed in the limb-brightened filaments, i.e., $I_{\text{IR}} \geq 3I_{\text{IR,fil}}$, as *not* being part of the superbubble. This procedure provides a mask tracing the regions of high IR brightness toward the Galactic

plane, and high-latitude fore- and background clouds well. Note that this procedure filters out the emission from, e.g., the OMCs as well; we ultimately add the contributions of the OMC and Barnard’s Loop apertures to get the full IR intensity of the superbubble and the relative contributions of the components (see Tab. 5.1). For the $H\alpha$ map, the background contamination is much less severe and a masking procedure is not necessary. In this respect, we will argue below that all of the observed $H\alpha$ in Fig. 5.1b is caused by photo-ionization from Orion OB1.

While the masking procedure accounts for the high-IR intensities of contaminating clouds toward the Galactic plane, it does not correct for the diffuse low-level background observed over the entire images. Therefore, we apply a *global* background subtraction to both the far-IR and $H\alpha$ maps by measuring the background level within a circular region of 0.4 degree radius at $(l,b) = (229.6, -33.7)$ *outside* of the superbubble aperture that appears to be free of obvious emission features and provides a proper representation of the diffuse background emission averaged over latitude. For both maps, we do not include the λ Ori region in our analysis as it appears to be encircled by an ionization-bounded H II region (Warren & Hesser 1977; Wall et al. 1996), and can be regarded as being separated from Orion OB1.

Table 5.1 lists two different values of L_{IR} . The first value is obtained by filling the masked region with the average IR brightness from the unmasked part of the superbubble aperture. In this way, we get an estimate of the full IR intensity of the entire superbubble if it were unaffected by foreground or background emission along the line of sight. The second value is obtained by setting the masked part to zero, therefore neglecting the masked part of the superbubble. The choice of including or excluding the masked part of the superbubble affects the inferred luminosities from the OMC and Barnard’s Loop as well, as these apertures are completely immersed in the masked region of the image, and the chosen intensity of the masked region thus effectively acts as a “global” background for both regions. Below, we will include the masked region in our interpretations, as we believe that the inclusion of this part of the superbubble is essential to the analysis of the total energetics of the region. However, we refer the reader to Table 5.1 for the implications of this choice and its impact on the derived parameters. The total far-IR luminosity is $L_{\text{IR}} = 4\pi I_{\text{tot}} S$, where I_{tot} and S are the total integrated intensity and projected surface area of the emitting region, respectively. For simplicity, we assume that the entire bubble is located at 400 pc. The measured IR luminosity is compared with stellar parameters of Orion OB1 through $\xi_{\star} = L_{\text{IR}}/L_{\star}$, where L_{\star} is the total luminosity of the Orion OB region ($1.7 \times 10^6 L_{\odot}$, re-evaluated at $d = 400$ pc, and excluding λ Ori; Warren & Hesser 1977; Wall et al. 1996). The parameter ξ_{\star} defines the fraction of stellar radiation that is captured by the dust and re-emitted in the IR averaged over all solid angles.

The $\text{Ly}\alpha$ photon rate, $N_{\text{Ly}\alpha}$, is calculated by converting the observed $H\alpha$ photon rate to a $\text{Ly}\alpha$ photon rate using the ratio $\alpha_{\text{B}}/\alpha_{\text{H}\alpha}$, where $\alpha_{\text{H}\alpha}$ is the effective recombination coefficient of $H\alpha$ ($1.31 \times 10^{-13} \text{ cm}^3 \text{ s}^{-1}$ at $T = 6000$ K, which is the electron temperature in Barnard’s Loop and the Eridanus filaments from Heiles et al. 2000; O’Dell et al. 2011; Madsen et al. 2006, we use this value throughout the superbubble), and α_{B} is the total recombination coefficient of hydrogen to all levels but the ground state ($2.6 \times 10^{-13} \text{ cm}^{-3} \text{ s}^{-1}$; Osterbrock & Ferland 2006). Case B recombination requires that $N_{\text{Ly}\alpha}$ equals the total amount of recombinations, which is a quantity that can directly be compared to Orion OB1 through $\xi_{\text{ion}} = N_{\text{Ly}\alpha}/N_{\text{ion}}$, where N_{ion} is the total number of ionizing photons from

Region	T_d (K)	L_{IR} ($10^5 L_\odot$)	ξ_\star	$L_{\text{Ly}\alpha}$ ($10^5 L_\odot$)	ξ_{ion}
Superbubble	19.5	7.9 (5.7) ^(a)	0.47 (0.34)	1.08	0.94
OMC	17.9	2.8 (2.9)	0.16 (0.17)	0.16	0.14
Barnard's Loop	19.6	0.5 (0.6)	0.03 (0.04)	0.20	0.17

Table 5.1: Global observational characteristics of the Orion-Eridanus superbubble. Listed are: the dust temperature, T_d ; the infrared luminosity, L_{IR} ; fraction of L_{IR} to the total luminosity of Orion OB1, ξ_\star ; luminosity measured from $\text{H}\alpha$ and converted to $\text{Ly}\alpha$, $L_{\text{Ly}\alpha}$; fraction of $\text{Ly}\alpha$ photons to the total amount of ionizing photons of Orion OB1, ξ_{ion} . The values between brackets denote the values measured when the masked part of the superbubble is set to zero (see text).^(a): The total IR luminosity in the superbubble + OMC + Barnard's Loop apertures.

Orion OB1 (2.7×10^{49} ph s⁻¹, O'Dell et al. 2011). This ratio measures the fraction of ionizing photons captured by the gas and converted to $\text{Ly}\alpha$. In order to directly compare with the IR luminosity L_{IR} , we convert $N_{\text{Ly}\alpha}$ to a luminosity through $L_{\text{Ly}\alpha} = N_{\text{Ly}\alpha} h\nu_\alpha$, where $h\nu_\alpha$ is the $\text{Ly}\alpha$ photon energy, and define $L_{\text{ion}} = N_{\text{ion}} h\nu_\alpha$, such that $\xi_{\text{ion}} = N_{\text{Ly}\alpha}/N_{\text{ion}} = L_{\text{Ly}\alpha}/L_{\text{ion}}$.

The calculated luminosities, L_{IR} and $L_{\text{Ly}\alpha}$, are denoted in Tab. 5.1. Table 5.1 shows that half of the total amount of stellar radiation of Orion OB1 is trapped in the superbubble and re-radiated in the IR, $\xi_\star \sim 0.5$. The molecular clouds account for about 35% of the total IR emission of the superbubble; the contribution from Barnard's Loop is negligible. In contrast, ξ_{ion} of the OMC (0.14) and Barnard's Loop (0.17) are roughly similar, which is because the Orion Nebula and IC 434 emission nebula are currently breaking out of the molecular clouds (Sec. 5.3.3) and are contained within the OMC aperture. Eventually, all ionizing photons are absorbed within the superbubble aperture ($\xi_{\text{ion}} \sim 1$). This implies that, on average, Orion OB1 can provide the necessary ionizing power to illuminate the $\text{H}\alpha$ structures detected in Fig 5.1c, including the $\text{H}\alpha$ filaments that run along the outer edge of the superbubble aperture. Nonetheless, it is possible that individual small-scale structures may still be too bright given their size and distance from Orion OB1 (Pon et al. 2014b). Note that some of these filaments lie outside of what has previously been thought to be the edges of the Orion-Eridanus superbubble (Reynolds & Ogden 1979; Heiles et al. 1999; Bally 2008; Pon et al. 2014a). The dust temperatures measured inside the superbubble aperture and Barnard's Loop are similar to that observed for the entire diffuse sky by *Planck* (see discussion in Sec. 5.3.1). Inside the OMC, this value is somewhat lower, which is what is expected for dense regions (Planck Collaboration et al. 2014a).

Tracing the superbubble structure through dust and gas

To investigate the gas and dust content in specific regions throughout the Orion-Eridanus region, we use apertures depicted in Fig. 5.1 that are defined such that the majority of $\text{H}\alpha$ and far-IR emission from the regions are enclosed (for example, the stratified emission from the limb-brightened emission of the superbubble wall; Fig. 5.2d), while a low background level is ensured through comparison with the *Planck* and LAB maps (the $\text{H}\alpha$ emission does not show a high background in general). As the diffuse background emission varies significantly over the entire Orion-Eridanus region, here we use *local*

background values to properly measure the luminosities contained in the apertures scattered over the Orion-Eridanus region. For the apertures at $b > -30$ degrees, we define a background at $(l,b) = (233.2, -28.6)$ within a circle of 0.4 degree radius. For the apertures at $b < -30$ degrees, we define a background at $(l,b) = (221.9, -49.5)$. Region 5 is an exception to this rule, as the previously defined background levels were not representative of the local value because of its location amongst high-latitude clouds. For region 5, $(l,b) = (176.3, -15.0)$ was chosen.

Ly α photons will be resonantly scattered many times in the HII region because of its large line cross section, but eventually be absorbed by dust, contributing to the heating of the dust. The ratio of heating rate by stellar photons, Γ_{UV} , to Ly α photons, $\Gamma_{Ly\alpha}$, can be written as (Tielens 2005):

$$\frac{\Gamma_{UV}}{\Gamma_{Ly\alpha}} = \frac{\pi a^2 n_d \bar{Q}_{abs} L_\star}{4\pi r^2 n^2 \alpha_B h\nu_\alpha}. \quad (5.1)$$

Here, πa^2 and n_d are the geometrical cross-section and number density of the grains, respectively, \bar{Q}_{abs} is the average radiation absorption efficiency of the dust, L_\star is the total luminosity of Orion OB1, r is the distance to the source, and n is the hydrogen number density of the gas. Assuming equilibrium between photo-ionization and recombination, for a shell surrounding an empty cavity we have $f_{ion} N_{ion} = 4\pi r^2 n^2 \alpha_B \Delta r$, where f_{ion} is the fraction of incident ionizing photons available that are absorbed by the gas locally. Then, Eq. 5.1 reduces to

$$\frac{\Gamma_{UV}}{\Gamma_{Ly\alpha}} = \frac{\pi a^2 n_d \bar{Q}_{abs} \Delta r}{f_{ion}} \left(\frac{L_\star}{N_{ion} h\nu_\alpha} \right) = \frac{\tau_d}{f_{ion}} \left(\frac{L_\star}{N_{ion} h\nu_\alpha} \right), \quad (5.2)$$

where τ_d is the (radial) absorption optical depth of the shell. With $L_\star = 1.7 \times 10^6 L_\odot$ and $N_{ion} = 2.7 \times 10^{49} \text{ ph s}^{-1}$ (Sec. 5.3.2), we have $(L_\star/N_{ion} h\nu_\alpha) \approx 15$ for Orion OB1, and therefore the ratio $\Gamma_{UV}/\Gamma_{Ly\alpha}$ equals unity for $\tau_d/f_{ion} \approx 0.07$.

We can make a priori estimates of f_{ion} for the regions defined in Fig. 5.1. For Barnard's Loop, we have measured an average $\xi_{ion} = 0.17$ over the entire structure (Table 5.1). A factor of 0.50 would be expected for a half-sphere geometry if Barnard's Loop were optically thick to ionizing photons. Possibly, a fraction of the ionizing photons from Orion OB1 is trapped within the OMCs before reaching Barnard's Loop, which would lead to $\xi_{ion,BL} = 0.50 - \xi_{ion,OMC} = 0.36$ (Table 5.1). Still, these numbers reveal that 50% - 66% of the ionizing photons pass through the half sphere encompassing Barnard's Loop. Hence, we estimate that f_{ion} is in the range $\sim 0.33 - 0.50$ for the Barnard's Loop apertures BL_{bot} and BL_{top}. The fact that Barnard's Loop is optically thin for the ionizing flux of Orion OB1 can also be inferred from the morphological appearance of the cometary clouds L1617 and L1622, which are located behind Barnard's Loop as measured from the Orion OB association and have sharp I-fronts on their sides facing the Belt stars (Bally et al. 2009). We note that the internal structure of Barnard's Loop may be more complex than that of a homogeneously distributed half-sphere assumed here. A patchy structure containing optically thick clumps ($f_{ion} \sim 1$) and holes through which the photons would leak unhindered ($f_{ion} \sim 0$) could, in principle, lead, on average, to an f_{ion} of order 0.33 - 0.50. However, Barnard's Loop, similar to region 1 and region 6, is not associated with H I. The remaining regions are associated with neutral hydrogen, where f_{ion} will be of

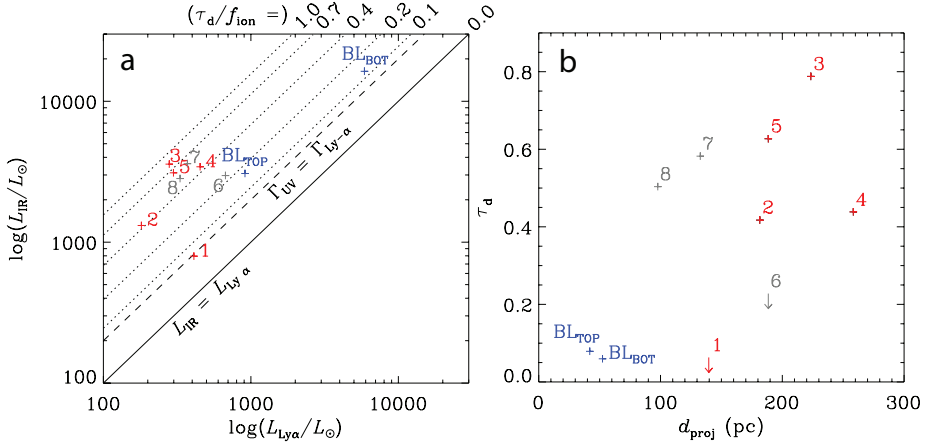


Figure 5.3: Apertures tracing the structure of the Orion-Eridanus superbubble. **(a)** Infrared versus Ly α luminosities measured in the apertures shown in Fig. 5.1. The solid line shows where the infrared and Ly α luminosities are equal. The lower dashed line shows where the infrared and Ly α heating rates are equal, corresponding to $\tau_d/f_{\text{ion}} = 0.07$ (see text), where τ_d is the dust optical depth at UV wavelengths and f_{ion} is the fraction of ionizing photons available absorbed by the gas. The dotted lines are similar, but for increasing τ_d . Overplotted are the luminosities measured in the apertures drawn in Fig. 5.1, color-coded as follows: regions 1-5 (red) are positioned along the projected outer shell of the superbubble aperture (Fig. 5.1c); Barnard’s loop (BL_{TOP} and BL_{BOT}) (blue); region 6 - and 8 (gray) are the Eridanus A filament and molecular clouds close to the Orion OB association. **(b)** The radial dust optical depth at UV wavelengths versus the projected distance toward the H α flux-weighted center of the superbubble.

order ~ 1 because of the small mean free path of ionizing photons through H I (Tielens 2005).

We measure both L_{IR} and $L_{\text{Ly}\alpha}$ within the apertures shown in Fig. 5.1 and compare these measurements with luminosities from Orion OB1. The structures contained in each defined aperture will subtend a solid angle Ω as measured from Orion OB1. Now, any ionizing photon that is absorbed by hydrogen and converted to Ly α will eventually contribute to the heating of the dust and, therefore, the total IR luminosity that emanates from each region can be written as

$$L_{\text{IR}} = L_{\text{UV}} + L_{\text{Ly}\alpha} = \tau_d L_{\star} \Omega_{\text{UV}} + f_{\text{ion}} N_{\text{ion}} h\nu_{\alpha} \Omega_{\text{Ly}\alpha}, \quad (5.3)$$

where L_{UV} is the dust luminosity provided by direct absorption of stellar photons. In the classical picture of an expanding superbubble, a dense, neutral shell will wrap around the 10^4 K region created by the reverse shock traced by bright H α emission (Weaver et al. 1977). Therefore, we can assume that the IR and H α trace structures that measure the same solid angle with respect to Orion OB1, $\Omega_{\text{UV}} = \Omega_{\text{Ly}\alpha}$, and we can write

$$\frac{(L_{\text{IR}}/L_{\star})}{(L_{\text{Ly}\alpha}/L_{\text{ion}})} = \frac{\tau_d}{f_{\text{ion}}} + \left(\frac{N_{\text{ion}} h\nu_{\alpha}}{L_{\star}} \right), \quad (5.4)$$

which describes the ratio between the amount of energy that is captured by the dust

and re-emitted in the IR, to the amount of energy that is captured by the gas and converted to Ly α .

Our results are shown in Fig. 5.3. All studied regions show $L_{\text{IR}} > L_{\text{Ly}\alpha}$ (Fig. 5.3a), which reveals that a (substantial) amount of stellar radiation is directly absorbed by the dust. Here we note that $L_{\text{IR}} = 2L_{\text{Ly}\alpha}$ when $\Gamma_{\text{UV}} = \Gamma_{\text{Ly}\alpha}$ (cf. Eq. 5.3). An interesting trend can be seen from Fig. 5.3a. The regions 2 - 5, positioned on filamentary structures seen in gas and dust along the outside of the superbubble aperture depicted in Fig. 5.1, reveal significantly higher fractions of $\tau_{\text{d}}/f_{\text{ion}}$ compared to the regions located in Barnard's Loop (BL_{bot}, BL_{top}). This implies that stellar photons, provided by Orion OB1 (Sec. 5.3.2), are more efficiently absorbed in regions 2 - 5 compared to those in Barnard's Loop. In other words, the dust optical depth for stellar photons associated with Barnard's Loop is very small. In Fig. 5.3b, we rewrite Eq. 5.4 for $\tau_{\text{d}}/f_{\text{ion}}$ and, together with our estimations for f_{ion} as described above, plot the derived dust optical depth in the regions as a function of projected distance d_{proj} from $(l,b) = (206.5,-18.0)$, the flux-weighted center of the bubble as measured from the H α emission (see Fig. 5.1b; Reynolds & Ogden 1979). We exclude λ Ori as it seems to be encircled by an ionization-bounded H II region. Still, in Sec. 5.3.3 we will show that the ionized gas in the λ Ori region exhibits the characteristics of a champagne flow (Tenorio-Tagle 1979), in which case the H II region will be density bounded on the side of the outward champagne flow, and radiation will likely be able to escape the region. However, the circular morphology of the λ Ori bubble detected in H α (Fig. 5.4) reveals that the champagne phase, if present, may not have fully developed (Sec. 5.3.3) and, therefore we will assume that the λ Ori H II region is still ionization bounded.

For the BL apertures, we plot the results for τ_{d} versus d_{proj} assuming $f_{\text{ion}} = 0.5$ (Sec. 5.3.2). For regions 1 and 6, the absence of a clear neutral HI filament prohibited us from predicting f_{ion} , and only an upper limit to τ_{d} is given. The results plotted in Fig. 5.3b, albeit suffering from low-number statistics, indicate a trend where τ_{d} rises with increasing d_{proj} .

From Fig. 5.3, it becomes apparent that dust associated with Barnard's loop is not able to capture all of the radiation emitted by the Orion OB1 association. In this context, the bright H α filament to the southeast that surrounds Barnard's Loop, from region 1 up to the Galactic plane (Fig. 5.1), is lit up by ionizing photons breaking through Barnard's Loop. A straight line from the flux-weighted center of the superbubble (Fig. 5.1), through Barnard's Loop to the outer filament in region 1, reveals a flux ratio of $F_{\text{BL}}/F_{\text{reg.1}} \sim 5$, where F_{BL} and $F_{\text{reg.1}}$ are the measured peak H α fluxes in Barnard's Loop and the outer filament in region 1, respectively. At a distance ratio of $d_{\text{BL}}/d_{\text{reg.1}} \sim 2.5$, this is consistent with both the structures absorbing a similar amount of ionizing photons, confirming $f_{\text{ion}} \sim 0.5$ for the Barnard's Loop apertures as was assumed in our derivations of τ_{d} above.

As a sanity check to our methodology, we also plot in Fig. 5.3 the results for region 6 (corresponding to the southern end of the Eri A filament), which reveals low τ_{d} compared to the other Eridanus filaments. However, the association of the Eridanus A filament with the superbubble is still controversial and is discussed thoroughly in Pon et al. (2014b). For completeness, we show the results for apertures located on the G203-37 and GS204-31 clouds (region 7 & 8) which are thought to be *inside* and at the near-side of the Orion-Eridanus superbubble (Snowden et al. 1995). The clouds are highly opaque to 0.25 keV radiation with intervening hydrogen column densities of $\sim 8 \times 10^{20}$ cm² (Snowden et al.

1995), translating to an optical depth at UV wavelength of $\tau_{UV} \sim 0.8$ using the relations given in Sec. 5.3.1, in rough agreement with our measurements shown in Fig. 5.3.

With $f_{ion} = 0.5$ for the Barnard’s Loop apertures, the dust optical depth as measured from the IR ($\tau_d = 0.06$ and $\tau_d = 0.08$ for BL_{top} and BL_{bot} , respectively; Fig. 5.3a & b) is in agreement with a homogeneous shell containing dust similar to that seen in the diffuse ISM ($\tau_{UV} = 0.07$; Sec. 5.3.1). Finally, we note that while $Ly\alpha$ contributes about 25-50% of the total energy absorbed by dust in Barnard’s Loop (Fig. 5.3a), this will have little effect on the dust temperature (Sec. 5.3.1) as T_d only weakly depends on the heating rate. In particular, $T_d \propto (\Gamma_{UV} + \Gamma_{Ly\alpha})^{1/6}$ for silicate grains (Tielens 2005).

5.3.3 Expanding shells within the Orion-Eridanus region

High- and intermediate velocity gas

The presence of HV absorption features of ionized gas between $-120 \text{ km s}^{-1} \lesssim v_{LSR} \lesssim -80 \text{ km s}^{-1}$ was detected in multiple lines of sight toward Orion (Cowie et al. 1979; Welty et al. 2002). In addition, IV features were detected between $-80 \text{ km s}^{-1} \lesssim v_{LSR} \lesssim -20 \text{ km s}^{-1}$ (Cowie & York 1978; Cowie et al. 1979; Huang et al. 1995; Welty et al. 2002). Both components show similar depletions, ion ratios, and physical conditions, albeit the IV gas contains column densities that exceed that of the HV gas by a factor of 3 (e.g., Welty et al. 2002). The HV gas, dubbed by Cowie et al. (1979) as “Orion’s Cloak”, has an angular diameter of at least 15° and is ascribed to a recent SN that, from its dynamical expansion scale, should have occurred some 3×10^5 yr ago.

Figure 5.4 shows $H\alpha$ velocity maps from the WHAM $H\alpha$ spectral survey (Haffner et al. 2003) of the Orion-Eridanus superbubble, covering the velocity space between $-80 \text{ km s}^{-1} \lesssim v_{LSR} \lesssim +80 \text{ km s}^{-1}$. Overplotted are sightlines from absorption line studies (Cowie & York 1978; Cowie et al. 1979; Huang et al. 1995; Welty et al. 2002). The HV and IV gas trace structures around Barnard’s Loop and the λ Ori ring that extend outside of the traditional limits of the Orion-Eridanus superbubble (Reynolds & Ogden 1979; Heiles et al. 1999; Bally 2008; Pon et al. 2014a), as demonstrated by the sightlines of κ Ori, λ Ori, and λ Eri. While it must be recognized that the distribution of the gases are somewhat patchy (Cowie et al. 1979), it is clear that the IV and HV gas trace two distinct components. Moreover, the HV gas seems to be confined to a more limited area compared to the IV gas, as reflected by the sightlines that show *only* the IV gas.

We note upfront that electron temperatures within Barnard’s Loop and λ Ori are determined at $\sim 6000 - 7500 \text{ K}$ (Reich 1978; Heiles et al. 2000; O’Dell et al. 2011; Madsen et al. 2006) which excludes that the HV gas originates from high-velocity wings of a thermal Gaussian line profile (the thermal broadening can be estimated with $\sqrt{2kT/m_H} \sim 10 \text{ km s}^{-1}$, where k is Boltzmann’s constant and m_H is the mass of a hydrogen atom). The velocity information of the Eridanus filaments are discussed in Pon et al. (2014b). Of particular interest here are the encircled regions toward the east of the superbubble, covering the Barnard’s Loop region and the λ Ori region, as well as smaller-scale bubbles.

Barnard’s Loop bubble

The intensity peak of Barnard’s Loop lies between $-20 \text{ km s}^{-1} \lesssim v_{LSR} \lesssim +20 \text{ km s}^{-1}$, but the structure is visible throughout the entire velocity space covered by the WHAM survey.

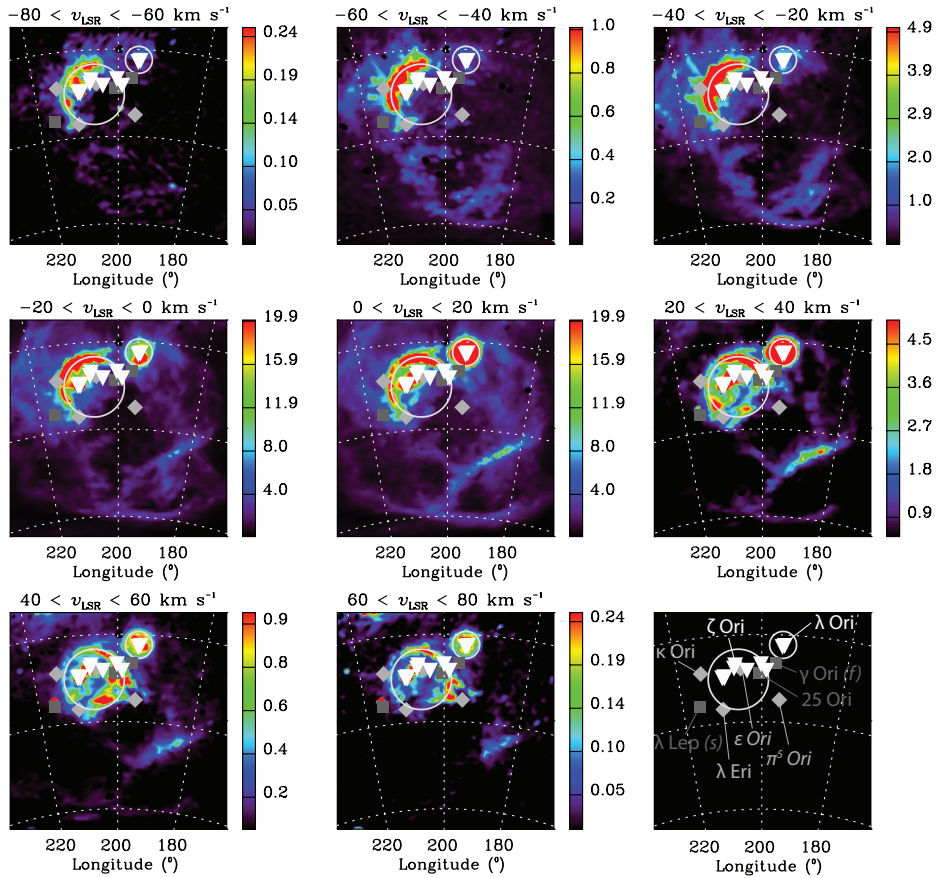


Figure 5.4: WHAM H α observations of the Orion-Eridanus superbubble. Shown are color-coded intensity maps (in units of Rayleigh) integrated over a velocity range in v_{LSR} that is indicated on top of each panel. Note the different scaling of each individual panel. Overplotted are lines of sight from absorption line studies (Cowie & York 1978; Cowie et al. 1979; Huang et al. 1995; Welty et al. 2002) that show *both* high-velocity and intermediate-velocity gas (*inverted triangles*), lines of sight that show *only* intermediate-velocity gas (*diamonds*), and lines of sight that do not show a clear detection of high-velocity or intermediate-velocity gas (*squares*). The classes are plotted in different gray scalings to make them discernable, and explicitly labeled are some stars in the lower right panel for orientation. The stars π^5 Ori and ϵ Ori are denoted in italics as observations only covered velocities of $|v_{\text{LSR}}| < 60 \text{ km s}^{-1}$ and $|v_{\text{LSR}}| < 100 \text{ km s}^{-1}$, respectively (Cowie et al. 1979). Measurements of HV/IV gas in λ Lep are hindered (Cowie et al. 1979) because of stellar rotation (*s*), while γ Ori lies at 77 pc (van Leeuwen 2007) and may trace foreground gas (*f*).

Here, we reveal the presence of an ionized filament, visible *only* at positive velocities $v_{\text{LSR}} > +20 \text{ km s}^{-1}$. This filament appears to form a complete bubble structure together with the bright crescent of Barnard’s Loop, centered on $(l,b) = (193,-20)$ with radius 14° . The lines of sight covered by the absorption survey of Cowie et al. (1979) indicate that the HV gas originates from the encircled H α bubble structure, or the ‘Barnard’s Loop Bubble’ (Fig.

5.4), suggesting a connection between both components. Cowie et al. (1979) estimated the size of Orion's Cloak at a minimum of 15 degrees that matches the size of the Barnard's Loop bubble. Thus, the Barnard's Loop bubble may well be part of the supernova remnant (SNR) associated with Orion's Cloak.

The most pronounced radial velocity effects are expected to originate from the center of an expanding bubble. For the HV gas, these velocities lie outside of the velocity range covered by the WHAM survey ($-80 \text{ km s}^{-1} \lesssim v_{\text{LSR}} \lesssim 80 \text{ km s}^{-1}$; Haffner et al. 2003), rendering WHAM unable to pick up the HV gas detected by *Copernicus* (Cowie et al. 1979) and the *Hubble Space Telescope* (Welty et al. 2002), although it is questionable whether WHAM would be able to pick up the low surface brightness of the HV gas expected in $\text{H}\alpha$ ($\sim 3 \times 10^{-3}$ Rayleigh; Cowie et al. 1979). The OMCs are roughly centered on $v_{\text{LSR}} = 10 \text{ km s}^{-1}$ in velocity space (Wilson et al. 2005); if we assume a systemic velocity toward the Orion region of $v_{\text{LSR}} = 10 \text{ km s}^{-1}$ and connect the HV gas with the expansion of the Barnard's Loop bubble, we estimate its expansion velocity at $v_{\text{exp}} = 100 \text{ km s}^{-1}$. However, it is not clear how much of the mass within the Barnard's Loop bubble (Sec. 5.4.3) is associated with this expansion velocity. The coverage of sightlines of the Orion-Eridanus region is limited, and the HV gas could in principle trace small, high-velocity components related to the Barnard's Loop bubble, rather than tracing the bulk expansion of the bubble itself. Here we implicitly assume that the bulk of the gas in the expanding shell is expanding at the adopted expansion velocity. The preshock densities for the HV gas toward ζ Ori ($n_0 = 3 \times 10^{-3} \text{ cm}^{-3}$; Welty et al. 2002) then implies that the bubble expands either into the Hot Intercloud Medium (HIM; $T \sim 10^6 \text{ K}$, $n \sim 3 \times 10^{-3} \text{ cm}^{-3}$) that pervades the Galactic Halo, or a pre-existing cavity, such as the superbubble interior. We defer a thorough discussion of the Barnard's Loop bubble and its connection to the HV gas to Sec. 5.4.

λ Ori bubble

The circular-symmetric H II region surrounding λ Ori has been known for a long time. Through a study of the star formation history of the λ Ori region, Dolan & Mathieu (1999) hypothesized that about 1 Myr ago, a supernova disrupted the parent molecular cloud and created the giant H II region seen to date, which is maintained by the remaining population of massive stars in the region. The expansion velocity of the H II region is traced by observations of the dense molecular shell surrounding the ionized gas, and is estimated at $v_{\text{exp}} = 16.5 \text{ km s}^{-1}$ expanding from the point $(l, b) = (195.8, -12.1)$ centered at $v_{\text{LSR}} = 3.8 \text{ km s}^{-1}$ in velocity space (Lang & Mashed 1998).

The main ionizing star λ Ori lies right at the (projected) heart of the bubble, which seems inconsistent with its proper motion ($\mu_{\alpha} \cos \delta = -0.34 \pm 0.60 \text{ mas}$ and $\mu_{\delta} = -2.94 \pm 0.33 \text{ mas}$, van Leeuwen 2007) with respect to the dense, molecular shell (Maddalena & Morris 1987; Lang & Mashed 1998). We calculate the LSR space velocity of λ Ori following the method described in Cox et al. (2012), using its proper motion (van Leeuwen 2007), radial velocity ($v_{\text{rad}} = 30.1 \text{ km s}^{-1}$; Gontcharov 2006), while correcting for the solar motion using parameters from Coşkunoğlu et al. (2011). We adopt a distance of 450 pc to the star (Dolan & Mathieu 2001). The calculated space motion of λ Ori is $v_{\text{rad}} = 18.2 \text{ km s}^{-1}$ with a position angle of 330 degrees (from north to east) inclined by 55 degrees in the plane of the sky. The trajectory is overplotted in Fig. 5.5, and reveals that it is unlikely

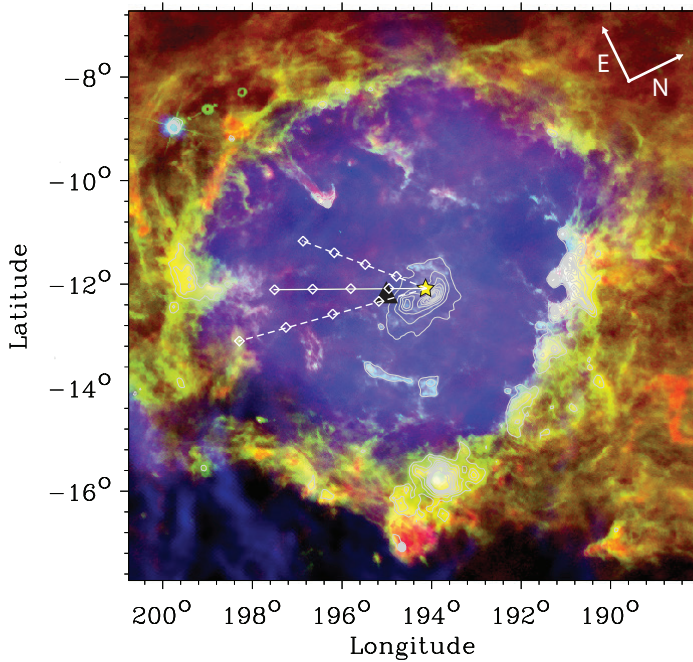


Figure 5.5: Three-color image of the λ Ori bubble. The color codes are the same as Fig. 5.1a. Overlaid are contours of IRAS $60\ \mu\text{m}$, with intensity levels: 100% (maximum intensity) - 90% - 80% - 70% - 60% - 50% - 40% - 30%. The solid line marks the past trajectory of the star λ Ori during 4 Myr given its current space motion. Open diamond symbols mark intervals of 1 Myr. The dashed lines are the extremes of possible space motion considering the errors in proper motion and distance to the star. The black triangle marks the center of expansion of the λ Ori bubble (Lang & Mashedier 1998).

that its current motion has been imparted at birth, since λ Ori would have then originated at the boundary between the molecular and ionized gas (the expected age of λ Ori is ~ 3 - 5 Myr; see Hernández et al. 2010, and references therein). However, its motion and distance from the center of expansion (Fig. 5.5) is consistent with the SN hypothesis that would have launched λ Ori on its current trajectory about 1 Myr ago.

We recognize the arc-shaped mid-infrared emission around λ Ori, which is the telltale signature of a dust wave, created by the interaction of dust entrained in a champagne flow with radiation pressure from the star, which is a common phenomenon inside interstellar bubbles (Ochsendorf et al. 2014a,b). Indeed, the radio continuum maps presented by Reich (1978) reveal an emission gradient within the ionized gas that is expected for a champagne flow (Tenorio-Tagle 1979). The emission gradient and the location of the dust wave reveals that the interior of the λ Ori bubble is venting into the surrounding medium toward the southeast. However, the overall distribution of the ionized gas is still roughly spherical (Fig. 5.4); an extended emission region that would accompany a developed H II region champagne flow is not detected. This may indicate that the champagne phase has just commenced and the bubble is on the verge of breaking out. The implications of these

observations shall be addressed in Sec. 5.4.3.

The WHAM observations in Fig. 5.4 reveal that the λ Ori H II region lights up at positive v_{LSR} (Fig. 5.4), extending longward of $v_{\text{LSR}} > 80 \text{ km s}^{-1}$. In addition, elevated emission surrounding the λ Ori region can be seen at the other velocity extreme of WHAM, i.e., $-80 \text{ km s}^{-1} \lesssim v_{\text{LSR}} \lesssim -60 \text{ km s}^{-1}$, possibly tracing the same component from Cowie et al. (1979), who detected faint HV gas features toward λ Ori. The FWHM of the H α line in the λ Ori region is $\sim 80 \text{ km s}^{-1}$, much broader than the thermal line width ($\sim 10 \text{ km s}^{-1}$; Sec. 5.3.3). Thus, both the HV gas and H α suggest higher velocities than that observed expansion velocity of the molecular shell ($v_{\text{exp}} = 16.5 \text{ km s}^{-1}$; Lang & Mashedier 1998). The discrepancy between velocities observed for the dense molecular ring and the ionized gas could indicate a fast blister flow (see above) which can lead to large line-of-sight variations, or a recent explosive event that has accelerated the gas in the bubble interior but has not yet coupled to the dense molecular ring.

GS206-17+13 and the Orion Nebula

Besides the obvious large-scale shells that are associated with Barnard's Loop and λ Ori, we note that the Orion complex harbors shell structures on all detectable scales. Below, we will discuss the degree-sized GS206-17+13 shell (Ehlerová & Palouš 2005) and the shell surrounding the Orion Nebula (O'Dell 2001; Güdel et al. 2008), but on even smaller scales there have been detections of many regions within the Orion A cloud that appear to have shell-like structures, presumably driven by H II regions from massive young stellar objects (Bally et al. 1987; Heyer et al. 1992). Both GS206-17+13 and the Orion Nebula emit at positive v_{LSR} (Fig. 5.4) with large line widths (FWHM $\sim 70 \text{ km s}^{-1}$) that can both be related to ionized (blister) flows as described below.

Ochsendorf & Tielens (2015) discussed the GS206-17+13 shell which is directly adjacent to the OMC B, has dimensions of $2^\circ \times 4^\circ$ ($14 \times 28 \text{ pc}$), and is approximately centered on the σ Ori star cluster. The formation of the shell is likely caused by the stellar winds of the Orion OB1b subgroup that formed the protrusion out of the OMC B. The bright H II emission that is projected inside part of the shell (the IC 434 emission nebula) is not related to the formation or history of GS206-17+13, as this gas originates from the champagne flow driven by the ionizing flux of the σ Ori cluster that has entered the pre-existing bubble cavity and is now approaching OMC B (Ochsendorf & Tielens 2015). Ionization of the cloud edge sets up a pressure discontinuity between the cloud and inter-cloud medium, and drives a shock front into the low-density bubble, while a rarefaction wave travels into the OMC B cloud. In panel 2a of Fig. 5.2, the shock front is visible at r_s , whereas the rarefaction wave is located at r_{rw} . Between the shock fronts, a champagne flow of ionized gas is set up (Tenorio-Tagle 1979), flowing from r_{rw} toward r_s .

The density structure of the champagne flow of the IC 434 region is well-characterized by an exponential density gradient (Ochsendorf & Tielens 2015), reaching from $n_{\text{H}} = 35 \text{ cm}^{-3}$ at the IF on the OMC B cloud surface, to 3.5 cm^{-3} at the location of σ Ori (r_* ; Fig. 5.2) where the flow reaches $\sim 30 \text{ km s}^{-1}$ (Mach number $\mathcal{M} \simeq 3$ for a 10^4 K gas), which is the typical maximum velocity reached for champagne flows (Tenorio-Tagle 1979). Therefore, the ionized gas will not accelerate much further (also reflected by the flattening of the emission profile behind r_* ; Fig. 5.2) and the density in the flow remains roughly similar up until the shock front, i.e., $\rho_1 \simeq 3.5 \text{ cm}^{-3}$. Then the preshock density

ρ_0 in which the shock front is moving can be determined through $\rho_1/\mathcal{M}^2 = \rho_0$ (Bedijn & Tenorio-Tagle 1981), from which we infer $\rho_0 = 0.4 \text{ cm}^{-3}$, which is far below that observed for electron densities within evolved Galactic H II regions of similar size ($\gtrsim 50 \text{ cm}^{-3}$; Paladini et al. 2012), however typical for densities observed within the Warm Ionized Medium (WIM; Tielens 2005). Moreover, the existence of the cometary clouds L1617 and L1622, which are located behind Barnard’s Loop as measured from the Orion OB association and have sharp I-fronts on their sides facing the Belt stars (Bally et al. 2009) reveal that the ionizing flux of the Belt stars must escape the GS206-17+13 shell, from which we conclude that the shell is incomplete and the bubble has likely ‘burst’. Hence, we posit that the bubble interior has been emptied in its past, and its contents was channeled into the Orion-Eridanus superbubble cavity.

The Orion Nebula is a prototypical blister H II region created by the young stars of the Trapezium ($< 1 \text{ Myr}$; Hillenbrand 1997; Bally 2008) with $\theta^1 \text{ Ori C}$ as the dominant ionizing source. The ionized gas is streaming from the near-side of the OMC at about 10 km s^{-1} (O’Dell 2001) and accelerates into the surrounding medium. Recent velocity measurement of $\theta^1 \text{ Ori C}$ reveal that the star may be moving away from the OMC at a velocity of 13 km s^{-1} (see O’Dell et al. 2009, and references therein), which would imply a dynamical timescale of the Orion Nebula of only $1.5 \times 10^4 \text{ yr}$, since the star is currently located $\sim 0.2 \text{ pc}$ away from the ionization front (IF). Indeed, the measured emission measure (EM) reveals that the thickness of the ionized gas layer is only 0.13 pc (Wen & O’Dell 1995) assuming a constant density, which is known to be $\sim 6 \times 10^3 \text{ cm}^{-3}$ at the IF (O’Dell 2001). X-ray emission from the $\sim 10^6 \text{ K}$ gas of the shocked stellar wind of $\theta \text{ Ori C}$ (Güdel et al. 2008) has been detected in the Extended Orion Nebula (EON) and confirms the leakage of the (hot) gas toward the southwest, with the Orion-Eridanus superbubble as the most likely outlet of the flow of material.

5.4 Discussion

Cowie et al. (1979) interpreted neutral absorption lines at $|v_{\text{LSR}}| \lesssim 20 \text{ km s}^{-1}$ toward stars in Orion as a thick, dense shell of swept-up material, partially ionized on the inside by the Orion OB association. This ionized component would be evident as the IV gas and Barnard’s Loop. However, the LV and IV gas are clearly separated in velocity space (Welty et al. 2002) toward $\zeta \text{ Ori}$ at $(l, b) = (206.5, -16.6)$. This velocity separation makes it unlikely that LV and IV trace the same component of the Orion-Eridanus superbubble. In this respect, Bally (2008) already noted that the velocity dispersion of the ensemble of atomic and molecular clouds in Orion ranges over $> 20 \text{ km s}^{-1}$. Therefore, we attribute the low-velocity neutral gas to clouds in the Orion region instead of a dense, neutral shell surrounding Orion. In addition, we have revealed the absence of a dense neutral shell surrounding Barnard’s Loop (Sec. 5.3.2), and have shown that the Loop is part of a (separate) complete shell structure that is spatially correlated with HV gas detected toward Orion (Cowie et al. 1979; Welty et al. 2002) as discussed in Sec. 5.3.3.

The above described results call for a thorough revisit of the structure, history, and subsequent evolution of the Orion-Eridanus superbubble. Below in Sec. 5.4.1, we will connect the different gas tracers to the components of the superbubble, and combine this with our observational work in order to derive a new and improved picture of the Orion-Eridanus region in Sec. 5.4.1 and Sec. 5.4.1. We relate our findings to the stellar content

of Orion OB1 in Sec. 5.4.2 and present a scenario for the future evolution of the Orion-Eridanus superbubble in Sec. 5.4.3.

5.4.1 Connecting the dots: an updated picture of the Orion-Eridanus superbubble

Probing the superbubble through absorption lines

Intermediate-velocity gas components are detected over a wide wavelength range, i.e., $-80 \text{ km s}^{-1} \lesssim v_{\text{LSR}} \lesssim -20 \text{ km s}^{-1}$ (Cowie & York 1978; Cowie et al. 1979; Huang et al. 1995; Welty et al. 2002). However, with high spectral resolution, high signal-to-noise ratio, and broad spectral coverage data, Welty et al. (2002) were able to locate the bulk of the IV gas toward ζ Ori in two single components at $v_{\text{lsr}} = -35.3 \text{ km s}^{-1}$ and $v_{\text{lsr}} = -31.6 \text{ km s}^{-1}$.

We link the IV gas to the outer superbubble wall through several observations. First, the bulk of the IV gas lies within the velocity space reported for the superbubble wall in H I ($-40 \text{ km s}^{-1} \lesssim v_{\text{LSR}} \lesssim 40 \text{ km s}^{-1}$; Brown et al. 1995). We note that by connecting the (ionized) IV to the superbubble wall, we assume that the outer wall toward ζ Ori is predominantly ionized along the line of sight. This might connect with our result that the eastern part of the superbubble wall does not exhibit a neutral shell, as was observed in region 1 of Fig. 5.1 and will be further discussed in Sec. 5.4.1. Second, the total H II column density ($\log[N(\text{H II})] = 18.44 \text{ cm}^{-2}$) and the postshock conditions of the IV gas toward ζ Ori ($n_1 = 0.16 \text{ cm}^{-3}$, $T_1 = 9\text{e}3 \text{ K}$; Welty et al. 2002) imply an ionized shell thickness of $\sim 5.6 \text{ pc}$, in close agreement with the measured thickness of 1 degree or $\sim 7 \text{ pc}$ of the H α filaments along regions 1 - 5 in Fig. 5.1. Third, the IV gas is widespread, extending well outside Barnard's Loop and encompassing the λ Ori region, tracing a distinct component over an area larger than the HV gas (Sec. 5.3.3). Even though the definite extent of the IV gas should be established through an absorption-line study that includes sightlines covering the entire region shown in Fig. 5.4, here we argue that the IV gas traces a structure significantly larger than the dimensions of the Orion-Eridanus superbubble described in previous works (Reynolds & Ogden 1979; Heiles et al. 1999; Bally 2008; Pon et al. 2014a).

The above results reveal that the IV gas may be linked to the outer superbubble wall, whose neutral component was defined in Brown et al. (1995). In Sec. 5.3.3, we have argued that the HV gas traces the fast expansion of the Barnard's Loop bubble through the correlation between the sightlines that exhibit HV features and the morphology of the Barnard's Loop bubble from H α (Fig. 5.4). A similar result was obtained for the λ Ori bubble. Both the Barnard's Loop bubble and the λ Ori bubble may be connected to recent SN explosions (Secs. 5.3.3 & 5.3.3) that could be at the origin of the HV gas. Finally, the LV gas is attributed to the ensemble of clouds in Orion (Bally 2008). As a caveat, we note that these conclusions are based on the study of a limited amount of sightlines that may not fully reflect the complexity of the Orion region (see Sec. 5.4.1). Nonetheless, based on the currently available data, we hypothesize that the different gas tracers trace separate components of the superbubble, summarized in Table 5.2.

Comp.	v_{LSR} (km s^{-1})	n_0 (cm^{-3})	n_1 (cm^{-3})	$\log[N_{\text{H}}]$ (cm^{-2})	ion. state	Ref.	Tracing
LV	-20 to 20	-	-	20.43	neutral	1	Atom./mol. clouds
IV	-80 to -20	-	0.16	18.44	ionized	1, 2, 3, 4	Superbubble wall
HV	-120 to -80	3×10^{-3}	0.1 - 0.2	17.88	ionized	1, 2	Nested shells

Table 5.2: The connection between observed gas velocities and components within the Orion-Eridanus region. Listed quantities are (if known): observed velocity extents, v_{LSR} ; preshock densities, n_0 ; postshock densities, n_1 ; total hydrogen column densities, N_{H} ; ionization state, and the components of the Orion-Eridanus superbubble that is traced by the specific gas velocities. The (column) densities quoted are observed in the line of sight toward ζ Ori. References are (1): Welty et al. (2002), (2): Cowie et al. (1979). (3): Cowie & York (1978) (4): Huang et al. (1995).

Extent of the outer superbubble wall

The extent and connection of the IV gas to the superbubble wall (Sec. 5.4.1) imply that the size of the Orion-Eridanus superbubble may be larger than previously thought. Indeed, Barnard’s Loop is part of a separate closed bubble structure, suggesting that it is not associated with the large-scale expanding superbubble structure defined in earlier works (e.g., Reynolds & Ogden 1979; Heiles et al. 1999; Bally 2008; Pon et al. 2014a). Here, we argue that the outer $\text{H}\alpha$ filament toward the east in Fig. 5.1 offers a prime candidate for representing the outer superbubble wall.

We have concluded that Barnard’s Loop is completely ionized by Orion OB1 and that ionizing photons are able to penetrate through. Moreover, in Secs. 5.3.2 and 5.3.2, we have shown that Orion OB1 can provide the necessary ionizing photons to illuminate the $\text{H}\alpha$ emission seen in Fig. 5.1, indicating that the IF lies well outside the previously defined bounds of the Orion-Eridanus superbubble, which may be possible for superbubble walls in general (Basu et al. 1999). However, the large-scale, coherent $\text{H}\alpha$ filament to the south-east is indicative of a limb-brightened shell, rather than a mere haphazard ISM structure which happened to be illuminated by ionizing photons piercing through Barnard’s Loop.

We note that often the extent of superbubbles is traced through diffuse X-ray emission. The photo-electric cross section for 0.25 keV photons is $\sim 4 \times 10^{-21} \text{ cm}^2 \text{ H}^{-1}$ (Morrison & McCammon 1983). By integrating the total foreground emission from the LAB survey (Kalberla et al. 2005), i.e., $-400 < v_{\text{LSR}} < 0 \text{ km s}^{-1}$ (which includes the near-side of the superbubble shell at velocities $-40 < v_{\text{LSR}} < 0 \text{ km s}^{-1}$; Brown et al. 1995), we infer that the 0.25 keV emission is confined to foreground HI column densities of $N_{\text{H}} \lesssim 3 \times 10^{19} \text{ cm}^{-2}$ (the superbubble cavity), where the optical depth for 0.25 keV X-ray photons is $\tau_x \lesssim 0.1$, while emission at 0.25 keV is absent from regions of $N_{\text{H}} \gtrsim 2 \times 10^{20} \text{ cm}^{-2}$ (i.e, Barnard’s Loop, and the east- and westside of the superbubble near the Galactic plane), where $\tau_x \gtrsim 0.6$. Thus, the clear anti-correlation of the 0.25 (and 0.75) keV emission (Fig. 5.1) with foreground HI limits the use of this tracer for many parts of the Orion-Eridanus region, especially toward the Galactic plane.

The association of Barnard’s Loop with a closed separate bubble, the IV gas that traces a region larger than the previously defined bounds of the Orion-Eridanus superbubble, and the mere presence of the large-scale, coherent $\text{H}\alpha$ filament to the south-east, has led us to believe that regions 1-5 (Fig. 5.3) trace the actual outer shell of the Orion-Eridanus

superbubble. Projected in the interior of the outer shell are the Barnard’s Loop bubble, the λ Ori bubble, and the smaller-scale expanding bubbles discussed in Sec. 5.3.3. This indicates that the superbubble in its entirety consists of separate structures, or successive *nested shells*, possibly connected to a series of SN explosions originating from Orion OB1 over the past 15 Myr (Bally 2008; Secs. 5.4.1 & 5.4.3). While hot plasma could exist between the $H\alpha$ filament and Barnard’s loop, the detection of the accompanying X-ray emission is hampered because of foreground absorption. Our hypothesis sprouted from studying the energetics of gas and dust (Sec. 5.3.2 and Sec. 5.3.2) and their morphological appearances (Fig. 5.1), combined with the connections between the different gas tracers with the components of the superbubble (Table 5.2). In the next subsection, we will discuss the temperature of the superbubble interior gas, as well as the global structure of the outer wall in order to substantiate our claim regarding the structure and extent of the Orion-Eridanus superbubble.

Temperature of the superbubble interior and structure of the outer wall

The evidence discussed in Sec. 5.4.1 indicates that the outer superbubble wall lies outside of Barnard’s Loop (Sec. 5.4.1), possibly extending toward the outer $H\alpha$ filament to the south-east (Fig. 5.1). Here, we quantify the temperature structure of the superbubble interior. First, we derive that the Barnard’s Loop bubble is moving supersonically toward the east, from which we conclude that the temperature in this direction cannot be as high as $\gtrsim 10^6$ K. After comparison with the cooling timescale for a gas at $< 10^6$ K, we infer that the medium between Barnard’s Loop and the outer $H\alpha$ filament must have cooled to $\sim 10^4$ K, appropriate for a gas photo-ionized by Orion OB1. We argue that mass-loading may cause temperature gradients within superbubble interiors, place our findings in the context of superbubble evolution, and discuss the structure of the outer wall.

The temperature structure of the superbubble interior can be estimated as follows. First, we define the isothermal sound speed, $c_s = (kT/\mu m_H)^{1/2}$, where μ is the mean mass per hydrogen nucleus ($= 0.61$ for a fully ionized medium). Towards the west of the Barnard’s Loop bubble, the temperature of the superbubble interior traced by the X-ray-emitting gas is estimated at $T_x = 2.1 \times 10^6$ K (Burrows et al. 1993), giving $c_s = 170$ km s^{-1} . We compare this with the Barnard’s Loop bubble expanding at ~ 100 km s^{-1} (Sec. 5.3.3), which implies that the remnant of the recent SN explosion (Secs. 5.3.3 and 5.4.3) is well within the radiative expansion phase (see below). During this phase, the velocity of the SNR decelerates with time as $\propto t^{-5/7}$ (Tielens 2005) if we assume that the ambient density in which the SNR propagates is distributed homogeneously. Adopting this time-velocity relation, the adiabatic expansion phase ($v_{\text{exp}} \gtrsim 250$ km s^{-1}) ended just below 10^5 yr, and the bright crescent of Barnard’s Loop has been moving subsonically for ~ 0.2 Myr (in case $c_s = 170$ km s^{-1}). When moving subsonically, sound waves will travel ahead of the shell and the structure would dissolve and merge with the ISM within a fadeaway timescale of (McKee & Ostriker 1977; Draine 2011b)

$$\tau_{\text{fade}} = 1.87 E_{51}^{0.32} n^{-0.37} \left(\frac{c_s}{10 \text{ km s}^{-1}} \right)^{-7/5} \text{ Myr}, \quad (5.5)$$

where E_{51} is the kinetic energy in numbers of 10^{51} erg, and n the ambient hydrogen number density. The current kinetic energy of the eastern half of the Barnard’s Loop bub-

ble measures $E_{51} \sim 0.34$ (Sec. 5.4.3), part of which may already have been thermalized (Mac Low & McCray 1988). However, the total kinetic energy delivered by a SN explosion typically does not exceed $E_{51} \sim 1$ (Veilleux et al. 2005), or $E_{51} \sim 0.5$ for the eastern half of the bubble. With $E_{51} = 0.5$, and parameters for the X-ray-emitting gas of the superbubble interior toward the west ($T_x = 2.1 \times 10^6$ K, $n_x = 6 \times 10^{-3}$ cm $^{-3}$; Burrows et al. 1993; Sec. 5.4.3), we calculate $\tau_{\text{fade}} \sim 0.2$ Myr, similar to the time Barnard's Loop has been moving subsonically in case it is moving within hot gas at a temperature exceeding 10^6 K.

The above-derived fadeaway timescale reveals that *if* Barnard's Loop would be moving to the east in an X-ray emitting gas such as that traced by *ROSAT* in the west part of the superbubble (Fig. 5.1), it must be long in the process of merging and dissolving with the hot gas. This actual process may cause the faintness of the H α emission of the Barnard's Loop bubble toward the west (Sec. 5.3.3), where the superbubble interior temperature is known to be at a temperature of $T_x = 2.1 \times 10^6$ K (Burrows et al. 1993; Fig. 5.1). Clearly, this does not affect the eastern part of the Barnard's Loop bubble in the same way, as exemplified by the bright crescent of Barnard's Loop. Alternatively, there may be a density gradient within the superbubble interior that may cause the brightness difference of the Barnard's Loop bubble between its east and west sides. Either way, the conclusion is that the Barnard's Loop bubble moves supersonically toward the east, in line with the findings of Cowie et al. (1979), who argued that the HV gas (associated with the near-side of the Barnard's Loop bubble; Sec. 5.3.3) traces a radiative shock. Consequently, the interior superbubble temperature toward the east cannot be at $\geq 10^6$ K, as is observed for the X-ray emitting gas toward the west.

Temperature differences within a superbubble interior can originate from thermal conduction and evaporation of the swept-up superbubble shell. This mechanism may cool the interior of the superbubble by increasing the interior density (Weaver et al. 1977; Mac Low & McCray 1988) such that radiative losses become important. Champagne flows and photo-ablation of molecular clouds enclosed in the superbubble can inject mass into the hot plasma, further lowering the temperature compared to that predicted by idealized models (a full discussion on the mass-loading mechanisms is deferred to Sec. 5.4.3). Gas below temperatures of 10^6 K cools rapidly. At an interior density of $n_x = 6 \times 10^{-3}$ cm $^{-3}$ (Burrows et al. 1993), the cooling timescale for a gas at 10^5 K equals $\tau_{\text{cool}} \sim kT/n\Lambda(T) \sim 10^5$ yr, where $\Lambda(T) \sim 5 \times 10^{-22}$ erg cm 3 s $^{-1}$ is the average value of the cooling function for gas at temperatures 10^4 K $\lesssim T \lesssim 10^6$ K (Dalgarno & McCray 1972). Mass-loading of the interior will shorten the cooling timescale. The detection of N v gas (Welty et al. 2002) toward ζ Ori traces $\sim 10^5$ K gas and confirms the presence of a thermally conductive layer (Chu 2008), providing information on the temperature structure of the superbubble wall and the interior temperature, but it is unclear if this conductive layer traces the outer superbubble wall, or the interior shell associated with the Barnard's Loop bubble. Furthermore, it is uncertain if this layer extends toward the outer H α filament given the lack of coverage of absorption line studies in this region (Fig. 5.4). In any case, the cooling timescale is short compared to that of the estimated age of the superbubble ($\lesssim 8$ Myr; Brown et al. 1994) and the supernova rate in Orion OB1 ($1 - 1.5$ Myr $^{-1}$; Bally 2008; Sec. 5.4.3) that may re-heat the interior gas (see below and Sec. 5.4.3). Consequently, if the temperature drops below 10^6 K, the medium between Barnard's Loop and the outer filament will settle at a temperature of $\sim 10^4$ K, as it is kept photo-ionized by Orion OB1 by

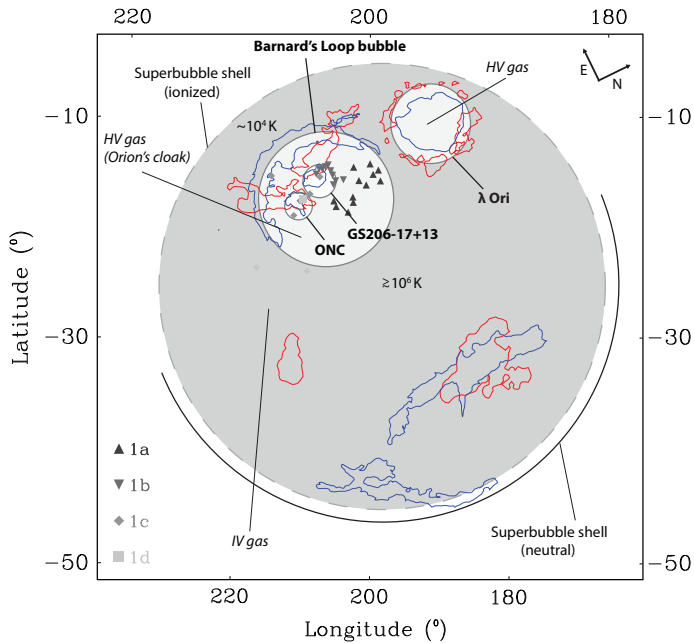


Figure 5.6: Schematic of the Orion-Eridanus superbubble and several of its major components. See Fig. 5.1 for the nomenclatures of the shown structures. The proposed outer shell of the Orion-Eridanus superbubble (dashed circle), blown by a series of SNe from an old subpopulation of the Orion OB association, is traced by an intermediate-velocity (IV) shock that sweeps up the ambient ISM (gray area). Towards the west, the superbubble is surrounded by a shell of neutral (*solid black line*) swept-up material, whereas this shell is completely ionized (*dashed gray line*) toward the east. The temperature in the superbubble interior seems to be lower toward the east ($\sim 10^4$ K) in the direction of the Galactic plane, compared to the X-ray emitting gas in the west ($\geq 10^6$ K). The outer shell encompasses several ‘nested’ smaller shells or bubbles (*solid gray circles*, denoted in boldface) that are more recently formed, such as the Barnard’s loop bubble, traced by high-velocity (HV) gas. Other examples of bubbles that may have been triggered by ongoing activity in Orion OB1 are the λ Ori bubble, GS206-17+13, and the shell surrounding the Orion Nebula cluster (ONC).

photons piercing through Barnard’s Loop (Sec. 5.3.2). Depending on the internal density, the medium between Barnard’s Loop and the outer filament may not be in pressure equilibrium with the (higher-density) outer $H\alpha$ filament.

In the early stages of its evolution, an outer superbubble wall is defined by a shell of swept-up material, the expansion of which is driven by an overpressurized interior medium (Tielens 2005). The superbubble initially expands through the Sedov-Taylor solution, but as the interior medium expands adiabatically, its pressure will decrease and the expansion slows down. The radiative phase commences when the expansion velocity decreases to ~ 250 km s^{-1} or a postshock temperature of $\sim 10^6$ K (Tielens 2005). At this point, radiative losses will become important, and the interior temperature (and pressure) will further drop. When the interior pressure reaches that of the ambient medium, the expansion of the superbubble wall will coast at constant radial momentum, thus slowing down as it sweeps up material from its surroundings. When the expansion velocity reaches

the local sound speed, the superbubble wall will disappear and merge with the ISM within a fadeaway timescale (Eq. 5.5). The interior pressure may even drop below that of the ambient medium if the cooling timescale ($\sim 10^5$ yr) is shorter than the pressure timescale or sound-crossing time. Currently, the distance between Barnard's Loop and the outer Halpha filament is roughly ~ 100 pc, such that the pressure timescale can be anywhere up to ~ 10 Myr for a 10^4 K medium, depending on the exact moment the region cooled toward this temperature. However, the medium between Barnard's Loop and the outer filament must have cooled within the time between successive expanding shells (regulated by the SN rate; 1 - 1.5 Myr $^{-1}$; Bally 2008). Thus, it may well be that the pressure inside the interior cannot adjust rapidly enough to the change in temperature and, in case no mass-loading occurs, it can reach a lower pressure compared to the ambient galactic medium. In case of an underpressurized interior, the expansion of the superbubble wall may halt and even reverse its movement if the pressure difference between the interior and the ambient medium is strong enough.

Given that the medium between Barnard's Loop and the outer H α filament is at 10^4 K and we are not able to constrain its density, one may question whether this medium in fact represents the WIM or Warm Neutral Medium (WNM; Tielens 2005). In this case, the outer H α filament is not the superbubble wall, but merely an ISM feature illuminated by photons escaping from Barnard's Loop. However, we have revealed that Barnard's Loop is part of a separate closed structure (Sec. 5.3.3), and argued that the superbubble wall extends beyond Barnard's Loop (addressed in Secs. 5.4.1 & 5.4.1). Surely, if one accepts that Barnard's Loop is expanding at 100 km s^{-1} and represents a SNR of age 0.3 Myr (Secs. 5.3.3 & 5.4.3), it may not be surprising that the superbubble wall lies further outwards as measured from Orion OB1, given that star formation has occurred over 15 Myr in Orion and that 10-20 SNe have gone of in its past (Bally 2008). Here, we argue that successive SN explosions may lead to the appearance of successive shells. In this scenario, the large-scale, coherent H α filament to the south-east represents a prime candidate to trace the actual outer superbubble wall. We defer a further discussion on the idea of successive shells and the evolution of the outer superbubble wall to Sec. 5.4.3.

We note that the outer H α filament (Fig. 5.1) does not contain a neutral shell that is expected for a sweeping superbubble wall (Fig. 5.2 & 5.3). The lack of a neutral shell may simply suggest that the swept-up ISM did not contain enough material to fully absorb the ionizing photons from Orion OB1. Alternatively, the east side of the superbubble, which is racing up the density ramp toward the Galactic plane, may not be moving supersonically anymore and has changed character from a shock wave to a sound wave, rendering it unable to sweep up additional mass. Using Eq. 5.5 and $E_{51} \sim 10$ (the total kinetic energy exerted Orion OB1; Brown et al. 1995; Bally 2008), we calculate for the east side of the bubble expanding toward the WNM of the Galactic plane ($n \sim 0.5 \text{ cm}^{-3}$, $c_s \sim 10 \text{ km s}^{-1}$), $\tau_{\text{fade}} \simeq 4 \text{ Myr}$, well below the estimated age of the superbubble ($\lesssim 8 \text{ Myr}$; Brown et al. 1994). Thus, we may be observing the east side of the superbubble as it is in the process of dissolving, already having lost its neutral shell and currently being completely ionized before it merges with the local material of the ISM. Eq. 5.5 does not apply to the west side of the superbubble as its expansion velocity (traced through H I; $\sim 40 \text{ km s}^{-1}$; Brown et al. 1995) implies that it moves supersonically through the WNM/WIM. However, for the ionized east side of the superbubble the expansion velocity is not constrained, and the question whether or not it is moving supersonically remains unanswered.

Summary: The structure of the Orion-Eridanus superbubble

We now have obtained the complete set of tools to derive an updated picture of the Orion-Eridanus region which we show in Fig. 5.6. Our results demonstrate that the superbubble consists of separate structures or *nested shells*, superimposed along line of sight. In particular, we have recognized a separate bubble (amongst others; Sec. 5.3.3), evident as the HV gas and the Barnard's Loop bubble in $H\alpha$ (Fig 5.4). This bubble expands *inside* the pre-existing cavity of the Orion-Eridanus superbubble, given its preshock density, its embedded nature in the Orion-Eridanus region (Fig. 5.6), and its likely origin through feedback from Orion OB1. The realization that Barnard's Loop is not part of the superbubble wall (Sec. 5.3.3), the IV gas that seems to trace a region larger than the previously defined bounds of the Orion-Eridanus superbubble (Sec. 5.4.1), and the presence of the large-scale, coherent $H\alpha$ filament to the south-east have led us to believe that the extent of the Orion-Eridanus superbubble is larger than previously thought. We have argued that the temperature of the superbubble interior between Barnard's Loop and the outer $H\alpha$ filament to the south-east cannot be as high as that observed for the X-ray emitting gas toward the west (Burrows et al. 1993) and, therefore, must have settled at 10^4 K (Sec. 5.4.1). The expansion of this outer $H\alpha$ filament may not be pressure-driven anymore. While this is an inevitable outcome during late stages of superbubbles and SNRs (Tielens 2005), the interior pressure drop may be accelerated through the effects of mass loading and radiative energy losses (Sec. 5.4.3). The observations (Fig. 5.1) indicate that the outer superbubble wall is surrounded by a shell of HI toward the west, whereas it may be completely ionized toward the east (Sec. 5.4.1).

We stress that the association of gas velocities with components in the superbubble (Table 5.2) is largely based on the analysis of a dozen of sightlines throughout the Orion side of the superbubble (Fig. 5.4). It is not clear how much mass is associated with these velocities (Sec. 5.4.3). Moreover, some of the gas tracers are not seen in particular lines of sight. This may be because we are tracing foreground stars, such as the sightline toward γ Ori located at 77 pc (van Leeuwen 2007), which could provide a constraint to the elongation of the bubble toward the Local Bubble (e.g., Bally 2008; Pon et al. 2014a), or incomplete spectral coverage (Cowie et al. 1979). Alternatively, the distribution of the gas components might be patchy (Cowie et al. 1979). Surely, the connections laid out in Table 5.2 may be oversimplified, as the Orion region is highly complex, containing dozens of filamentary clouds, and must bear the marks of multiple SNRs (Bally 2008) that are breaking out of a region that contains a lot of substructure. Further observations are needed to firmly constrain the extent of the distinct gas components in order to derive the detailed structure of the Orion-Eridanus superbubble, and to recognize the existence of conductive layers that would provide more insight in the temperature distribution throughout the superbubble interior.

The observations of the gas and dust have revealed that Orion OB1 can be the source of ionization of the $H\alpha$ filaments encompassed within the entire region shown in Fig. 5.1 (Sec. 5.3.2). We have connected the IV gas with the outer superbubble wall. We note that the preshock density of the IV is not known. However, given a postshock density of 0.16 cm^{-3} (Welty et al. 2002) and shock velocity of 40 km s^{-1} (Brown et al. 1995), a shock moving through the WNM ($T = 8000 \text{ K}$, $c_s \sim 10 \text{ km}^{-1}$) would have a preshock density of order $\sim 0.01 \text{ cm}^{-3}$ (J-type shocks increase densities by \mathcal{M}^2 ; Tielens 2005), which is somewhat low for the WNM in the Galactic plane. Higher densities for the Orion-Eridanus

shell of $1 - 5 \text{ cm}^{-3}$ are quoted toward the Eridanus filaments in the west (e.g., Reynolds & Ogden 1979), indicating that the expansion occurs somewhat anisotropically, which can also be inferred by appreciating the complex morphology of the superbubble. In any case, the shock velocity of the IV gas ($\sim 40 \text{ km s}^{-1}$) is not fast enough to ionize hydrogen: therefore, the Eridanus filaments (and the IV gas) are photo-ionized by Orion OB1, which was already noted by Reynolds & Ogden (1979) and Welty et al. (2002). We note that Pon et al. (2014a) explored other mechanisms of ionization, but concluded that Orion OB1 most likely causes the observed ionization state of the IV gas. When the spherical geometry from Fig. 5.6 is adopted for the outer superbubble wall, and assuming a diameter of the supershell of 45 degrees (equivalent to a radius of 160 pc) with expansion velocity of $\sim 40 \text{ km s}^{-1}$, the dynamical age of the shell is $\sim 4 \text{ Myr}$, consistent with the age of the Orion OB1a subgroup, minus a main sequence lifetime of 3 - 5 Myr for its most massive stars (Bally 2008). Naturally, stellar winds during the first few Myr of the lifetime of the OB association may have contributed to the formation and expansion of the superbubble wall as well.

In conclusion, considering that star formation had been occurring for 10 - 15 Myr in Orion OB1 and the presence of at least four distinct subgroups (Blaauw 1964; Bally 2008), it may not be surprising that the Orion-Eridanus superbubble consists of a set of nested shells. Our results connect well with recent work from Schlafly et al. (2015), who show that the OMCs are in turn part of an ancient ring of dust. Possibly, the ring represents the remainder of a large bubble that pushed the OMCs out of the Galactic plane toward their current location. Still, the hierarchy of bubbles does not end at the possible progenitor of the Orion-Eridanus superbubble defined by Schlafly et al. (2015). Indeed, it has been argued that the Gould's Belt that includes all nearby OB associations are associated with a large expanding ancient (30 - 60 Myr) supershell known as Lindblad's ring (see Bally 2008, and references therein). The Gould's Belt of stars and OB associations may therefore represent sequential star formation when the Lindblad's ring cooled and collapsed to form dark clouds, out of which the evolution of the Orion region commenced.

5.4.2 The nested shells and their relation to Orion OB1

The recent discovery that the OMCs may be part of an ancient ring of dust (Schlafly et al. 2015), the uncovering of an extended foreground population toward Orion A (Alves & Bouy 2012; Bouy et al. 2014), and the mysterious origin of some of the brightest stars in Orion (α Ori, β Ori, and κ Ori; Bally 2008) illustrate that our current understanding of the Orion region is still limited. Bally (2008) proposed that the bright stars may be part of a foreground group about 150 pc in front of Orion OB1, and together constitute the three most massive members of this population still present to date. Alternatively, some of the massive stars from Orion OB1 may have been ejected as runaways (space velocities in excess of $> 40 \text{ km s}^{-1}$) in the direction of the Local Bubble before exploding as SNe: up to 25% of the OB stars end up as runaways (Zinnecker & Yorke 2007). Such stars could be linked to the odd geometry of the Orion-Eridanus superbubble (Pon et al. 2014a), which appears to be elongated toward the Local Bubble.

One must keep in mind that most of the distance determinations toward the Orion stellar populations are based on photometric indicators (e.g. Brown et al. 1994). Although the

Hipparcos mission determined parallaxes for many stars in the Orion region, the distance to the young populations ($\sim 300 - 400$ pc) translates to *Hipparcos* parallax errors of 30 - 40% (given a precision of 1 milliarcsecond; Perryman et al. 1997). Thus the detailed distribution of the stellar population along the line of sight can, as of yet, not be determined (see also de Zeeuw et al. 1999b). In this respect, the *Gaia* mission (de Bruijne 2012; Perryman et al. 2001) is expected to dramatically improve the distance and age determinations of the stars and subgroups in Orion. The entire Orion region lies well within the range where *Gaia* parallaxes will be accurate to 10% or better over a large range of spectral types. This will allow to constrain the relationship between the stellar content and the nested shells seen in the Orion-Eridanus superbubble, and to address the importance of triggered star formation (Elmegreen & Lada 1977) in Orion, for which one needs *precise* measurements of proper motion, radial velocities, and ages.

5.4.3 Evolution of the Orion-Eridanus superbubble

In this section, we will exploit the results drawn from the previous sections to derive an updated picture of the evolution of the Orion-Eridanus superbubble, regulated by a balance between processes that mass-load the superbubble interior, controlling its temperature and density structure (Cowie et al. 1981; Hartquist et al. 1986), and feedback from Orion OB1 that sweeps up and collects the injected interior mass in expanding shells before thermalizing or cooling (Mac Low & McCray 1988). These processes determine the momentum of the superbubble wall and the thermal pressure of the interior, which drives the superbubble expansion out into the ambient Galactic medium.

First, in Sec. 5.4.3 we summarize masses and energetics as observed from different components of the Orion-Eridanus superbubble. From this, we conclude that the Barnard's Loop bubble is a SNR (associated with a SN explosion that occurred 3×10^5 yr ago; Sec. 5.3.3; Cowie et al. 1979), and argue in Sec. 5.4.3 that the SNR has swept through the inner parts of the superbubble to collect mass that has been introduced through champagne flows and thermally evaporating clouds. Behind the Barnard's Loop bubble, champagne flows from IC 434, the Orion Nebula, and λ Ori continue to mass-load the superbubble interior until a next SN explosion will start the cycle all over again. The net effect is a gradual disruption of the star-forming reservoir and the subsequent outward transportation of processed material, where it will ultimately pressurize the superbubble interior, or add momentum to the outer superbubble wall. We will argue that at the current rate, the OMCs will be able to power the expansion and evolution of the Orion-Eridanus superbubble for another 20 - 30 Myrs, before they are depleted and run out of steam, at which point the superbubble will disappear and merge with the surrounding ISM.

Masses and energetics of the Orion-Eridanus superbubble

Hot gas ($\gtrsim 10^6$ K; Table 5.3) from the superbubble interior has been characterized by Burrows et al. (1993), who inferred a temperature of $T_x \sim 2 \times 10^6$ K and a total luminosity at X-ray wavelengths of $L_x \approx 8.0 \times 10^{35}$ erg s $^{-1}$, when assumed that the X-ray emitting region is spherical and its actual 'hook-shaped' appearance results after foreground absorption by MBM 18 and MBM 20 (Fig. 5.1; Burrows et al. 1993). The authors deduce the following parameters for the hot gas: when 400 pc is taken as the distance toward the superbubble, the radius of the X-ray emitting region is $r_x = 70$ pc, its density is $n_x = 6 \times$

	M ($10^3 M_\odot$)	v_{exp} (km s^{-1})	E_{th} (10^{49} erg)	E_{kin} (10^{49} erg)	Form	Ref.
<i>Hot gas ($\geq 10^6$ K)</i>						
Superbubble interior	1.8	-	62	-	Thermal energy	(1)
BL bubble interior	(0.02)	-	(0.65)	-	Thermal energy	TW
<i>Ionized gas (10^4 K)</i>						
Superbubble	84	15 ^(a)	14	19	Swept-up shell	(2)
BL bubble	6.7	100	1	67	Swept-up shell	TW
λ Ori	2 - 6	30	0.5	3	Champagne flow	(3, 4)
GS206-17+13	3	30	0.5	3	Champagne flow	TW
IC 434	0.1	30	0.02	0.1	Champagne flow	(5)
Orion Nebula	0.02	30	0.003	0.02	Champagne flow	(6)
<i>Neutral gas (10^2 K)</i>						
Superbubble	250	40	-	370	Swept-up shell	(7)
GS206-17+13	3.4	8	-	0.2 ^(b)	Swept-up shell	(5)
Orion Nebula (Veil)	2.3	2	-	0.01	Swept-up shell	TW
<i>Molecular gas (10 K)</i>						
OMC A	105	-	-	-	Molecular cloud	(9)
OMC B	82	-	-	-	Molecular cloud	(9)
λ Ori	11	16.5	-	6	Swept-up shell	(10)
<i>Stars</i>						
Ori 1a	1.6	-	-	-	Stellar cluster	(11)
Ori 1b	1.3	-	-	-	Stellar cluster	(11)
Ori 1c	1.8	-	-	-	Stellar cluster	(11)
Ori 1d (ONC)	1.8	-	-	-	Stellar cluster	(12)
Ori 1d (NGC2024)	0.2	-	-	-	Stellar cluster	(13)
σ Ori	0.2	-	-	-	Stellar cluster	(14)
(λ Ori)	(0.6)	-	-	-	Stellar cluster	(15)

Table 5.3: Masses and energetics of the Orion-Eridanus superbubble. Listed quantities are: mass, M ; the expansion velocity, v_{exp} ; and the thermal (E_{th}) and kinetic (E_{kin}) energy. ^(a): the expansion velocity in H α and H I are not measured at the same position causing the discrepancy between both numbers. ^(b): This value has been revised downwards compared to Ochsendorf & Tielens (2015), who determined the kinetic energy assuming an abrupt energy input appropriate for supernova remnants (Chevalier 1974). Here, we argue that the energy input has been continuous through stellar winds (see text) and instead use $E_{\text{kin}} = 1/2 M v_{\text{exp}}^2$. References: (1) Burrows et al. (1993); (2) Reynolds & Ogden (1979); (3) Reich (1978); (4) van Buren (1986); (5) Ochsendorf & Tielens (2015); (6) Wilson et al. (1997); (7) Brown et al. (1995); (8) van der Werf et al. (2013); (9) Wilson et al. (2005); (10) Lang & Masheder (1998); (11) Brown et al. (1994); (12) Hillenbrand (1997); (13) Comeron et al. (1996); (14) Sherry et al. (2004); (15) Barrado y Navascués et al. (2004). TW refers to this work.

10^{-3} cm^{-3} (Burrows et al. 1993), and contains a total mass $M_x = 230 M_\odot$ after adopting a spherical geometry. However, if we adopt the (larger) geometry from Fig. 5.6, and account for possible missing X-ray emission because of foreground absorption (Fig. 5.1 and Sec. 5.4.1), the total mass within a region of $r_x = 160$ pc would amount to $M_x = 1800$

M_{\odot} . Table 5.3 also denotes a value for the hot gas inside the Barnard’s Loop bubble of radius 35 pc in case it were filled with gas of the same characteristics as observed in the superbubble. As noted before (Sec. 5.4.1), the high column densities for the Barnard’s Loop region prohibits the detection of diffuse X-rays toward the east side of the Barnard’s Loop bubble. Hot gas is detected toward the west side where the H I foreground column is much lower, but it is unclear if this emission traces hot gas from the Barnard’s Loop bubble or the entire Orion-Eridanus superbubble.

Ionized gas ($\sim 10^4$ K; Table 5.3) in the Orion-Eridanus region is associated with the outer H α filaments of the superbubble, the Barnard’s Loop bubble shell, and the champagne flows of the λ Ori bubble, GS206-17+13, the IC 434 emission nebula, and the Orion Nebula (Sec. 5.3.2 & Sec. 5.3.3). For Barnard’s Loop, the total ionized mass is estimated at $M = 6700 M_{\odot}$ by adopting a half-sphere geometry with thickness 1° , outer radius of 7° , and density $n_{\text{H}} = 3.4 \text{ cm}^{-3}$ (Sec. 5.3.1). The western half of the complete bubble (Fig. 5.4) is much fainter, which implies that the density in the Barnard’s Loop bubble varies significantly between both parts (Sec. 5.4.1). Assuming $v_{\text{exp}} = 100 \text{ km s}^{-1}$ (Sec. 5.3.3), $E_{\text{kin}} = 3.4 \times 10^{50} \text{ erg}$. The total energy that has been injected in the region can then be estimated at $E_{\text{kin}} = 6.7 \times 10^{50} \text{ erg}$ by assuming spherical symmetry. This energy should be compared to the typical kinetic energy provided per SN ($10^{50} - 10^{51} \text{ erg}$, depending on the efficiency at which it couples to the ISM; Veilleux et al. 2005) as well as the wind mechanical energy input. By adopting typical wind parameters ($\dot{M} = 1 \times 10^{-6} M_{\odot} \text{ yr}^{-1}$, $v_{\infty} = 2000 \text{ km s}^{-1}$) for the 7 most-massive stars in the Orion OB association, and assuming the lifetime of Orion’s Cloak at $3 \times 10^5 \text{ yr}$ (Sec. 5.3.3; Cowie et al. 1979), the total mechanical luminosity exerted by the Orion OB association is $L_{\text{mech}} = 8.4 \times 10^{49} \text{ erg}$, of which $\sim 20\%$ couples to the surrounding medium as kinetic energy (van Buren 1986). Thus, the (combined efforts of) stellar winds from the Orion OB1 stars seem insufficient to provide the measured kinetic energy of the Barnard’s Loop bubble and we associate the Barnard’s Loop bubble with a recent supernova explosion.

Table 5.3 reflects the omnipresence of champagne flows in the Orion region, consistent with the findings of Ochsendorf et al. (2014b), who showed that H II region champagne flows are ubiquitous throughout the Galactic plane, and illustrated the importance of this phase to the turbulent structure of the ISM. Still, the amount of material that is eroded from the molecular clouds and delivered by champagne flows in the form of kinetic energy of the fast moving ionized gas is difficult to determine, and estimates over the lifetime of the star will depend most critically on the ionizing luminosity and main sequence lifetime of the ionizing star (e.g., Whitworth 1979). Here, we will follow Tielens (2005) and adopt a ‘typical’ blister phase that will accelerate $M_{\odot} \sim 3 \times 10^3 M_{\odot}$ of ionized gas to 30 km s^{-1} , providing a kinetic energy of $E_{\text{kin}} \sim 3 \times 10^{49} \text{ erg}$. We use this value for the champagne flow of the GS206-17+13 bubble that has occurred in the past (Sec. 5.3.3). For comparison, the ionized interior density of the λ Ori region, that seems to be on the verge of breaking out (Sec. 5.3.3), is quoted to be between $2000 M_{\odot}$ (van Buren 1986) and $6000 M_{\odot}$ (Reich 1978); this would add a similar amount of mass and kinetic energy to the superbubble interior as the GS206-17+13 shell did. The Orion Nebula has just recently entered the champagne phase (Sec. 5.3.3) and only contains some $\sim 20 M_{\odot}$ of ionized gas (Wilson et al. 1997). The IC 434 region is a special case, as the champagne flow originates from a chance encounter between the σ Ori star cluster and the Orion B molecular cloud (Ochsendorf et al. 2014a; Ochsendorf & Tielens 2015). Still, the star has

already eroded $100 M_{\odot}$ and will add another $350 M_{\odot}$ to the ionized gas before it plunges into the molecular cloud (for a current distance of 3.5 pc and a closing velocity of $\sim 10 \text{ km s}^{-1}$; Ochsendorf & Tielens 2015).

Neutral gas ($\sim 10^2 \text{ K}$; Table 5.3) is present in the superbubble wall (Brown et al. 1995), and the slowly expanding shells of the λ Ori region (Lang & Mashedier 1998), the GS206-17+13 bubble (Ochsendorf & Tielens 2015), and the Orion Nebula that is encapsulated by the neutral ‘Veil’ (e.g., van der Werf et al. 2013). The GS206-17+13 is a stellar wind-blown-bubble (Sec. 5.3.3). The Orion Nebula Veil contains a total neutral column density of $N_{\text{H}} = 5.8 \times 10^{21} \text{ cm}^{-2}$, has a size of at least 1.5 pc, as it is common to the Orion Nebula and M43, and shows only minor blue shifted velocities with respect to the background OMC ($\sim 2 \text{ km s}^{-1}$). This implies that the mechanical feedback of the Trapezium through, e.g., the champagne flow or stellar winds has not yet coupled as kinetic energy to the surrounding neutral gas, consistent with the young age of the Trapezium stars ($< 1 \text{ Myr}$; Hillenbrand 1997) and, perhaps, the very small dynamical time inferred for the Orion Nebula since the onset of the champagne flow ($\sim 1.5 \times 10^4 \text{ yr}$; O’Dell et al. 2009). Here, we estimate the total H I mass for the Orion Veil by assuming that the measured column density by van der Werf et al. (2013) is homogeneously distributed over a shell with a radius of 2 pc, large enough to cover both the M43 region as well as the entire Extended Orion Nebula (Güdel et al. 2008).

Molecular gas ($\sim 10 \text{ K}$; Table 5.3) is detected in dozens of small cometary clouds, but largely concentrates in the Orion molecular clouds, which constitute the main reservoir of the dense gas out of which star formation occurs. As described by, e.g., Bally (2008), the ages and locations of the subgroups in Orion OB1 indicate that star formation has propagated through the ‘proto-Orion cloud’ sequentially. The kinetic energy associated with the expansion of the λ Ori molecular shell ($6 \times 10^{49} \text{ erg}$) is consistent with expansion driven by either the overpressure of photo-ionized gas (Spitzer 1978) that deposits some $10^{49} - 10^{50} \text{ erg}$ to the surrounding medium (Ochsendorf et al. 2014b) over the lifetime of λ Ori ($\sim 10 \text{ Myr}$), or a SN explosion (Veilleux et al. 2005), or a wind-blown origin (Weaver et al. 1977), as $L_{\text{mech}} = 2 \times 10^{50} \text{ erg}$ for λ Ori (van Buren 1986) assuming an age of 5 Myr (Bally 2008), a fraction of which will couple as kinetic energy. Some previous works favor a SN origin for the λ Ori bubble, which would also explain the current space motion of the λ Ori star (see Sec. 5.3.3).

Stars are listed for comparison, where we have included the separate subgroups from the Orion OB1 association (1a, 1b, 1c, and 1d; Blaauw 1964; Brown et al. 1994). The masses in the 1a, 1b, and 1c subgroups have been determined using the results in Brown et al. (1994), who constructed the initial mass function (IMF) and through this reported the number of stars initially found in the 2 - $120 M_{\odot}$ mass range for each subgroup. We complement this by estimating the contribution from low mass stars below the completion limit of the Brown et al. (1994) study (0.08 - $2 M_{\odot}$) using a standard IMF (Kroupa 2001), normalized to the results from Brown et al. (1994). Table 5.3 lists the resulting total masses, assuming an upper stellar mass limit set by the age of each subgroup. In Orion OB1a, stars more massive than $13 M_{\odot}$ have exploded as SNe, while the (younger) age of the Orion 1b and 1c subgroups imply an upper mass limit of about $20 M_{\odot}$ (Bally 2008). Orion OB1d is the youngest subgroup and includes many star-forming clusters (Bally 2008), and here we only include the two largest components, the Orion Nebula Cluster in OMC A, and NGC 2024 in OMC B. The σ Ori group is noteworthy here, as it has

traditionally been assigned to Orion OB1b based on its spatial location amongst the Belt stars, but its traversed space motion reveals that the cluster might have originated from the Orion OB1c region (Ochsendorf & Tielens 2015). We have bracketed the λ Ori region in Table 5.3 as it is separated from the star clusters that are associated with the OMCs, and does not directly influence the scenario that will be outlined in Sec. 5.4.3.

Summary: Most of the mass of the Orion-Eridanus superbubble resides in the outer superbubble wall, while the nested shells that process and sweep-up the interior material (see Sec. 5.4.3) constitute only a small part. The molecular clouds still represent a large reservoir of mass, comparable to that located in the superbubble wall. Most of the energy is found in the form of kinetic energy of the expansion of the superbubble wall. Still, about 10 - 15% of the total energy is located in thermal energy of the hot gas of the superbubble interior, and a comparable amount lies within the kinetic energy of the ionized gas. The thermal energy of the hot gas created by fast shocks is large compared to the thermal energy of the 10^4 K ionized gas delivered through photo-ionization from Orion OB1. Finally, when all subgroups in Table 5.3 are combined, stars comprise some $\sim 6.9 \times 10^3 M_{\odot}$ or 3 - 4% of the molecular material within the OMCs.

Mass-loading and cleansing of the interior

The expanding shells in the interior of the Orion-Eridanus superbubble are the manifestation of feedback from Orion OB1. When moving supersonically, the shockwaves associated with the shells sweep up the interior mass of the superbubble, acting as a mechanism to remove any material that may have been introduced to the medium in the past. In this respect, the mass ($6.7 \times 10^3 M_{\odot}$) and radius (35 pc) of the shell surrounding the Barnard's Loop bubble can be combined to show that the average density of the swept-up medium contained $\sim 1 \text{ cm}^{-3}$. We note that the density of the swept up material only slightly exceeds what would be expected for the WNM of the Galaxy, which would be consistent with the Barnard's Loop bubble being a superbubble wall expanding into the ambient Galactic medium. However, we render this scenario unlikely given the short dynamical timescale of the Barnard's Loop bubble (~ 0.3 Myr; Sec. 5.3.3) compared to the Orion star forming region (~ 15 Myr; Bally 2008), the preshock density of the HV gas ($\sim 3 \times 10^{-3} \text{ cm}^{-3}$; Welty et al. 2002) and its nested appearance within the entire Orion-Eridanus superbubble (Figs. 5.1 & 5.4). The increased density is about two orders of magnitude above that what is expected for a superbubble interior ($\sim 10^{-2} \text{ cm}^{-3}$; Weaver et al. 1977), which provides convincing evidence that the superbubble interior must have been mass-loaded since the last supernova passed through and cleansed the interior.

Photo-ionization feedback from Orion OB1 ultimately creates champagne flows that channel 10^4 K gas from the H II regions into the superbubble cavity, where it will mix with the hot gas ($\geq 10^6$; Chu 2008). The injected mass will significantly lower the temperature of the superbubble interior and increase its density. The total mass delivered to the interior by a typical champagne flow over the lifetime of a massive star ($\sim 3 \times 10^3 M_{\odot}$) only slightly exceeds the mass that makes up the hot gas of the entire superbubble ($1.8 \times 10^3 M_{\odot}$). However, this extra mass will be injected in a small portion of the interior (see below). In addition, champagne flows will dump kinetic energy in the form of turbulent motion into the hot cavity. In principle, the injected turbulent energy is more than the thermal energy of the hot gas provided by the SN that lead to the formation of the Barnard's Loop bubble (Table 5.3). However, dissipation of this turbulence will lead to

temperatures of only $\sim 10^4$ K (for a flow speed of ~ 30 km s $^{-1}$; Table 5.3; Tielens 2005). The cooling function peaks at these temperatures (Dalgarno & McCray 1972) such that this excess energy will be mainly radiated away. Nevertheless, adding and mixing in the champagne gas will mass-load and cool the hot superbubble interior gas. In addition, thermal evaporation from the dozens of clouds that are submersed in the hot gas of the superbubble, most notably the Orion Molecular clouds, will contribute to the mass-loading of the hot gas. It is difficult to constrain the relative contributions to the mass-loading of the hot gas through thermal and photo-evaporation, as the thermal evaporation rate is a steep function on temperature ($\propto T^{5/2}$; Cowie & McKee 1977), while photo-evaporation rates depend on the ionizing luminosity and main sequence lifetime of the ionizing star (e.g., Whitworth 1979; Bodenheimer et al. 1979). Nonetheless, we can infer that the *combined* effects of the mass-loading mechanisms have introduced some $6.7 \times 10^3 M_{\odot}$ of material into the superbubble cavity over the past 3×10^5 yr given by the mass and age of the H α shell associated with the Barnard's Loop bubble that acts to cleanse the interior of the superbubble close to the OMCs. These numbers imply an average evaporation rate (or cloud destruction rate) of $\sim 1 \times 10^{-2} M_{\odot} \text{ yr}^{-1}$, which is an order of magnitude above the current photo-erosion rate in the Orion Nebula, if we use a total ionized gas mass of $20 M_{\odot}$ (Wilson et al. 1997) and a dynamical lifetime of 1.5×10^4 yr (O'Dell et al. 2009). Part of this discrepancy may be because the Orion Nebula still resides in an early phase of evolution and the region has not fully broken out of its natal cloud. Nonetheless, mass-loading of the superbubble interior increased the density by a factor of ~ 100 compared to that expected in case the region within the Barnard's Loop bubble were filled with hot gas of the same characteristics as observed in the superbubble (Table 5.3). Over time, this will have a rigorous effect on the thermal behavior of the interior gas.

We note that the preshock density derived for the HV gas associated with the Barnard's Loop bubble in the line of sight toward ζ Ori (Sec. 5.3.3) is $3 \times 10^{-3} \text{ cm}^{-3}$, while we have derived an average density of 1 cm^{-3} for the medium in which the Barnard's Loop bubble has expanded in its 3×10^5 yr lifetime. Surely, the mass-loading mechanisms described here concentrate toward the center of star formation, i.e., the OMCs. There are believed to have been 10 - 20 SN explosions within Orion in the last 12 Myr (Bally 2008). With an expansion velocity of ~ 30 km s $^{-1}$ for the gas introduced through photoablation and champagne flows (Table 5.3), a supernova rate of 1 - 1.5 Myr $^{-1}$ will not allow the injected mass to disperse and fill the entire volume of the superbubble before being swept-up by a subsequent SNR. Thus, the increased densities due to mass-loading from the OMCs will be mainly concentrated within 30 - 45 pc surrounding the OB association (consistent with the radius of the Barnard's Loop bubble), whereas the surrounding medium will have a much lower density. The low temperature in the eastern part of the superbubble between Barnard's Loop and region 1 (Sec. 5.4.1) may also be caused by the effects of mass-loading. This would imply that other 'routes' of mass-loading affect the density and temperature structure of this region, such as enclosed clouds toward the Galactic plane, the straight evaporation of the superbubble wall, or SNRs that dissipate before reaching the superbubble wall (see below). However, as we have not been able to constrain the density structure of this region, the importance of mass-loading remains unclear.

In contrast to the shell of the Barnard's Loop bubble that is kept photo-ionized by Orion OB1 (Sec. 5.3.2), the neutral shells surrounding λ Ori and GS206-17+13 have had the chance to cool radiatively and collapse to form dense media. While they may add

to the mass-loading of the superbubble interior through thermal evaporation, their slow expansion renders them unimportant compared to the total energetics of the superbubble (Table 5.3). Still, these dense shells may be the site for a new generation of stars as they are prone to gravitational instabilities (Zavagno et al. 2007; Pomarès et al. 2009; Martins et al. 2010).

The supernova remnant associated with the Barnard's Loop bubble has exploded $\sim 3 \times 10^5$ yr ago and currently expands at 100 km s^{-1} , implying that it is well in the momentum-conserving snow plow phase (e.g., Tielens 2005). The postshock gas contains densities ($n = 3.4 \text{ cm}^{-3}$; Sec. 5.3.1) and temperatures ($T = 6000 \text{ K}$; Heiles et al. 2000; O'Dell et al. 2011; Madsen et al. 2006) that would allow the gas to cool rapidly ($\tau_{\text{cool}} \sim kT/n\Lambda(T) \sim 4 \times 10^4 \text{ yr}$, where $\Lambda(T) \approx 6 \times 10^{-25} \text{ erg cm}^3 \text{ s}^{-1}$; Dalgarno & McCray 1972). However, Barnard's Loop is kept photo-ionized by Orion OB1 (Sec. 5.3.2), prohibiting the cooling and collapse of the gas to form a dense neutral shell. In this case, the shockwave will continue to gather mass until it becomes subsonic, from which point it will dissipate and pressurize the interior, thus effectively displacing material from the origin of the blast wave toward the outskirts of the superbubble interior.

To get a feeling how far the displacement of material will reach, we can compare radii and expansion velocities of the Barnard's Loop bubble ($r = 35 \text{ pc}$, $v_{\text{exp}} = 100 \text{ km s}^{-1}$) and the superbubble ($r = 160 \text{ pc}$, $v_{\text{exp}} = 40 \text{ km s}^{-1}$) to estimate that the Barnard's Loop bubble will catch up with the outer wall within $\sim 2 \text{ Myr}$ if both structures decelerate at the same rate (in the radiative expansion phase, the velocity of the SNR decelerates with time as $\propto t^{-5/7}$; Tielens 2005). At this moment, the isothermal sound speed in the outer regions of the superbubble toward the east is $\sim 10 \text{ km s}^{-1}$ (for $T \sim 10^4 \text{ K}$; Sec. 5.4.1). If one assumes the lifetime of Barnard's Loop at $3 \times 10^5 \text{ yr}$, and adopt the time-velocity relation of the SNR above, the adiabatic expansion phase ($v_{\text{exp}} \gtrsim 250 \text{ km s}^{-1}$) ended just below 10^5 yr and it will take another $\sim 7 \text{ Myr}$ to reach 10 km s^{-1} if the density ahead of the SNR is homogeneous. This timescale far exceeds that derived for the Barnard's Loop bubble to catch up with the superbubble wall. Thus, Barnard's Loop will be able to cross the superbubble radius and reach the outer wall, where the shockwave will eventually thermalize and the swept-up material will transfer its mass and momentum by condensing onto the superbubble wall (Mac Low & McCray 1988). The outer superbubble wall may therefore be accelerated as various interior shells such as Barnard's loop catch up to it. In between such pulses, it could be coasting and slowing down as it sweeps up surrounding gas in a momentum conserving interaction, or it may be dissolving in case it moves subsonically (Sec. 5.4.1).

We note that densities in the outer parts of the superbubble are smaller compared to the mass-loaded region close to the OB association ($\sim 1 \text{ cm}^{-3}$; see above). In this case, the resulting pressure drop will accelerate the interior SNR once again when it reaches the edge of the mass-loading region, which already seems to be the case for the Barnard's Loop bubble, given the preshock density of $3 \times 10^{-3} \text{ cm}^{-3}$ in the line of sight toward $\zeta \text{ Ori}$ (Welty et al. 2002). Indeed, toward the west side of the superbubble, the temperature of the interior is much higher and the SNR will accelerate, but it may go subsonic and dissolve earlier compared to the east side of the bubble: this may be at the root of the faintness of the $H\alpha$ emitting shell in this direction (Sec. 5.4.1). Towards the east, the density gradient could be smaller because of the lower temperature that may be accompanied by an increase in density, and the amount of acceleration will decrease accordingly.

If 10 - 20 SN explosions occurred in the Orion region in the past 12 Myr (Bally 2008), and each SNR adds $\sim 7 \times 10^3 M_{\odot}$ of material to the superbubble wall (Table 5.3), this will amount to $0.7 - 1.4 \times 10^5 M_{\odot}$ and account for a significant fraction (20 - 40 %) of its total mass. Thus, the mass of the superbubble wall without the addition from SNRs would account for $1.9 - 2.6 \times 10^5 M_{\odot}$. With a radius of 160 pc, we can estimate the average ISM density into which the superbubble has expanded at $n \sim 0.15 - 0.2 \text{ cm}^{-3}$, consistent with the WNM within one or two scale heights of the Galactic plane. Finally, as the timescale between successive SNe is of the same order as the timescale for the Barnard's Loop bubble to catch up with the outer wall, it may not be necessary to expect multiple layers of expanding shells between the Orion OB association and the superbubble wall.

Efficiency of star formation in the Orion molecular clouds

Given a total mass of $\sim 2 \times 10^5 M_{\odot}$ for the OMCs combined, a supernova rate of $1 - 1.5 \text{ Myr}^{-1}$ (Bally 2008) and swept-up mass of $\sim 7 \times 10^3 M_{\odot}$ per SNR (the mass of the H α emitting part of the Barnard's Loop bubble), we estimate that at this rate the reservoir of cloud material will be depleted within 20 - 30 Myr through thermal evaporation and erosion from champagne flows alone, similar to calculated cloud lifetimes from Williams & McKee (1997). Thus, material is effectively removed from the molecular clouds and incorporated in expanding shells that might form stars of their own. Furthermore, the molecular clouds will be disrupted by each supernova blast wave that mark the end of a cycle of star formation. All of these effects should be considered if one attempts to simulate the lifecycle of molecular clouds and the efficiency of star formation, which is well known to be limited by various forms of stellar feedback (for a recent review, see Krumholz et al. 2014).

The gradual erosion of the OMCs puts a firm upper limit on the lifetime of the molecular clouds. Over the past 10 - 15 Myr, some $\sim 10^5 M_{\odot}$ has already been lost from the OMCs to the superbubble wall, which implies that the original molecular reservoir (the 'proto-Orion' cloud) contained some $\sim 3 \times 10^5 M_{\odot}$ (Table 5.3). At present, the major subgroups of the Orion OB association (Blaauw 1964; Brown et al. 1994) constitute some $6.9 \times 10^3 M_{\odot}$ of stellar mass. The ages of the subgroups imply that many stars have already exploded as supernova (Sec. 5.4.3; Bally 2008), and we estimate from the adopted IMF that about 20% of the initial mass of the 1a, 1b, and 1c subgroups has been lost through SN explosions, increasing the total mass that has been incorporated into stars over the last 10 - 15 Myr toward $\sim 7.4 \times 10^3 M_{\odot}$. With a remaining cloud lifetime of the OMCs of 20 - 30 Myr, at the current rate, some $\sim 2.2 \times 10^4 M_{\odot}$ or 7.5% of the molecular mass can be converted into stars over the lifetime of the clouds consistent with predictions by, e.g., Williams & McKee (1997). However, it is unclear if star formation will proceed similarly as stellar feedback may trigger star formation *and* disrupt the clouds, while the molecular reservoir steadily diminishes (see, e.g., Evans et al. 2009; Hopkins et al. 2011; Krumholz et al. 2014 for more thorough discussions regarding the mechanisms that involve star formation rates and molecular cloud lifetimes).

Summary: the rejuvenation of the Orion-Eridanus superbubble

We have argued that appreciable amounts of mass will be removed from the molecular clouds and be mass-loaded into the interior of the superbubble through destructive cham-

pagne flows and thermal evaporation of clouds embedded in the hot gas of the superbubble interior. Explosive feedback from stellar winds and, in particular, supernovae take care of the subsequent transportation of the mass-loaded material toward the outskirts of the superbubble through the formation of expanding nested shells. For the Barnard's Loop bubble toward the east, photo-ionization by Orion OB1 does not allow it to radiatively cool and collapse, and it will plaster the mass and add momentum to the superbubble wall that will continue to drive the expansion of the superbubble. In case it would go subsonic before reaching the outer wall, the shell would dissolve, thermalize, and pressurize the interior. This cycle repeats as long as there is ongoing star formation and OB stars can maintain (the photo-ionization of) the cleansing shells that deposit the mass toward the outer regions.

5.4.4 Dust processing in superbubbles

An interesting consequence of the constant mass-loading of the superbubble is that each supernova explosion within the superbubble cavity will interact with a significant amount of 'fresh' interstellar gas that carries along dust in its wake through entrainment. The efficiency of dust entrainment in photo-evaporation flows was investigated by Ochsendorf & Tielens (2015) for the IC 434 champagne flow, revealing that the dust-to-gas ratio within the flow is similar to that seen in the diffuse ISM (~ 0.01). Thus, each single SNR from the Orion OB1 association will encounter a new reservoir of gas and dust within the superbubble cavity, introduced by champagne flows from the H II regions and from photo-evaporation flows of the thermally evaporating clouds. This finding contrasts with that of McKee (1989), who previously estimated the timescale for SNR shocks to destroy a typical dust grain within the ISM. McKee (1989) assumed that only the first supernova within an OB association would destroy an amount of dust equivalent to that located in an ISM volume containing $\sim 1300 M_{\odot}$ of gas. Following supernovae from the OB association would hammer surrounding gas already cleansed of its dust component. Following McKee (1989), the *effective* SN rate is equal to

$$\tau_{\text{SN}}^{-1} = (q_{\text{I}} f_{\text{I}} + [f_{\text{II,OB}} q_{\text{II,OB}} + f_{\text{II,field}} q_{\text{II,field}}] f_{\text{II}}) \kappa_{\text{SN}} \text{ yr}. \quad (5.6)$$

Here, q_{I} is the correlation factor of the SNe of type Ia (~ 0.38 ; Heiles 1987), relating the location of the SN to their position above the disk of the Galaxy (i.e., it measures the effective interaction of the SNe with the amount of gas in their environment), and f_{I} is the fraction of supernovae of type Ia (~ 0.5 ; Narayan 1987). Similarly, f_{II} ($= 1 - f_{\text{I}}$) measures the fraction of supernova of type II, part of which occur in OB associations, described by $f_{\text{II,OB}}$ (~ 0.75 ; see Zinnecker & Yorke 2007, and references therein), and in the field, denoted with $f_{\text{II,field}}$ ($= 1 - f_{\text{II,OB}}$), originating from runaways and isolated stars with correlation factor $q_{\text{II,field}}$ (~ 0.6 ; using values for the scale height of the WNM by Heiles 1987). Finally, κ_{SN} is the intrinsic SN rate in the Galaxy ($\sim 2 \times 10^{-2} \text{ yr}^{-1}$; Diehl et al. 2006).

Under the assumption that superbubbles do not replenish their dust content after the first SNR, McKee (1989) arrived at a correlation factor of $q_{\text{II,OB}} = 0.1$ and, together with a rather low value for the fraction of type II SNe in OB associations, $f_{\text{II,OB}} = 0.5$, derived an effective SN rate of $\tau_{\text{SN}} = 125 \text{ yr}$. In this work, we have shown that dust entrainment accompanying mass-loading of the superbubble interior replenishes the dust content in-

side the superbubble after each SNR from the OB association, i.e., $q_{\text{II,OB}} = 1$. In addition, we use the more recently derived fraction of OB stars that are located in OB associations from Zinnecker & Yorke (2007), $f_{\text{II,OB}} = 0.75$. These changes lead to shorter effective supernova rate of $\tau_{\text{SN}} = 90$ yr, implying that the SNRs within superbubbles destroy dust more efficiently and, subsequently, the dust lifetime against SNR shocks must be revised downwards by 30%.

The processing of dust inside the superbubble can also be probed directly from depletion studies. Welty et al. (2002) noted that in the HV and IV gas toward ζ Ori, the gas-phase abundances of Al, Si and Fe are slightly elevated compared to that observed in warm, diffuse clouds. However, the carbon abundance is *significantly* raised in the HV gas to near-solar abundances. For comparison, depletion studies of the Cold Neutral Medium (CNM) and the WNM show a pattern where a thin coating on interstellar dust gets sputtered and re-accreted, as the grains cycle from clouds to the diffuse phase of the ISM (Tielens 1998, 2013). Whilst in the WNM, the reservoir of gas and dust typically encounters a 100 km s^{-1} passing shock, destroying some 10 - 30% of the silicate volume (Jones et al. 1996). However, these shock velocities would only destroy 15% of the carbonaceous dust and lead to minor variations in the carbon depletion, as $\sim 50\%$ of the carbon is in the gas phase (Cardelli et al. 1996; Sofia et al. 2004). Therefore, instead of passing shocks, we attribute the enhanced carbon abundance to sputtering of the grains inside the hot gas of the Orion-Eridanus superbubble. The sputtering timescale τ_{sput} (Tielens et al. 1994) in the X-ray emitting gas ($T \sim 10^6 \text{ K}$, $n \sim 0.01 \text{ cm}^{-3}$) implies that large $0.1 \mu\text{m}$ silicate grains are hardly affected ($\tau_{\text{sput}} > 20 \text{ Myr}$), yet, small $\sim 10 \text{ \AA}$ (carbonaceous) grains are quickly eroded ($\tau_{\text{sput}} < 1 \text{ Myr}$), releasing the carbon into the gas-phase. We argue that this may be a general characteristic for dust that is processed inside superbubbles. Indeed, dust entering the heliosphere also shows a significant increase of gas-phase carbon, implying that the grains are sputtered within the hot gas of the Local Bubble (Frisch & Slavin 2013).

5.5 Summary

The general picture that emerges from the multitude of data is that the Orion-Eridanus superbubble is larger and more complex than previously thought, consisting of a series of nested shells which we depict in Fig. 5.6. With the data currently at hand, we have discussed the following structures, ordered in size from bottom up:

- The youngest shell surrounds the Orion Nebula cluster located in Orion A (age $< 1 \text{ Myr}$; Bally 2008).
- Next, there is the 2 to 4 degree HI and dust shell GS206-17+13, approximately centered on the σ Ori cluster, but likely blown by stellar winds from the Belt stars (age $\sim 5 \text{ Myr}$; Ochsendorf & Tielens 2015).
- Barnard's Loop is part of a complete bubble structure not related to the outer edge of the Orion-Eridanus superbubble. It is instead associated with a supernova remnant (age $\sim 3 \times 10^5 \text{ yr}$), and is connected with high-velocity gas ("Orion's Cloak") detected in absorption studies (Cowie et al. 1979; Welty et al. 2002). All of the previous shells are projected in the interior of this young 7 degree radius bubble, which expands at high velocity ($v_{\text{exp}} \sim 100 \text{ km s}^{-1}$).

- The Barnard's Loop bubble and the λ Ori bubble (~ 5 Myr; Bally 2008) expand in the interior of the $\sim 45 \times 45$ degree shell that is related to intermediate-velocity gas from the aforementioned absorption studies and created by the collective effects of Orion's stars: the Orion-Eridanus superbubble (age $\sim 5 - 10$ Myr).

As we can recognize several distinct subgroups and well defined clusters, star formation in the Orion-Eridanus region must have been highly episodic over the last 10 - 15 Myr. It may therefore not be surprising that the Orion-Eridanus superbubble consists of a set of nested shells. Each "burst" of star formation may have produced a subgroup consisting of several clusters that disrupted parts of the pre-existing molecular cloud. The formation of each subgroup and the resulting UV radiation can ionize large amounts from the dense reservoir of molecular gas in the region that, together with thermal evaporation of the molecular clouds, constantly mass-load and cool the hot gas inside the superbubble cavity. Stellar winds and supernovae accelerate, sweep-up, and compress these "poisoned" plasmas in an episodic fashion to form nested shells within the Orion-Eridanus superbubble, such as the Barnard's Loop bubble, the λ Ori bubble, the GS206-17+13 shell, and the Orion Nebula (see Fig. 5.6). The shells may cool, collapse, fragment, and be incorporated in a next generation of stars. However, for the Barnard's Loop bubble, this shell cooling is inhibited by photo-ionization from the OB association. We have noted that in its turn, the Orion-Eridanus superbubble has previously been associated with the ancient supershell known as Lindblad's ring, which may have cooled and collapsed to form the Gould's Belt of stars that includes the Orion OB association, extending the hierarchy of nested shells and bubbles toward greater sizes and into history. The continuous replenishment of dust in the superbubble cavity through entrainment in ionized flows has led us to conclude that dust processing from interior supernova remnants is more efficient than previously thought. To conclude, the cycle of mass-loading, cleansing, and star formation ceases when feedback has disrupted the molecular reservoir, from which the superbubble will disappear and merge with the ISM.

Acknowledgements

The authors would like to thank the anonymous referee for detailed comments that significantly increased the quality of this paper. Studies of interstellar dust and chemistry at Leiden Observatory are supported through advanced ERC grant 246976 from the European Research Council, through a grant by the Dutch Science Agency, NWO, as part of the Dutch Astrochemistry Network, and through the Spinoza premie from the Dutch Science Agency, NWO. JB was supported in part by National Science Foundation (NSF) grant AST-1009847.

6

Summary & outlook

In this thesis, I have addressed many aspects of the interaction between stars and the matter residing in the ISM. Much of this work has relied on observations of recent infrared space observatories. However, with the end of the *Spitzer*, *Herschel*, *Planck*, and WISE missions, the influx of (far-)IR to submillimeter observations will slow considerably. Nonetheless, the archives still provide a wealth of information, while SOFIA, together with ground-based facilities, such as the recently commissioned *Atacama Large Millimeter Array* (ALMA), will continue to define the research questions that will be addressed with the next generation of (space) telescopes. Looking beyond the era of the *Hubble Space Telescope* (HST), *Hipparcos*, and the IR space missions from the last decade, we will have the *James Webb Space Telescope* (JWST), *Gaia*, while future IR missions are already on the drawing board, such as the *Space Infrared Telescope for Cosmology and Astrophysics* (SPICA). This chapter is devoted to summarize the main results from the first four years of my academic career, to specify and formulate the questions that have remained and have arisen during this course, and to highlight some of the promising opportunities in the field that shimmer on the horizon.

Chapters 2 & 3: Dust waves & dust characterization in H II regions

- **Results:** we have developed a new method to study the properties of interstellar dust. Observations of gas and dust at the interface between molecular clouds and H II regions were exploited, and we developed a model that describes the interaction of a dusty ionized flow of gas with nearby (massive) stars, where radiation pressure stalls dust and force it to flow around the star to form a dust wave. In this way, we were able to constrain important parameters of the dust grains within ionized regions. Some of the results are puzzling, and seem to contrast with other studies of interstellar dust.
- **Open questions:** The dust grain size distribution from the IC 434 region is bimodal, consisting of large micron-sized fluffy/porous grains and small compact particles. We have hypothesized in Ch. 3 that grain properties may reflect their previous environment, linking the presence of large grains in the IC 434 H II region to the molecular clouds from which they are ‘freshly’ evaporated. The dust population that is introduced into the H II region will be processed as it is suddenly exposed to the harsh conditions in the ISM, such as gas-grain friction, (thermal) sputtering, and interstellar shocks. Perhaps, dust in the diffuse ISM, far away from dense molecular clouds, represents an ‘equilibrium state’ after the grains are fully processed by the ISM. The models from, e.g., Draine & Li (2007) do seem to reproduce and dominate dust emission properties of diffuse clouds and complete galaxies (e.g., Smith

et al. 2007). However, it is very important to note that observations performed with beams that integrate a large part or even a complete galaxy will not detect the (micro-)processes that may occur between the dense and diffuse phases of the ISM at \sim pc scales. Yet, it is these regions that could be physically interesting and where important physical parameters of the grains may be probed, as is illustrated by the results from Ch. 2 and 3. Does interstellar dust in the diffuse ISM represent a steady state configuration, or do the grains undergo a steady evolution? Perhaps the relevant question is: what are the processing timescales of interstellar dust when transitioning between different phases of the ISM?

Specifically, Coulomb interactions between gas and dust may be less efficient in the IC 434 region than predicted by theory. In the RCW 120 and RCW 82 H II regions, the location of the dust waves are compatible with this finding (Ch. 4). Is it the physical conditions of the region, the intrinsic grain properties, or the charging mechanism of the grains that we do not fully understand? In case of the latter, how does this impact the photo-electric heating efficiency from (small) grains?

- **The way forward:** the results from Ch. 2 and 3 stress that we need to stay critical as we advance our knowledge concerning interstellar dust. At the distance of Orion, *Spitzer* and *Herschel* offered the necessary angular resolution (< 1 pc) to separate the dust emission coming from the H II region from that located in the bright PDRs. In addition, and as will be discussed below, we were also able to recognize the existence of dust waves inside interstellar bubbles throughout the Galactic plane, the exploitation of which may provide valuable information on dust in H II regions and the evolution of the grains between different phases of the ISM. However, *Herschel* lacks the sensitivity to detect the faint, diffuse emission from dust in a large sample of H II regions, especially at $70 \mu\text{m}$, a crucial regime to distinguish between warm and cold components of dust within H II regions (Ch. 3). The diffuse dust from the IC 434 region could not be detected at $70 \mu\text{m}$ by *Herschel*, but was recovered using IRAS observations. The photometric sensitivity of *Herschel* is limited by thermal noise emission (mostly from the telescope itself) and the noise of the readout electronics. SPICA (Swinyard et al. 2009) appears to be the next space-based satellite that will peer into the far-IR. SPICA will provide a telescope similar to *Herschel*, but will be cooled to $\lesssim 6$ K, thus removing its self-emission and reaching a sensitivity of up to two orders of magnitude greater as compared to *Herschel*, and will be equipped with photometric, spectroscopic, and coronagraphic capabilities. With SPICA, we will be able to improve the dust observations in the IC 434 region and extend similar studies of dust in H II regions to much greater distances, and hence probe a large sample of H II regions that vary in density, physical size, environment, and source luminosity.

Galactic studies of H II regions are often complicated by confusion that will affect the process of separating contributions from dust emission related to structures along the line of sight, dust that is located in the PDRs of H II regions, and grains that are mixed inside the ionized gas. In this regard, the large Magellanic cloud offers a unique opportunity to study dust evolution, given the location offset from the Galactic plane, its face-on appearance, and its relative proximity. JWST will be crucial here, because at the distance of the Large Magellanic cloud (50 kpc; Walker

2012), its large mirror (6.5 m) will offer the angular resolution ($\sim 0.25''$ or 1 pc at 10 μm) that will allow to resolve dust populations from individual H II regions, such as the 30 Doradus region, and perhaps dust waves surrounding individual stars. Indeed, studies of OB stars in the LMC and SMC have revealed a population of ‘dusty OB stars’ with dramatic mid-IR excesses (Bonanos et al. 2010; Sheets et al. 2013), well explained by the dust wave scenario. The study of dusty OB stars and dust evolution between different phases of the ISM could provide quantitative information on dust properties across the large Magellanic cloud and the cycling of matter on a galaxy-wide scale.

Lastly, while advances in observational facilities are clearly desirable to develop our understanding of interstellar dust and its relation to the structure and evolution of the ISM, it must be noted that laboratory work also provides a promising avenue for future research on interstellar dust. Recent measurements on laboratory analogues of interstellar silicate materials provide clues to the optical properties of interstellar silicates, but the analysis of this data is challenging (see Jones 2014, and references therein). In addition, photo-electric yields for carbonaceous and silicate materials as measured by Willis et al. (1973) and Abbas et al. (2006) differ by up to an order of magnitude. The results reveal a clear size dependence on photo-electric emission and a significant difference in yields measured from bulk materials compared to those measures on individual dust grains. More laboratory work is needed to better constrain fundamental properties of interstellar dust, such as their intrinsic composition and photo-electric yields.

Chapter 4: Interstellar bubbles & stellar feedback mechanisms

- **Results:** we studied the expansion of Galactic H II regions and the formation of dust waves therein. The bubbles seen in *Spitzer* and *Herschel* surveys of the Galactic plane offer a unique opportunity to study the formation of dust waves and stellar feedback mechanisms in relative young regions of simple geometry. At the same time, dust waves offer a natural explanation for the presence and morphology of dust in H II regions, and provide direct evidence for bubble flows that may be a key source of turbulence controlling the structure of the ISM on small scales.
- **Open questions:** The existence of radiation-pressure-driven dust waves in interstellar bubbles questions the importance of stellar winds during the formation of H II regions. Do main sequence stars really have weak winds? How does this translate to the relative contributions to the dynamics of H II regions from stellar winds (Weaver et al. 1977), overpressure of ionized gas (Spitzer 1978), or radiation pressure on dust grains (Krumholz & Matzner 2009)? We have shown that the importance of dust as an intermediary of radiative feedback depends heavily on the assumed gas and grain properties. If the right conditions are met, radiation pressure may be an important mechanism of stellar feedback to H II region dynamics, or even galactic outflows.
- **The way forward:** The results from Ch. 4 illustrate that we still do not fully understand the main sources of energy that drive the complex and chaotic appearance of the ISM seen to date (Ch. 1). In order to advance our knowledge on

the processes that govern the interactions between gas, dust, and stars, we must first understand the individual components. The characterization of interstellar dust has been discussed above. The IR surveys of the Galactic plane and nearby galaxies have opened up the IR sky as never before, offering important information about the structure and dynamics of the dusty ISM. However, complementary high-resolution, high-sensitivity radio spectroscopic surveys are needed to resolve the distribution of the gas component and its dynamics. Indeed, radio recombination line (RRL) measurements trace many physical properties of ionized gas, such as temperature, density, metallicity, and perhaps most importantly, its kinematics (see Thompson et al. 2015, and references therein). Current spectroscopic surveys are limited, as there is a tradeoff between sensitivity and angular resolution. On the one hand, single-dish surveys like SIGGMA (Liu et al. 2013) on Arecibo offer the sensitivity to trace interstellar plasmas down to electron densities of $n_e \sim 10 \text{ cm}^{-3}$, but only at several arcminutes of resolution. On the other hand, interferometric surveys such as THOR (Bühr et al. 2015) offer better angular resolution ($\sim 10''$), but its sensitivity only allows to trace high-density plasmas at $n_e \gtrsim 1000 \text{ cm}^{-3}$.

The future *Square Kilometer Array* (Dewdney et al. 2009), with its bandwidth, survey speed, and unprecedented sensitivity, will provide a unique opportunity to perform deep spectroscopic surveys of ionized gas down to densities below 50 cm^{-3} for the entire Galactic Plane at a $\sim 2''$ resolution, offering a synergy with ALMA studies of higher-frequency recombination lines. Moreover, its coverage includes multiple transitions of light radicals and molecules (Thompson et al. 2015). Thus, the SKA will revolutionize our understanding of the kinematic structure of the ionized (and molecular) component of the ISM at a resolution comparable to those of the IR surveys of the Galactic plane, allowing to directly quantify the coupling between gas and dust, and the importance of the various feedback mechanisms to the structure and evolution of the ISM.

Chapter 5: Evolution of superbubbles & the connection to star formation and molecular clouds lifetimes

- **Results:** we have performed an observational analysis of the Orion-Eridanus superbubble using the tools developed in the previous chapters. The synergy of different datasets resulted in an updated picture of the morphological and dynamical structure of the superbubble. Furthermore, we proposed a scenario for its future evolution. The Orion molecular clouds gradually evaporate and mass-load the interior of the superbubble through destructive champagne flows and thermal evaporation of clouds embedded in the hot gas. Explosive feedback mechanisms accelerate, sweep-up, and compress these ‘poisoned’ plasmas in an episodic fashion to form nested shells within the Orion-Eridanus superbubble that may cool, collapse, and fragment, to form stars of their own. The shells rejuvenate the superbubble by cleansing the interior and by plastering the mass and add momentum to the outer wall, driving the further expansion of the superbubble.
- **Open questions:** the results from this chapter revealed that the structure and evolution of the Orion-Eridanus superbubble is more complex than previously thought,

exhibiting an active interplay between stellar feedback, ISM evolution, and star formation. However, one can question whether the Orion-Eridanus superbubble can be viewed as a prototypical example for superbubbles in general. Is ‘rejuvenation’ of a superbubble a common phenomenon? How does this affect the lifecycle of molecular clouds and their integrated star formation efficiency? Is there a connection between the nested shells and the existence of separate subgroups in the Orion OB association? Is triggered star formation at play in the Orion region? Does the superbubble eventually blow out of the plane and ‘feed’ the Galactic halo?

- **The way forward:** The all-sky surveys from WISE and *Planck* have mapped the extremely large region on the sky covered by the Orion-Eridanus superbubble (45×45 degrees), while the position of the superbubble outside of the galactic plane allowed for the detection of the ionized gas component and its kinematics at optical wavelengths. Acquiring similar datasets of Galactic superbubbles, as well as those within nearby galaxies, will be limited by either confusion, extinction, sensitivity, or spatial resolution. An exception to this rule are the superbubbles located in the Magellanic clouds (Lopez et al. 2011; Pellegrini et al. 2011; Lopez et al. 2014). JWST will play a crucial role here by obtaining high-resolution and sensitive images of the dust structure of bubbles and superbubbles throughout the Magellanic clouds. The detection of $24 \mu\text{m}$ emission from dust waves within superbubble structures will provide information on the dynamics of interior flows and the evaporation of molecular clouds that fuels the expansion of superbubbles (Ch. 5).

The disk-halo connection of galaxies and the importance of superbubble blowouts remains poorly understood, in part because the emission from the gas and dust of extended haloes is very faint and hard to detect. Highly ionized gas species can be traced with absorption lines studies, but the studied amount of sightlines are sparse and left at the mercy of available background sources. JWST, equipped with an integral-field-unit and an unprecedented sensitivity, may be able to trace the emission structure and dynamics of galactic winds of many nearby galaxies, such as that observed in M82 (e.g., Engelbracht et al. 2006). Together with our work on the various forms of stellar feedback in Ch. 4 and the evolution of superbubbles in Ch. 5, we may be able to further develop our understanding to the origin of these galactic winds and establish the disk-halo connection within galaxies.

Even within nearby star forming regions, proper motions and the three-dimensional distribution of stars are poorly constrained by photometric indicators or the astrometric accuracy offered by *Hipparcos* (van Leeuwen 2007), such that questions whether or not star formation is triggered in Orion OB1 remain open and controversial. *Gaia* (de Bruijne 2012) will measure parallaxes and proper motions at an accuracy two orders of magnitude higher than *Hipparcos*, delivering astrometric, photometric, and spectroscopic data of over a billion stellar objects, thus providing the necessary measurements to determine positions, distances, motions, and luminosities of nearby stars. In this way, we will obtain the three-dimensional distribution of nearby stars that is essential to address the importance of, e.g., triggered star formation (Elmegreen & Lada 1977) in Orion (Ch. 5), for which one needs *precise* measurements of proper motion, radial velocities, and ages. In this way, the circle of interactions between gas, dust, and stars in the ISM of Orion will be completed.

Summary

In conclusion, exciting times lie ahead, as considerable potential lies within the exploitation of future facilities that will provide us with the right tools to advance our knowledge of the interplay of gas, dust, and stars in the ISM. Concretely, and in direct relation to the contents of this thesis, JWST will allow us to probe the origin and evolution of interstellar dust over a much larger distance, and we will be able to compare the results from Ch. 2 and 3 from this thesis to that of more distant regions than Orion, out to the Magellanic clouds. Future radio telescopes, like the SKA, will allow us to address the importance of stellar feedback mechanisms after charting the gaseous structure of the Milky Way by peering through the Galactic plane with unbiased surveys (Ch. 4). *Gaia* will provide the definite location of stellar populations within Orion to assess the connection between the stars and the nested shells of the Orion-Eridanus superbubble (Ch. 5).

Final remarks

This outlook has mainly focussed on observational prospects, as observations lie at the root of many of the questions addressed in this thesis and, more importantly, reflects my personal interests. However, it is my belief that breakthroughs and revolutions in astronomy will only be possible through the combined efforts of theorists, modelers, experimentalists, and observers from the physical, chemical, and biological sciences, while future generations of talented scientists need to keep inspired with images and mind-bending questions that come along while investigating the vast richness of the Universe.

The golden era of (far-)IR space observatories has, at the moment, temporarily slowed its pace. Still, a vast wealth of observational data remains unexplored, perhaps exemplified through the contents of this thesis, where I have formulated and addressed some of the puzzling questions that have arisen while looking at Orion, classically one of the best studied regions of the sky. Only when we fully grasp the complex processes that govern galactic ecologies in the local Universe, will we be able to relate this to observations of the early Universe at high-redshifts, and fully appreciate the capabilities that will be offered by future facilities.

Bibliography

- Abbas, M. M., Tankosic, D., Craven, P. D., et al. 2006, *ApJ*, 645, 324
- Abergel, A., Bernard, J. P., Boulanger, F., et al. 2002, *A&A*, 389, 239
- Abergel, A., Teyssier, D., Bernard, J. P., et al. 2003, *A&A*, 410, 577
- Allamandola, L. J., Hudgins, D. M., & Sandford, S. A. 1999, *ApJL*, 511, L115
- Allen, L. E. & Davis, C. J. 2008, Low Mass Star Formation in the Lynds 1641 Molecular Cloud, ed. B. Reipurth, 621
- Alves, J. & Bouy, H. 2012, *A&A*, 547, A97
- Anantharamaiah, K. R., Viallefond, F., Mohan, N. R., Goss, W. M., & Zhao, J. H. 2000, *ApJ*, 537, 613
- Anderson, L. D. & Bania, T. M. 2009, *ApJ*, 690, 706
- Anderson, L. D., Zavagno, A., Deharveng, L., et al. 2012, *A&A*, 542, A10
- André, P., Men'shchikov, A., Bontemps, S., et al. 2010, *A&A*, 518, L102
- Andrews, B. H. & Thompson, T. A. 2011, *ApJ*, 727, 97
- Aniano, G., Draine, B. T., Gordon, K. D., & Sandstrom, K. 2011, *PASP*, 123, 1218
- Arthur, S. J. 2012, *MNRAS*, 421, 1283
- Arthur, S. J. & Henney, W. J. 1996, *ApJ*, 457, 752
- Arthur, S. J., Kurtz, S. E., Franco, J., & Albarrán, M. Y. 2004, *ApJ*, 608, 282
- Auer, L. H. & Mihalas, D. 1969, *ApJL*, 156, L151
- Baines, M. J., Williams, I. P., & Asebiomo, A. S. 1965, *MNRAS*, 130, 63
- Ballesteros-Paredes, J., Klessen, R. S., & Vázquez-Semadeni, E. 2003, *ApJ*, 592, 188
- Bally, J. 2008, Handbook of Star Forming Regions, Vol. 4, ed. B. Reipurth (The Northern Sky ASP Monograph Publications), p. 459
- Bally, J., Langer, W. D., Stark, A. A., & Wilson, R. W. 1987, *ApJL*, 312, L45
- Bally, J., Walawender, J., Reipurth, B., & Megeath, S. T. 2009, *AJ*, 137, 3843
- Barnard, E. E. 1894, Popular Astronomy, 2, 151
- Barnard, E. E. 1919, *ApJ*, 49, 1
- Barrado y Navascués, D., Stauffer, J. R., Bouvier, J., Jayawardhana, R., & Cuillandre, J.-C. 2004, *ApJ*, 610, 1064
- Basu, S., Johnstone, D., & Martin, P. G. 1999, *ApJ*, 516, 843
- Bauschlicher, Jr., C. W. 2002, *ApJ*, 564, 782
- Bazell, D. & Dwek, E. 1990, *ApJ*, 360, 142
- Beaumont, C. N. & Williams, J. P. 2010, *ApJ*, 709, 791
- Beckwith, S. V. W., Sargent, A. I., Chini, R. S., & Guesten, R. 1990, *AJ*, 99, 924
- Bedijn, P. J. & Tenorio-Tagle, G. 1981, *A&A*, 98, 85
- Béjar, V. J. S., Zapatero Osorio, M. R., Rebolo, R., et al. 2011, *ApJ*, 743, 64
- Benjamin, R. A., Churchwell, E., Babler, B. L., et al. 2003, *PASP*, 115, 953
- Bernard, J.-P., Paradis, D., Marshall, D. J., et al. 2010, *A&A*, 518, L88
- Bertoldi, F. 1989, *ApJ*, 346, 735
- Bihr, S., Beuther, H., Ott, J., et al. 2015, ArXiv e-prints
- Bisnovatyi-Kogan, G. S. & Silich, S. A. 1995, Reviews of Modern Physics, 67, 661
- Blaauw, A. 1961, *Bul. Astr. Ins. of the Neth.*, 15, 265
- Blaauw, A. 1964, *ARA&A*, 2, 213
- Blomme, R., Prinja, R. K., Runacres, M. C., & Colley, S. 2002, *A&A*, 382, 921

- Bock, D. C.-J., Large, M. I., & Sadler, E. M. 1999, *AJ*, 117, 1578
- Bodenheimer, P., Tenorio-Tagle, G., & Yorke, H. W. 1979, *ApJ*, 233, 85
- Bohlin, R. C., Savage, B. D., & Drake, J. F. 1978, *ApJ*, 224, 132
- Boissé, P., Rollinde, E., Hily-Blant, P., et al. 2009, *A&A*, 501, 221
- Bonanos, A. Z., Lennon, D. J., Köhlinger, F., et al. 2010, *AJ*, 140, 416
- Bouret, J.-C., Lanz, T., Hillier, D. J., et al. 2003, *ApJ*, 595, 1182
- Bouy, H., Alves, J., Bertin, E., Sarro, L. M., & Barrado, D. 2014, *A&A*, 564, A29
- Brown, A. G. A., Blaauw, A., Hoogerwerf, R., de Bruijne, J. H. J., & de Zeeuw, P. T. 1999, in NATO Advanced Science Institutes (ASI) Series C, Vol. 540, NATO Advanced Science Institutes (ASI) Series C, ed. C. J. Lada & N. D. Kylafis, 411
- Brown, A. G. A., de Geus, E. J., & de Zeeuw, P. T. 1994, *A&A*, 289, 101
- Brown, A. G. A., Hartmann, D., & Burton, W. B. 1995, *A&A*, 300, 903
- Brown, D. & Bomans, D. J. 2005, *A&A*, 439, 183
- Burrows, D. N., Singh, K. P., Nousek, J. A., Garmire, G. P., & Good, J. 1993, *ApJ*, 406, 97
- Caballero, J. A. 2007a, *A&A*, 466, 917
- Caballero, J. A. 2007b, *A&A*, 466, 917
- Caballero, J. A. 2008, *MNRAS*, 383, 750
- Caballero, J. A., Béjar, V. J. S., Rebolo, R., et al. 2007, *A&A*, 470, 903
- Caballero, J. A., Valdivielso, L., Martín, E. L., et al. 2008, *A&A*, 491, 515
- Cardelli, J. A., Clayton, G. C., & Mathis, J. S. 1989, *ApJ*, 345, 245
- Cardelli, J. A., Meyer, D. M., Jura, M., & Savage, B. D. 1996, *ApJ*, 467, 334
- Carey, S. J., Noriega-Crespo, A., Mizuno, D. R., et al. 2009, *PASP*, 121, 76
- Castor, J., McCray, R., & Weaver, R. 1975, *ApJL*, 200, L107
- Cesarsky, D., Lequeux, J., Ryter, C., & Gérin, M. 2000, *A&A*, 354, L87
- Chandrasekhar, S. 1943, *ApJ*, 97, 255
- Chevalier, R. A. 1974, *ApJ*, 188, 501
- Chini, R., Kruegel, E., & Kreysa, E. 1986, *A&A*, 167, 315
- Chu, Y.-H. 2008, in IAU Symposium, Vol. 250, IAU Symposium, ed. F. Bresolin, P. A. Crowther, & J. Puls, 341–354
- Chu, Y.-H. & Mac Low, M.-M. 1990a, *ApJ*, 365, 510
- Chu, Y.-H. & Mac Low, M.-M. 1990b, *ApJ*, 365, 510
- Churchwell, E., Povich, M. S., Allen, D., et al. 2006, *ApJ*, 649, 759
- Churchwell, E., Watson, D. F., Povich, M. S., et al. 2007, *ApJ*, 670, 428
- Coşkunoğlu, B., Ak, S., Bilir, S., et al. 2011, *MNRAS*, 412, 1237
- Comeron, F. & Kaper, L. 1998, *A&A*, 338, 273
- Comeron, F., Rieke, G. H., & Rieke, M. J. 1996, *ApJ*, 473, 294
- Compiègne, M., Abergel, A., Verstraete, L., et al. 2007, *A&A*, 471, 205
- Compiègne, M., Verstraete, L., Jones, A., et al. 2011, *A&A*, 525, A103
- Condon, J. J., Cotton, W. D., Greisen, E. W., et al. 1998, *AJ*, 115, 1693
- Cowie, L. L. & McKee, C. F. 1977, *ApJ*, 211, 135
- Cowie, L. L., McKee, C. F., & Ostriker, J. P. 1981, *ApJ*, 247, 908
- Cowie, L. L., Songaila, A., & York, D. G. 1979, *ApJ*, 230, 469
- Cowie, L. L. & York, D. G. 1978, *ApJ*, 220, 129
- Cox, N. L. J., Kerschbaum, F., van Marle, A.-J., et al. 2012, *A&A*, 537, A35
- Crowther, P. A., Lennon, D. J., & Walborn, N. R. 2006, *A&A*, 446, 279

- Dale, J. E., Bonnell, I. A., Clarke, C. J., & Bate, M. R. 2005, *MNRAS*, 358, 291
- Dale, J. E., Ngoumou, J., Ercolano, B., & Bonnell, I. A. 2013, *MNRAS*, 436, 3430
- Dalgarno, A. & McCray, R. A. 1972, *ARA&A*, 10, 375
- de Bruijne, J. H. J. 2012, *A&SS*, 341, 31
- de Zeeuw, P. T., Hoogerwerf, R., de Bruijne, J. H. J., Brown, A. G. A., & Blaauw, A. 1999a, *AJ*, 117, 354
- de Zeeuw, P. T., Hoogerwerf, R., de Bruijne, J. H. J., Brown, A. G. A., & Blaauw, A. 1999b, *AJ*, 117, 354
- Decin, L., Cox, N. L. J., Royer, P., et al. 2012, *A&A*, 548, A113
- Deharvang, L., Schuller, F., Anderson, L. D., et al. 2010, *A&A*, 523, A6
- Deharvang, L., Zavagno, A., Anderson, L. D., et al. 2012, *A&A*, 546, A74
- Dennison, B., Simonetti, J. H., & Topasna, G. A. 1998, *PASA*, 15, 147
- Dewdney, P. E., Hall, P. J., Schilizzi, R. T., & Lazio, T. J. L. W. 2009, *IEEE Proceedings*, 97, 1482
- Diehl, R., Halloin, H., Kretschmer, K., et al. 2006, *Nature*, 439, 45
- Dolan, C. J. & Mathieu, R. D. 1999, *AJ*, 118, 2409
- Dolan, C. J. & Mathieu, R. D. 2001, *AJ*, 121, 2124
- Draine, B. 1989, in *IAU Symposium*, Vol. 135, *Interstellar Dust*, ed. L. J. Allamandola & A. G. G. M. Tielens, 313
- Draine, B. T. 1978, *ApJS*, 36, 595
- Draine, B. T. 2011a, *ApJ*, 732, 100
- Draine, B. T. 2011b, *Physics of the Interstellar and Intergalactic Medium* (Princeton University Press)
- Draine, B. T. & Li, A. 2007, *ApJ*, 657, 810
- Draine, B. T. & Salpeter, E. E. 1979, *ApJ*, 231, 77
- Dreyer, J. L. E. 1888, *MemRAS*, 49, 1
- Dufay, J. 1957, *Galactic nebulae and interstellar matter*.
- Dunne, B. C., Points, S. D., & Chu, Y.-H. 2001, *ApJS*, 136, 119
- Dyson, J. E. 1968, *A&SS*, 1, 388
- Ehlerová, S. & Palouš, J. 2005, *A&A*, 437, 101
- Elmegreen, B. G. & Lada, C. J. 1977, *ApJ*, 214, 725
- Engelbracht, C. W., Kundurthy, P., Gordon, K. D., et al. 2006, *ApJL*, 642, L127
- Evans, II, N. J., Dunham, M. M., Jørgensen, J. K., et al. 2009, *ApJS*, 181, 321
- Everett, J. E. & Churchwell, E. 2010, *ApJ*, 713, 592
- Fazio, G. G., Hora, J. L., Allen, L. E., et al. 2004, *ApJS*, 154, 10
- Ferland, G. J. 2003, *ARA&A*, 41, 517
- Field, G. B., Goldsmith, D. W., & Habing, H. J. 1969, *ApJL*, 155, L149
- Finkbeiner, D. P. 2003, *ApJS*, 146, 407
- Flagey, N., Boulanger, F., Noriega-Crespo, A., et al. 2011, *A&A*, 531, A51
- Fogel, M. E. & Leung, C. M. 1998, *ApJ*, 501, 175
- Freyer, T., Hensler, G., & Yorke, H. W. 2003, *ApJ*, 594, 888
- Frisch, P. C. & Slavin, J. D. 2013, *Earth, Planets, and Space*, 65, 175
- Fryxell, B., Olson, K., Ricker, P., et al. 2000, *ApJS*, 131, 273
- Galliano, F., Madden, S. C., Tielens, A. G. G. M., Peeters, E., & Jones, A. P. 2008, *ApJ*, 679, 310
- Gandhi, P., Isobe, N., Birkinshaw, M., et al. 2011, *PASJ*, 63, 505

- Garay, G., Rodriguez, L. F., Moran, J. M., & Churchwell, E. 1993, *ApJ*, 418, 368
- Gatto, A., Walch, S., Low, M.-M. M., et al. 2015, *MNRAS*, 449, 1057
- Gaustad, J. E., McCullough, P. R., Rosing, W., & Van Buren, D. 2001, *PASP*, 113, 1326
- Gibb, A. G. 2008, Star Formation in NGC 2068, NGC 2071, and Northern L1630, ed. B. Reipurth, 693
- Gibb, A. G., Little, L. T., Heaton, B. D., & Lehtinen, K. K. 1995, *MNRAS*, 277, 341
- Gilbert, A. M. & Graham, J. R. 2007, *ApJ*, 668, 168
- Girichidis, P., Federrath, C., Banerjee, R., & Klessen, R. S. 2011, *MNRAS*, 413, 2741
- Gontcharov, G. A. 2006, *Astronomy Letters*, 32, 759
- Güdel, M., Briggs, K. R., Montmerle, T., et al. 2008, *Science*, 319, 309
- Gudennavar, S. B., Bubbly, S. G., Preethi, K., & Murthy, J. 2012, *ApJS*, 199, 8
- Gvaramadze, V. V., Langer, N., & Mackey, J. 2012a, *MNRAS*, 427, L50
- Gvaramadze, V. V., Weidner, C., Kroupa, P., & Pflamm-Altenburg, J. 2012b, *MNRAS*, 424, 3037
- Habart, E., Abergel, A., Walmsley, C. M., Teyssier, D., & Pety, J. 2005, *A&A*, 437, 177
- Habing, H. J. 1968, *Bul. Astr. Ins. of the Neth.*, 19, 421
- Haffner, L. M., Reynolds, R. J., Tufte, S. L., et al. 2003, *ApJS*, 149, 405
- Harper-Clark, E. & Murray, N. 2009, *ApJ*, 693, 1696
- Hartmann, J. 1904, *ApJ*, 19, 268
- Hartquist, T. W., Dyson, J. E., Pettini, M., & Smith, L. J. 1986, *MNRAS*, 221, 715
- Heiles, C. 1979, *ApJ*, 229, 533
- Heiles, C. 1984, *ApJS*, 55, 585
- Heiles, C. 1987, *ApJ*, 315, 555
- Heiles, C. 2001, *ApJL*, 551, L105
- Heiles, C., Haffner, L. M., & Reynolds, R. J. 1999, in *Astronomical Society of the Pacific Conference Series*, Vol. 168, *New Perspectives on the Interstellar Medium*, ed. A. R. Taylor, T. L. Landecker, & G. Joncas, 211
- Heiles, C., Haffner, L. M., Reynolds, R. J., & Tufte, S. L. 2000, *ApJ*, 536, 335
- Henney, W. J. 2007, *How to Move Ionized Gas: An Introduction to the Dynamics of HII Regions*, ed. T. W. Hartquist, J. M. Pittard, & S. A. E. G. Falle, 103
- Henney, W. J., Arthur, S. J., & García-Díaz, M. T. 2005, *ApJ*, 627, 813
- Herbig, G. H. 1995, *ARA&A*, 33, 19
- Hernández, J., Hartmann, L., Megeath, T., et al. 2007, *ApJ*, 662, 1067
- Hernández, J., Morales-Calderon, M., Calvet, N., et al. 2010, *ApJ*, 722, 1226
- Herschel, W. 1785, *Royal Society of London Philosophical Transactions Series I*, 75, 213
- Herschel, W. 1789, *Royal Society of London Philosophical Transactions Series I*, 79, 212
- Hester, J. J., Scowen, P. A., Sankrit, R., et al. 1996, *AJ*, 111, 2349
- Heyer, M. H., Morgan, J., Schloerb, F. P., Snell, R. L., & Goldsmith, P. F. 1992, *ApJL*, 395, L99
- Hildebrand, R. H. 1983, *QJRAS*, 24, 267
- Hill, A. S., Joung, M. R., Mac Low, M.-M., et al. 2012, *ApJ*, 750, 104
- Hillenbrand, L. A. 1997, *AJ*, 113, 1733
- Hoffleit, D. & Jaschek, C. 1982, *The Bright Star Catalogue*
- Hony, S., Van Kerckhoven, C., Peeters, E., et al. 2001, *A&A*, 370, 1030
- Hopkins, P. F., Quataert, E., & Murray, N. 2011, *MNRAS*, 417, 950
- Houck, J. R., Roellig, T. L., van Cleve, J., et al. 2004, *ApJS*, 154, 18

- Howarth, I. D. & Prinja, R. K. 1989, *ApJS*, 69, 527
- Huang, J.-S., Songaila, A., Cowie, L. L., & Jenkins, E. B. 1995, *ApJ*, 450, 163
- Huenemoerder, D. P., Oskinova, L. M., Ignace, R., et al. 2012, *ApJL*, 756, L34
- Huygens, C. 1659, *Systema Saturnium*
- Iliev, I. T., Whalen, D., Mellema, G., et al. 2009, *MNRAS*, 400, 1283
- Inoue, A. K. 2002, *ApJ*, 570, 688
- Israel, F. P. 1978, *A&A*, 70, 769
- Jones, A. 2014, ArXiv e-print 1411.6666
- Jones, A. P., Tielens, A. G. G. M., & Hollenbach, D. J. 1996, *ApJ*, 469, 740
- Juvela, M. & Ysard, N. 2012, *A&A*, 539, A71
- Kahn, F. D. 1969, *Physica*, 41, 172
- Kalberla, P. M. W., Burton, W. B., Hartmann, D., et al. 2005, *A&A*, 440, 775
- Kaper, L., van Loon, J. T., Augusteijn, T., et al. 1997, *ApJL*, 475, L37
- Kapteyn, J. C. 1914, *ApJ*, 40, 43
- Kelsall, T., Weiland, J. L., Franz, B. A., et al. 1998, *ApJ*, 508, 44
- Koenig, X. P., Allen, L. E., Gutermuth, R. A., et al. 2008, *ApJ*, 688, 1142
- Kroupa, P. 2001, *MNRAS*, 322, 231
- Krumholz, M. R., Bate, M. R., Arce, H. G., et al. 2014, *Protostars and Planets VI*, eds. Henrik Beuther, Ralf S. Klessen, Cornelis P. Dullemond, and Thomas Henning (University of Arizona Press), p. 243
- Krumholz, M. R. & Matzner, C. D. 2009, *ApJ*, 703, 1352
- Krumholz, M. R., Stone, J. M., & Gardiner, T. A. 2007, *ApJ*, 671, 518
- Kudritzki, R.-P. & Puls, J. 2000, *ARA&A*, 38, 613
- Kudritzki, R. P., Puls, J., Lennon, D. J., et al. 1999, *A&A*, 350, 970
- Kurucz, R. L. 1993, *VizieR Online Data Catalog*, 6039, 0
- Kwok, S. 1975, *ApJ*, 198, 583
- Lada, C. J. & Lada, E. A. 2003, *ARA&A*, 41, 57
- Lang, W. J. & Mashedier, M. R. W. 1998, *PASA*, 15, 70
- Laor, A. & Draine, B. T. 1993, *ApJ*, 402, 441
- Lee, H.-T., Chen, W. P., Zhang, Z.-W., & Hu, J.-Y. 2005, *ApJ*, 624, 808
- Lee, T. A. 1968, *ApJ*, 152, 913
- Lenorzer, A., Mokiem, M. R., de Koter, A., & Puls, J. 2004, *A&A*, 422, 275
- Li, A. & Draine, B. T. 2001, *ApJ*, 554, 778
- Li, A. & Draine, B. T. 2002, *ApJ*, 572, 232
- Liu, B., McIntyre, T., Terzian, Y., et al. 2013, *AJ*, 146, 80
- Lopez, L. A., Krumholz, M. R., Bolatto, A. D., Prochaska, J. X., & Ramirez-Ruiz, E. 2011, *ApJ*, 731, 91
- Lopez, L. A., Krumholz, M. R., Bolatto, A. D., et al. 2014, *ApJ*, 795, 121
- Mac Low, M.-M. & McCray, R. 1988, *ApJ*, 324, 776
- Mac Low, M.-M., McCray, R., & Norman, M. L. 1989, *ApJ*, 337, 141
- Mac Low, M.-M., van Buren, D., Wood, D. O. S., & Churchwell, E. 1991, *ApJ*, 369, 395
- Maddalena, R. J. & Morris, M. 1987, *ApJ*, 323, 179
- Maddalena, R. J., Morris, M., Moscowitz, J., & Thaddeus, P. 1986, *ApJ*, 303, 375
- Madsen, G. J., Reynolds, R. J., & Haffner, L. M. 2006, *ApJ*, 652, 401
- Marcolino, W. L. F., Bouret, J.-C., Martins, F., et al. 2009, *A&A*, 498, 837
- Martin, P. G., Roy, A., Bontemps, S., et al. 2012, *ApJ*, 751, 28

- Martins, F., Mahy, L., Hillier, D. J., & Rauw, G. 2012, *A&A*, 538, A39
- Martins, F., Pomarès, M., Deharveng, L., Zavagno, A., & Bouret, J. C. 2010, *A&A*, 510, A32
- Martins, F., Schaerer, D., & Hillier, D. J. 2005a, *A&A*, 436, 1049
- Martins, F., Schaerer, D., Hillier, D. J., & Heydari-Malayeri, M. 2004, *A&A*, 420, 1087
- Martins, F., Schaerer, D., Hillier, D. J., et al. 2005b, *A&A*, 441, 735
- Mathews, W. G. 1969, *ApJ*, 157, 583
- Mathis, J. S., Rumpl, W., & Nordsieck, K. H. 1977, *ApJ*, 217, 425
- McCrary, N. & Graham, J. R. 2007, *ApJ*, 663, 844
- McCray, R. & Kafatos, M. 1987, *ApJ*, 317, 190
- McKee, C. 1989, in IAU Symposium, Vol. 135, Interstellar Dust, ed. L. J. Allamandola & A. G. G. M. Tielens (Dordrecht: Kluwer)
- McKee, C. F. & Ostriker, J. P. 1977, *ApJ*, 218, 148
- Megeath, S. T., Gutermuth, R., Muzerolle, J., et al. 2012, *AJ*, 144, 192
- Mennella, V., Colangeli, L., & Bussoletti, E. 1995, *A&A*, 295, 165
- Menten, K. M., Reid, M. J., Forbrich, J., & Brunthaler, A. 2007, *A&A*, 474, 515
- Messier, C. 1771, Catalogue des Nébuleuses des amas d'Étoiles
- Molinari, S., Swinyard, B., Bally, J., et al. 2010, *PASP*, 122, 314
- Morrison, R. & McCammon, D. 1983, *ApJ*, 270, 119
- Murray, N., Quataert, E., & Thompson, T. A. 2005, *ApJ*, 618, 569
- Najarro, F., Hanson, M. M., & Puls, J. 2011, *A&A*, 535, A32
- Najarro, F., Kudritzki, R.-P., Hillier, D. J., et al. 1998, in Astronomical Society of the Pacific Conference Series, Vol. 131, Properties of Hot Luminous Stars, ed. I. Howarth, 57
- Narayan, R. 1987, *ApJ*, 319, 162
- Neugebauer, G., Habing, H. J., van Duinen, R., et al. 1984, *ApJL*, 278, L1
- Norman, C. A. & Ikeuchi, S. 1989, *ApJ*, 345, 372
- Ochsendorf, B. B., Cox, N. L. J., Krijt, S., et al. 2014a, *A&A*, 563, A65
- Ochsendorf, B. B. & Tielens, A. G. G. M. 2015, *A&A*, 576, A2
- Ochsendorf, B. B., Verdolini, S., Cox, N. L. J., et al. 2014b, *A&A*, 566, A75
- O'Dell, C. R. 2001, *ARA&A*, 39, 99
- O'Dell, C. R., Ferland, G. J., Porter, R. L., & van Hoof, P. A. M. 2011, *ApJ*, 733, 9
- O'Dell, C. R., Henney, W. J., Abel, N. P., Ferland, G. J., & Arthur, S. J. 2009, *AJ*, 137, 367
- O'Dell, C. R., Wen, Z., & Hu, X. 1993, *ApJ*, 410, 696
- Ormel, C. W., Paszun, D., Dominik, C., & Tielens, A. G. G. M. 2009, *A&A*, 502, 845
- Ossenkopf, V. & Henning, T. 1994, *A&A*, 291, 943
- Osterbrock, D. E. & Ferland, G. J. 2006, *Astrophysics of gaseous nebulae and active galactic nuclei* (University Science Books)
- Ott, S. 2010, in Astronomical Society of the Pacific Conference Series, Vol. 434, Astronomical Data Analysis Software and Systems XIX, ed. Y. Mizumoto, K.-I. Morita, & M. Ohishi, 139
- Paladini, R., Umana, G., Veneziani, M., et al. 2012, *ApJ*, 760, 149
- Pannekoek, A. 1929, *Publications of the Astronomical Institute of the University of Amsterdam*, 2, 1
- Paradis, D., Paladini, R., Noriega-Crespo, A., et al. 2011, *ApJ*, 735, 6

- Parker, Q. A. & Phillipps, S. 1998, *PASA*, 15, 28
- Pavel, M. D. & Clemens, D. P. 2012, *ApJ*, 760, 150
- Pellegrini, E. W., Baldwin, J. A., & Ferland, G. J. 2011, *ApJ*, 738, 34
- Peri, C. S., Benaglia, P., Brookes, D. P., Stevens, I. R., & Isequilla, N. L. 2012, *A&A*, 538, A108
- Peri, C. S., Benaglia, P., & Isequilla, N. L. 2015, ArXiv e-prints
- Perryman, M. A. C., de Boer, K. S., Gilmore, G., et al. 2001, *A&A*, 369, 339
- Perryman, M. A. C., Lindegren, L., Kovalevsky, J., et al. 1997, *A&A*, 323, L49
- Petrosian, V. 1973, in IAU Symposium, Vol. 52, *Interstellar Dust and Related Topics*, ed. J. M. Greenberg & H. C. van de Hulst, 445
- Pirogov, L. E. 2009, *Astronomy Reports*, 53, 1127
- Planck Collaboration, Abergel, A., Ade, P. A. R., et al. 2014a, *A&A*, 571, A11
- Planck Collaboration, Ade, P. A. R., Aghanim, N., et al. 2014b, ArXiv e-print 1409.2495
- Planck Collaboration, Ade, P. A. R., Aghanim, N., et al. 2014c, *A&A*, 571, A1
- Planck Collaboration, Ade, P. A. R., Aghanim, N., et al. 2011, *A&A*, 536, A23
- Plekan, O., Cassidy, A., Balog, R., Jones, N. C., & Field, D. 2011, *Physical Chemistry Chemical Physics (Incorporating Faraday Transactions)*, 13, 21035
- Poglitsch, A., Waelkens, C., Geis, N., et al. 2010, *A&A*, 518, L2
- Pomarès, M., Zavagno, A., Deharveng, L., et al. 2009, *A&A*, 494, 987
- Pon, A., Johnstone, D., Bally, J., & Heiles, C. 2014a, *MNRAS*, 444, 3657
- Pon, A., Johnstone, D., Bally, J., & Heiles, C. 2014b, *MNRAS*, 441, 1095
- Povich, M. S., Stone, J. M., Churchwell, E., et al. 2007, *ApJ*, 660, 346
- Puls, J., Kudritzki, R.-P., Herrero, A., et al. 1996, *A&A*, 305, 171
- Puls, J., Vink, J. S., & Najarro, F. 2008, *A&A Reviews*, 16, 209
- Raga, A. C., Cantó, J., & Rodríguez, L. F. 2012, *Rev. Mexicana Astron. Astrofis.*, 48, 199
- Raicevic, M. 2010, PhD thesis
- Rathborne, J. M., Jackson, J. M., & Simon, R. 2006, *ApJ*, 641, 389
- Reich, W. 1978, *A&A*, 64, 407
- Reynolds, R. J. & Ogden, P. M. 1979, *ApJ*, 229, 942
- Rieke, G. H., Young, E. T., Engelbracht, C. W., et al. 2004, *ApJS*, 154, 25
- Rijkhorst, E.-J., Plewa, T., Dubey, A., & Mellema, G. 2006, *A&A*, 452, 907
- Rogers, H. & Pittard, J. M. 2013, *MNRAS*, 431, 1337
- Rosenberg, M. J. F., Berné, O., Boersma, C., Allamandola, L. J., & Tielens, A. G. G. M. 2011, *A&A*, 532, A128
- Roussel, H. 2012, ArXiv e-prints
- Salgado, F., Berné, O., Adams, J. D., et al. 2012, *ApJL*, 749, L21
- Sandstrom, K. M., Bolatto, A. D., Bot, C., et al. 2012, *ApJ*, 744, 20
- Sandstrom, K. M., Peek, J. E. G., Bower, G. C., Bolatto, A. D., & Plambeck, R. L. 2007, *ApJ*, 667, 1161
- Schaerer, D. & de Koter, A. 1997, *A&A*, 322, 598
- Schlafly, E. F., Green, G., Finkbeiner, D. P., et al. 2014, *ApJ*, 786, 29
- Schlafly, E. F., Green, G., Finkbeiner, D. P., et al. 2015, *ApJ*, 799, 116
- Sheets, H. A., Bolatto, A. D., van Loon, J. T., et al. 2013, *ApJ*, 771, 111
- Sherry, W. H., Walter, F. M., & Wolk, S. J. 2004, *AJ*, 128, 2316
- Shu, F. H. 1992, *The physics of astrophysics. Volume II: Gas dynamics*.
- Silich, S. & Tenorio-Tagle, G. 2013, *ApJ*, 765, 43

- Silich, S. A., Tenorio-Tagle, G., Terlevich, R., Terlevich, E., & Netzer, H. 2001, *MNRAS*, 324, 191
- Simón-Díaz, S., Caballero, J. A., & Lorenzo, J. 2011, *ApJ*, 742, 55
- Simpson, R. J., Povich, M. S., Kendrew, S., et al. 2012, *MNRAS*, 424, 2442
- Smith, J. D. T., Armus, L., Dale, D. A., et al. 2007, *PASP*, 119, 1133
- Snowden, S. L., Burrows, D. N., Sanders, W. T., Aschenbach, B., & Pfeffermann, E. 1995, *ApJ*, 439, 399
- Snowden, S. L., Egger, R., Freyberg, M. J., et al. 1997, *ApJ*, 485, 125
- Sod, G. A. 1978, *Journal of Computational Physics*, 27, 1
- Sofia, U. J., Lauroesch, J. T., Meyer, D. M., & Cartledge, S. I. B. 2004, *ApJ*, 605, 272
- Spitzer, L. 1962, *Physics of Fully Ionized Gases*
- Spitzer, L. 1978, *Physical processes in the interstellar medium* (New York Wiley-Interscience)
- Stanke, T., Smith, M. D., Gredel, R., & Szokoly, G. 2002, *A&A*, 393, 251
- Steinacker, J., Pagani, L., Bacmann, A., & Guieu, S. 2010, *A&A*, 511, A9
- Strömgren, B. 1939, *ApJ*, 89, 526
- Swinyard, B., Nakagawa, T., Merken, P., et al. 2009, *Experimental Astronomy*, 23, 193
- Szczepanski, J. & Vala, M. 1993, *ApJ*, 414, 646
- Tenorio-Tagle, G. 1979, *A&A*, 71, 59
- Thompson, M., Beuther, H., Dickinson, C., et al. 2015, in *Advancing Astrophysics with the Square Kilometre Array (AASKA14)*, 126
- Tielens, A. G. G. M. 1983, *ApJ*, 271, 702
- Tielens, A. G. G. M. 1998, *ApJ*, 499, 267
- Tielens, A. G. G. M. 2005, *The Physics and Chemistry of the Interstellar Medium* (Cambridge University Press)
- Tielens, A. G. G. M. 2008, *ARA&A*, 46, 289
- Tielens, A. G. G. M. 2013, *Interstellar PAHs and Dust*, ed. T. D. Oswalt & G. Gilmore (Springer Science+Business Media Dordrecht)
- Tielens, A. G. G. M. & Hollenbach, D. 1985, *ApJ*, 291, 722
- Tielens, A. G. G. M., McKee, C. F., Seab, C. G., & Hollenbach, D. J. 1994, *ApJ*, 431, 321
- Toalá, J. A. & Arthur, S. J. 2011, *ApJ*, 737, 100
- Toalá, J. A. & Guerrero, M. A. 2013, *A&A*, 559, A52
- Toalá, J. A., Guerrero, M. A., Chu, Y.-H., et al. 2012, *ApJ*, 755, 77
- Townsend, L. K., Feigelson, E. D., Montmerle, T., et al. 2003, *ApJ*, 593, 874
- Trumpler, R. J. 1930, *Lick Observatory Bulletin*, 14, 154
- Turner, J. L. 2009, *Extreme Star Formation*, ed. H. A. Thronson, M. Stiavelli, & A. Tielens, 215
- van Boekel, R., Waters, L. B. F. M., Dominik, C., et al. 2003, *A&A*, 400, L21
- van Buren, D. 1986, *ApJ*, 306, 538
- van Buren, D. 1993, in *Astronomical Society of the Pacific Conference Series*, Vol. 35, *Massive Stars: Their Lives in the Interstellar Medium*, ed. J. P. Cassinelli & E. B. Churchwell, 315
- van Buren, D., Mac Low, M.-M., Wood, D. O. S., & Churchwell, E. 1990, *ApJ*, 353, 570
- van Buren, D. & McCray, R. 1988, *ApJL*, 329, L93
- van Buren, D., Noriega-Crespo, A., & Dgani, R. 1995, *AJ*, 110, 2914
- van der Werf, P. P., Goss, W. M., & O'Dell, C. R. 2013, *ApJ*, 762, 101

- van Leeuwen, F. 2007, *A&A*, 474, 653
- van Loon, J. T. & Oliveira, J. M. 2003, *A&A*, 405, L33
- Veilleux, S., Cecil, G., & Bland-Hawthorn, J. 2005, *ARA&A*, 43, 769
- Veneziani, M., Ade, P. A. R., Bock, J. J., et al. 2010, *ApJ*, 713, 959
- Verdolini, S. 2014, PhD thesis
- Vink, J. S., de Koter, A., & Lamers, H. J. G. L. M. 2000, *A&A*, 362, 295
- Walch, S., Whitworth, A. P., Bisbas, T. G., Wünsch, R., & Hubber, D. A. 2013, *MNRAS*, 435, 917
- Walch, S. K., Whitworth, A. P., Bisbas, T., Wünsch, R., & Hubber, D. 2012, *MNRAS*, 427, 625
- Walker, A. R. 2012, *A&SS*, 341, 43
- Wall, W. F., Reach, W. T., Hauser, M. G., et al. 1996, *ApJ*, 456, 566
- Warren, Jr., W. H. & Hesser, J. E. 1977, *ApJS*, 34, 115
- Warren, Jr., W. H. & Hesser, J. E. 1978, *ApJS*, 36, 497
- Watson, C., Povich, M. S., Churchwell, E. B., et al. 2008, *ApJ*, 681, 1341
- Weaver, R., McCray, R., Castor, J., Shapiro, P., & Moore, R. 1977, *ApJ*, 218, 377
- Weingartner, J. C. & Draine, B. T. 2001, *ApJ*, 548, 296
- Weingartner, J. C., Draine, B. T., & Barr, D. K. 2006, *ApJ*, 645, 1188
- Welty, D. E., Jenkins, E. B., Raymond, J. C., Mallouris, C., & York, D. G. 2002, *ApJ*, 579, 304
- Wen, Z. & O'Dell, C. R. 1995, *ApJ*, 438, 784
- Whitworth, A. 1979, *MNRAS*, 186, 59
- Wilkin, F. P. 1996, *ApJL*, 459, L31
- Williams, J. P. & McKee, C. F. 1997, *ApJ*, 476, 166
- Willis, R. F., Feuerbacher, B., & Fitton, B. 1973, in IAU Symposium, Vol. 52, Interstellar Dust and Related Topics, ed. J. M. Greenberg & H. C. van de Hulst, 303
- Wilson, B. A., Dame, T. M., Masheder, M. R. W., & Thaddeus, P. 2005, *A&A*, 430, 523
- Wilson, R. W., Jefferts, K. B., & Penzias, A. A. 1970, *ApJL*, 161, L43
- Wilson, T. L., Filges, L., Codella, C., Reich, W., & Reich, P. 1997, *A&A*, 327, 1177
- Wood, D. O. S. & Churchwell, E. 1989, *ApJS*, 69, 831
- Wright, E. L., Eisenhardt, P. R. M., Mainzer, A. K., et al. 2010, *AJ*, 140, 1868
- Yorke, H. W. 1986, *ARA&A*, 24, 49
- Yorke, H. W. & Sonnhalter, C. 2002, *ApJ*, 569, 846
- Zavagno, A., Pomarès, M., Deharveng, L., et al. 2007, *A&A*, 472, 835
- Zinnecker, H. & Yorke, H. W. 2007, *ARA&A*, 45, 481

Curriculum Vitae

I was born on May 8, 1986 on the countryside of the municipality of Wijhe, the Netherlands, where I enjoyed most of my childhood. After moving to Schalkhaar and finishing high school in Deventer, I took a year off to retreat and prepare myself to make a well-thought decision for my future path.

I decided to move to Amsterdam to study Physics & Astronomy in 2005, a track that I finished 6 years later with a Master's thesis on massive star formation in collaboration with prof. dr. Lex Kaper. During the last year of my study, I was fortunate enough to be offered a position at the University of Leiden to work together with prof. dr. Xander Tielens on studying the photo-chemistry of polycyclic aromatic hydrocarbons, which I started in the fall of 2011. Due to several unforeseen factors, in particular because of my amazement after witnessing awe-inspiring images of the infrared sky, I quickly diverted from the path that was laid out for my years at the Sterrewacht. Instead, I started to study the interaction of stars with the interstellar medium of galaxies using multi-wavelength observations, a choice that has led to the very existence of this thesis. During my PhD, I have been a teaching assistant for the course Special Relativity during three academic years and co-supervised a master's thesis project. I have led successful observing proposals and performed on-site observations with the Isaac Newton Telescope on La Palma and twice with the Very Large Telescope in Chili. Lastly, I have visited my collaborators and presented my work in the Netherlands, France, Germany, Austria, and various institutes throughout the United States.

In the fall of 2015, I will move to the United States to continue my research on star formation and the interstellar medium at the Johns Hopkins University in Baltimore, Maryland.

Publications

1st author:

- [1] **B. B. Ochsendorf**, A. G. A. Brown, J. Bally & A. G. G. M. Tielens
'*Nested shells reveal the rejuvenation of the Orion-Eridanus superbubble*'
ApJ, 808, 111 (2015)
- [2] **B. B. Ochsendorf** & A. G. G. M. Tielens
'*A bimodal dust grain distribution in the IC 434 H II region*'
A&A 576, A2 (2015)
- [3] **B. B. Ochsendorf**, S. Verdolini, N. L. J. Cox, O. Berné, L. Kaper & A. G. G. M. Tielens
'*Radiation-pressure-driven dust waves inside bursting interstellar bubbles*'
A&A 566, A75 (2014)
- [4] **B. B. Ochsendorf**, N. L. J. Cox, S. Krijt, F. Salgado, O. Berné, J. P. Bernard, L. Kaper & A. G. G. M. Tielens
'*Blowing in the wind: The dust wave around σ Ori AB*'
A&A 563, A65 (2014)
- [5] **B. B. Ochsendorf**, L. E. Ellerbroek, R. Chini, O. E. Hartoog, V. Hoffmeister, L. B. F. M. Waters & L. Kaper
'*First firm spectral classification of an early-B pre-main-sequence star: B275 in M 17*'
A&A 536, L1 (2011)

2^{nd+} author:

- [6] M. Kama, E. Caux, A. Lopez-Sepulcre, V. Wakelam, C. Dominik, C. Ceccarelli, M. Lanza, F. Lique, **B. B. Ochsendorf**, D. C. Lis, R. N. Caballero & A. G. G. M. Tielens
'*Depletion of chlorine into HCl ice in a protostellar core*'
A&A 574, A107 (2015)
- [7] N. L. J. Cox, J. Cami, L. Kaper, P. Ehrenfreund, B. H. Foing, **B. B. Ochsendorf**, S. H. M. van Hooff & F. Salama
'*VLT/X-shooter survey of near-infrared diffuse interstellar bands*'
A&A 569, A117 (2014)
- [8] L. Kaper, L. Ellerbroek, **B. B. Ochsendorf** & R. N. Caballero
'*Studying the formation of massive stars with VLT/X-shooter*'
AN 332, 3, 232 (2011)
- [9] B. Acke, M. Min, M. E. van den Ancker, J. Bouwman, **B. B. Ochsendorf**, A. Juhasz & L. B. F. M. Waters
'*On the interplay between flaring and shadowing in disks around Herbig Ae/Be stars*'
A&A 502, L17-L20 (2009)

Nederlandse samenvatting

Het interstellaire medium

Orion is een van de meest herkenbare constellaties aan de winterse sterrenhemel. Het welbekende zandloperfiguur van Orion staat helder en imposant tussen andere sterren in het gebied. Het menselijk oog is echter alleen gevoelig voor een klein gedeelte van het elektromagnetische spectrum. Wat aan het blote oog voorbijgaat zijn bijvoorbeeld gamma-, röntgen-, ultraviolet-, infrarood, en radiostraling. Orion laat zich van zijn beste kant zien in vele van deze golflengte regimes. Neem het (verre) infrarood (figuur 1), waarin recente ruimtetelescopen zoals *Spitzer*, *Herschel*, en *Planck* een beeld registreren waarover zelfs Christiaan Huygens en Charles Messier niet hadden kunnen dromen na hun ontdekking van de Orionnevel in zichtbaar licht. In het infrarood lijkt Orion in vuur en vlam te staan, waar chaotische en complexe structuren zich door elkaar strengelen. Deze ingewikkelde structuren zijn waarschijnlijk het gevolg van interacties van sterren met de materie die tussen de sterren ligt. Inderdaad, de ruimte tussen de sterren is niet leeg, maar bestaat uit een ijl plasma van atomen, moleculen, en stof (kleine deeltjes van silicaat, koolstof, en ijs). We noemen deze ruimte het *interstellaire medium* (ISM).

De moleculen en het stof in het ISM lichten op door sterlicht te absorberen en deze opnieuw uit te stralen in het infrarood. Zoals figuur 6.1 duidelijk laat zien geven het stof en de moleculen een goede weergave over de structuur van het ISM in Orion, welke erg complex blijkt te zijn op alle waarneembare niveaus. De moleculen die we in dit figuur zien zijn Polycyclische Aromatische Koolwaterstoffen (PAKs), geraamtes van hexagonale koolstofringen met waterstofatomen aan de randen. Deze PAKs hebben ultraviolet fotonen nodig om te fluoriseren. Fotonen met deze energie worden snel geabsorbeerd door materie, waardoor de PAKs alleen de buitenste randen van de wolken in het ISM laten zien. Stof daarentegen kan verhit worden door allerlei soorten fotonen, ook door diegene met minder energie. De minder energetische fotonen kunnen tot diep in dezelfde wolken reiken. Samen geven de PAKs en het stof een zeer gedetailleerd beeld hoe het ISM in Orion is opgebouwd.

Interstellair stof maakt ongeveer 1 procent op van de totale massa van materie in het ISM, de overige 99 procent ligt in het gas. Ondanks de kleine hoeveelheid massa die stof omvangt vergeleken met het gas, is het een erg belangrijke component van het ISM. Stof absorbeert sterlicht en zendt deze opnieuw uit op langere golflengtes, zoals in het infrarood. De aanwezigheid van stof in het ISM zorgt ervoor dat het licht van achtergelegen objecten zwakker wordt. Daarnaast kan het oppervlakte van stofkorrels als een katalysator dienen voor vele chemische reacties. Stofkorrels kunnen ook als een schild dienen om bepaalde moleculen te beschermen tegen de hoog-energetische fotonen van sterren. Verder kunnen de mantels van stofkorrels elementen vasthouden en loslaten als gevolg van veranderingen in de fysische eigenschappen van hun omgeving. Op deze manier bepalen ze de gas abundanties, en daarmee de koeling van het ISM, omdat deze gassen energie wegstralen door lijnemissie wanneer ze in de gasfase terechtkomen. Tegelijkertijd speelt het foto-elektrisch effect op het oppervlakte van stofkorrels een dominante rol in de verhitte van het ISM. Interstellair stof is daarom op vele vlakken een belangrijke pion in de fysische en chemische structuur van het ISM. Desondanks weten we

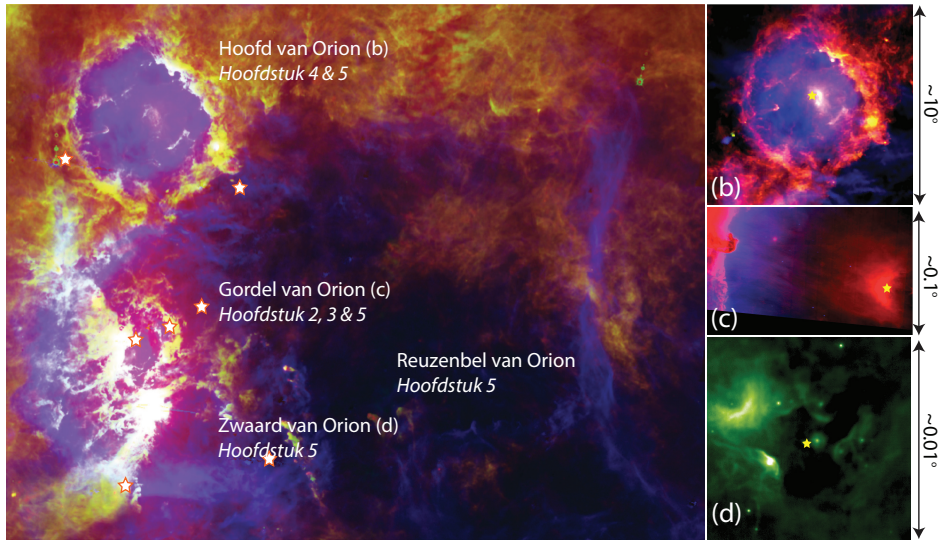


Figure 6.1: (a) Een drie-kleuren figuur van het Orion-Eridanus gebied. Het blauw geeft geïoniseerd gas weer, terwijl het groen Polycyclische Aromatische Koolwaterstoffen (PAKs) laten zien. Rood laat koude stofkorrels zien op een temperatuur van ongeveer 20 Kelvin. De PAKs volgen de geïllumineerde randen van de wolken van koud stof, zodat groen en rood hier samen geel vormen. De grootte van dit beeld is ongeveer 28 bij 38 graden aan de hemel (vergelijk: de volle maan heeft een diameter van ongeveer 0.5 graden). De herkenbare sterren van het sterrenbeeld Orion zijn weergegeven, en expliciet genoemd zijn gebieden die het onderwerp vormen van verschillende hoofdstukken in dit proefschrift. (b) - (d): Infrarood boogvormige structuren zijn te zien rond sterren in Orion (gele asterisken) op elke waarneembare schaal. De boogstructuren zijn *stofgolven* die oplichten door stofkorrels die verhit worden door de centrale ster. Figuur (b) heeft een diameter van 10 graden en laat het gebied van λ Ori zien, het 'hoofd van Orion'. Figuur (c) is van de grootte van enkele tientallen boogminuten en laat de ster σ Ori zien in de 'gordel van Orion'. Rechtsboven zien we ook de beroemde paardenkopnevel. Figuur (d) is enkele tientallen boogseconden groot, en is gefocust op de ster θ^1 Ori C, de meest massieve ster in het 'zwaard van Orion', verantwoordelijk voor de ionisatie van de Orionnevel (hoofdstuk 1 & 5). De stofgolven kunnen worden gebruikt om de interacties tussen sterren en het ISM te bestuderen en geven weer hoe belangrijk de beweging van materie in het ISM is.

eigenlijk nog niet goed wat de precieze eigenschappen van stof in het ISM zijn.

De interacties tussen sterren en materie in het interstellair medium

Ook al zijn er maar een aantal dozijn sterren in Orion met het blote oog te zien, weten we tegenwoordig dat in de afgelopen 15 miljoen jaar ongeveer tienduizend sterren zich hebben gevormd in Orion. Deze stergroep in zijn geheel noemen we de Orion OB associatie. Het interessante is dat deze sterren zich hebben gevormd in groepen of clusters afzonderlijk van elkaar in de tijd. In elke groep vormen zich zware en minder zware sterren. De meest zware zullen zich het meest snel ontwikkelen, en ook het meest snel sterven. Zware sterren ioniseren het gas om hen heen met hoog-energetische fotonen. Het geïoniseerde gas zal een temperatuur van ongeveer 10.000 Kelvin bereiken, wat erg hoog

is vergeleken met het neutrale materiaal eromheen (wat hooguit 100 Kelvin bereikt). De druk van het geïoniseerde gebied, wat astronomen een H II gebied noemen, zal daarom veel hoger zijn vergeleken met het omliggende neutrale gebied: het geïoniseerde gebied zal expanderen. Tijdens zijn leven blaast een zware ster als het ware een bel van geïoniseerd materiaal in het ISM. Daarnaast verliezen zware sterren tijdens hun leven veel materie en accelereren ze deze met hun straling tot intense sterwinden. Tenslotte zal een ster die minstens acht maal zo zwaar is als onze Zon zijn leven eindigen in een spectaculaire explosie: een supernova. Een zware ster zal door de voorgenoemde processen de structuur en beweging van het nabije ISM bepalen.

Naast het ioniseren van het gas, sterwinden, en supernovae kunnen sterren op nog een andere manier de materie van het ISM in beweging te zetten. De straling van de ster is veruit de grootste bron van energie van een ster, en een groot deel wordt opgebruikt in het ioniseren van het omliggende gas. Deze energie zal voornamelijk worden uitgestraald en wordt niet gebruikt in de dynamiek van het ISM. Echter, de fotonen dragen ook *stralingsdruk* met zich mee. Wanneer de fotonen opgevangen worden, danwel door het gas, danwel door het stof, zullen ze stralingsdruk overdragen in de vorm van momentum. Omdat stofdeeltjes typisch een fractie van een micrometer groot zijn (10^{-6} meter), terwijl bijvoorbeeld een waterstofaatom van de orde van een tiende nanometer groot is (10^{-10} meter), zijn de stofdeeltjes veel efficiënter in het absorberen van stralingsdruk. Wanneer het foton wordt geabsorbeerd, zal er momentum worden overgebracht naar het stofdeeltje, en deze zal worden geaccelereerd. Hierna kan het stof botsen met de zwerm van gasdeeltjes om zich heen, waardoor ook het gas in beweging wordt gezet. Stof kan zo indirect stralingsdruk omzetten in de beweging van materie in het ISM. Echter, dit mechanisme is niet goed begrepen en hangt van vele factoren af, met name de structuur en de compositie van het stof in het ISM.

Zware sterren zijn erg zeldzaam vergeleken met minder zware sterren. Echter, op de bovengescreven manieren bepalen ze de structuur en de evolutie van het ISM met de energie die gepaard gaat met hun fotonen, sterwinden, en supernovae. De vrijgekomen energie veroorzaakt schokgolven welke de materie om de sterren in beweging zet. De overdracht van momentum via stralingsdruk op het stof kan ook een belangrijke bijdrage hierin leveren. De materie wordt opgeveegd en samengeperst in expanderende schillen. Deze schillen kunnen afkoelen en fragmenteren, en in de individuele klonten van materie kunnen nieuwe groepen van sterren zich vormen. De dood van de ene ster kan dus tot de geboorte van een ander leiden. Dit proces noemen we sequentiële stervorming, en dit is wat we denken dat de groepvorming in de Orion OB associatie kan verklaren.

Dit proefschrift

Fotonen, sterwinden, en supernovae zijn dus allemaal bronnen van energie waardoor er een terugkoppeling ontstaat vanuit de sterren met het gas en het stof in het ISM. Deze terugkoppelingen hebben niet alleen het ISM in Orion, maar ook die in de gehele Melkweg zijn complexe en chaotische uiterlijk gegeven (hoofdstuk 1). Er zijn echter nog vele vragen die nog steeds onbeantwoord blijven. Hoe vormen zware sterren zich, en hoe bepalen ze de structuur van het ISM? Wat zijn de relatieve contributies van terugkoppeling naar het ISM via hun sterwinden, supernovae, en de overdracht van momentum via interstellair stof? Wat zijn de precieze eigenschappen van interstellair stof, en hoe evolueert het als het tussen moleculaire wolken en het diffuse ISM beweegt?

In dit proefschrift proberen we vele van deze vragen te beantwoorden door gebruik te maken van observaties van Orion, een van de meest en best bestudeerde gebieden aan de hemel. Ondanks de complexe structuur van Orion kan het op een zeer gedetailleerde manier bestudeerd worden. Dit komt omdat Orion uit het vlak van de Melkweg staat, zodat er weinig voorgrond of achtergrond materiaal is die niet tot het gebied hoort. Orion staat ook relatief dichtbij, zodat we erg gedetailleerde beelden kunnen verkrijgen van het gebied. Daarnaast geeft de nabijheid de mogelijkheid om de beweging van sterren in de Orion OB associatie in kaart te brengen, om zo een driedimensionaal beeld te krijgen van de sterren en hun relatie tot de materie in het ISM van Orion.

In hoofdstuk 2 en 3 van dit proefschrift bouwen we een model om de interactie van een ster met een geïoniseerde stroom van gas te bestuderen. Deze stroom van gas trekt stof met zich mee door momentum overdracht. Wanneer het stof richting de ster beweegt, zal het onder invloed van stralingsdruk afremmen, terwijl het gas het stof zal blijven proberen te accelereren. De balans tussen de krachten bepaalt de beweging van het stofdeeltje, wat uiteindelijk resulteert in een boogvormige distributie van stof om een ster. Deze boogstructuren zijn te zien op alle schalen in Orion (Figuur 1b, 1c, en 1d), en noemen we *stofgolven*. In hoofdstuk 2 en 3 laten we zien dat stofgolven een unieke kans geven om interstellair stof op een nieuwe manier te bestuderen. We bepalen vervolgens enkele belangrijke eigenschappen van het stof in Orion, en laten zien dat de resultaten de validiteit van bestaande modellen van interstellair stof op de proef stellen.

In hoofdstuk 4 laten we zien dat stofgolven overal in de Melkweg te zien zijn, en dan met name binnen de H II gebieden of interstellaire bellen welke zware sterren blazen tijdens hun leven. De fysische condities van interstellaire bellen zijn ideaal voor het vormen van stofgolven. Stofgolven geven een verklaring voor de aanwezigheid en morfologie van stof binnen H II gebieden, en geven direct bewijs dat de bellen aan het leeglopen zijn, en zo hun druk in het omliggende medium dissiperen. We onderzoeken welke fysische parameters belangrijk zijn in de koppeling tussen het stof en het gas, en onder welke omstandigheden stralingsdruk belangrijk kan zijn in de dynamische structuur van het ISM.

In hoofdstuk 5 bestuderen we de Orion-Eridanus reuzenbel, een gigantische variant van een interstellaire bel die is ontstaan door de gezamenlijke effecten van ionisatie, sterwinden, stralingsdruk, en supernovae vanuit de Orion OB associatie. We gebruiken data van de nieuwste telescopen om zo een nieuw beeld te schetsen over de morfologie en evolutie van het gehele gebied. De data laat zien dat de Orion-Eridanus reuzenbel nog groter en complexer is dan dat eerder werd gedacht, en dat de totale morfologie beschreven kan worden als een serie van schillen die in elkaar genesteld zijn. De genestelde schillen zijn het gevolg van materiaal dat evaporeert van de moleculaire wolken in Orion, welke vervolgens word opgeveegd door een supernova in een expanderende schil. De supernovae en expanderende schillen ruimen zo de boel op in het centrale gedeelte van de reuzenbel en verplaatsen vervolgens het materiaal naar de buitenkant, waar het samensmelt met de buitenste rand van de reuzenbel. De cyclus van stervorming, evaporatie, en de schoonmaak van het centrale gedeelte van de reuzenbel door supernovae gaat door totdat de moleculaire wolken compleet zijn geëvaporeert of uiteengereten zijn, waarna de reuzenbel zal samensmelten met het ISM.

In een zin samengevat richt dit proefschrift zich op een verbeterd begrip over het samenspel van sterren met het gas en stof in het ISM, door het sterrenbeeld Orion als voorbeeld te nemen.

Acknowledgements

This PhD thesis is the culmination of exactly one decade of a steep but steady path in my attempt to master as many facets of astronomy as possible. In retrospect, I can say that it has been a great ride. I feel very fortunate that I spend much of my time doing what I love to do. However, there have been numerous occasions that I have leaned on the professionalism, insightfulness, kindness, or support of my family, friends, colleagues, and supervisors. It is here that I take the opportunity to acknowledge the contributions that have mattered.

From the start of my study ‘Physics & Astronomy’ at the University of Amsterdam, I knew that I was bound for the astronomy track. A special thanks here to my thesis supervisors throughout the years. Rens, your enthusiasm about even my most trivial findings during my Bachelor’s thesis research have always amazed me; thank you for luring me into the ‘low-energy’ side of astrophysics. Lex, you are an incredible manager, and your motivation and kind touch during my Master’s thesis research gave me the confidence to apply for a PhD position in Leiden. Co-supervisor Lucas, thanks for the endless stream of IDL scripts. You have written an amazing book on planet-hunting. Xander, thank you for giving the opportunity to pursue and distill my scientific interests during my PhD years, while not losing sight of squeezing the scientific best out of me. Each of you have had a profound impact on the way I view and conduct science.

The atmosphere at the sterrewacht is great for conducting research, but is also made very comfortable through the presence of my fellow PhD students and various postdoctoral researchers, in particular, my officemates at Huygens Lab 426: Ainil, Lynn, Pablo, Pedro, and Suklima. Also thanks to the rest of the ISM group. Alessandra, Alex (2x), Carl, Caroline, Francisco, Heather, Irene, Koen, Matteo, Mattia, Mihkel, Monica, Tiffany, and of course Marissa: thanks for the much-needed distractions in and around the observatory. Special thanks to Sebastiaan: it has been a pleasure sharing this path with you over the past ten years that has led us from the infamous exams of quantum physics, via ice blizzards on the slopes of Roque de los Muchachos, to being each other’s paronymph. I have no hesitation in saying that you will make a great astronomer.

My friends in Amsterdam, many of which that have been with me since my time in Deventer. Kim, Lode, Karel, Joris, Sezayi, Matthijs, Erik, Pieter, Isabelle, Barbara, Florie, Jacob, Tommy, Tomas, and many others: thanks for all those good memories. Please keep the nest warm while we are away.

Chris, Frank, and Gijs: growing up with three big brothers to look up against has taught me to always aim high. It is remarkable to see how we all have chosen our own unique paths. Mum and dad, your daring and adventurous move to leave the Netherlands for another place far, far, away is an example for many, showing that it is never too late to follow a dream. It is interesting to see how the strength of a relationship can be correlated with distance separated from one another. I hope we can all stay in close contact, even though we will soon be spread out over even more continents.

Jule, you came and dictated our lives in a fantastic way. No matter what kind of day I went through, one smile from you puts everything in perspective. Angie, you are the one thing that holds everything together. A simple acknowledgement does not even get near the gratitude that you deserve. *Te amo.*

